

MEMOIRS  
OF THE  
FACULTY OF ENGINEERING  
OSAKA CITY UNIVERSITY

---

VOL. 55

---

DECEMBER 2014

PUBLISHED BY THE  
GRADUATE SCHOOL OF ENGINEERING  
OSAKA CITY UNIVERSITY

This Memoirs is annually issued. Selected original works of the members of the Faculty of Engineering are compiled herein. Abstracts of paper presented elsewhere during the current year are also compiled in the latter part of the volume.

All communications with respect to Memoirs should be addressed to:

Dean of the Graduate School of Engineering  
Osaka City University  
3-3-138, Sugimoto, Sumiyoshi-ku  
Osaka 558-8585, Japan

Editors

Kouichi TSUJI

Tatsurou WAKIMOTO

Hideo TAKEUCHI

Tomohito TAKUBO

Eriko SATO

Masumi FUJIMOTO

Toru ENDO

MEMOIRS OF THE FACULTY OF ENGINEERING  
OSAKA CITY UNIVERSITY

VOL. 55

DECEMBER 2014

CONTENTS

Regular Articles ..... 1

*Physical Electronics and Informatics*

*Applied Physics and Electronics*

**Influence of Absorbing Substrates on Laser Oscillation of Quantum-Well Microtube Lasers**  
*Makoto HOSODA and Naoki KATAYAMA* ..... 1

*Urban Engineering*

*Urban Design and Engineering*

**Response of Larval and Postlarval Greasyback Prawns to Hypoxia**  
*Susumu YAMOCHI, Ken IKEDA and Kazuma MUTSUTANI* ..... 9

**An Analysis on Influence Factors to Use Frequency and WTP of Shopping Support Services for People in Food Desert**  
*Noboru ISE and Yasuo HINO* ..... 19

**Formation of Waterside Spaces with Groins**  
*Yasumasa FUKUSHIMA and Takashi UCHIDA* ..... 27

**Sensitivity Analysis on Influence of Fabrication Tolerance of High Strength Bolted Friction Type Joint to its Slip Strength**  
*Toshikazu TAKAI, Takashi YAMAGUCHI and Kiyonori YAMASHINA* ..... 35

**Study on Applicability of High Durability Friction Grip Joints with High Strength Countersunk Head Bolts for Steel Bridge Structures**  
*Akiko TABATA and Takashi YAMAGUCHI* ..... 43

<b>A Path to Creating an Opportunity for Communication using the “Machizukuri Pattern”</b> <i>Yasutomi SAKUMA</i> .....	51
<b>Approach to Improve Driving Condition on Desert highway from Viewpoint of Road Safety</b> <i>Zulpikar KERAM and Yasuo HINO</i> .....	57
<b>Abstracts of Papers Published in Other Journals</b> .....	63
<i>Mechanical and Physical Engineering</i>	
<i>Mechanical Engineering</i> .....	65
<i>Applied Mathematicsg</i> .....	74
<i>Physical Electronics and Informatics</i>	
<i>Applied Physics and Electronics</i> .....	75
<i>Electric and Information Engineering</i> .....	88
<i>Applied Chemistry and Bioengineering</i>	
<i>Applied Chemistry and Bioengineering</i> .....	92
<i>Urban Engineering</i>	
<i>Architecture and Building Engineering</i> .....	113
<i>Urban Design and Engineering</i> .....	115

MEMOIRS  
OF THE  
FACULTY OF ENGINEERING  
OSAKA CITY UNIVERSITY

---

VOL. 55

---

DECEMBER 2014

PUBLISHED BY THE  
GRADUATE SCHOOL OF ENGINEERING  
OSAKA CITY UNIVERSITY



# Influence of Absorbing Substrates on Laser Oscillation of Quantum-Well Microtube Lasers

Makoto HOSODA and Naoki KATAYAMA

(Received October 14, 2014)

## Synopsis

We evaluated the influence of absorbing substrates on laser oscillation of quantum-well microtube lasers. We calculated absorption loss of whispering gallery modes propagating in hollow semiconductor microtubes with a separation distance from the substrate by the finite-difference-time-domain (FDTD) method. Even under the non-contact condition to the substrate, evanescent waves leaked from the tube-wall are absorbed by the substrate, which is known as the photon-tunneling phenomenon. Our simulation result shows that separation distances from one micron to several tens of microns decrease the loss to  $10^{-3}$ . When the optical gain from the quantum well (QW) or quantum dots (Q-dots) in the microtube wall was able to overcome the above absorption loss, laser oscillation from the QW- and Q-dot-microtubes occurred.

**KEYWORDS:** Quantum-well microtube, Whispering gallery mode, Photon tunneling

## 1. Introduction

Since quantum-well microtube proposed and demonstrated as a new type of quantum-well (QW) optical device by Hosoda et al.,<sup>1)</sup> many studies have been conducted on the systems, e.g. optical devices using quantum-dots (Q-dots) in microtubes. Recently, Kipp et al. have found sharp optical resonance by a kind of whispering gallery mode in a cylindrical optical micro-cavity formed by the microtubes,<sup>2)</sup> and the physical background of this experimental result has been corroborated by a simulation result from Hosoda et al.<sup>3)</sup>

Based on these findings, microtubes containing QWs or Q-dots have attracted a lot of attention as high quality factor (Q-factor) cavities, which allow achievement of ultralow threshold semiconductor lasers, and many studies have concentrated on creating a structure to achieve this. To establish the above characteristics, mechanical structures of the optical resonators, as well as emission properties of the quantum structures, have been studied with promising results.<sup>4-6)</sup> Laser oscillation from these structures by optical excitation has also been reported.<sup>7-9)</sup> However, cavity loss by substrate absorption has not yet been clarified.

To increase the Q-factor, decrease of cavity loss is important. One of the losses comes from absorption by the substrate of light circularly propagating around the cylindrical cavity. In this report, we evaluate optical loss by leakage of light from the microtube wall to the absorbing substrate, which mechanically supports the microtube. This estimation is thought to be important for design of current injection microtube lasers, but those have not been achieved thus far. The evaluation is performed by the finite-difference-time-domain (FDTD) method with realistic values of a QW microtube.

## 2. Overview of QW microtube

Figure 1 shows the structure and fabrication method of the QW microtube.

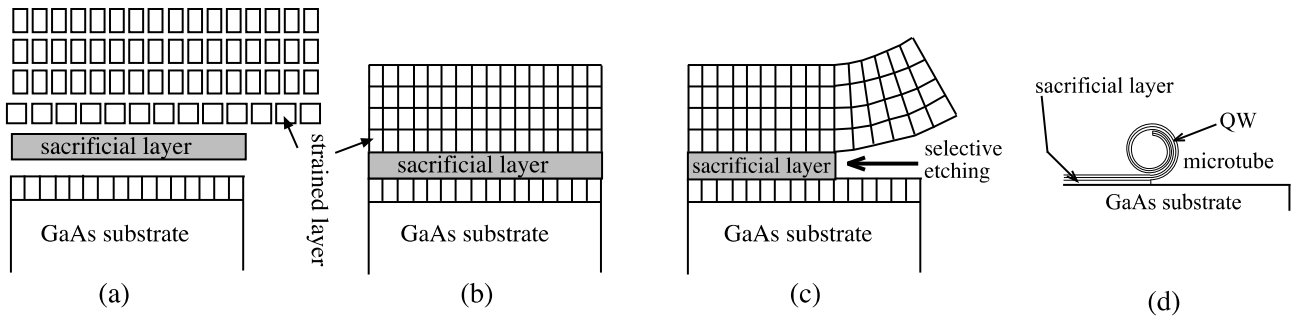


Fig. 1 Fabrication method of QW-microtube. (a) Growth sequence by Molecular-Beam Epitaxy. (b) After growth. (c) Fabrication of microtube by selective etching. (d) Completion of microtube formation.

The sample is fabricated by rolling a thin heterostructure film. First, a multilayered thin semiconductor film is grown on a (100)-oriented intrinsic GaAs substrate by molecular beam epitaxy. An example of the growth sequence is shown in Fig. 1(a): from the substrate, a 200-nm GaAs buffer layer; a 0.4-nm/0.4-nm x 100 Al<sub>0.52</sub>Ga<sub>0.48</sub>As/AlAs digital alloy sacrificial layer; a 7-nm In<sub>0.19</sub>Ga<sub>0.81</sub>As strained layer; a 10-nm Al<sub>0.75</sub>Ga<sub>0.25</sub>As bottom barrier; a 2-nm, i.e. 7-monolayer (ML) GaAs QW; a 10-nm Al<sub>0.75</sub>Ga<sub>0.25</sub>As top barrier, and a 10-nm GaAs cap layer.

On this occasion, the InGaAs layer suffers compressive strain, and does not relax since the thickness is less than the critical thickness. After growth, the sacrificial layer is selectively etched with HF:H<sub>2</sub>O (1:10), then the upper layer is released from the substrate and rolled up from the cleavage surface due to the strain relaxation effect of the InGaAs layer, as shown in Figs. 1(c) and (d).

The sample is subsequently soaked in pure water and dried with care to prevent microstructural damage or sticking due to the surface tension of the water meniscus. Finally, the rolled-up film forms a microtube.

Figure 2 shows the fabricated QW-microtubes. The cross section of the microtube in Fig. (c) indicates that these microtubes are perfectly hollow, and the wall thickness is several tens of nanometers. Therefore, it is proved that the quantum structure illustrated in Fig. 1 can be successfully fabricated.

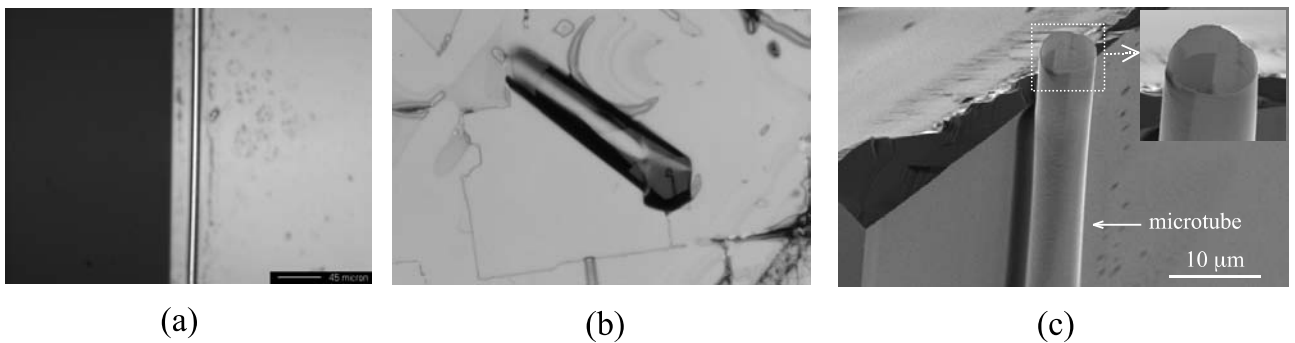


Fig. 2 (Color online) Photograph of microtubes. (a) Optical microscope image of a microtube rolled up from a cleavage surface (left side in the image). (b) Optical microscope image of a microtube. Hollow structure can be seen. (c) Vertical SEM image of the microtube 6-microns in diameter in (a).

Figure 3 shows a schematic figure of a kind of whispering gallery mode generated in hollow microtubes, which can be established as described in Ref. 3. Our simulation under the condition of a microtube isolated from the substrate shows sharp peaks with high Q-factor caused by the resonance of the whispering gallery modes, as shown in Fig. 4. Therefore, a low-threshold laser may be achieved.

However, actual systems shown in Figs. 1 and 2 contact the substrate. This causes decay in the optical intensity of the mode, which is caused by absorption of light by the substrate. To avoid this problem, separation of the microtube from the substrate is needed. Since the microtube is supported by the substrate and cannot be detached from it, a method is used that grooves a ditch into the substrate just under the

microtube,<sup>2)</sup> as shown in Fig. 5. However, there has been no report regarding how deep of a groove is sufficient to reduce the absorption of light running around the microcavity. Therefore, we evaluated this.

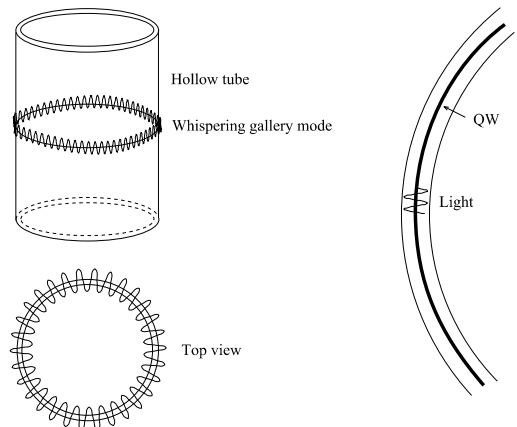


Fig. 3 Schematic figure of optical resonance in hollow cylindrical microcavity.

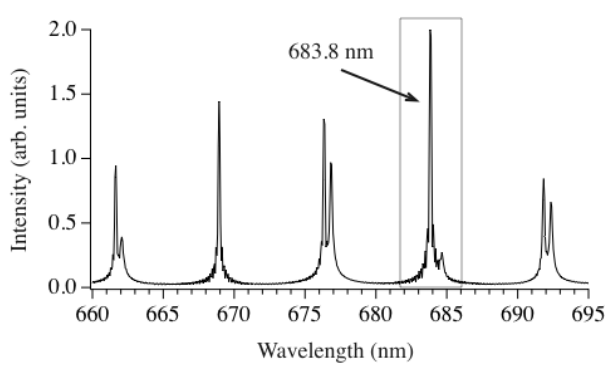


Fig. 4 Calculated resonance peaks of whispering gallery modes in a QW-microtube.

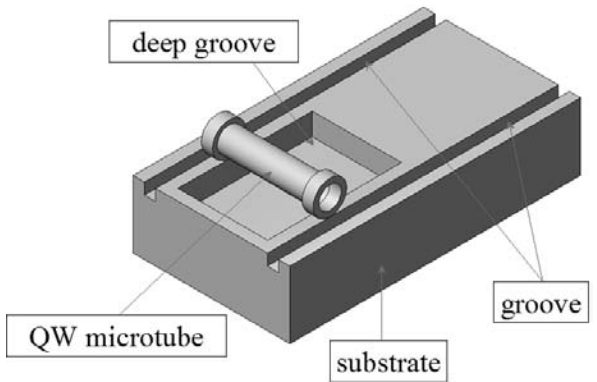


Fig. 5 Schematic figure of microtube on deep groove cut on substrate.

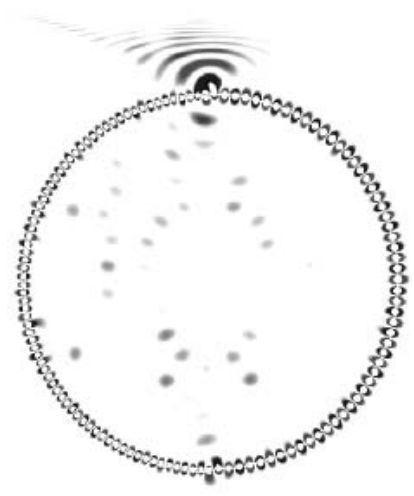


Fig. 6 (Color online) Calculated intensity of whispering gallery mode in free-standing microtube.

### 3. Simulation result and discussion

Simulation is done by the FDTD method. By comparing the light intensity in microtubes separated from the substrate with finite distance to intensity in a free-standing microtube with infinite distance from the substrate, decrease in the optical intensity by absorption was studied.

Figure 6 shows distribution of the light intensity of a whispering gallery mode established in a free-standing microtube. The scattering at the upper portion of the tube is caused by a notch in the rolled-up tube.<sup>3)</sup> Figure 7 shows the simulation condition under finite separation distance. In the rolled-up tube, there are two notches at the upper and lower positions, as shown in Fig. 7. Under the lower notch, the substrate is positioned with a separating distance, which is a key parameter in the simulation. The diameter of the tube is 6 microns, and this is the real diameter of the tube shown in Fig. 2. We adopted the sharp peak at 683.8 nm in Fig. 4 for the whispering gallery mode in our simulation, since it has a high Q-factor. This emission wavelength is possible under uniaxial strained QW.<sup>1)</sup>

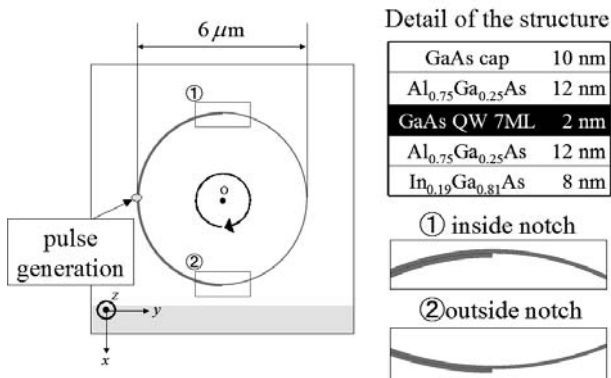


Fig. 7 Schematic figure of simulation condition.

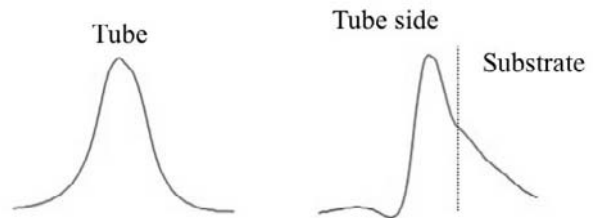


Fig. 9 Spatial distribution of light intensity around tube wall.

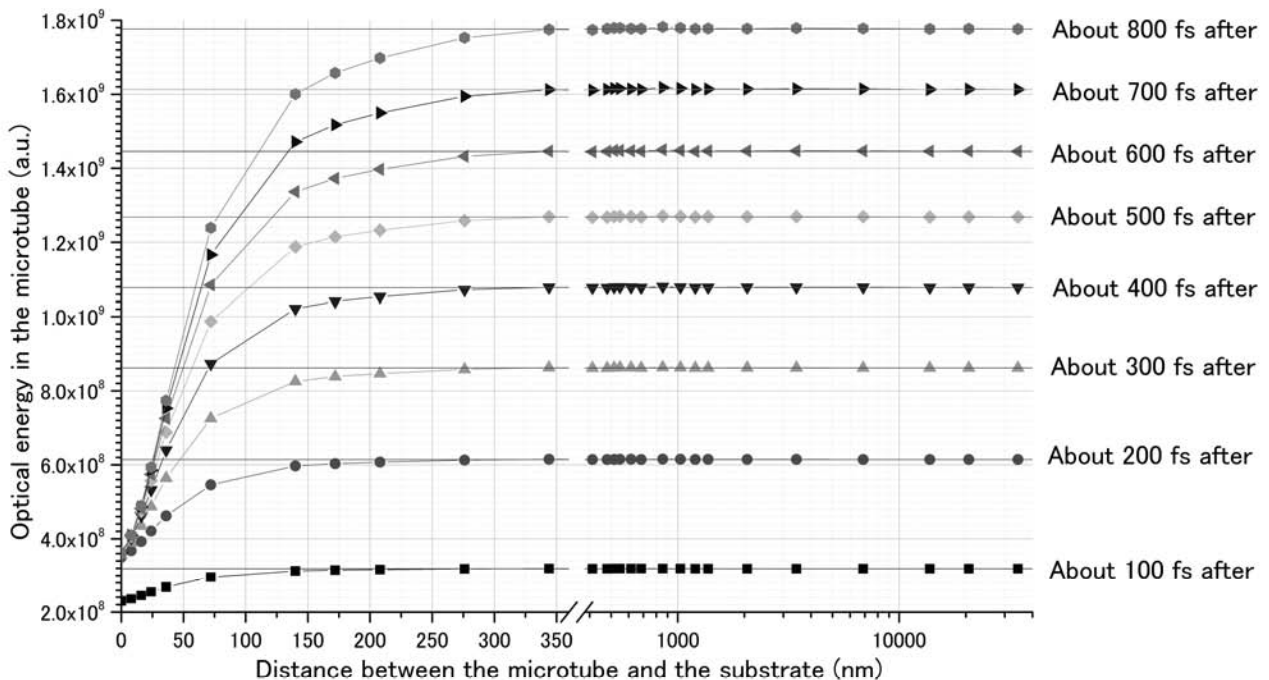


Fig. 8 (Color online) Evolution of light intensity in microtube vs. separation distance from substrate.

Figure 8 shows calculated evolution of light intensity in the microtube. In the calculation, an optical pulse of longer than 1-ps pulse width is injected from the left side of the microtube, as shown in Fig. 7; then, it runs around the tube periphery. Since the tube diameter is 6 microns, optical pulse circling the tube periphery

counterclockwise arrives at the bottom of the tube, where the nearest point to the substrate (cf. Fig. 7) is within 100 fs. In addition, the pulse going clockwise also arrives there within several hundreds of fs. When the absorption by the substrate occurs at that point, pulse intensity decreases. Therefore, when the separation distance is short, the light intensity is greatly decreased, as shown in Fig. 8.

Why does the decrease occur under non-zero value of the separation distance? This is because photon tunneling<sup>10)</sup> occurs. Since the wall thickness of the microtube is far thinner than the light wavelength, i.e. 42-nm wall thickness versus 683.8-nm light wavelength, the distribution of light intensity going around the tube wall greatly seeps out from the tube wall as evanescent wave.<sup>3)</sup> The electromagnetic wave soaked out from the tube wall is influenced by the boundary condition of the propagation. When an absorbing material exists sufficiently close but is not in contact, this configuration causes absorption, i.e. photon tunneling. The left side of Fig. 9 shows the distribution of the light intensity around the tube wall at normal propagation. In contrast, the distribution is changed at a position that comes close to the substrate, as shown in the right figure. Evanescent wave soaked from the wall can enter into the substrate in this condition, which means photon tunneling.<sup>10)</sup>

Figure 10 shows light absorbed into the substrate under slight separation from the substrate. In this case, Snell's law also applies, even under the photon tunneling condition, as shown in the figure.

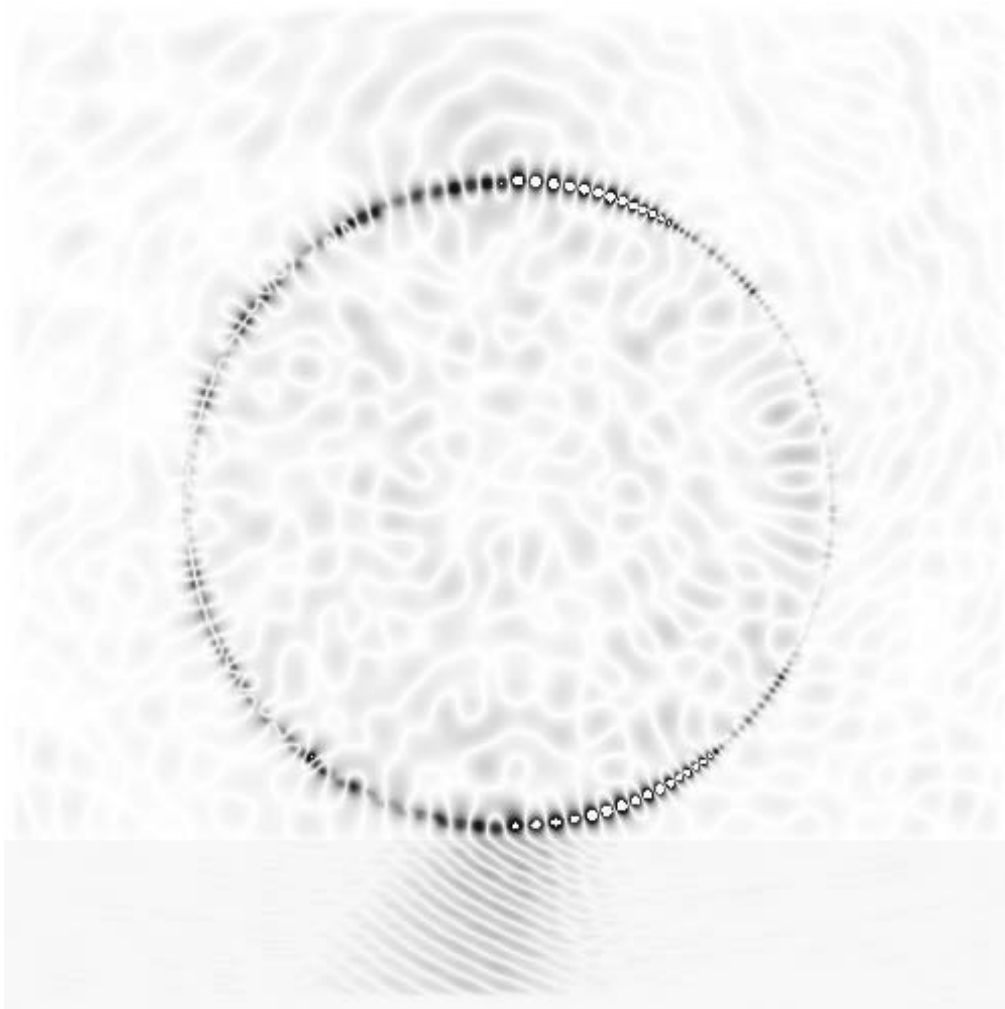


Fig. 10 (Color online) Absorption of light going clockwise in periphery of microtube slightly separated from substrate. The propagating direction of the absorbed light by photon tunneling adheres to Snell's law.

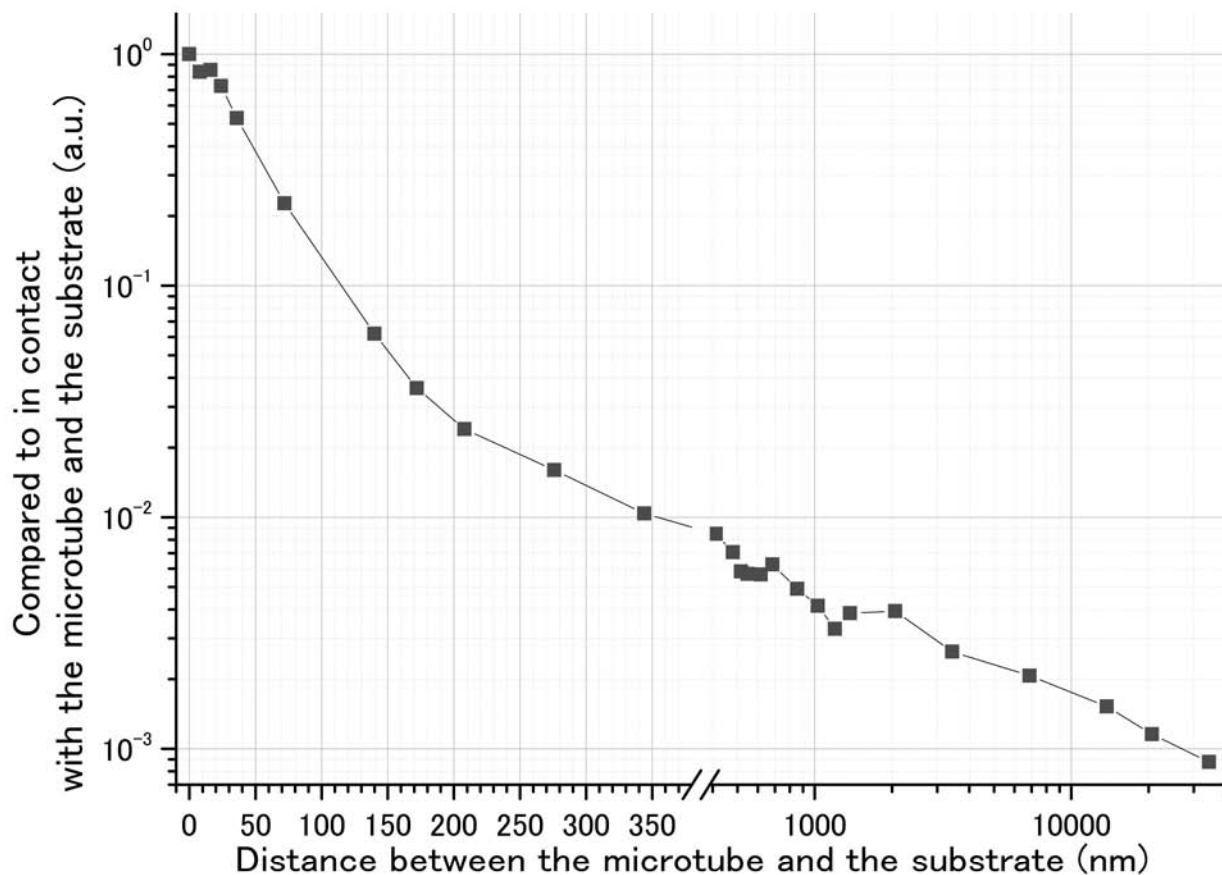


Fig. 11 Absorption rate of separated microtube compared to in-contact one.

Figure 11 shows the absorption rate of separated microtube compared to that of an in-contact one (separation distance = 0) as a function of the separation distance. At distance greater than  $3 \times 10^4$  nm, i.e. approx. 50 times the light wavelength propagating in the tube wall, one-thousandth of an improvement in the absorption loss is achieved compared to the in-contact tube. From this result, separation distance of one micron to several tens of microns might be sufficient for visible light wavelengths when optical gain from QW or Q-Dots in microtubes is sufficiently high to be able to overcome the absorption loss, which may easily generate laser oscillation in QW- and Q-dot-microtube systems.

#### 4. Conclusions

We calculated absorption loss of whispering gallery modes in hollow semiconductor microtubes with finite separation distance from the substrate. Our simulation result shows that separation greater than 50-times the optical wavelength is sufficient for easily establishing laser oscillation from the QW- and Q-dot- microtubes.

#### 5. References

- 1) M. Hosoda et al., *Appl. Phys. Lett.* **83**, 1017 (2003).
- 2) T. Kipp, H. Welsch, C. Stelrow, C. Heyn, and D. Heitmann, *Phys. Rev. Lett.* **96**, 077403 (2006).
- 3) M. Hosoda and T. Shigaki, *Appl. Phys. Lett.* **90**, 181107 (2007).

- 4) C. Strelow, C. M. Schultz, H. Rehberg, H. Welsch, C. Heyn, D. Heitmann, and T. Kipp, *Phys. Rev. B* **76**, 045303 (2007).
- 5) V. A. B. Quiñones, L. Ma, S. Li, M. Jorgensen, S. Kiravittaya, and O. G. Schmidt, *Appl. Phys. Lett.* **101**, 151107 (2012).
- 6) C. Strelow, C. M. Schultz, H. Rehberg, M. Sauer, H. Welsch, A. Stemmann, C. Heyn, D. Heitmann, and T. Kipp, *Phys. Rev. B* **85**, 155329 (2012).
- 7) F. Li and Z. Mi, *Optics express* **17**, 19933 (2009).
- 8) C. Strelow, M. Sauer, S. Fehring, T. Korn, C. Schüller, A. Stemmann, and T. Kipp, *Appl. Phys. Lett.* **95**, 221115 (2009).
- 9) H. Junseok, S. Bhowmick, and P. Bhattacharya, *IEEE J. Quantum Electron.* **48**, 927 (2012).
- 10) R. Y. Chiao and A. M. Steinberg, *Progress in Opt.* **37**, 345 (1997).



# Response of Larval and Postlarval Greasyback Prawns to Hypoxia

Susumu YAMOCHI\* , Ken IKEDA\*\* and Kazuma MUTSUTANI\*\*\*

(Received September 30, 2014)

## Synopsis

Laboratory experiments were carried out using an oxygen and salinity gradient column to clarify the response to hypoxia of larval and postlarval greasyback prawns. The survival rate of the greasyback prawns increased in postlarval stage compared to mysis stage. They escaped from hypoxia at dissolved oxygen concentrations less than 2.1-2.6 mgO<sub>2</sub> l<sup>-1</sup> for mysis larvae (10 days after hatching), less than 2.1-2.7 mgO<sub>2</sub> l<sup>-1</sup> for P4 postlarvae (14 days after hatching) and less than 1.2-1.7 mgO<sub>2</sub> l<sup>-1</sup> for P15 postlarvae (25 days after hatching). These results suggested that greasyback prawns strengthen their levels of tolerance to hypoxia in correspondence to the advancement of life stage from early postlarvae (P5) to late postlarvae (P15).

KEYWORDS: Hypoxia, Avoidance, Survival rate, Greasyback prawn, Larvae, Postlarvae, Oxygen-salinity gradient column

## 1. Introduction

Osaka Bay is well known as a rich sea where a total amount of 225 species of fisheries organisms, together with 15000- 28000 tons of annual fishing catch, have been recorded in recent years. A gradual restoration of dissolved oxygen (DO) has been observed in the bottom layer of the central and southern part of Osaka Bay, due mainly to a regulation of sewage discharge. However, concentrations of dissolved oxygen are still low, and below 3.6 mgO<sub>2</sub> l<sup>-1</sup> at harbor areas of inner Osaka Bay in summer, which is thought to be a crucial level of dissolved oxygen required for the healthy growth of the marine benthic animals (Yanagi, 1989; Pihl et al., 1991; Kodama et al., 2006).

A committee of the Ministry of the Environment, Japan showed the importance of dissolved oxygen in the bottom water as an indicator of water quality, and examined its target values to maintain sound marine benthic biological resources. Yamochi et.al (1998) examined the tolerance to hypoxia of several benthic fish and crustaceans of Osaka Bay and demonstrated that dissolved oxygen should not drop below 1.6 mlO<sub>2</sub> l<sup>-1</sup> (2.3 mgO<sub>2</sub> l<sup>-1</sup>) for longer than 1 day, and be kept higher than 2.6 mlO<sub>2</sub> l<sup>-1</sup> (3.7 mgO<sub>2</sub> l<sup>-1</sup>) on average in summer to maintain sound populations of demersal fishes and crustaceans of the bay.

Greasyback prawn, *Metapenaeus ensis* is a major fishery species of Osaka Bay and known as a benthic crustacean highly enduring of hypoxic conditions (Yamochi et.al, 1995). Oda et al. (1997) analyzed the relationship between hypoxia and population dynamics of the juvenile greasyback prawn in Osaka Bay using a numerical model where they assumed all juveniles of the prawns escaped from hypoxia at a concentration of 2.1mgO<sub>2</sub> l<sup>-1</sup>. However, there is so far little information on the minimum dissolved oxygen required for the sound habitats for the whole life history of the greasyback prawns, including their larval stage. Therefore, we need more information on the physiological and/or ecological responses to hypoxia of the larval greasyback prawns, since the larval stage is expected to be less tolerant to severe oxygen conditions compared to adults of the same species.

The present paper attempts to clarify the change of tolerance or avoidance to hypoxia in correspondence to the growth of larval and postlarval greasyback prawns. For this purpose laboratory experiments were done to examine the survival or avoidance of hypoxia of the mysis and postlarval stage of the greasyback prawns using an oxygen and salinity gradient glass column.

---

\* Professor, Department of Environmental Urban Engineering

\*\* Technical expert, Water Department of Osaka City Government

\*\*\* Senior Researcher, Research Institute of Environment, Agriculture and Fisheries, Osaka Prefecture

## 2. Methods

### 2.1 . Preparation of oxygen and salinity gradient column

Two liters of filtered seawaters (ca.30 in salinity) were concentrated or diluted to 40 and 20 salinity respectively, and added into two glass flasks. Seawater with high salinity was ventilated by N<sub>2</sub> gas to reduce the concentration of dissolved oxygen (Flask A in Figure1), while those with low salinity were aerated to adjust its concentration (Flask B in Figure1). The two flasks were connected to each other with Tygon tubing and the seawater in each flask gently stirred, then poured into a glass column of 86cm in height and 5cm in diameter using a roller pump (Furue Science Co., model RP-NB) at a flow rate of 120 ml min<sup>-1</sup> (Tanaka, 1991). Prior to the addition of seawater to the glass column, the concentration of dissolved oxygen was checked with an Oxygurd DO meter (Type Handy Polaris). We referred to a glass column with salinity gradient but with no oxygen gradient as the control column where no ventilation of N<sub>2</sub> gas was made, and only salinity gradient was formed in the column.

### 2.2. Test organism

Mysis and postlarvae of the greasyback prawns, which were hatched and grown at the Mie Prefectural Sea Farming Center, were transferred to the laboratory and employed for the experiment (Figure 2). All larval and postlarval greasyback prawns were exposed to the seawater for ca.3 hours with gentle aeration before the experiment. Averaged body length was ca.2 mm for mysis (10 days after hatching), ca.3 mm for P4-stage postlavae (14 days after hatching) and ca.13 mm for P15-stage postlavae (25 days after hatching).

### 2.3. Observation

Pre-observation was carried out to confirm whether the oxygen and salinity gradient was maintained for 24 hours in a condition without the larvae of greasyback prawns. Dissolved oxygen was monitored at intervals of 3 hours for 24 hours at every 10cm depth of the oxygen and salinity gradient column with an Oxygurd DO meter. Density was checked at a water temperature of 25 °C using 4 standard density floats of 1.0150, 1.0175, 1.0200 and 1.0225 g cm<sup>-3</sup> (Shibayama Scientific Co. LTD.), and was converted into salinity according to the Manual on Oceanographic Observation (Japan Meteorological Agency, 1999). As shown in Table 1, the oxygen gradient was kept for 24 hours when no larvae or postlarvae of greasyback prawn were added to the column except for lower layers at 6 hours. No clear difference was found in the position of each density float in the column before and after the experiment, which meant that salinity gradient was almost constant and didn't change for 24 hours. All of the seawaters used for the experiment were sterilized by autoclaving at 121°C for 5 min prior to the experiment.

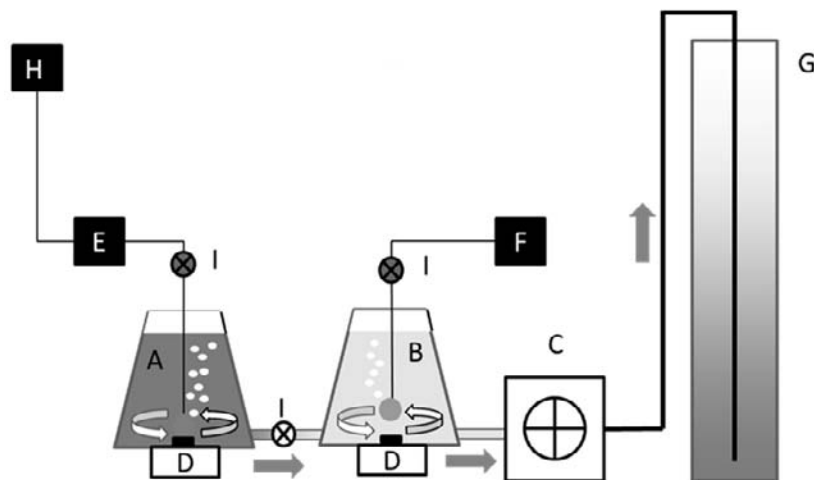


Fig.1: Schematic diagram of the experimental apparatus.

A: condensed seawater, B: diluted seawater, C: roller pump, D: stirrer, E: flow meter, F: air pump, G: oxygen and salinity gradient glass column, H:N<sub>2</sub> gas, I: stopper valve

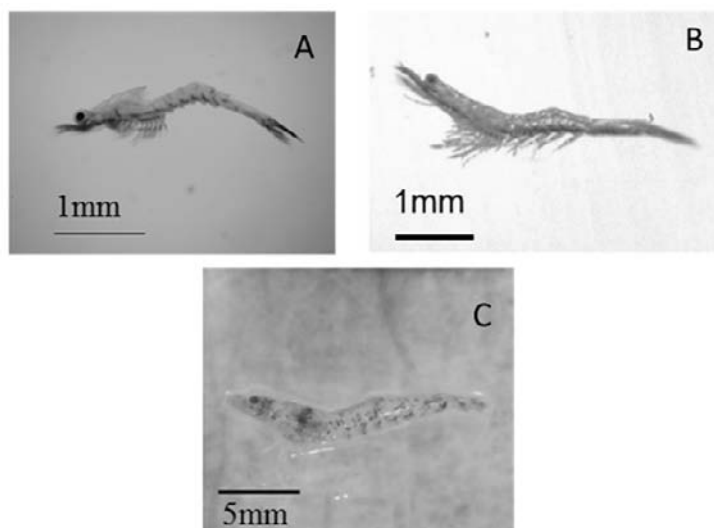


Fig. 2 : Mysis and postlarva of the greasyback prawn

A: Mysis (10 days after hatching), B:P4 stage postlarva (14 days after hatching), C:P15 stage postlarva (25 days after hatching)

Table 1: Changes of dissolved oxygen concentration in the oxygen and salinity gradient column.

Depth (cm)	Time (h)								
	0	3	6	9	12	15	18	21	24
0	6.3	6.5	6.5	6.5	6.5	6.5	6.5	6.5	6.5
10	6.5	6.7	6.0	6.7	6.7	6.7	6.7	6.7	6.7
20	5.4	5.4	5.3	5.4	5.4	5.4	5.4	5.4	5.4
30	4.7	4.8	4.5	4.8	4.8	4.8	4.8	4.8	4.8
40	4.3	4.1	4.0	4.1	4.1	4.1	4.1	4.1	4.1
50	3.9	3.8	3.4	3.8	3.8	3.8	3.8	3.8	3.8
60	3.5	3.4	2.8	3.4	3.4	3.4	3.4	3.4	3.4
70	3.1	3.2	1.9	3.2	3.2	3.2	3.2	3.2	3.2
Bottom	2.9	3.0	1.7	3.0	3.0	3.0	3.0	3.0	3.0

\* Value is shown in  $\text{mgO}_2 \text{ l}^{-1}$ .

Fifteen individuals of mysis, P4 and P15-stage larvae of greasyback prawn were added to the surface layer of the seawater (0-10 cm depth from the surface) on 0.5 hour before the onset of observation. Each glass column was kept at  $25 \pm 1$  °C with a photoperiod of 12 hours light and 12 hours dark at a photon density of  $90\text{-}100 \mu\text{mol m}^{-2} \text{ sec}$ . We observed the number of individuals of the larval or postlarval greasyback prawn at every 1cm depth from the surface to the bottom of the column at 3 hours intervals and compared with those of the control one. An overall percentage of distribution of the larval or postlarval greasyback prawns was calculated by averaging the percentage of distribution of each observation time at layers of 0-30 cm, 30-60 cm and 60 cm-bottom, respectively. Vertical distributions of dissolved oxygen were checked at 8 hours intervals to confirm the oxygen gradient to be maintained.

### 3. Results

#### 3.1. Survival rate

Survival rates of the larval and postlarval greasyback prawns in the oxygen and salinity gradient column were shown in Table 2. We regarded larval and postlarval greasyback prawns as dead in the following case:

- (1) They lost their mobility and showed no response when touched with a needle in the fresh seawaters.
- (2) Their body color has changed from yellowish brown to pink.

In addition, data from 0 to 15 hours were used since dissolved oxygen concentrations remarkably decreased owing to the effects of decomposition of dead prawns at the bottom of the column after 16 hours. Survival rate of the mysis-stage larvae decreased to 60.0% when dissolved oxygen concentrations dropped to 0.9-1.6 mgO<sub>2</sub> l<sup>-1</sup> at the bottom of the column (case 4), while the rate was kept at a range of 86.7 to 100% at 1.8-2.0 mgO<sub>2</sub> l<sup>-1</sup> (case 3), 2.3-2.6 mgO<sub>2</sub> l<sup>-1</sup> (case 2), 2.8-3.3 mgO<sub>2</sub> l<sup>-1</sup> (case 1) and 5.8-5.9 mgO<sub>2</sub> l<sup>-1</sup> (control). The P4-stage postlarvae showed a high survival rate of 93.3% under dissolved oxygen concentrations of 2.0-2.3 mgO<sub>2</sub> l<sup>-1</sup> (case 3), 2.1-2.7 mgO<sub>2</sub> l<sup>-1</sup> (case 2), 2.7-3.1 mgO<sub>2</sub> l<sup>-1</sup> (case 1) and 5.3-5.7 mgO<sub>2</sub> l<sup>-1</sup> (control) but the survival rate remarkably decreased (53.3%) at 1.6-1.7 mgO<sub>2</sub> l<sup>-1</sup> (case 4). In contrast, the P15-stage postlarvae endured hypoxic seawaters for 15 hours and showed high survival rates of 86.7-100% even when they encountered dissolved oxygen concentrations of 0.2-1.7 mgO<sub>2</sub> l<sup>-1</sup> (case 4), 0.7-2.3 mgO<sub>2</sub> l<sup>-1</sup> (case 3), 0.3-2.7 mgO<sub>2</sub> l<sup>-1</sup> (case 2), 1.1-3.1 mgO<sub>2</sub> l<sup>-1</sup> (case 1) and 1.5-5.7 mgO<sub>2</sub> l<sup>-1</sup> (control) at the bottom of the column. No clear difference was observed in the tolerance of hypoxia between the mysis and P4 postlarval stage of the greasyback prawns.

Table 2: Survival rate of the larval and postlarval greasyback prawns.

Stage	Control	Oxygen - salinity gradient column			
		Case1	Case2	Case3	Case4
Mysis larvae	86.7	100	86.7	86.7	60.0
P4-stage postlarvae	93.3	93.3	93.3	93.3	53.3
P15-stage postlarvae	93.3	100	100	93.3	86.7

\* Value is survival rate of 0-15 hours and shown in percentage.

\*\*Initial dissolved oxygen concentration at the bottom of the column, Case1:3.1-3.3 mgO<sub>2</sub> l<sup>-1</sup>, Case2:2.6-2.7 mgO<sub>2</sub> l<sup>-1</sup>, Case3:2.0-2.3 mgO<sub>2</sub> l<sup>-1</sup>, Case4:1.6-1.7 mgO<sub>2</sub> l<sup>-1</sup>, Control:5.7-5.9 mgO<sub>2</sub> l<sup>-1</sup>

### 3.2. Avoidance

#### 1) Mysis

Distributions of the mysis-stage larvae of the greasyback prawns in the oxygen and salinity gradient column were shown in Table 3. Avoidance of the larvae to hypoxia was analyzed based on the results of 0-15 hours of the time course, since dissolved oxygen decreased at the upper or middle layer of the column between 16 and 24 hours. When dissolved oxygen at the bottom of the column at 0-16 hours was 2.8-3.3 mgO<sub>2</sub> l<sup>-1</sup> (case 1), a 71% of the live larvae distributed at a layer of 0-60 cm from the water surface. In cases 2 and 3 (dissolved oxygen at the bottom of the column at 0-16 hours was 2.3-2.6 mgO<sub>2</sub> l<sup>-1</sup> for case 2 and 1.8-2.0 mgO<sub>2</sub> l<sup>-1</sup> for case 3), a total of 84.6% and 94.0% of the mysis-stage larvae were observed at the 0-60 cm layer. A marked decline of individuals of the surviving larvae was found from 15 to 18 hours in case 4, resulting in only a few larvae remained at the end of the experiment. At 0-15 hours of the case 4 (dissolved oxygen at the bottom: 0.9-1.6 mgO<sub>2</sub> l<sup>-1</sup>), the percentage of distribution of the live mysis larvae attained 91.2% at the 0-60 cm layer.

#### 2) P4-stage postlarva

Distributions of the P4-stage postlarvae of the greasyback prawns in the oxygen and salinity gradient column were depicted in Table 4. As dissolved oxygen decreased in the column after 16 hours as with the mysis-stage experiment, avoidance of the P4 postlarvae to hypoxia was analyzed based on the results of 0-15 hours. In the control column, the percentages of distribution of the postlarvae were ca. 60% at the bottom of the column, while those in the oxygen and salinity gradient column were low and showed 46.6% at dissolved oxygen concentrations of 2.7-3.1 mgO<sub>2</sub> l<sup>-1</sup> in case 1, 37.5% at 2.4-2.7 mgO<sub>2</sub> l<sup>-1</sup> in case 2, 25.6% at 2.0-2.3 mgO<sub>2</sub> l<sup>-1</sup> in case 3 and 18.8% at 1.6-1.7 mgO<sub>2</sub> l<sup>-1</sup> in case 4. As a result, the percentage of distribution of the P4-stage postlarvae at the bottom of the column clearly decreased with decreasing dissolved oxygen. In contrast, they were well observed at a layer of 30-60 cm from the surface in each oxygen and salinity gradient column where dissolved oxygen concentration ranged between 3.2-5.2 mgO<sub>2</sub> l<sup>-1</sup> (case 1), 3.6-4.7 mgO<sub>2</sub> l<sup>-1</sup> (case 2), 3.6-4.4 mgO<sub>2</sub> l<sup>-1</sup> (case 3), and 2.8-4.7 mgO<sub>2</sub> l<sup>-1</sup> (case 4).

#### 3) P15-stage postlarva

Table 5 showed distributions of the P15-stage postlarvae of the greasyback prawns in the oxygen and

Table 3 : Distributions of the mysis-stage larvae of the greasyback prawns.

Depth (cm)	DO concentration (mg l <sup>-1</sup> )				Salinity start	Number of individuals									
	start	8h	16h	24h		start	3h	6h	9h	12h	15h	18h	21h	24	
Control	surface -10	6.6	6.6	6.6	5.5	21.7	2	0	2	1	0	1	4	3	2
	10-20	6.1			5.0	23.5	0	1	1	0	1	0	1	0	2
	20-30	6.4		5.8	4.4	25.3	2	2	1	4	3	2	2	2	2
	30-40	6.1			4.3	27.1	3	2	7	4	0	2	3	3	1
	40-50	6.1	5.9	5.9	5.6	28.9	2	3	1	3	3	3	1	2	2
	50-60	6.0			5.6	30.7	1	0	0	0	4	4	0	1	0
	60-70	6.0		5.9	5.9	32.5	3	0	0	1	2	1	0	0	0
	70-bottom	6.0			5.7	34.2	0	4	0	0	0	0	1	1	1
	bottom	5.9	5.5	5.8	4.7	36.0	2	2	1	0	0	0	0	0	0
Case1	surface -10	6.6	6.6	6.3	5.1	21.6	1	0	1	0	1	1	1	4	3
	10-20	6.2		5.1	3.5	23.6	1	1	1	3	1	2	1	1	4
	20-30	5.7	5.4	4.9	3.6	25.4	1	2	0	2	2	3	2	4	4
	30-40	5.1		4.7	3.9	27.3	1	2	2	3	2	1	7	4	1
	40-50	4.8	4.3	4.5	3.7	29.1	4	3	1	1	1	0	2	1	1
	50-60	4.3		3.9	3.9	31.0	3	2	4	5	3	3	0	0	0
	60-70	3.8	3.8	3.6	3.8	32.9	2	2	3	1	2	4	1	0	0
	70-bottom	3.4		3.3	3.7	34.7	1	1	0	0	2	1	0	0	0
	bottom	3.3	3.0	2.8	3.2	36.6	1	2	3	0	1	0	0	0	0
Case2	surface -10	6.5	6.4	5.8	4.7	22.6	1	3	4	1	0	0	7	5	3
	10-20	5.8			3.1	24.3	4	2	1	0	1	1	0	2	2
	20-30	5.0	5.0	4.4	3.3	26.1	2	3	1	1	1	3	3	0	1
	30-40	4.7			3.4	27.8	2	3	3	2	3	2	2	3	1
	40-50	4.2	3.9	4.1	3.3	29.5	3	2	0	5	2	0	1	1	0
	50-60	3.9			3.4	31.2	1	1	2	3	5	4	0	0	0
	60-70	3.3	3.3	3.3	3.3	32.9	0	0	2	2	1	1	0	1	0
	70-bottom	2.9			3.0	34.6	0	0	0	0	0	0	0	0	0
	bottom	2.6	2.5	2.3	2.5	36.3	2	1	1	1	0	2	0	0	1
Case3	surface -10	6.7	6.3	6.3	4.5	22.4	2	3	1	2	1	1	7	5	4
	10-20	5.6			4.1	24.3	4	3	0	2	1	1	1	1	2
	20-30	4.8	4.7	4.1	2.7	26.2	3	2	3	2	1	2	2	4	2
	30-40	4.1			2.5	28.2	4	2	2	3	7	0	2	2	2
	40-50	3.5	3.7	3.5	2.5	30.1	2	3	2	4	3	6	0	1	1
	50-60	3.0			2.5	32.1	0	2	1	0	0	3	1	0	0
	60-70	2.6	2.6	2.6	2.4	34.0	0	0	1	0	0	0	0	0	0
	70-bottom	2.1			2.4	35.8	0	0	2	0	0	0	0	0	0
	bottom	2.0	1.8	1.8	1.4	37.7	0	0	2	0	0	0	0	0	0
Case4	surface -10	6.4	6.3	5.9	4.6	23.0	0	2	1	1	1	0	1	1	1
	10-20	5.7		4.9	3.4	24.7	2	2	0	0	0	1	0	0	1
	20-30	4.8	4.5	4.5	2.9	26.4	5	2	5	2	2	2	1	1	0
	30-40	4.2		4.2	2.6	28.1	1	5	3	2	2	3	0	0	0
	40-50	3.5	3.2	3.6	2.4	29.8	4	0	1	4	3	2	1	0	0
	50-60	2.8		2.8	2.4	31.5	0	1	1	0	0	1	0	1	0
	60-70	2.2	2.3	2.0	2.0	33.1	0	0	0	0	0	0	0	0	0
	70-bottom	1.9		1.5	1.4	34.8	0	0	0	1	1	0	0	0	0
	bottom	1.6	1.3	0.9	0.7	36.5	2	2	0	0	0	0	0	0	0

■ : showed dark period

Table 4 : Distributions of the P4-stage postlarvae of the greasyback prawns.

	Depth (cm)	DO concentration (mg l <sup>-1</sup> )				Salinity start	Number of individuals									
		start	8h	16h	24h		start	3h	6h	9h	12h	15h	18h	21h	24h	
Control	surface -10	6.6		6.3	5.9	22.1	0	0	0	0	0	0	0	0	0	0
	10-20	6.5			5.1	23.8	0	0	0	0	0	1	0	0	0	0
	20-30	6.2		5.7	5.1	25.5	0	0	0	0	0	1	0	0	0	0
	30-40	6.4			5.5	27.3	0	0	1	0	2	0	0	0	0	0
	40-50	6.1		5.7	5.5	29.0	0	2	1	3	4	1	2	0	0	0
	50-60	6.0			5.3	30.7	0	0	4	4	0	1	2	0	0	0
	60-70	5.8		5.6	5.4	32.4	0	0	2	2	2	1	3	0	1	1
	70-bottom	5.8			5.2	34.1	1	0	1	1	1	0	2	1	1	1
	bottom	5.7		5.3	4.0	35.8	14	13	6	5	6	9	4	12	9	9
Case1	surface -10	6.6	6.2	5.7	4.8	21.2	0	0	0	0	0	0	0	0	0	0
	10-20	6.1		4.8	3.6	23.2	1	1	0	0	0	0	0	2	0	0
	20-30	5.6	5.4	4.1	3.0	25.3	1	2	1	5	1	0	5	2	2	2
	30-40	5.2		3.6	3.0	27.3	0	1	3	6	0	4	1	3	2	2
	40-50	4.5	4.5	3.6	2.3	29.3	0	1	0	0	1	1	1	1	1	1
	50-60	4.2		3.2	2.4	31.3	0	0	1	0	2	1	1	1	0	0
	60-70	3.6	3.6	3.5	2.1	33.3	1	0	3	1	2	1	1	0	0	0
	70-bottom	3.1		2.8	2.2	35.3	0	0	3	0	3	0	2	1	1	1
	bottom	3.1	3.1	2.7	1.2	37.4	12	10	4	3	5	7	1	1	0	0
Case2	surface -10	6.3	5.9	6.3	5.4	21.9	0	1	0	0	0	0	0	0	0	0
	10-20	5.5			4.5	23.7	1	0	1	2	1	1	0	0	1	1
	20-30	5.1	4.4	4.8	3.6	25.6	0	1	4	3	0	3	4	0	1	1
	30-40	4.7			3.2	27.4	0	1	4	2	3	0	2	2	0	0
	40-50	4.0	3.7	4.2	2.7	29.2	2	3	1	1	2	1	1	1	2	2
	50-60	3.6			2.6	31.1	0	1	1	1	1	3	1	2	2	2
	60-70	3.2	3.1	3.2	2.4	32.9	2	1	0	1	1	2	0	0	0	0
	70-bottom	3.0			2.1	34.7	0	1	0	0	1	1	0	2	0	0
	bottom	2.7	2.1	2.4	1.9	36.5	10	6	4	5	5	3	2	2	1	1
Case3	surface -10	6.4	6.4	5.7	5.5	21.9	0	0	1	0	0	0	1	1	0	0
	10-20	5.6			4.2	23.7	0	1	3	0	2	0	0	1	0	0
	20-30	5.3	5.2	4.4	3.8	25.5	1	3	0	0	2	3	0	2	1	1
	30-40	4.4			3.4	27.3	1	1	2	2	2	3	3	0	0	0
	40-50	4.0	3.8	3.8	2.7	29.0	1	1	2	3	1	6	0	2	2	2
	50-60	3.6			2.4	30.8	2	2	1	2	1	0	0	2	3	3
	60-70	2.9	2.9	2.6	2.5	32.6	1	1	2	1	1	1	2	0	1	1
	70-bottom	2.5			1.9	34.4	1	1	1	2	2	1	1	1	2	2
	bottom	2.3	2.4	2.0	1.5	36.1	8	5	2	4	3	0	5	3	1	1
Case4	surface -10	6.1	6.2	5.6	5.5	21.6	1	1	1	0	0	0	2	0	0	0
	10-20	5.5		4.9	3.9	23.5	1	0	0	1	0	1	0	0	0	0
	20-30	5.2	4.9	4.3	3.6	25.4	1	2	3	1	2	1	1	2	2	2
	30-40	4.7		3.8	3.3	27.2	1	2	3	2	4	1	2	0	1	1
	40-50	4.0	4.2	3.4	2.7	29.1	2	2	2	5	2	3	0	2	1	1
	50-60	3.3		2.8	2.3	30.9	1	1	1	1	1	1	2	0	0	0
	60-70	2.5	2.4	2.0	1.6	32.8	1	1	0	0	1	1	0	0	0	0
	70-bottom	2.0		1.8	1.4	34.6	0	1	0	0	0	0	0	0	0	0
	bottom	1.7	1.7	1.6	0.8	36.5	7	2	2	2	0	0	0	0	0	0

■ : showed dark period

Table 5 : Distributions of the P15-stage postlarvae of the greasyback prawns.

Depth (cm)	DO concentration (mg l <sup>-1</sup> )				Salinity	Number of individuals									
	start	8h	16h	24h		start	start	3h	6h	9h	12h	15h	18h	21h	24h
Control	surface -10	6.6	6.2	5.7	5.1	22.1	0	1	0	3	0	0	0	0	0
	10-20	6.5	6.1	5.0	4.4	23.8	2	2	0	2	0	0	0	0	0
	20-30	6.2	5.8	4.8	3.8	25.5	0	2	0	0	2	1	0	1	0
	30-40	6.4	5.7	5.1	3.7	27.3	0	1	2	0	2	0	1	1	1
	40-50	6.1	5.8	5.2	3.7	29.0	0	2	2	1	0	0	0	0	1
	50-60	6.0	5.8	5.4	4.4	30.7	0	0	0	0	0	0	0	1	4
	60-70	5.8	5.8	5.5	1.6	32.4	0	0	3	0	1	1	1	3	7
	70-bottom	5.8	5.8	2.1	1.3	34.1	0	0	0	0	2	1	2	2	1
bottom	5.7	5.6	1.5	1.1	35.8	13	7	8	8	7	11	10	6	0	
Case1	surface -10	6.6	5.5	4.6	4.2	21.2	0	1	0	1	0	0	0	0	1
	10-20	6.1	5.1	4.3	2.6	23.2	0	1	1	0	0	0	0	0	3
	20-30	5.6	4.9	3.8	2.1	25.3	0	1	1	0	1	1	1	2	3
	30-40	5.2	4.7	3.5	1.5	27.3	2	1	0	1	2	4	4	5	6
	40-50	4.5	4.0	3.3	1.1	29.3	1	2	0	1	3	2	1	5	2
	50-60	4.2	3.5	3.1	0.9	31.3	0	0	2	1	2	0	3	3	0
	60-70	3.6	2.9	2.1	0.7	33.3	2	1	0	2	3	0	4	0	0
	70-bottom	3.1	2.2	1.3	0.4	35.3	2	1	0	3	1	2	2	0	0
bottom	3.1	1.2	1.1	0.3	37.4	8	7	11	6	3	6	0	0	0	
Case2	surface -10	6.3	5.3	5.2	4.8	21.9	1	4	1	2	0	0	0	0	1
	10-20	5.5	5.1	5.0	4.5	23.7	0	1	0	1	0	1	0	1	1
	20-30	5.1	4.9	4.4	4.3	25.6	0	1	1	1	1	0	2	0	3
	30-40	4.7	4.6	4.1	3.5	27.4	0	0	1	0	0	2	0	1	0
	40-50	4.0	4.5	3.3	2.8	29.2	0	0	1	2	3	0	0	1	0
	50-60	3.6	3.5	2.3	2.4	31.1	0	1	3	3	1	2	0	2	0
	60-70	3.2	3.2	1.7	0.5	32.9	0	4	2	1	0	0	3	0	0
	70-bottom	3.0	1.8	1.2	0.5	34.7	2	0	3	2	0	0	0	0	0
bottom	2.7	1.3	0.3	0.1	36.5	12	4	3	3	10	0	0	0	0	
Case3	surface -10	6.4	5.2	5.2	5.4	21.9	0	3	1	0	0	0	0	1	1
	10-20	5.6	5.0	4.7	4.8	23.7	0	3	1	0	0	1	0	1	1
	20-30	5.3	4.8	4.1	3.6	25.5	0	1	1	1	0	5	0	2	4
	30-40	4.4	4.4	3.7	2.6	27.3	0	0	1	1	3	0	2	0	3
	40-50	4.0	4.3	3.2	1.8	29.0	0	0	0	0	1	1	1	2	4
	50-60	3.6	3.7	2.6	1.3	30.8	1	0	0	2	2	2	6	2	0
	60-70	2.9	2.8	1.6	1.1	32.6	0	0	3	1	3	3	3	0	0
	70-bottom	2.5	1.9	1.2	0.7	34.4	1	0	1	0	0	1	1	1	0
bottom	2.3	1.3	0.7	0.1	36.1	13	8	7	10	5	1	0	4	0	
Case4	surface -10	6.1	5.3	5.2	5.2	21.6	2	2	0	0	0	0	0	0	2
	10-20	5.5	5.1	4.7	4.3	23.5	2	0	0	0	0	0	0	0	0
	20-30	5.2	4.9	3.9	1.8	25.4	0	5	0	1	0	0	2	7	6
	30-40	4.7	4.5	3.0	1.4	27.2	1	1	0	1	1	0	3	0	4
	40-50	4.0	3.6	2.2	1.1	29.1	2	1	1	1	3	4	2	2	0
	50-60	3.3	3.1	1.5	0.6	30.9	1	0	7	7	5	5	3	2	0
	60-70	2.5	2.1	1.2	0.2	32.8	0	0	0	2	2	0	0	0	0
	70-bottom	2.0	1.8	0.7	0.1	34.6	2	1	4	1	0	2	0	1	0
bottom	1.7	1.2	0.2	0.1	36.5	5	4	2	1	2	2	3	0	0	

■ : showed dark period

salinity gradient column. As dissolved oxygen concentrations largely decreased by 16 hours in all oxygen and salinity gradient columns together with the control one, we used data of 0 to 8 hours for analyzing the avoidance to hypoxia of the P15-stage postlarvae. The percentage of distribution at the bottom of the column showed 57.8% in case 1 (1.2-3.1 mgO<sub>2</sub> l<sup>-1</sup>), 42.2% in case 2 (1.3-2.7 mgO<sub>2</sub> l<sup>-1</sup>) and 62.2% in case 3 (1.3-2.3 mgO<sub>2</sub> l<sup>-1</sup>), which had no remarkable difference with the value of 62.2% of the control column (5.6-5.7 mgO<sub>2</sub> l<sup>-1</sup>). However, only 2-5 individuals of the P15 postlarvae were observed at the bottom when dissolved oxygen decreased between 1.2 and 1.7 mgO<sub>2</sub> l<sup>-1</sup> in case 4. Although dissolved oxygen strikingly declined after 8 hours, P15-stage postlarvae survived in the latter half of the experiment except for case 2 where 10 individuals became inactive at 12 hours and died thereafter.

Table 6 : Criteria of avoidance to hypoxia for the mysis or postlarvae of the greasyback prawns.

Stage	DO concentration (mgO <sub>2</sub> l <sup>-1</sup> )
Mysis-stage larvae	2.1-2.6
P4-stage postlarvae	2.1-2.7
P15-stage postlarvae	1.2-1.7

#### 4. Discussion

Miller et al. (2002) examined the hypoxic tolerance of 13 species of marine and estuarine fishes, crustaceans and a bivalve and reported that mortality attained 14-22% for crustaceans even in the control test due to their metamorphosis and molting. They also suggested that the responses to hypoxia can be compared to each other if the mortality in the control is below these percentages. In the present experiment mysis-stage greasyback prawns showed a mortality of 13.3% in the control column which is lower than a range described by Miller et al. (2002). Yamochi et al. (1995) carried out indoor experiments and field surveys on the hypoxic tolerance of the juvenile greasyback prawn, indicating that they can survive for 24 hours at dissolved oxygen saturations of 20-27% (1.4-1.9 mgO<sub>2</sub> l<sup>-1</sup>) with LC-50 being less than 7-12% (0.50-0.87 mgO<sub>2</sub> l<sup>-1</sup>) at 25 °C. And the juvenile greasyback prawn can survive at low concentrations of dissolved oxygen compared with juvenile kuruma prawn *Marsupenaeus japonicus*, young swimming crab *Portunus trituberculatus*, and young common brackish goby *Acanthogobius flavimanus*. The juvenile greasyback prawn's habitat was at the bottom of the mouth of the Yodo river, Osaka, where oxygen saturation decreased to 12-55% in summer. These findings lead to a conclusion that the greasyback prawns can dominate in hypoxic habitats depending on their excellent ability of tolerance to hypoxic conditions. In the present study, P15 postlarvae of the greasyback prawns, whose body length were ca.15 mm survived at a rate of 86.7% for 15 hours and 80.0% for 24 hours at highly hypoxic conditions of 0.1-3.1 mgO<sub>2</sub> l<sup>-1</sup> (Tables 2 and 4). This well coincided with occurrence of the juvenile greasyback prawns with 25-40 mm body length in the hypoxic estuary of the Yodo river. Although the mortality sharply increased at 0.7-1.6 mgO<sub>2</sub> l<sup>-1</sup> for mysis and at 0.8-1.7 mgO<sub>2</sub> l<sup>-1</sup> for P4 postlarvae, no clear increase in mortality was observed at 0.1-1.7 mgO<sub>2</sub> l<sup>-1</sup> for P15 postlarvae. This suggests that the greasyback prawns may acquire hypoxic tolerance between P4 and P15 postlarval stage, and they then succeed in occupying their habitats in hypoxic coastal areas or river mouths owing to their prominent tolerance to low oxygen.

Statistical analysis ( $\chi^2$  test) was used to determine the concentration of dissolved oxygen where the larvae or postlarvae started avoiding. In this case, we employed the experimental data of 0-15 hours which had no large decline of the concentrations of dissolved oxygen. A statistical difference was detected in the vertical distribution of the mysis-stage larvae between case 3 (dissolved oxygen concentration at the bottom: 1.8-2.0 mgO<sub>2</sub> l<sup>-1</sup>) and control. In addition, there was a statistical difference of the distribution between case 3 and control even when data of the 70cm-bottom layer were excluded ( $P < 0.10$ ). Therefore, the upper limit of avoidance against hypoxia in the mysis-stage larvae was estimated to be 2.1-2.6 mgO<sub>2</sub> l<sup>-1</sup>. Vertical distributions of the P4-stage postlarvae were different in case 2, case 3 and case 4 if compared to the control ( $P < 0.05$ ). This suggests that the upper limit of avoidance in P4-stage larvae was between 2.1-2.7 mgO<sub>2</sub> l<sup>-1</sup> (dissolved oxygen concentrations at the bottom of the column in case 2). After growing into P15-stage larvae, the statistical difference of vertical distribution ( $P < 0.05$ ) was only confirmed between case 4 (dissolved oxygen concentration at the bottom: 1.2-1.7 mgO<sub>2</sub> l<sup>-1</sup>) and control, but not between case 1, case 2, case 3 and control when compared the number of individuals of the larvae at the bottom. This indicates that P15-stage larvae of the greasyback prawns start avoidance to hypoxia at 1.2-1.7 mgO<sub>2</sub> l<sup>-1</sup>. As a conclusion, the larvae of the greasyback prawns avoid hypoxia at dissolved oxygen concentrations below 2.1-2.6 mgO<sub>2</sub> l<sup>-1</sup> for mysis larvae, below 2.1-2.7 mgO<sub>2</sub> l<sup>-1</sup> for P4 postlarvae and below 1.2-1.7 mgO<sub>2</sub> l<sup>-1</sup> for P15 postlarvae (Table 6). These results reveal that physiological limit of avoidance to hypoxia of the larval greasyback prawns becomes low in correspondence to the development of life stage, especially from early postlarvae to late postlarvae. This also corresponds with the findings that survival rate of the greasyback prawns increase depending on the stage from early postlarvae (P4) to late postlarvae (P15).

Ohtomi et al.(2006) reported that the rate of settlement of the larval mantis shrimp *Oratosquilla oratoria* decreased depending on the hypoxic conditions in Tokyo Bay. Further, Kusakabe et al.(2002) demonstrated that hypoxic bottom water could affect the distribution of juvenile southern rough shrimp *Trachysalambria curvirostris* in August in Osaka Bay. These results lead to a conclusion that the juvenile greasyback prawns can dominate in hypoxic habitats of inner Osaka Bay owing to their excellent ability of tolerance to hypoxic conditions, but spatial distribution of the greasyback prawns changed and their growth was inhibited by hypoxia when they were in mysis or early postlarval stage.

#### Acknowledgements

The authors express their sincere thanks to Mr. H.Yamane of the Mie Prefectural Sea Farming Center, Japan for his kind support in obtaining the larval greasyback prawns for the present experiment. This research was conducted based on the financial support of the Ministry of the Environment, Japan and Japan Society for the Promotion of Science.

#### References

- Kodama, K., Horiguchi, T., Kume, G., Nagayama, S., Shimizu, T., Shiraishi, H., Morita, M. and Shimizu, M. (2006), "Effects of hypoxia on early life history of the stomatopod *Oratosquilla oratoria* in a coastal sea", Marine Ecology Progress Series, 324, 197-206.
- Kusakabe, T., Nabeshima, Y. and Ishiwatari, T. (2002), "Settlement of juvenile southern rough shrimp, *Trachysalambria curvirostris* in Osaka Bay", Aquaculture Science, 50(1), 31-36 (in Japanese).
- Miller, D.C., Poucher, S.L. and Coiro, L. (2002), "Determination of lethal dissolved oxygen levels for selected marine and estuarine fishes, crustaceans, and a bivalve ", Marine Biology, 140, 287-296.
- Oda, K., Ishikawa, K., Kido, K., Nakamura, Y., Yamochi, S. and Taguchi, K. (1997), "Population dynamics model of *Metapenaeus ensis* larvae stage in Osaka Bay ", Proceedings of Coastal Engineering, JSCE, 44(2), 1196-1200 (in Japanese).
- Ohtomi, J., Furota, T. and Kawazoe, H. (2006), "Change in spatial distribution with development for larval Japanese mantis shrimp *Oratosquilla oratoria* (Stomatopoda, Squillidae) in Tokyo Bay, Japan", Nippon Suisan Gakkaishi, 72(3), 382-389 (in Japanese).
- Pihl, L., Baden, S.P. and Diaz, R.J. (1991), "Effects of periodic hypoxia on distribution of demersal fish and crustaceans", Marine Biology, 108, 349-360.
- Tanaka, Y. (1990), "Changes in the egg and larval densities of striped beakperch (Pisces; Oplegnathidae) during development ", Memoirs of the Faculty of Agriculture of Kinki University, 23, 19-24.
- The Oceanographic Society of Japan (1981), "Manuals for oceanographic observation ", Japan Meteorological Agency (Ed), 429 p. (in Japanese).
- Yamochi, S., Ariyama, H. and Sano, M. (1995), "Occurrence and hypoxic tolerance of the juvenile *Metapenaeus ensis* at the mouth of the Yodo river, Osaka ", Fisheries Science, 61(3), 391-395.
- Yamochi, S., Ariyama, H. and Sano, M. (1998), "Environmental restoration of coastal habitats in the inner part of Osaka Bay – Quality of seawater, bottom sediment and benthic fauna in the vicinity of a planned tidal flat at the port of Sakai-Senboku, and response of marbled sole, *Pleronectes yokohamae* to hypoxia-", Umi no kenkyu (Oceanography in Japan ), 7(5), 293-303 (in Japanese).
- Yanagi, T. (1989), "A summary of symposium on oxygen-deficient water mass", Bulletin on Coastal Oceanography, 26(2), 141-145 (in Japanese).



# An Analysis on Influence Factors to Use Frequency and WTP of Shopping Support Services for People in Food Desert

Noboru ISE\* and Yasuo HINO\*\*

(Received October 3, 2014)

## Synopsis

Recently, the food desert problem has been becoming serious problem in mainly rural areas of Japan, because it must be improved by local responsibility according to local needs. Although some estimation methods of the number of people in food desert (PFD) were developed, the estimations of the demand for and profit from shopping support service will be also required. Therefore, this paper mainly aims to gain the fundamental knowledge not only to develop the estimation model of the demand for shopping support service for PFD but also to evaluate the profit of them at local level, by the factor analysis including individual attributes and area characteristics.

As a result, some important findings, concerned with influence factors to use frequency and WTP of shopping support services, came out of this study. These results must be useful information to introduce the suitable shopping support services for PFD in consideration of local needs.

**KEYWORDS:** People in food desert, Shopping support service, Use frequency, WTP, Factor analysis

## 1. Introduction

Recently, the food desert problem become serious in mainly rural areas of Japan, because of recent social changes: 1) declining in level of public transport services, 2) declining birth rate and growing proportion of elderly people, 3) increasing nuclear families and 4) decreasing the number of local commercial facilities and so on. Therefore, Ministry of Economy, Trade and Industry (METI) and Ministry of Agriculture, Forestry and Fisheries (MAFF) have been making various efforts to solve the food desert problem, such as estimation of the number of PFD based on original methods and publishing of the shopping accessibility aid manual and so on. On the other hand, Ise *et al.* (2013) and Hirai *et al.* (2012) pointed out that the estimation methods developed by METI and MAFF are impossible to estimate the number of PFD at local level, and they had conducted fundamental studies to develop the new estimation method of the number of PFD.

It can be said that the following matters are essential to decide the shopping support service for local needs: 1) the number of PFD, 2) the demand for each shopping support service, 3) the profit from introducing each of them and 4) discussion with various kind of parties such as local government, local residents, private companies and academic experts and so on. However, manuals mentioned above are not enough knowledge to do that, because they do nothing but introduce some of pioneering projects.

Kuramochi *et al.* (2014) developed the discrete choice model to estimate the number of delivery service users based on the questionnaire survey for elderly people in rural areas. Tanimoto *et al.* (2012) determined five choice patterns of shopping support services by combination of two shopping support services and relative use frequency of them transformed into ordinal scale, and developed the multinomial probit model to estimate the number of users of “transport support service” and “delivery service” considering mental and physical functions of elderly people. However, there are some issues in these researches: 1) not considering non-elderly people and 2) they cannot estimate the use frequency of shopping support services for PFD.

Kishino *et al.* (2011) clarified the relationship between use frequency of shopping support services and some valuables such as individual attributes, family structure and physical ability and so on. However, some findings from this research is not enough to estimate the demand of shopping support services because they analyzed the relationship between use frequency of shopping support services and some valuables separately.

Therefore, this paper mainly aims to gain the fundamental knowledge to develop the model for

---

\* Associate Professor, Department of Civil Engineering, National Institute of Technology, Wakayama College

\*\* Professor, Department of Civil Engineering, Osaka City University

estimating the demand for each shopping support service for PFD and the profit from introducing each of them at local level, from the analysis of factors influencing use frequency and WTP of shopping support services for PFD considering individual attributes and area characteristics.

## 2. Outline of Target Town

Hidakagawa town in Wakayama, Japan is the target town in this study, which was created by the municipal merger between Kawabe town, Nakatsu village, and Miyama village in May 2005, as shown in Figure 1. This town is located at the center of Wakayama prefecture, which has an area of 331.65 km<sup>2</sup> (35km from east to west in width, 10km from north to south in width). Population size is very small (population is 10,509 and the number of household is 3,750). The density of population is also very small, but the ratio of elderly people is 10.4% higher than the national average (20.1%). In addition to the above, this town faces some problems such as decreasing of population and increasing of nuclear families. A railway is located in the southwest of this town, but there are only two stations. In addition to a few stations, train runs once every hour. Bus, community bus and share-ride taxi run in this town, but they run about two to eight times a day. All these things make it clear that the conditions of public transport in this town are poor. A lot of local residents pointed out that the conditions of public transport and daily shopping are poor, in the first long-term comprehensive development plan of this town.

As mentioned above, it is very urgent and important to support for grocery shopping of people in food desert in this town.

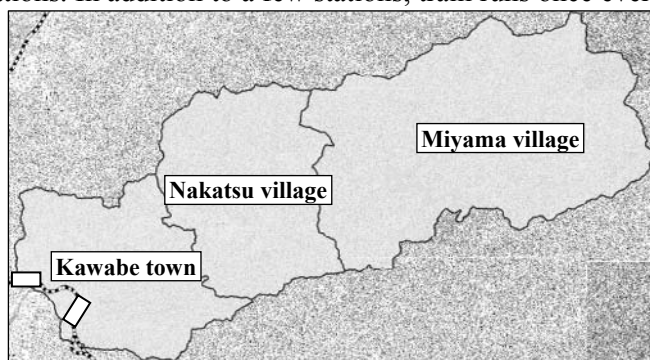


Figure 1. Hidakagawa town as the study field

## 3. Outline of Questionnaire Survey

The questionnaire survey was conducted from October to November 2013, in order to clarify the factors influencing use frequency and WTP of shopping support services for PFD. The main questionnaire items are individual attributes, conditions of public transport, condition of grocery shopping, difficulty with grocery shopping, user frequency and potential needs of shopping support services as shown in Table 1. The respondents are local residents except students and pupils, who were randomly sampled in Hidakagawa town. As a result, 1749 respondents were obtained from distributed 6000 questionnaire sheets.

Table 1. Main items of questionnaire survey

Items	Details
Individual attributes	<ul style="list-style-type: none"> <li>• Address, • Sex, • Age, • Household composition,</li> <li>• Certification of care need, • Pain-free walking time,</li> <li>• Availability of car and motorbike</li> </ul>
Conditions of public transport	<ul style="list-style-type: none"> <li>• Walking time to get to the nearest station</li> <li>• Walking time to get to the nearest stop of bus (including share-ride taxi)</li> </ul>
Conditions of grocery shopping	<ul style="list-style-type: none"> <li>• Type of the nearest grocery store</li> <li>• Distance from home to the nearest grocery store</li> <li>• Conditions of mobile grocery stores and grocery delivery</li> <li>• Presence of the person who support grocery shopping</li> </ul>
Difficulty with grocery shopping	<ul style="list-style-type: none"> <li>• Difficulty with grocery shopping</li> </ul>
Use frequency of shopping support services	<ul style="list-style-type: none"> <li>• Use frequency of shopping support services such as “going out”, “mobile grocery store”, and “grocery delivery”</li> </ul>
Needs of shopping support services	<ul style="list-style-type: none"> <li>• Needs of improvement of each support for grocery shopping</li> <li>• Intention to use each improved support for grocery shopping</li> <li>• Willingness to pay for each improved support for grocery shopping</li> </ul>

## 4. Conditions of Public Transport and Present Situation of PFD

### 4.1. Conditions of public transport

As for the accessibility to the nearest station, all residents in Nakatsu and Miyama villages and a half of residents in Kawabe town cannot access to the nearest station within 30 minutes on foot, as shown in Figure 2, because of the location of each residential area (See Figure 1). On the other hand, almost all of residents may be able to access to the nearest bus stop within 15 minutes on foot, as shown in Figure 3.

However, from a different angle, about 10 % more of residents must be not able to access to any public transport within 15 minutes on foot.

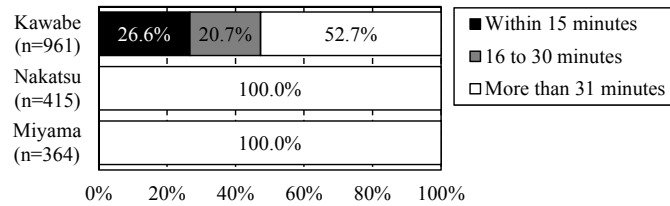


Figure 2. Walking time to get to the nearest station

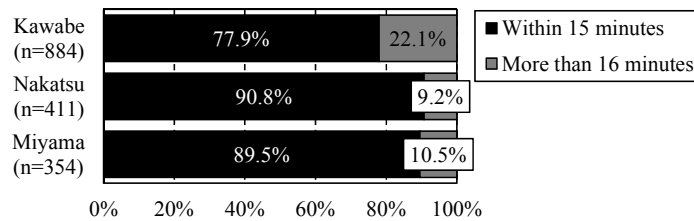


Figure 3. Walking time to get to the nearest bus stop

### 4.2. Ratio and age distribution of PFD

The Figure 4 shows the ratio and age distribution of PFD. PFD is respondents who answered “Usually difficult”, “Sometimes difficult” and “Seldom difficult”, to question “Do you have difficulty with grocery shopping”. As a result, it can be seen that other factors except conditions of public transport may have an influence on difficulty with grocery shopping, as the ratio of PFD of Nakatsu village is the highest in Hidakagawa town. On the other hand, it can be said that residents of under 65 years old should be taken into consideration, in order to estimate the number of PFD and consider some shopping support services for PFD.

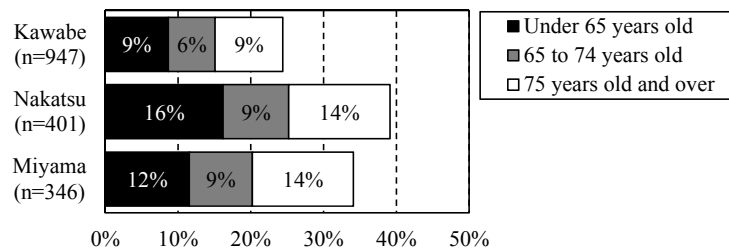


Figure 4. Ratio and age distribution of PFD

### 4.3. Use frequency of shopping support services of PFD

The use frequency of each shopping support service of PFD is summarized in Figure 5. In an analysis of use frequency of “transport support service”, the frequency of go out shopping by local public transport such as bus and taxi should be focused. However, the number of users of local public transport is very small. Therefore, all respondents who go out for shopping are included in this analysis, and this result is used for comparing with use frequency of other shopping support services. In analyses of use frequency of “mobile vendor” and “home delivery service”, respondents who answered “do not use” or “no service” are not included.

According to “go out shopping” of Figure 5, the ratio of those who go out shopping one to three times

a week is 65%. It is inferred that people in rural area buy a lot of foods at one time, in order to reduce inconvenience of going out shopping.

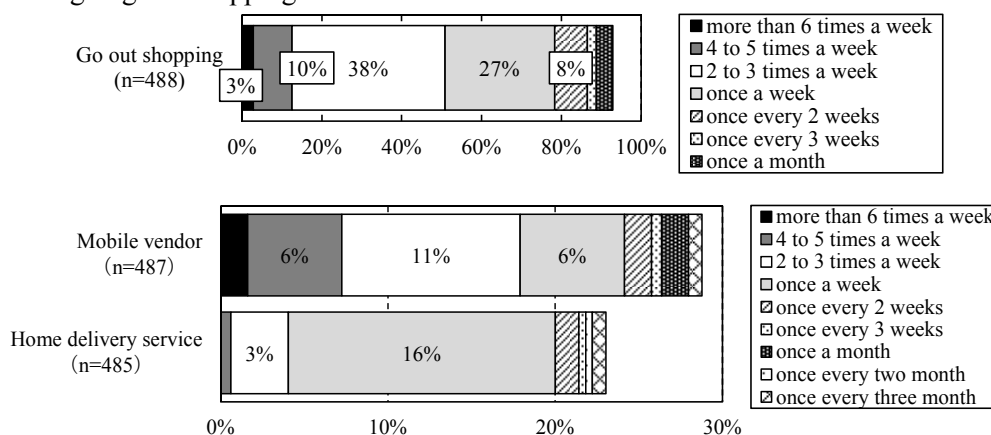


Figure 5. Use frequency of each shopping support services for PFD

#### 4.4. Willingness to pay (WTP) for the use of shopping support services for PFD

Figure 6 shows the WTP for the use of each shopping support service for PFD. WTP in this study means one-way fare for transport support service, pay-per-use fee for mobile vendor and pay-per-use fee for home delivery service.

77% of respondents are willing to pay for transport support service, and most of WTP ranges from 100 JPY to 700 JPY. The ratio of respondents who are willing to pay for mobile vendor and home delivery service is lower than that for transport support service. It might be because users of mobile vendor and home delivery service can only do shopping and cannot buy some foods from many.

On the other hand, there are a few respondents who are willing to pay more than 1500 JPY for mobile vendor and home delivery service. It can be said that mobile vendor and home delivery service are very important for people with limited access to shopping facilities.

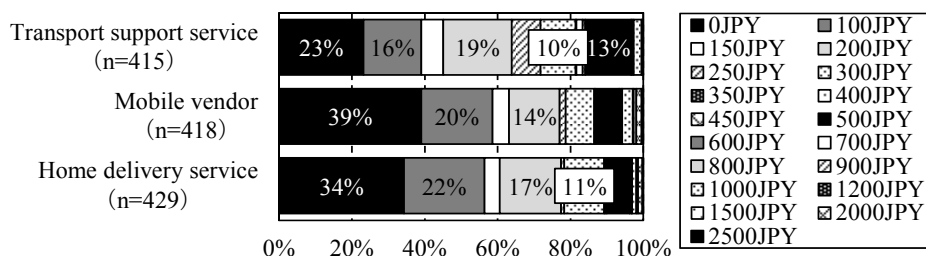


Figure 6. WTP for the use of each shopping support service for PFD

### 5. Analysis of Factors Influencing Use Frequency of Shopping Support services for PFD

In this chapter, factors influencing use frequency of shopping support services for PFD are clarified by using quantification theory type I.

As mentioned in section 4.3, the frequency of go out shopping by local public transport such as bus and taxi should be focused, in order to gain the fundamental knowledge to model demand for transport support service. However, the number of users of local public transport is very small. Therefore, all respondents who go out shopping are included in this analysis, and this result is used for comparing with use frequency of other shopping support services.

As shown in Figure 5, options of use frequency setting in this questionnaire survey have different unit such as “1(time/week)” and “1(time/2weeks)”. And some of them have a range such as “2~3(times/week)”. Therefore, unit of use frequency was converted to “times/day”. For example, “4~5(times/week)” is converted into “4.5/7(times/day)” and “1(time/month)” is converted into “1/28(times/day)”. In addition, “less than 1(time/month)” and “do not use” are converted into 0(times/day). In analyses of mobile vendor and home delivery service, only respondents who can use these services are included. Independent variables using for

these analyses achieve statistical significance based on one-way analysis of variance. And, all results also do not have problem of “multi-collinearity”.

### 5.1. Go out shopping

The result of Figure 7 indicates that, those who go out shopping comparatively frequently have following characteristics: 1) under 65 years old, 2) pain-free walking time is more than 21 minutes and 3) possible to use a car (driving by oneself and others). Therefore, it can be seen that decline in physical performance with age makes people decrease the frequency of go out shopping. And, other factors influencing the frequency of go out shopping are the distance from home to central area of Hidakagawa town, the distance from home to the nearest grocery store, presence of the people who support grocery shopping and assortment of foods.

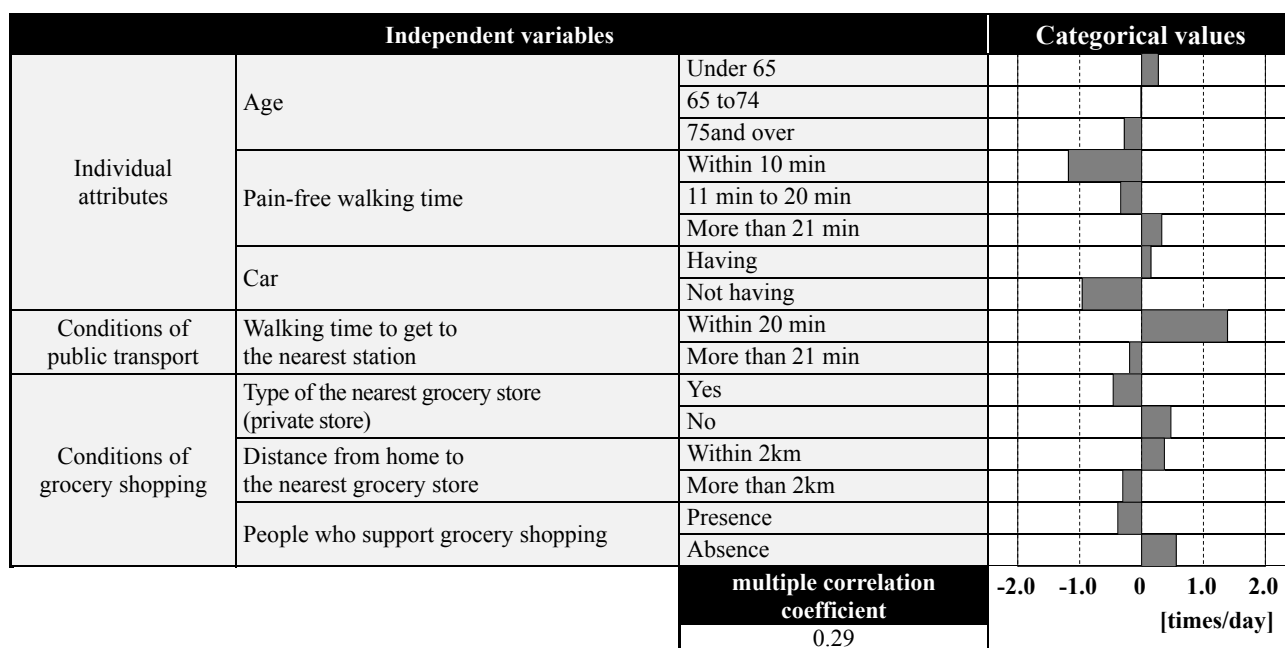


Figure 7. Analysis on factors influencing frequency of go out shopping

### 5.2. Mobile vendor

Figure 8 makes it clear that factors influencing use frequency of mobile vendor are different from those of go out shopping. In other words, the use frequency of mobile vendor increases with age. In addition, people living in areas poorly served by local public transport and grocery stores, depend strongly on mobile vendor. Accordingly, mobile vendor is used frequently as a supplement or alternative to go out shopping, because of the decline in physical performance with age and poor local public transport and grocery stores.

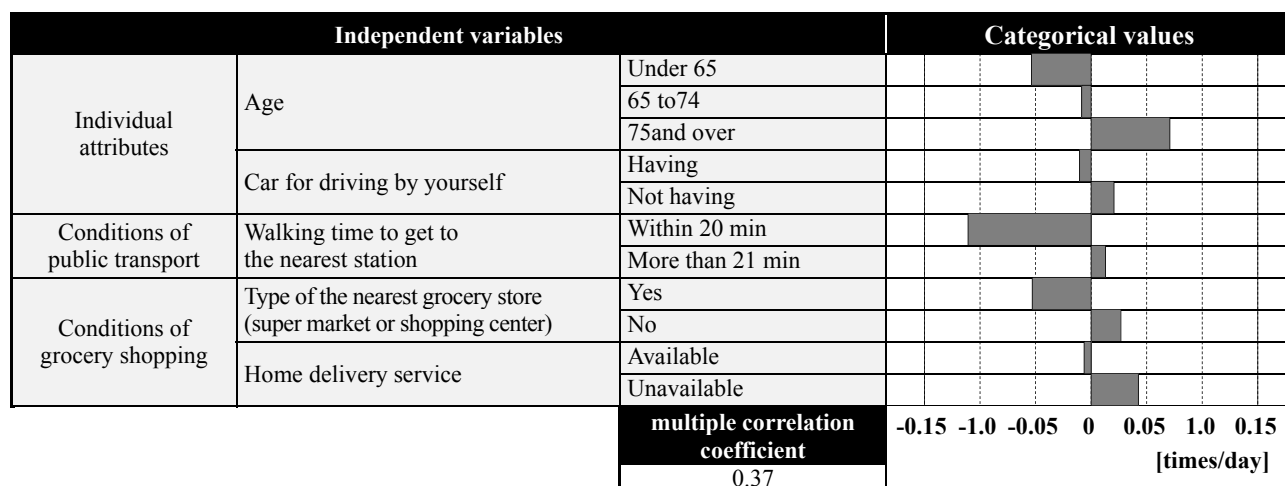


Figure 8. Analysis on factors influencing use frequency of mobile vendor

### 5.3. Home delivery service

Figure 9 makes it clear that factors influencing use frequency of home delivery service are similar with those of mobile vendor. That is to say, people living in areas poorly served by local public transport and grocery stores, depend strongly on home delivery service.

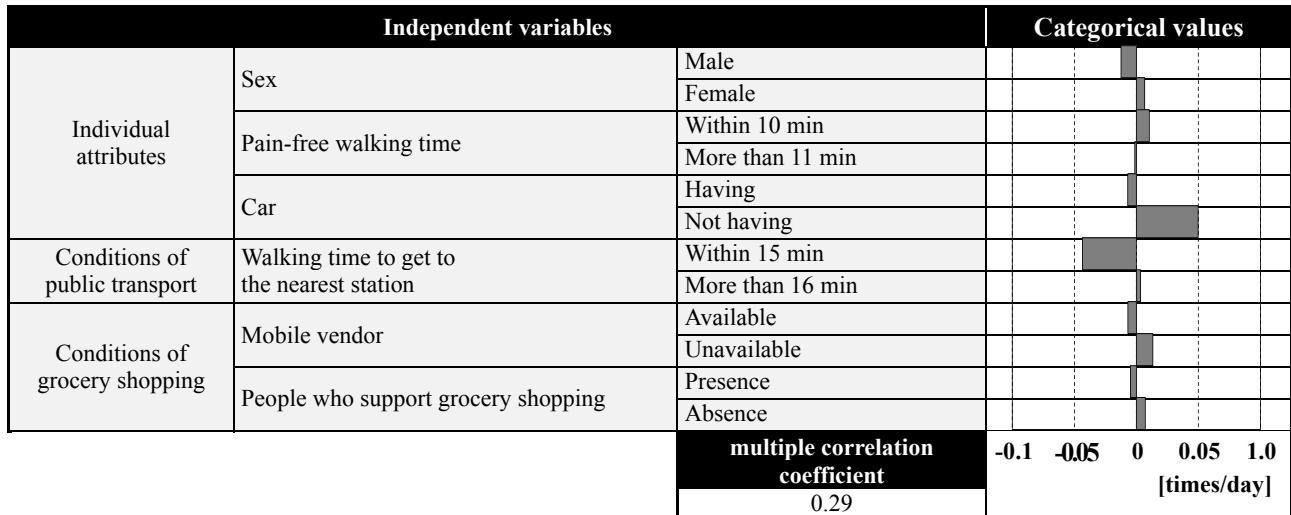


Figure 9. Analysis on factors influencing use frequency of home delivery service

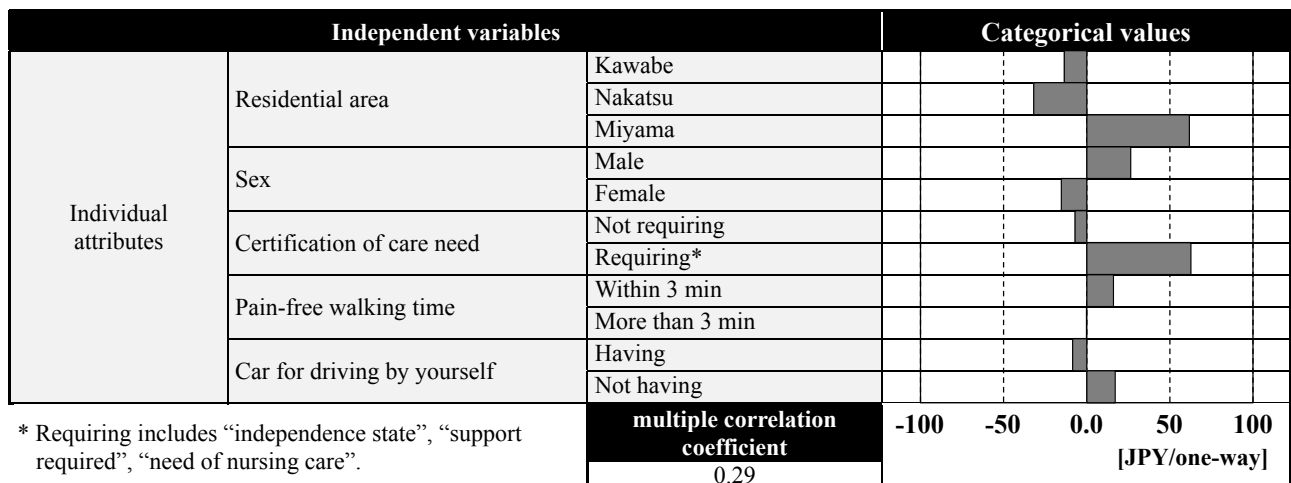
## 6. Analysis of Factors Influencing WTP for the Use of Shopping Support Services for PFD

In this chapter, factors influencing WTP for the use of shopping support services for PFD are clarified by using quantification theory type I. As with the analysis in Chapter 5, Independent variables using for these analyses achieve statistical significance based on one-way analysis of variance. And, all results also do not have problem of “multicollinearity”.

### 6.1. Transport support service

As shown in Figure 10, those who are willing to pay comparatively high for transport support service, have following characteristics: 1) independence state, support required and need of nursing care, 2) pain-free walking time is less than 3 minutes and 3) impossible to use a car (driving by oneself). It is probable that, although people become dependent on mobile vendor and home delivery service due to decline in physical performance with age, they have potential demand for transport support service.

Factors related to accessibility of local public transport and shopping environment, do not achieve statistical significance. “Residential area” was used as explanatory variable instead of “walking time to get to



\* Requiring includes “independence state”, “support required”, “need of nursing care”.

Figure 10. Analysis on factors influencing WTP for the use of transport support service

the nearest station”, because options of “walking time to get to the nearest station” cannot express in detail the differences in distance from home to central area of Hidakagawa town. As a result, “residential area” achieved statistical significance, and transport support service is the most necessary in Miyama village where is the farthest area from central area of Hidakagawa town.

### 6.2. Mobile vendor

There are a few explanatory variables which achieve statistical significance (Figure 11). However, those who are willing to pay comparatively high for mobile vendor, has following characteristics: 1) more than 60 years old, 2) pain-free walking time is less than 3 minutes and 3) walking time to get to the nearest station is more than 26 minutes. That is, individual attributes have a great influence on WTP for the use of mobile vendor, as is case in WTP for the use of transport support service.

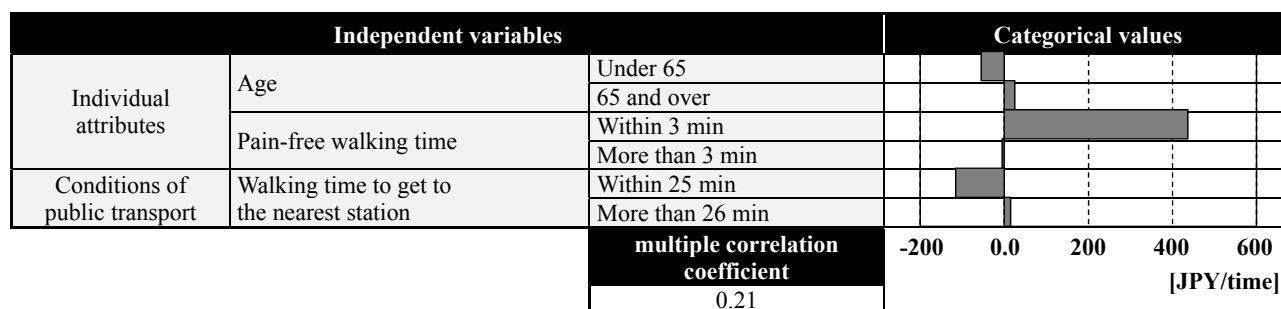


Figure 11. Analysis on factors influencing WTP for the use of mobile vendor

### 6.3. Home delivery service

There is no explanatory variable which achieves statistical significance. Therefore, it is said that, other factors which do not considered in this research, have an influence on WTP of home delivery service. As a result of calculating average WTP of each shopping support service, transport support service is 221 JPY, mobile vendor is 205 JPY and home delivery service is 185 JPY. Hence, average WTP for the use of home delivery service is the lowest in other average WTP.

From the above, although people become dependent on mobile vendor and home delivery service due to decline in physical performance with age, they have potential demand for transport support service, as it was mentioned in 6.1.

## 7. Conclusion

This study mainly aimed to gain the fundamental knowledge to develop the model for estimating the demand for each shopping support service for PFD and the profit from introducing each of them at local level, from the analyses of factors influencing use frequency and WTP of shopping support services for PFD considering individual attributes and area characteristics.

As a result, all factor analysis except WTP of home delivery service clarified some factors influencing use frequency and WTP of shopping support services for PFD. Factors influencing the frequency of go out shopping by using bus and taxi, are not clarified, because the number of users of local public transport is very small. However, some findings from 5.1 were very useful to compare with other factor analysis about use frequency.

Other major findings are summarized as follows.

- 1) There are difficulties for people to go out shopping, because of the decline in physical performance with age and poor local public transport and shopping facilities. And, those who have difficulty to go out shopping, depend on mobile vendor and home delivery service.
- 2) As for the WTP for the use of transport support service and mobile vendor, elderly and disabled people are willing to pay more high than others.
- 3) Those who decrease in physical performance with age, depend on mobile vendor and home delivery service. However, they need an improvement of transport support service, because Average WTP for the use of transport support service is also highest.

### Acknowledgements

This study was supported by JSPS KAKENHI Grant-in-Aid for young Scientists (B) of which number is 25820253.

### References

- 1) Ministry of Economy, Trade and Industry, *Report of research group to consider the future of logistics for supporting the infrastructure for local life* (2010).
- 2) Ministry of Agriculture, Forestry and Fisheries, *Present situation and future policy of food desert problem* (2012).
- 3) Ministry of Economy, Trade and Industry, *Second edition of "Shopping Accessibility Aid Manual"* (2011).
- 4) Ministry of Agriculture, Forestry and Fisheries, *Guidebook for considering shopping support service for people in food desert* (2014).
- 5) N. Ise and M. Shoji, *An Analysis on Influencing Factors on Difficulty of Shopping Accessibility by Considering Individual Attributes and Area Characteristics*, *Journal of Traffic Engineering*, Vol.33, 463-466 (2013).
- 6) H. Hirai, M. Minami, *Estimation of the Number of People in Food Desert targeting Elderly People in Morioka city Iwate Prefecture*, *Proceedings of Infrastructure Planning* (CD-ROM), Vol.46, 5pages (2012).
- 7) H. Kuramochi, K. Tanimoto and S. Tsuchiya, *Shopping Support in Rural Depopulated Areas:Focusing on Delivery Services*, *Journal of Sociotechnology*, Vol.11, 33-43 (2014).
- 8) K. Tanimoto and K. Onishi, *A Consideration on the Choice of Support Services of Daily Life according to Physical and Mental Function of Elder People*, *Proceedings of Infrastructure Planning* (CD-ROM), Vol.45, 4pages (2012)
- 9) K. Kishino, H. Kita, T. Ochi and H. Yotsutsuji, *A Fundamental Analysis on the Methods to Have Opportunities of Daily Activities in Rural Area*, *Journal of Traffic Engineering*, Vol.31, 393-398 (2011)

# Formation of Waterside Spaces with Groins

Yasumasa FUKUSHIMA\* and Takashi UCHIDA\*\*

(Received October 3, 2014)

## Synopsis

River management in recent years involves measures for waterside management emphasizing the environment and utilization as well as river improvement and irrigation. This study addresses the formation of waterside spaces with groins as a part of waterside management emphasizing the environment and utilization, using typical groin management cases in which planning we have been engaged. This report presents our knowledge obtained through processes from planning, business implementation, and subsequent degradation by aging.

KEYWORDS: River environment, waterside space, waterside management, groin, land–water ecotone

## 1. Study Background and Objectives

Groins in Japan have been used from ancient times to control streams and mainly to protect riverbanks from flooding. Groins have been used for securing water transportation routes in modern times since Meiji, represented by Krippen groins constructed by Dutch engineer Johannis de Rijke. River management in recent years involves measurements for waterside management focusing on environment and utilization as well as river improvement and irrigation. Diverse streams generated by groins have contributed to flood control and to the rehabilitation and creation of excellent river environments.

This study addresses effective planning and maintenance management methods for the formation of a waterside spaces with groins as a part of waterside management, with emphasis on environment and utilization, using three typical groin management cases in which planning we have been engaged. Using them as examples, we share our knowledge obtained through processes related to planning, business implementation, and subsequent aging degradation.

## 2. Tasks in Groin Management Areas

Tasks in the following three areas of waterside management have been promoted by application of groins.

### 2.1 Case 1: Kizugawa Waterside Plaza<sup>1)</sup>

The Waterside Plaza was constructed for environmental learning integrated with protected lowland facilities in the neighborhood of the Nagarebashi Bridge, downstream of the Kizugawa River of the class-A Yodogawa River system. The emergence of river banks and loss of land–water ecotones had been advancing by the development of an ultra-low water channel (Fig. 1). The task was to rehabilitate sand river beaches (large-scale sandbars) that used to be there.

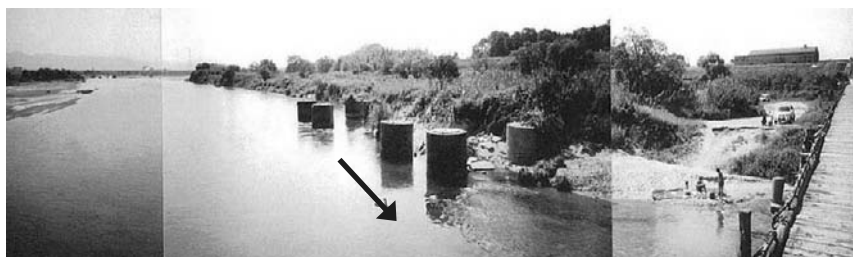


Fig. 1 View before construction (Case 1).

---

\* Student, Doctor Course of Department of Civil Engineering

\*\* Professor, Department of Civil Engineering

## 2.2 Case 2: Kizugawa Kasagi area <sup>2)</sup>

This area is located upstream of the Kizugawa River of the class-A Yodogawa River system, at the foot of Mt. Kasagi, which is designated as a historic site and beauty spot of Japan. The site has been used by a neighboring elementary school for canoe school lessons and fieldwork related to water quality as part of environmental education. Development has been in progress for its use as a "Waterfront Fun School."

A waterside environment that provides safety and environment in harmony is necessary for multi-purpose usage patterns such as water wildlife observation and canoeing. However, this site had lost a sandbar that once existed there (Fig. 2). Therefore, it was required that a gentle waterside environment (land–water ecotone) be created, which would not spoil the landscape but which would secure safety at the time of canoe boarding or wildlife observation at the waterside.



Fig. 2 View before construction (Case 2).

## 2.3 Case 3: The Yoshiminegawa River, Kyoto <sup>3)</sup>

Nature-friendly river works were advanced on the Yoshiminegawa River of the class-A Yodogawa River system. At the river bend (Fig. 3), which is a planning site, establishment of a land–water ecotone was advanced for creating waterside utilization or a habitat of a good ecosystem on the inner bank. At the same time, policies for protecting river banks were required while creating deep water in the water colliding front incorporated with low-water bed works by crosspiece structures on the upper and lower streams.



Fig. 3 View before construction (Case 3).

## 3. Measures with Groins and Aging Degradation after Construction

### 3.1 Measures with groins

Groin construction was conducted as described below, according to the tasks of each construction area. Table 1 presents project details for each area.

#### 1) Case 1: Kizugawa Waterside Plaza

Plans were made to reclaim a large-scale sandbar with the combination of diverse structures comprising five sets of impermeable and permeable groins. Specifically, three short impermeable low-water groins were positioned at the uppermost stream aiming at changing flow direction, and one permeable low-water groin for building up a varied sandbar and one impermeable low-water groin for forming a reliable sandbar were installed downstream.

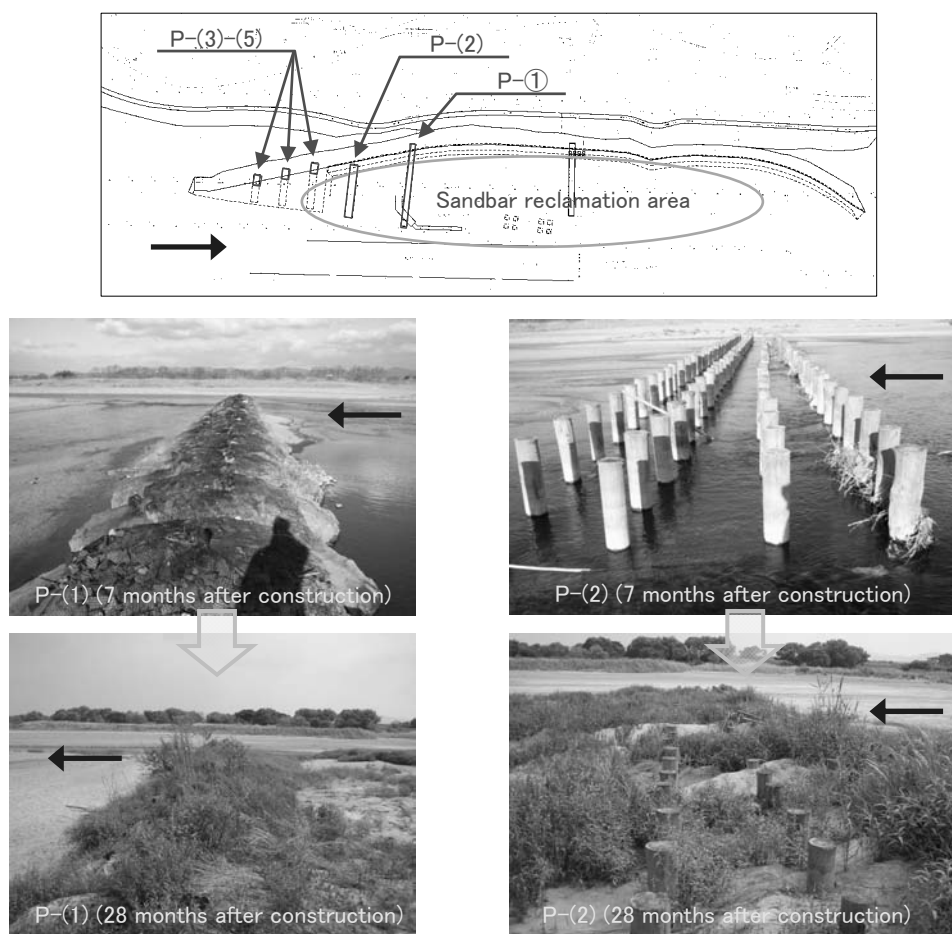


Fig. 4 Project outline and aspect after construction (Case 1).

Table 1 Detailed groin plan in each case

Area name	Kizugawa Waterside Plaza (Case 1)			Kizugawa Kasagi area (Case 2)	Yoshiminegawa River, Kyoto (Case 3)
River name and river system	Kizugawa River, the Class-A Yodogawa River system			Kizugawa River, Class-A Yodogawa River system	Yoshiminegawa River, Class-A Yodogawa River system
Estimated high-water discharge	6,200 m <sup>3</sup> /s			6,200 m <sup>3</sup> /s	160 m <sup>3</sup> /s
Estimated high-water inclination	1/1300			1/220	1/125
Segment	Segment 2-1			Segment M	Segment 1
Groin number	P-(1)	P-(2)	P-(3)-(5)	K-(1) - (3)	Y-(1)-(4)
Groin type	impermeable low water groin (overflow groin)	permeable low water groin	impermeable low water groin (overflow groin)	impermeable low water groin (overflow groin)	impermeable low water groin (overflow groin)
Groin structure detail	Bagged cobbles	Pile dike + bagged cobbles	Bagged cobbles	Stone-Net™	Natural stone joint structure
Objective of installation	Sandbar formation	Sandbar formation	Hydraulic jump	Sandbar formation	Deep water formation, river bank protection
Number of groins	1 (lowermost stream)	1 (middle)	3 (uppermost stream)	3	4
Installation angle	85°, inclined	85°, inclined	85°, inclined	75°, inclined	70°, inclined
Groin crown height	low-water level + 0.5 m (+1.6 m of river bed)	low-water level + 0.5 m (+1.7 m of river bed)	low-water level + 0.5 m (+1.7 m of river bed)	ordinary water level (+0.5 - 1.0 m of river bed)	ordinary water level (river bed elevation)
Groin length (ratio to ordinary river width)	74.5 m (1/4.3)	47.9 m (1/6.7)	9.6 m (1/33.3)	10.0 m (1/10)	2.0 m (foot protection width)
Year of construction	FY 2005	FY 2005	FY 2005	FY 2010	FY 2009

## 2) Case 2: Kizugawa Kasagi area

It was planned in this area to install groins as a necessary minimum reversible artifact harmonized with the landscape. Their environmental effects were to be used to reclaim the original scenery of this area (sandbar). Then it was intended to recover a waterside environment securing safety and environmental diversity. Specifically, it was scheduled to place three impermeable groins to encourage the formation of a small-scale sandbar for river utilization immediately downstream of the groin.

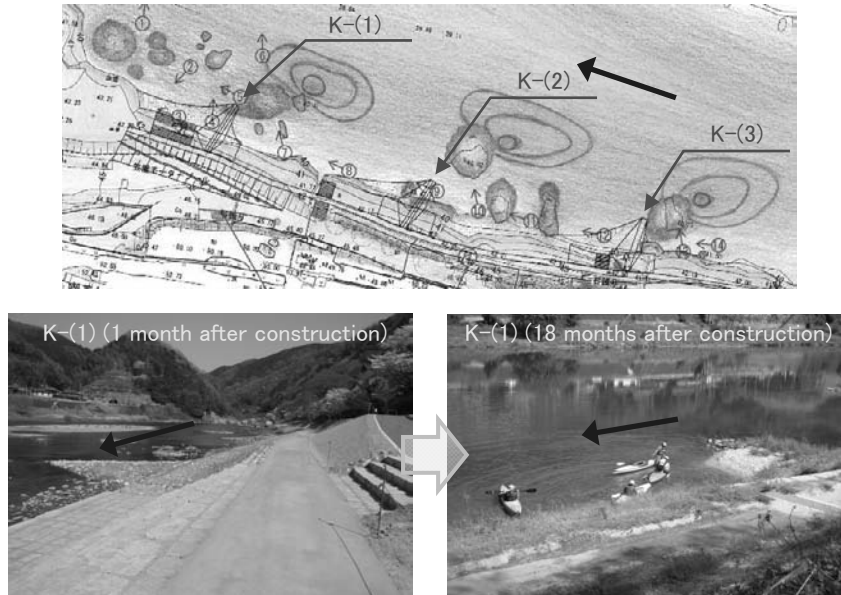


Fig. 5 Program outline and aspect after construction (case 2).

## 3) Case 3: Yoshiminegawa River, Kyoto

The project included the installation of four sets of short impermeable groins at a water collision front, and encouraged the creation and sustainment of a deep water area by the scouring effect of groin edges. It was anticipated that deep water areas created by this formation would induce an ordinary water route to the water colliding front, which contributes also to sustainment of a land-water ecotone on the opposite bank.

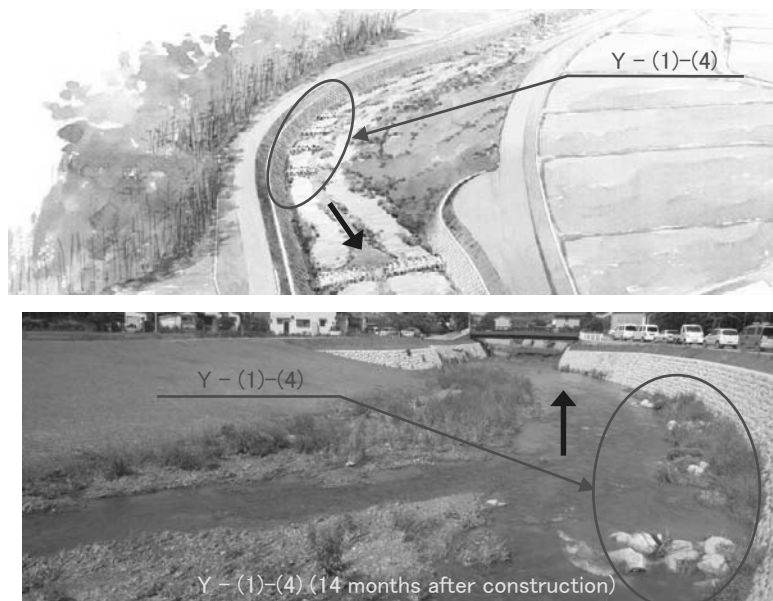


Fig. 6 Construction rendering and aspect after construction (case 3).

### 3.2 Aging degradation after groin construction

In response to the tracking result of aging degradation of groins after construction, the circumstances from construction to the present are organized, from the viewpoints of (a) environmental, (b) utilization, and (c) river improvement aspects.

#### 1) Case 1: Kizugawa Waterside Plaza

##### (a) Environmental aspect

A large-scale sandbar was formed between groins P-(1) and P-(2) and downstream therefrom, where sandbar formation had been expected, within half a year after groin installation. The sedimentation trend has been sustained since. A sandbar of about +1.0 – 2.0 m high above the groin installation level is stable today.

Regarding the sandbar formation effect by groins, the sedimentation effect of an impermeable groin (P-(1)) developed more quickly than with a permeable groin (P-(2)). However, a more complex sandbar was formed by a permeable groin. Rooting of herbs has progressed on sand accumulated up to near the crown of groins. Willows have flourished since about five years after installation.

As for the banks, although emergence of the low water channel was remarkable by division from the water area before construction, the regeneration of waterside vegetation such as *Phragmites japonica* is observed today.

##### (b) Utilization aspect

Because the steep banks, deep water, and fast stream were considered dangerous, almost no river users ventured around the waterside or water area before construction. However, since a sandbar was formed after construction, children have come to play in the water, people stroll on the sandbar, and tourists visiting to the water's edge have become a common sight.

##### (c) River improvement aspect

Because groins P-(1) and P-(2) were constructed as inclined, aiming at sedimentation, only their edges showed a prominent scouring effect, although scouring has been observed that causes modification on a revetment foundation. Groins P-(3)–(5) were also built as inclined, but groins of the minimum length as much as foot protection width have allowed the effects of a scouring section at the groin edge to extend near the bank (revetment foundation protection). This has modified the revetment slightly, but no particular problem has been reported to date because this is a revetment of gentle slope with high flexibility made of bag bodies. Moreover, the scouring is within the range of the maximum depth.

#### 2) Case 2: Kizugawa Kasagi area

##### (a) Environmental aspect

A sandbar was formed downstream from groins K-(1)–(3), where sandbar formation was intended, within half a year after groin installation, and a sandbar of about + 1.0 m high above the river bed elevation is stable at present. Herb rooting has been observed only on the groin crowns above ordinary water since around half a year after groin construction. Nevertheless, no trees have grown there yet.

As for the river bank situation, although the water depth had reached nearly one meter from the waterside immediately before construction, a land–water ecotone has been created by a sandbar. It is sustained today.

##### (b) Utilization aspect

Steep banks and deep water were regarded as dangerous before construction. However, canoe school lessons have been held safely since the sandbar was formed.

##### (c) River improvement aspect

Although all three sets were planned originally to be rockwork groins covered by natural stone anchored to wire gauze (Stone-Net™) in the planning phase, it was found that a rockwork groin of natural stones had been installed instead on the uppermost stream at the time of construction. Its stone-only structure permitted stones to be washed away within half a year after construction. Nevertheless, no noticeable damage occurred in the remaining two rockwork groins covered by Stone-Net™ even today, more than three years after construction.

Only the groin edges showed a prominent scouring effect, although no scouring was observed to cause modification on the revetment foundation.

### **3) Case 3: The Yoshiminegawa River, Kyoto**

#### **(a) Environmental aspect**

The scouring trend of edges has been sustained at all groins Y-(1)–(4), so that deep water of about - 1.0 m depth from the groin installation level is stable today, three and a half years after installation. This stability leads an ordinary water route to the water colliding front side. Therefore, it contributes to sustainment of a land–water ecotone on the inner bank. Sedimentation effects are evident downstream of groins, except for one set on the uppermost stream, in spite of the minimum groin lengths of as much as the foot protection width.

Moreover, since the groin crown height was set as high as designed river bed level, the groins had been supposed to be underwater a full year so that no herb rooting had been anticipated. However as deep water formed and the ordinary water level was lowered more than assumed, herbs have taken root on the groin crown and on the sandbar between groins, which have not resulted in tree growth causing river flow impediment.

#### **(b) Utilization aspect**

Steep banks made the waterside almost inaccessible before construction. However, waterside utilization by community residents has become popular by access via the land–water ecotone on the inner bank after construction.

#### **(c) River improvement aspect**

Inclined groins aiming at creation and sustainment of deep water areas by scouring at groin edges have produced a prominent scouring trend around the edges. A groin length as short as the minimum foot protection width had raised concerns that the effect of the scouring section at the groin edge would extend to the revetment foundation protection (near the bank). However, the revetment foundation protection of groins (revetment embedment) was in a sedimentation trend except for one set on the uppermost stream, so that no damage such as modification of revetment by excessive scouring has been observed.

## **4. Important Matters in Evaluation, Planning, and Maintenance Management of Groins in Waterside Space Forming**

The effect of groins for waterside space formation is evaluated based on measures with groins and their aging degradation after construction in the three areas. Points of discussion include important matters from the viewpoint of the structure type and scale in the planning phase, and tasks and important matters in maintenance management.

### **4.1 Groin type**

Comparison in the identical area (Case 1) revealed that an impermeable groin shows a greater sedimentation effect than a permeable groin, and that the latter forms a more complex sandbar than the former, so that the latter improves waterside diversity to a greater degree. However, herb rooting on a sandbar deposited up to near the crown (picket top) allows a permeable groin to hold earth and sand even at a flood. Therefore, it was verified that a permeable groin tends to be an impermeable groin not only in terms of geometry but in terms of its effects.

The structure of a permeable groin projected from the river bed tends to catch down-flowing objects, which might not be preferred on a landscape, so that maintenance management is necessary, including removal. Because they also might threaten the safety of facilities at a flood, it is necessary to perform sufficient examination in consideration of the collision of flowing-down objects and load at the time of complete occlusion, as well as fluid force by a stream, at the planning phase.

### **4.2 Groin length**

It was verified that the groin length was about 1/10 of ordinary river width as Cases 1 and 2, which suffices for forming a land–water ecotone by sufficient sandbar sedimentation effects.

Concerns arose that the minimum groin length as long as a foot protection width as Case 3 can hardly

anticipate sedimentation effects because the scouring effect of groin edges extends to the river bank. Nevertheless, sandbar formation by sedimentation has been confirmed near the river bank even by the minimum length of groins. In other words, a groin as long as the foot protection width can promote the formation and sustainment of deep water and river bank protection at a water collision front simultaneously.

### 4.3 Groin height

Standard practices give an upward inclination of about 1/10 toward the river bank side so that a groin edge becomes at ordinary water-level elevation. Planning was carried out based on this in Cases 1 and 2, aimed at formation of a land–water ecotone by the sandbar sedimentation effect. Results confirmed sufficient sandbar formation effects.

However, because groins are above the ordinary water level, herb rooting proceeds. Trees such as willows flourish. Because these results raise fears that fallen trees might damage groins during a flood, maintenance management such as cutting trees is also necessary. It is important to plan projects related to sandbar formation effects and emergence of groin crowns in a tradeoff relation, while taking care of maintenance management.

When aiming at the formation and sustainment of deep water, it is necessary to suppress sedimentation near a groin and to suppress the emergence of groin crowns that impede derivation of a water route. Therefore, it is effective to make the groin height as high as the river bed level, as was done in Case 3.

### 4.4 Constituent materials

Groins have been made from stone and wood from ancient times. Rockwork in an impermeable groin and stone packing to a wooden mattress for foot protection in a pile groin require skillful workmanship. Although no change in using a lot of stone or wood has occurred even today, it has become possible to secure the required performance without any skillful workmanship using techniques such as bagged cobbles, Stone-Net™, and a natural stone joint structure used in Cases 1–3. Therefore, it is necessary to use such new technologies actively.

## 5. Conclusion

Documentation by the Kyushu and Tohoku Regional Development Bureaus compiled based on experiences to date are useful in groin planning. Practically, there are many projects planned in reference to these even in Kansai district. However, factors surrounding groin planning such as the flow regime, bed materials, and vegetation situation of a river vary among areas. Their effects cannot be compiled uniformly into documentation, but an analytical method of groins suitable for the area must be applied.

This study has evaluated the formation of a waterside space with groins using typical groin management cases we have planned. Using them as examples, based on our knowledge obtained through the processes from planning, business implementation, and to subsequent aging degradation, we have proposed important matters related to planning and maintenance management. It is expected to be necessary in the future to conduct analyses and evaluation of the effect and tasks of groins based on the case of each area, and to establish an effective method for the planning phase or maintenance management.

## References

- 1) Y. Fukushima, K. Kawamura: Establishment of Waterside Plaza by Regeneration of Sandy River, Kinki Regional Development Bureau, Ministry of Land, Infrastructure and Transport, Proceedings of Regional Technical Research Conference 2002, pp. environmental/community improvement 22-1 - 22-6, 2002.
- 2) S. Noumi, Y. Hotta, M. Tsuruhara: Tasks and Measures Related to Improvement and Sustainment of River Environment, - Case Study on "Waterfront Fun School Project" in Kizugawa Kasagi area -, Technical Report, Technical meeting 2010, Naigai Engineering Co. Ltd. , 4pp. , 2010.
- 3) S. Noumi, Y. Fukushima: Planning and Designing of Falling Works with Gentle Slope of Crosspiece Structure, - Application and Effect of Nature-friendly river work onto the Yoshiminegawa River -, Technical Report, Technical meeting 2008, Naigai Engineering Co. Ltd. , 4pp. , 2008.



# Sensitivity Analysis on Influence of Fabrication Tolerance of High Strength Bolted Friction Type Joint to its Slip Strength

Toshikazu TAKAI\*, Takashi YAMAGUCHI\*\* and Kiyonori YAMASHINA\*\*\*

(Received October 7, 2014)

## Synopsis

This study focuses on fabrication tolerance of high strength bolted friction type joint. Statistical values of fabrication tolerances of the joints related to its slip strength are obtained from investigations of past researches and studies. The coefficients of variation of thickness and width of the plates are small. And, the coefficients of variation of yield point, Poisson's ratio and thickness of coating are large.

Based on the tolerances, the influence of the tolerances of joint to its slip strength with extremely thick plates is evaluated by FEM sensitivity analysis. This paper cleared predominant factors of fabrication tolerances affects the slip strength of the joint. And, the influence of tolerance to slip strength is approximately 10% in the maximum.

**KEYWORDS:** Fabrication tolerance, Slip strength, High strength bolted friction type joint, Sensitivity analysis

## 1. Introduction

In Japan, design codes of structure are changing from allowable stress design to limit state design. For example, design code for railways structures<sup>1)</sup> have already introduced limit state design in 1992, and also performance based design in 2009. Performance based design is partially introduced to Japan specifications for highway bridge<sup>2)</sup> in 2004, but the specification is still based allowable stress design method. To update the specification, many investigations and researches are being carried out.

This study focuses on fabrication tolerance of high strength bolted friction type joint. Tolerances related to slip strength of the joint are investigated. Based on statistical characteristics obtained the investigation, the influence of the tolerance to slip strength of the joint is evaluated by FEM analysis. This paper cleared predominant factors of fabrication tolerances affects slip strength of the joint.

## 2. Investigation of fabrication tolerance

Fabrication tolerances are obtained from investigations of past researches and studies<sup>3)-7)</sup>. This study focuses on parameters related to strength of connected member and mechanical aspect of joints. The former parameters are thickness, width, yield point, Young's modulus, Poisson's ratio and warp of the plate. The latter parameters are slip coefficient of joint, bolt preload and thickness of coating on connected surface.

The tolerances are obtained by referring past researches, so samples used measurements have various properties. The values are nondimensionlized as Table 1 and totaled. Especially, plate warp is totaled as positive and negative direction shown in Fig. 1. Mean value and coefficient of variation (C.V.) delivered from standard deviation (S.D.) is obtained as statistical values of the tolerance. These values are shown in Table 2.

---

\* Student, Doctor Course of Department of Urban Engineering

\*\* Professor, Department of Urban Engineering

\*\*\* Student, Master Course of Department of Urban Engineering

Table 1 Nondimensionalization of parameters

Tolerance Parameter		Nondimensionalization
yield point	$\sigma_y$	measured value/lower yield point
Young's modulus	$E$	measured value/nominal value (*1)
Poisson's ratio	$\nu$	measured value/nominal value (*2)
thickness of plate	$t$	measured value/design value
width of plate	$W$	measured value/design value
plate warp	—	amount of warp/warp measure length
slip coefficient	$\mu$	measured value/design slip coefficient (*3)
bolt preload	$N$	measured value/normal bolt preload (*4)
thickness of coating	—	measured value/design value

(\*1) 200,000 N/mm<sup>2</sup>      (\*2) 0.3  
 (\*3) 0.45                      (\*4) 205 kN

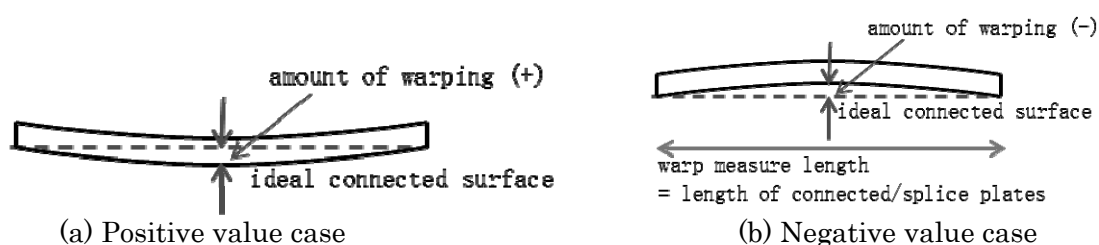


Fig. 1 Measurement method of warp of plates

Table 2 Statistical values obtained from investigation

Tolerance Parameter		Reference	Number of samples	mean $m$	S.D. $\sigma$	C.V.
yield point	$\sigma_y$	5), 6), 7)	13,442	1.1592	0.1078	9.3%
Young's modulus	$E$	5), 6)	943	1.0009	0.0475	4.7%
Poisson's ratio	$\nu$	5), 6)	459	0.9293	0.0895	9.6%
thickness of plate	$t$	3)	2,520	1.0085	0.0056	0.6%
width of plate	$W$	3)	1,260	1.0104	0.0048	0.5%
plate warp	—	3)	222	0.0002	0.0011	—
slip coefficient	$\mu$	3)	27	1.5901	0.0751	4.7%
	$\mu_3$			1.6955	0.0959	5.7%
bolt preload	$N$	3)	303	0.9560	0.0190	2.0%
thickness of coating	—	4)	60	1.1148	0.1147	10.3%

The largest and smallest number of samples is 13,442 and 27, respectively. The C.V. of thickness and width of plate are small as 0.5%. However, the C.V. of yield point, Poisson's ratio and thickness of coating are large as 10%. And, the C.V. of Young's modulus, slip coefficient and bolt preload are also large as 5%.

$\mu$  of slip coefficient is obtained as a slip load of a joint divided by a bolt preload measured at start of loading to joint.  $\mu_3$  is obtained as the slip load divided by a bolt preload measured at the occurrence of slip of the joint. The slip coefficient  $\mu_3$  is almost same as friction coefficient. The difference between the C.V. of  $\mu$  and that of  $\mu_3$  are 1%. These values have the same distribution.

### 3. Evaluation of influence of fabrication tolerance to slip strength of joint

#### 3.1 FEM model

FEM Analysis is calculated by Abaqus/Standard 6.9. FEM model is made referring past

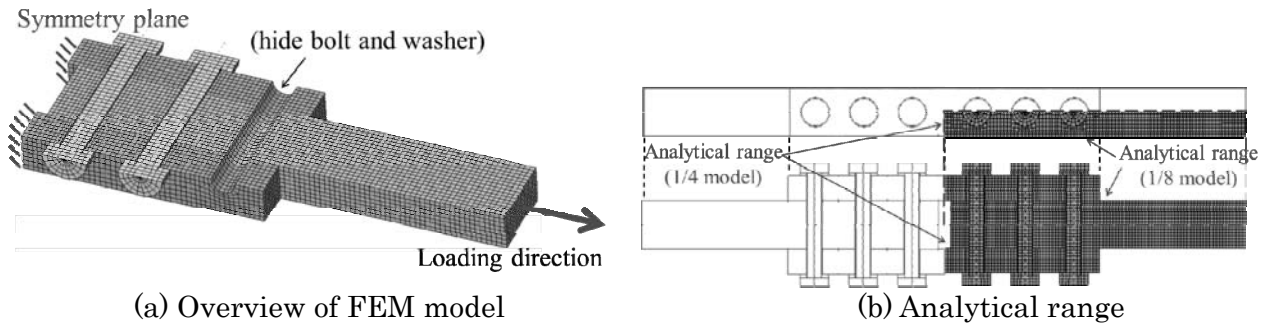


Fig. 2 FEM model

Table 3 Material properties

	Stress (MPa)	Plastic strain ( $\mu$ )
Plates (SM490Y, JIS)	355	0
	356	16,400
	427	35,100
	457	52,800
Bolt, Washer (F10T, JIS)	900	0
	900	4,400
	1,000	42,900

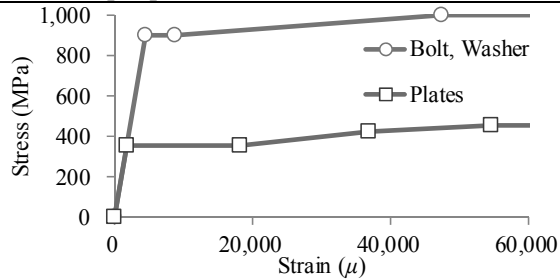


Table 4 Dimensions of joint for Analysis

Analysis Series		A	C	G	I
High strength bolt	the number of bolts	3	12	3	12
	Bolt grade	M22-F10T (JIS)			
	Preload	kN 205			
	Yield point	MPa 900			
Connected/Splice plate	Steel grade	SM490Y (JIS)			
	Width	mm 75	226	50	126
	Thickness	mm 75 (Connected plate)			
		mm 38 (Splice plate)			
	Bolt hole	mm 24.5 (diameter)			
Yield point	MPa 355				
Joint property	the number of friction surface	2			
	Friction coef.	0.72			
	Bolt pitch	mm 75			
	Edge length	mm 40			
Design slip strength	kN	886	3,542	886	3,542
Design yielding strength of plate	kN	1,345	5,365	679	2,702
Slip/yielding strength ratio $\beta$		0.66		1.3	

study<sup>8)</sup>. The model contains the solid element. The size of the element is 5 mm. The shape of the model is shown in Fig. 3. One fourth or one eighth part is modelled regarding its symmetry. Stress strain curves are shown in Table 4. The yield behavior of bolt and washer hardly affect slip behavior of joint. So, stress-strain curves of the bolt and washer are based on nominal values based on Japanese Standard<sup>9)</sup>. However, yield behavior of connected plate and splice plate affects the slip behavior. So, the stress-strain curves of plates based on results of coupon tests that are carried out in advance.

### 3.2 Dimensions of joint for FEM analysis

Dimensions of joints for analysis are shown in Table 4. These cases are a combination of the

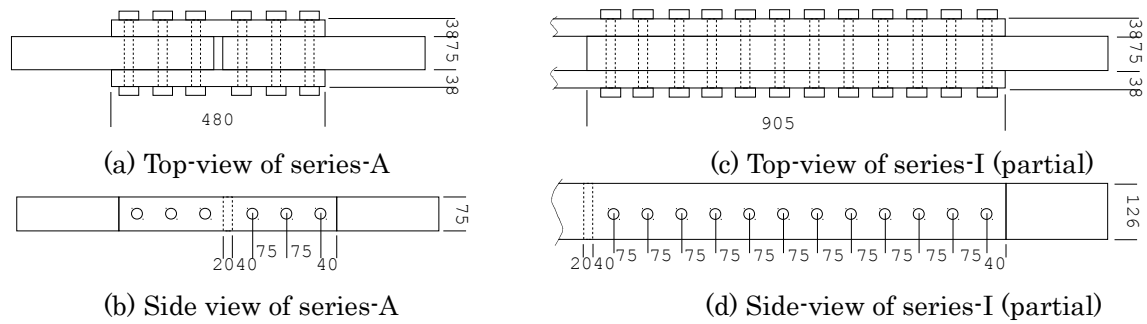


Fig. 3 Examples of joint shape for analysis

Table 5 Conditions given to FEM analysis

Series	Tolerance parameter		Input value			Percentage	
			$m-2\sigma$	$m$	$m+2\sigma$	$m-2\sigma$	$m+2\sigma$
All Series	yield point	$\sigma_y$ (MPa)	278	355	432	-21.6%	21.6%
	Young's modulus	$E$ (N/mm <sup>2</sup> )	181,006	200,000	218,994	-9.5%	9.5%
	Poisson's ratio	$\nu$ —	0.246	0.3	0.354	-18.0%	18.0%
	thickness (conn. pl.)	$t$ (mm)	74.2	75	75.8	-1.1%	1.1%
			(splice pl.)	37.6	38	38.4	-1.1%
	slip coefficient	$\mu$ —	0.652	0.72	0.788	-9.4%	9.4%
bolt preload	$N$ (kN)	197	205	213	-3.9%	3.9%	
Series A	width of plate	$W$ (mm)	74.3	75	75.7	-0.9%	0.9%
	plate warp	— (mm)	-1.1	0	1.1	—	—
Series C	width of plate	$W$ (mm)	223.8	226	228.2	-0.9%	0.9%
	plate warp	— (mm)	-1.1	0	1.1	—	—
Series G	width of plate	$W$ (mm)	49.5	50	50.5	-0.9%	0.9%
	plate warp	— (mm)	-4.1	0	4.1	—	—
Series I	width of plate	$W$ (mm)	124.8	126	127.2	-0.9%	0.9%
	plate warp	— (mm)	-4.1	0	4.1	—	—

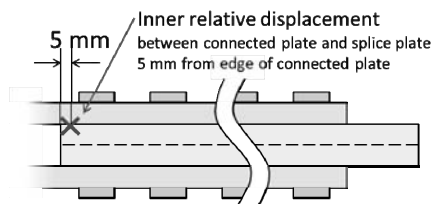


Fig. 4 Measurement point of relative displacement

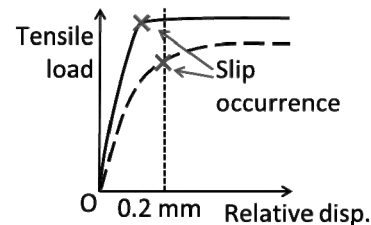


Fig. 5 Example of slip behavior

number of bolts in a line and slip/yield strength ratio  $\beta$ . Some cases contain 3 bolts in a line as not-long joint. And, other cases contain 12 bolts as long joint. A tensile load applied to a not-long joint makes a major slip that occurs at one time. However, a long joint usually have smaller slip coefficient than not-long joint. In the long joint, partial slip occurs in smaller level of tensile load applied before the entire major slip occurs. So, the behavior makes the slip coefficient small. Slip/yield strength ratio  $\beta$  is obtained as a slip strength divided by a yield strength of connected or splice plates. In the case  $\beta = 0.66$ , major slip occurs before yielding of plates. But  $\beta = 1.33$ , yield occurs before major slip. So in later case, slip behavior is usually affected by yield behavior.

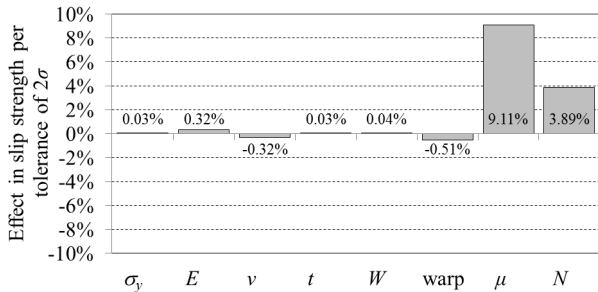
The joint consists of extremely thick plates that are connected plate of 75 mm and splice plates of 38 mm. Thick plates have been used commonly in members of bridges in recent days. The grade of high strength bolt is F10T M22 whose diameter of bolt shank is 22 mm.

Table 6 Results of Analysis

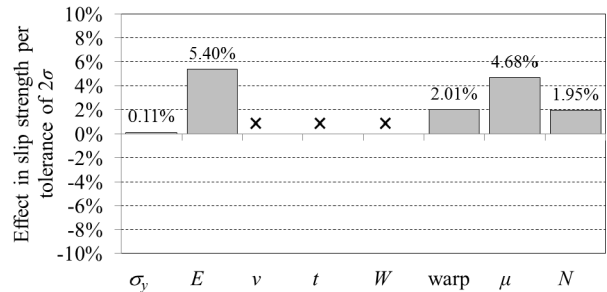
Series	Tolerance parameter	Slip strength (kN)			Regression		Series	Tolerance parameter	Slip strength (kN)			Regression	
		<i>m-2σ</i>	<i>m</i>	<i>m+2σ</i>	Slope*	Intercept			<i>m-2σ</i>	<i>m</i>	<i>m+2σ</i>	Slope*	Intercept
A	yield point $\sigma_y$	858.2	858.8	858.8	0.15	858.8	yield point $\sigma_y$	<i>714.2</i>	832.2	842.6	32.1	832.2	
	Young's modulus $E$	855.9		861.3	1.4		819.6	842.2		5.7			
	Poisson's ratio $\nu$	861.9		856.3	-1.4		—	<i>764.4</i>		831.5	16.8		
	thickness of plate $t$	858.4		858.9	0.12		$\mu$	764.6		885.2	30.1		
	width of plate $W$	858.4		859.1	0.18		$N$	804.6		855.9	12.8		
	plate warp	<i>866.4</i>		857.7	-2.2		yield point $\sigma_y$	2209		2267	14.6		
	slip coefficient $\mu$	780.4		936.7	39.1		Young's modulus $E$	2142		2368	56.7		
	bolt preload $N$	825.4		892.3	16.7		Poisson's ratio $\nu$	2258		2262	0.89		
C	yield point $\sigma_y$	2902	2908	2909	1.7	2908	thickness of plate $t$	2245	2272	6.9	2258	2258	
	Young's modulus $E$	2745		3059	78.5		width of plate $W$	2241	2263	5.4			
	plate warp	<i>3049</i>		3166	29.2		plate warp	<i>2244</i>	2341	24.3			
	slip coefficient $\mu$	2766		3038	68.1		slip coefficient $\mu$	2145	2368	55.7			
	bolt preload $N$	2851		2964	28.3		bolt preload $N$	2214	2302	22.2			

\* slope per tolerance of 1.0xS.D. ( $\sigma$ )

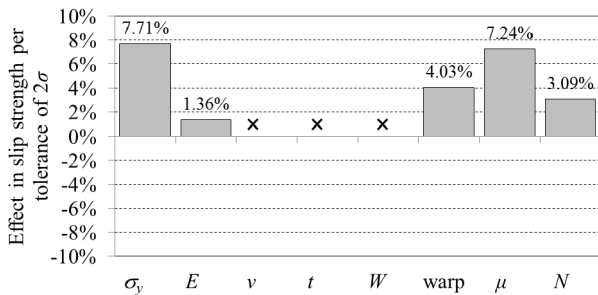
*Italic* and gray color indicates a value determined as relative displacement of 0.2 mm.



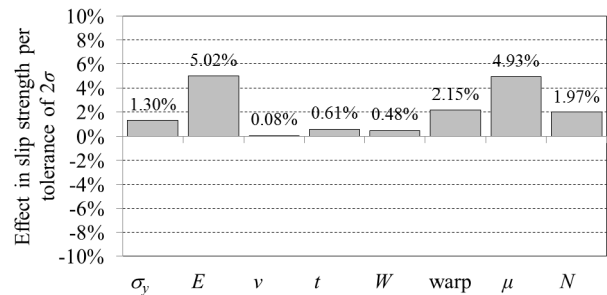
(a) Series-A (3 bolts,  $\beta = 0.66$ )



(b) Series-C (12 bolts,  $\beta = 0.66$ )



(c) Series-G (3 bolts,  $\beta = 1.3$ )



(d) Series-I (12 bolts,  $\beta = 1.3$ )

Fig. 6 Influence of tolerance to slip strength of joint

Tolerance values of parameters given to each FEM models are shown in Table 5. The amount of tolerance is twice as large as S.D. shown in Table 2. A tolerance value is given in each case. Combinations of tolerance parameters are not considered.

### 3.3 Definition of slip occurrence in FEM analysis

Slip strength is determined by a tensile load applied to the joint and the relative displacement measured inner side of the connected surface shown in Fig. 4. The measured point is 5 mm from the edge of the connected plate. As shown by the solid line in Fig. 5, in case maximum tensile load is obtained before relative displacement reaches 0.2 mm, the slip strength is determined by the maximum tensile load. On the other hand, as shown by dash line, relative displacement reaches 0.2 mm before the maximum tensile load is obtained, the slip strength is determined by the tensile load at the relative displacement reaches 0.2 mm<sup>3), 8), 10), 11)</sup>.

### 3.4 Evaluations and discussions

Results of FEM analysis are summarized in Table 6. Slip strength is obtained according to the

definition of slip occurrence. The slip strengths written with italic letters are determined by the relative displacement, and others are determined by the maximum tensile load. In all cases of series-C and I, that are  $\beta = 1.3$  cases, slip strength is determined by relative displacement. Yield behavior affects slip behavior in these cases.

Values of regression show expressions determined by linear regression using the results of  $m - 2\sigma$ ,  $m$  and  $m + 2\sigma$  cases. The intercept of the regression line is equal to slip strength of  $m$  case. A large value of the slope indicates that the tolerance parameter strongly affects to the slip strength.

Fig. 6 shows the influence in slip strength per tolerance of twice of S.D.  $2\sigma$ . The value is obtained the percentage to the slip strength of mean case  $m$  of a value increased two times of slope.

As shown in Fig. (a), slip strength of joints of series-A is affected strongly by slip coefficient  $\mu$  and bolt preload  $N$ . These parameters affect over 2% of slip strength. In other series, series-C, G and I,  $\mu$  and  $N$  also affect strongly to the strength. However, the influence of other parameters of series-A is less than 0.5%. The influence is very small.

In  $\beta = 1.3$  cases, the influence of yield point  $\sigma_y$  is large. The influences of  $\sigma_y$  of series-G and I are larger than that of series-A and C, respectively.  $\beta$  of the joints equals 1.3. And, yield behavior of connected and splice plate affects to slip behavior before slip occurs. So, the tolerance of  $\sigma_y$  affects the slip strength strongly.

The influences of Young's modulus  $E$  of series-C and I are larger than that of series-A and G, respectively. The joints of the series-C and I are long joints and have 12 bolts. Slip strength of the joints is determined by relative displacement. So, the tolerance of Young's modulus  $E$  relates to elastic elongation of connected and splice plates affects slip strength strongly.

The influences of  $\mu$  and  $N$  of Series-C and I are smaller than those of series-A and G, respectively. And,  $\mu$  of a long joint is usually smaller than that of a not-long joint. Thus, the stress of a cross section of connected and splice plates of long joint is probably smaller than that of not-long joint.

#### 4. Conclusions

This study focuses on fabrication tolerance of high strength bolted friction type joint. The tolerances focused are related to slip strength of the joint. Based on the tolerances, the influence of the tolerances to strength of the joint is evaluated by FEM analysis. Conclusions and remarks are as follows;

- 1) Statistical values of fabrication tolerances of joints related to slip strength of the joint are obtained from investigations of past researches and studies. The coefficients of variation of thickness and width of the plates are small as 0.5%. And, the coefficients of variation of yield point, Poisson's ratio and thickness of coating are large as 10%.
- 2) Based on the statistical values of the investigation, FEM analysis is carried out. In all series of analysis, tolerances of slip coefficient  $\mu$  and bolt preload  $N$  of joints affect strongly to slip strength of the joint. And, in the cases of  $\beta = 1.3$  or long joint, tolerances of yield point  $\sigma_y$  and Young's modulus  $E$  also affect strongly to the strength. The former parameter would be affected by yield behavior before slip occurs. The latter parameter would be affected by elongation of connected and splice plates of long joint.

#### 5. References

- 1) Railway Technical Research Institute, *Design Standards for Railway Structures and Commentary*, 2009.7 (in Japanese)

- 2) Japan Road Association, *Specifications for Highway Bridges*, 2012.3 (in Japanese)
- 3) Public Works Research Institute, Osaka City University, *Report on rationalistic design of high strength bolted friction type joint*, Cooperative Research Report, No. 428, 2012.1 (in Japanese)
- 4) Jun Murakoshi, Naoki Toyama, Mamoru Sawada, Atsuro Ootake, Takashi Yamaguchi, Xue PENG, “Research on influence of coating condition of connected surface to slip coefficient of high strength bolted friction type joint”, *Proceedings of Annual Conference of the Japan Society of Civil Engineers*, I-341, pp. 681-682, 2012.9 (in Japanese)
- 5) Study Group on Steel Structures in Tokai, “Evaluation of resistant strength of steel structure member and application for reliability design (No. 1)”, *Bridge and Foundation Engineering*, pp.33-41, 1980.11 (in Japanese)
- 6) Hirofumi Aoki, Masaki Nozawa, “Average and coefficient of variation of mechanical property of steel for structure (No. 1)”, 2336, *Summaries of technical paper of annual meeting Architectural Institute of Japan*, pp. 1123-1124, 1980.9 (in Japanese)
- 7) Hirofumi Aoki, Masaki Nozawa, “Average and coefficient of variation of mechanical property of steel for structure (No. 2)”, 2337, *Summaries of technical paper of annual meeting Architectural Institute of Japan*, pp. 1125-1126, 1980.9 (in Japanese)
- 8) Toshikazu Takai, Xue Peng, Honghe Sun, Takashi Yamaguchi “Study on Slip Behaviour of High Strength Bolted Friction Type Joint with Extremely Thick Plates by Using Finite Element Analysis” *IABSE Symposium Report, Rotterdam 2013*, RTM-0195, pp. 439-446, 2013.5
- 9) JIS B1186 bolt Japanese Industrial Standards Committee, *Sets of high strength hexagon bolt, hexagon nut and plain washers for friction grip joints*, JIS B 1186, 2013.6 (in Japanese)
- 10) Xue Peng, Takashi Yamaguchi, Toshikazu Takai, Jun Murakoshi, Mamoru Sawada, “FEA Study on the Slip Behavior of High Strength Multi Bolted Friction Type Joints with Thick Plates by Structural Dimensions”, *Journal of Japan Society of Civil Engineers*, Ser. A1, Vol. 69, No. 3, pp. 452-466, 2013.9 (in Japanese)
- 11) Xue Peng, Takashi Yamaguchi, Toshikazu Takai, “FEA Study on the Slip Coefficient of High Strength Bolted Friction Type Joint with Thick Plates Considering Structural Dimensions”, *The 12th Japan-Korea Joint Symposium on Steel Bridges*, pp. 314-322, 2013.9



# Study on applicability of high durability friction grip joints with high strength countersunk head bolts for steel bridge structures

Akiko TABATA\* and Takashi YAMAGUCHI\*\*

(Received October 7, 2014)

## Synopsis

The authors focused on the high strength bolted friction grip joints with countersunk head bolts which can finish the surface of the connection plate flat smoothly and prevent from functional depression due to corrosion. Firstly we carried out Finite Element Analysis in order to evaluate the contact pressure of double shear connected friction joints with countersunk heads varying the angle of countersunk head. Secondly, we have compared the slip strength of the joints which has the optimum countersunk head angle with that of the joint with the normal high strength bolt through the standard slippage test considering variation of plate thickness and the yield strength of the base and splice plates. As a result, it has concluded that the slip strength of the joints with countersunk heads exceeds the required design slip strength which has specified in JSHB and that its slip coefficients is about 10% lower than that with normal head bolts.

**KEYWORDS:** Countersunk head bolt; contact pressure; slippage test; slip coefficient; slip to yield resistance ratio

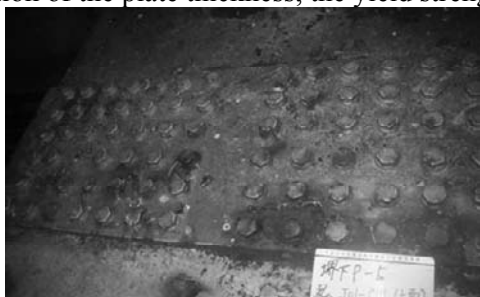
## 1. Introduction

High strength bolted friction grip joints have been generally applied to connections of the steel structures from the viewpoint of economical rationality and reliability. The paint on the connection tends to deteriorate due to rust or shortage of the thickness of the paint at the corner edge. Because corrosion is accelerated at a place where drainage is poor and water is readily stagnant (See Pic.1). Moreover, asphalt pavement on the steel deck tends to be damaged by the existence of the bolt heads in it.

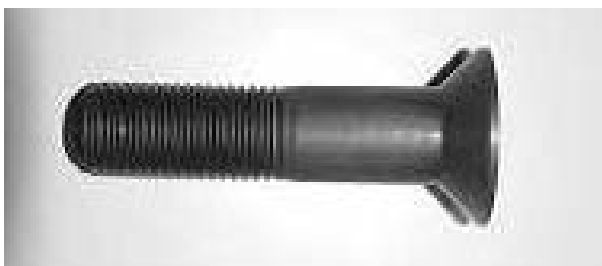
Therefore, the authors focused on the high strength bolted friction grip joints with countersunk head (See Pic.2) which can finish the surface of the splice plate flat smoothly and prevent from functional decline due to corrosion.

However joints with high strength countersunk head bolt has been already applied to the bearing type of the connection, there is almost no research paying attention to the friction grip joints with countersunk head bolts. When employing a friction grip joints with countersunk head bolts, it is necessary to verify the performance of the joint which can satisfy the required functions as a connection.

In this study, firstly we carried out FEA (Finite Element Analysis) varying the angle of countersunk head in order to evaluate the contact pressure of double shear connected friction joints with countersunk heads. Also, we have investigated the influence on load transferring mechanism by using countersunk head bolt for frictional joints. Secondly, we have compared the slip strength of the joints which has the optimum countersunk head angle with the normal high strength bolts through the standard slippage test focusing on variation of the plate thickness, the yield strength of the base and the splice plates.



Pic.1 Corrosion damage of joint of steel pier



Pic.2 High strength countersunk head bolt

---

\* Student, Doctor Course of Department of Urban Engineering

\*\* Professor, Department of Urban Engineering

## 2. Mechanical Behavior from FEA

### 2.1 Outline of FEA and FE models

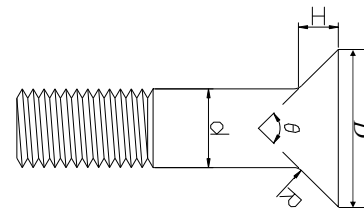
The axisymmetric FEA was conducted by ABAQUS Standard 6.9[1]. Double shear connected joint are dealt with in the analysis. .

The countersunk head bolt for FEA is shown in Fig.1. In order to evaluate the slip strength with countersunk head bolts, the angle of countersunk head is changed as 60, 70, 80, 90, and 110 degrees. For a comparison, the joint with the hexagon head bolt shown in Fig.2 is also dealt with. All of analytical cases in this analysis are tabulated in Fig.1 and 2.

An example of the FEA model, CD-90 is shown in Fig.3. The thickness of the splice plate and the base plate is 16mm and 32mm respectively, and the length of the splice plate and the main plate is 50 and 70 mm respectively referring to the minimum spacing distance between bolts specified in Ref. [2] .Diameter of the bolt hole is 24.5 mm, which is the standard value also specified in Ref. [2].

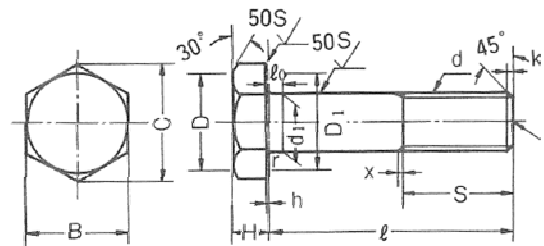
A contact boundary which can consider contact, friction, and separation is installed into the analytical surface between the splice and the base plate.

In order to clarify distribution of the contact pressure on the contact surface, the area where two surfaces are expected to be contact has fine mesh division. Friction coefficient for the contact surface is both 0.5 between the splice and the base plate, and also between the splice and countersunk bolt head surface. Design bolt axial force 205kN for F10T (M22) is installed into the bolt. The steel material is SS400( $\sigma_y=235\text{MPa}$ ), elastic modulus E is  $2 \times 10^5\text{MPa}$ , and poisson's ration is 0.3. The FE model of the joint with hexagon head bolt (HD model) is also shown in Fig.4. Dimensions of the splice plate and the base plate are the same of CD series.



case name	Angle of countersunk head $\theta$ (degree)	Diameter of bolt neck d (mm)	Diameter of bolt head D (mm)	Curvature of bolt head and bolt neck R (mm)	Thickness of bolt head H (mm)
CD-60	60	22.0	34.7	3.0	11.0
CD-70	70	22.0	37.5	3.0	11.0
CD-80	80	22.0	40.5	3.0	11.0
CD-90	90	22.0	44.0	3.0	11.0
CD-110	110	22.0	53.5	3.0	11.0

Fig. 1: Countersunk head bolt



case name	Diameter of bolt neck $d_1$ (mm)	Diameter of bolt head B (mm)	Diameter of bolt head C (mm)	Diameter of bolt head D (mm)	Curvature R (mm)	Thickness of bolt head H (mm)
HD	22.0	36.0	41.6	34.0	3.0	14.0

Fig. 2: Hexagon head bolt

## 2.2 Analytical results and discussions

### 2.2.1 Contact pressure distribution

Distribution of contact pressure at the contact surface between the splice and the base plate obtained from the FEA is shown in Fig.5. The vertical axis is contact pressure (MPa) and horizontal axis is the distance from the hole edge. As shown in Fig.5, it is found that high contact pressure over yield strength occurs around the hole edge in CD series comparing with that of HD. Its maximum value is that of CD-110. As the angle of countersunk head increase, contact pressure tends to become higher around the hole edge. On the other hands, the existence area of contact pressure of CD series is smaller than that of HD. The minimum case of the existence area of contact pressure is CD-110. Therefore, the FEA results indicate that contact pressure of CD series is higher than that of HD and is distributed in smaller area.

### 2.2.2 Shear stress distribution

Fig.6 shows the shear stress distribution on the contact surface. Arrow diagram of nodal force at the contact surface and the deformation are also shown in Fig.7. To understand deformation characteristics with ease, each displacement is multiplied by 100. It is understood from these two Figures that high shear stress occurs

near the bolt hole edge .due to the friction force by the local deformation of the splice plate.

### 2.2.3 Maximum stress

An example of stress contours of Von-Mises of CD-90 is depicted in Fig.8. High stress concentration over the yielding stress between the countersunk head and the shank is observed when the design bolt axial force, 205kN is applied. Maximum stresses of all cases when the design bolt axial force is applied are tabulated in Table 1. It is found that the maximum stress of CD series is higher than that of HD, and that the case that the angle of countersunk head is 90 degrees shows lowest maximum stress. The reason is considered that the stress at the corner part between bolt shank and bolt head depends on the magnitude of the contact force along the perpendicular direction to the countersunk head and the distance from here to the applied point. It has concluded that the most suitable angle of the countersunk head is 90 degrees.

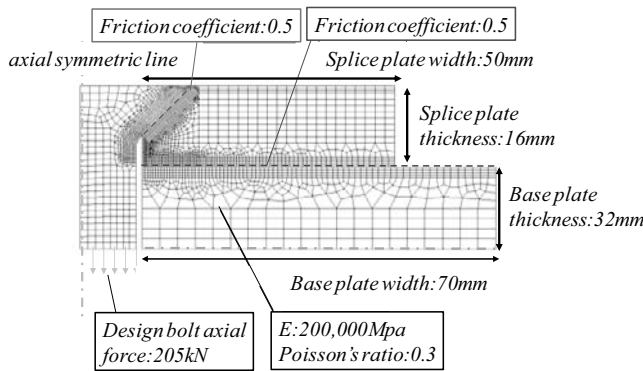


Fig.3: FEA model for CD-90

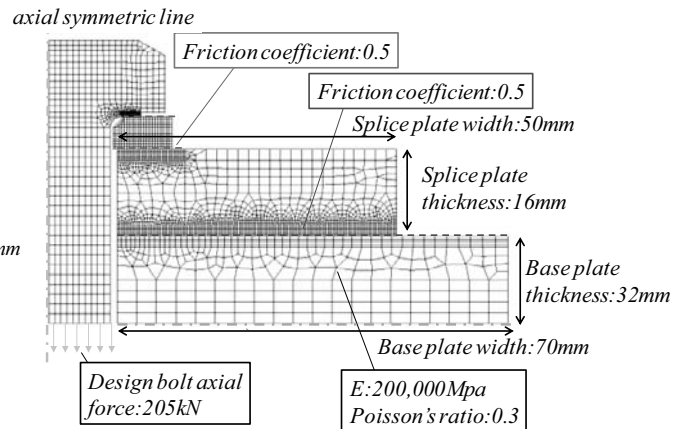


Fig.4: FEA model for HD

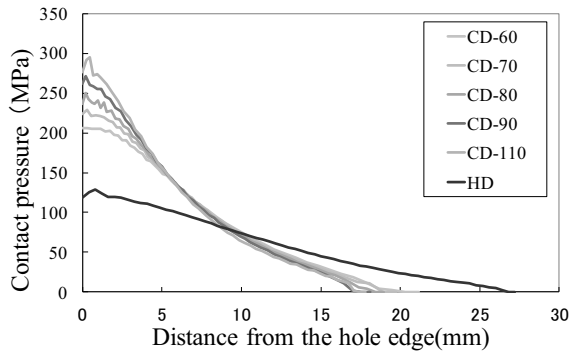


Fig.5: Contact pressure distribution on the contact surface

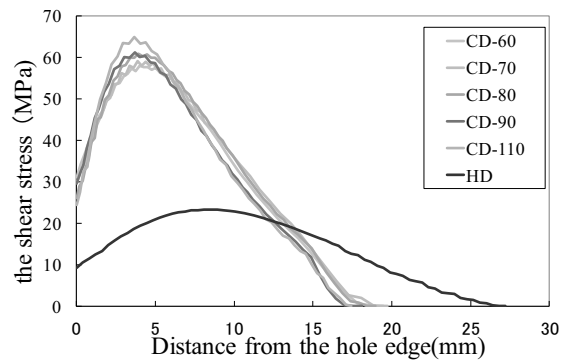


Fig.6: Shear stress distribution on the contact surface

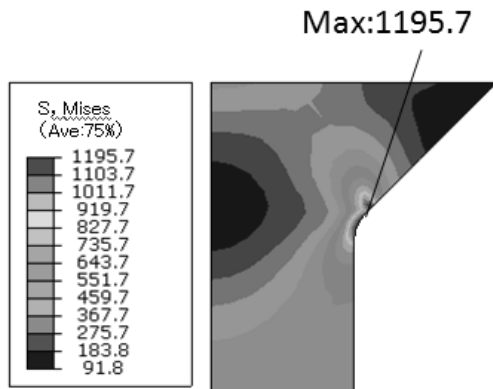


Fig.8: Stress contours of Mises(CD-90)

Table 1: Maximum stress

case name	Maximum stress ( $\times 10^3$ , MPa)
CD-60	1.593
CD-70	1.416
CD-80	1.227
CD-90	1.196
CD-110	1.364
HD	1.056

### 3. Slippage test

#### 3.1.Outline of the slippage test and specimens

In order to clarify the behaviour of friction joints with high strength countersunk head bolts for steel bridge structures, we have carried out the standard slippage test taking into account for steel material grade, slip to yield resistance ratio  $\beta$ , and the number of contact surface(double or single shear). Geometrical configurations of the specimens for the slippage test are shown in Fig.9. The structural parameters of the specimens are listed in Table 2. The angle of the countersunk head is fixed 90 degrees based of the analytical results described in chapter 2 and in Ref. [3]. Contact surface of the plates are painted by inorganic zinc-rich paint with more than 75 $\mu$ m thickness. Pic.3 shows the specimen with the countersunk head bolts. Structural parameters in this experiment are explained in detail as follows;

- a) Steel material grade (SS400, SM490) : Investigated is influence of local yielding around the bolt holes on the slip resistance.
- b) Slip to yield resistance ratio  $\beta$  : This is for clarification of the difference of mechanical behaviour between slipping type( $\beta < 1.0$ ) and yielding type( $\beta > 1.0$ ).  $\beta_d$  (See Table2) is the ratio calculated by the friction coefficient(0.5) and the nominal yield resistance.  $\beta_e$  is the ratio calculated by the slip coefficient obtained from the experiment for the specimen of slipping type and yield stress obtained from the material test (See Table 3).
- c) Number of the contact surface (double or single shear): Difference of behaviour caused by different number of the contact surface and eccentricity between the base and splice plate is investigated.

In the experiment, bolt axial force for the hexagon head bolt is measured by the strain gauge which glued on the bolt shank as shown in Pic.4. Bolt axial force for the countersunk head bolt is also measured from the strain gauges glued on the bolt head in consideration of preventing from stiffness decrease by the holes for the strain gauge wires as shown in Pic.4. The slippage test is executed by using universal testing machine (1,000kN) of Osaka City University. To clarify the slip behaviour with ease, fixed and slipped sides are set in advance by changing the bolt axial force. The bolts at fixed side are tightened with 10% higher of the design bolt axial force. Tensile load is applied until the major slip at the slipped side is observed. As shown in Fig.10, measured are relative displacements between the base plate and the splice plate, applied tensile load and bolt axial forces. In this experiment, the definition of slip occurrence is when the relative displacement at  $\delta_3$  becomes 0.2 mm in accordance with the specification of Architectural Institute of Japan [4].

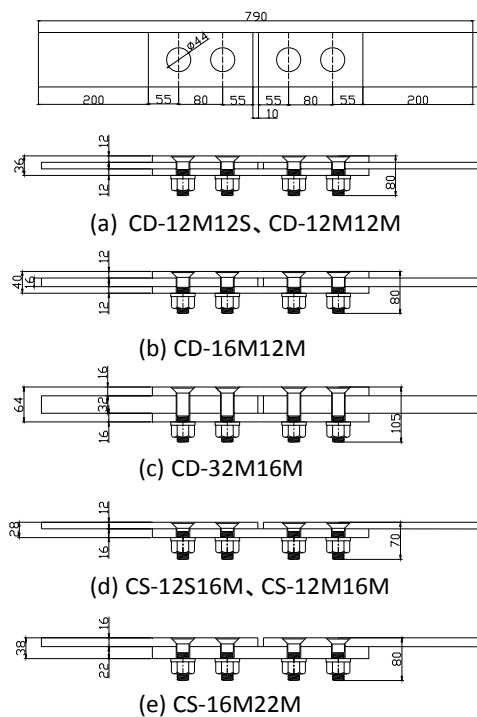


Fig.9: Geometrical configurations of the Specimen for slippage test (mm)

Table 2: List of specimens and experimental parameters

	Base plate		Splice plate		Number of the contact surface	Slip to yield resistance ratio $\beta_d$	Slip to yield resistance ratio $\beta_e$	Number of the specimen	Yield strength of base plate $P_y$ (kN)
	grade	mm	grade	mm					
<i>Countersunk head bolt</i>									
CD-12M12S	SM490	12	SS400	12	double	1.39	1.72	3	346
CD-12M12M	SM490	12	SM490	12		1.39	1.72	3	346
CD-16M12M	SM490	16	SM490	12		1.04	1.28	3	466
CD-32M16M	SM490	32	SM490	16		0.52	0.66	3	899
CS-12S16M	SS400	12	SM490	16	single	1.08	1.21	3	230
CS-12M16M	SM490	12	SM490	16		0.78	0.96	3	309
CS-16M22M	SM490	16	SM490	22		0.57	0.69	3	429
<i>Hexagon head bolt</i>									
HD-12M12S	SM490	12	SS400	12	double	1.39	1.93	3	346
HD-12S12M	SM490	12	SM490	12		1.39	1.93	3	346
HD-16M12M	SM490	16	SM490	12		1.04	1.43	3	466
HD-32M16M	SM490	32	SM490	16		0.52	0.74	3	899
HS-12S16M	SS400	12	SM490	16	single	0.96	1.21	3	257
HS-12M16M	SM490	12	SM490	16		0.70	0.96	3	346
HS-16M22M	SM490	16	SM490	22		0.52	0.73	3	466

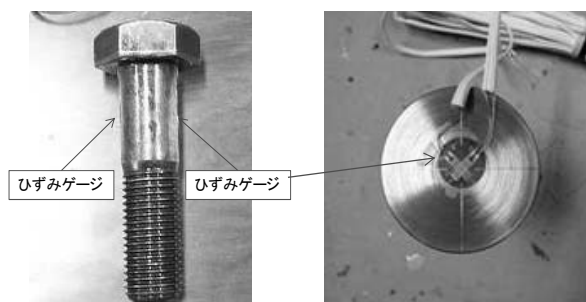


(a) surface of countersunk hole



(b) After tightened of bolts

Pic.3: Overview of the Specimen



(a) Hexagon head

(b) Countersunk head

Pic.4: Strain gauges for bolt axial force measurement

Table 3: Results of the material test

Material	Thickness	Yield strength	Tensile strength	Elastic modulus	Poisson's ratio
	mm	N/mm <sup>2</sup>	N/mm <sup>2</sup>	N/mm <sup>2</sup>	
SM490	32	338.2	500.5	$2.07 \times 10^5$	0.28
SM490	22	344.0	533.6	$2.11 \times 10^5$	0.29
SM490	16	350.5	526.2	$2.10 \times 10^5$	0.29
SM490	12	347.0	516.5	$2.09 \times 10^5$	0.29
SS400	12	275.8	434.5	$2.09 \times 10^5$	0.29

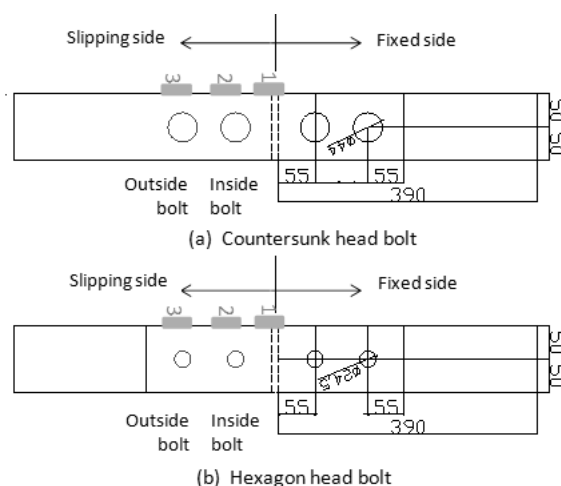


Fig.10: Dimensions of the specimen and measured location of relative displacements

### 3.2. Experimental Results and discussions

#### 3.2.1. Definition of the slip coefficient

Experimental results are summarized in Table.4. Each obtained slipping resistance force and slip coefficient are tabulated. The slip coefficient  $\mu_1$  is the ratio of the slipping resistance force divided by the total bolt axial

force before slippage test as shown in the equation (1),

$$\mu_1 = \frac{P}{m * n * N_1} \quad (1)$$

$\mu_1$  : slip coefficient

P : slipping resistance force at  $\delta_3=0.2\text{mm}$  (kN)

m : number of the splice plate

n : number of the bolt

$N_1$  : average of two bolts axial force before slippage test(kN)

The slip coefficient  $\mu_0$  is the ratio of the slipping resistance force divided by design bolt axial force as shown in the equation (2),

$$\mu_0 = \frac{P}{m * n * N_0} \quad (2)$$

$N_0$  : design bolt axial force (205kN)

The slip coefficient  $\mu_2$  is the ratio of the slipping resistance force divided by total bolts axial force when slipping occurs as shown in the equation (3),

$$\mu_2 = \frac{P}{m * n * N_2} \quad (3)$$

$N_2$  : average bolt axial force at slip (kN)

### 3.2.2. Effectiveness of the steel material grade

In order to clarify the slip resistance under various steel grades (SS400, and SM490), it is compared with the slip coefficient of CD-12M12M and CD-12M12S as yielding type. Also CS-12M16M and CS-12S16M as slipping type are investigated.

As shown in Table.4, slip coefficient of CD-12M12M ( $\mu_1=0.46$ ) is approximately 2% higher than that of CD-12M12S ( $\mu_1=0.45$ ). In addition, CS-12M16M ( $\mu_1=0.51$ ) is also approximately 11% higher than that of CS12S16M ( $\mu_1=0.46$ ).

These results indicate that slip coefficients becomes higher by using high strength steel SM490 for the splice plate with countersunk bolt holes. The improvement of the slip coefficient for the slipping type by using higher strength steel is more effective than that of the yielding type.

### 3.2.3. Slip to yield resistance ratio $\beta$ and number of the contact surface

Fig.11 shows the relationship between slip coefficient  $\mu_1$  and slip to yield resistance ratio  $\beta_e$ . It is observed that slip coefficient  $\mu_1$  has a tendency to get lower by increase of  $\beta_e$  regardless of bolt type, steel material grade, and number of the contact surface.

Maximum slip coefficient  $\mu_1$  is 0.66(CD-32M16M)/0.74(HD-32M16M) for CD/HD series respectively. These are both slipping type. Minimum slip coefficient  $\mu_1$  is 0.45(CD-12M12S) /0.48(HD-12M12S) for CD/HD series respectively. These are both yielding type. It is summarized that slip coefficients  $\mu_1$  for the countersunk head specimens are approximately 10% lower than those for hexagon head specimens in spite of number of the contact surface.

The reason is considered that the contact pressure of the joints with countersunk head reduce due to progress

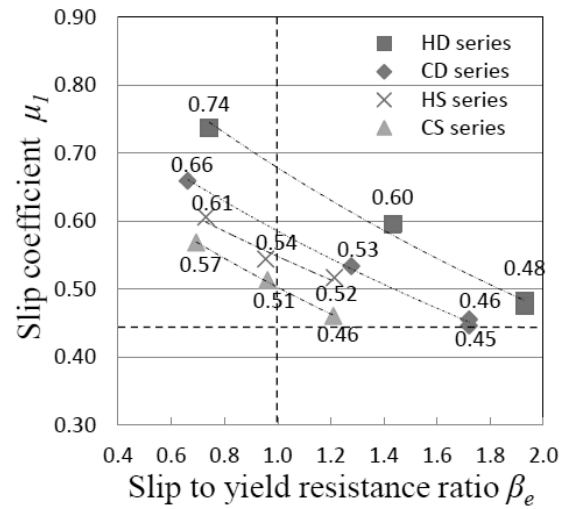


Fig.11: Relationship between  $\mu_1$  and  $\beta_e$

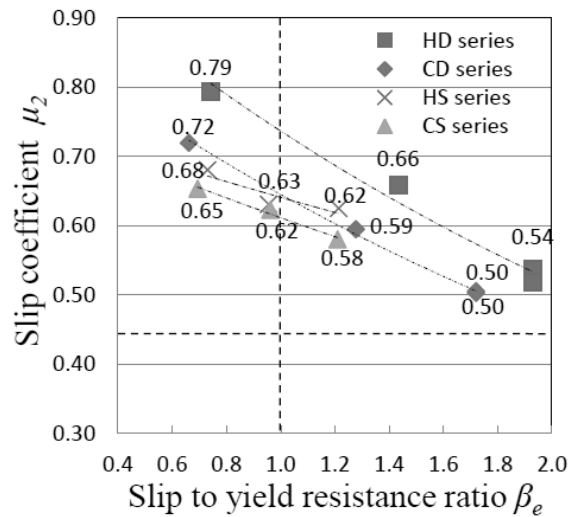


Fig.12: Relationship between  $\mu_2$  and  $\beta_e$

Table 4: Summary of experimental results

Specimen	Slip Resistance P	Axial force before test N1	Axial force at slipping N2	Slip coefficient (P/N1)		Slip coefficient (P/205kN)		Slip coefficient (P/N2)		decreasing rate of axial force		
	kN	kN	kN	$\mu_1$	Ave.	$\mu_0$	Ave.	$\mu_2$	Ave.	Ratio	Ave.	
<i>Double shear series</i>												
CD-12M12S	364.79	208.97	186.96	0.44	0.45	0.44	0.45	0.49	0.50	0.89	11.2%	
	366.05	207.69	186.89	0.44		0.45		0.49		0.90		
	386.07	209.30	182.08	0.46		0.47		0.53		0.87		
HD-12M12S	363.91	192.37	178.15	0.47	0.48	0.44	0.46	0.51	0.54	0.93	9.9%	
	387.99	195.99	168.83	0.49		0.47		0.57		0.86		
	379.76	197.95	181.39	0.48		0.46		0.52		0.92		
<i>decreasing rate of slip coefficient (C/H)</i>					6.2%		2.2%		7.4%			
CD-12M12M	384.51	209.20	189.91	0.46	0.46	0.47	0.46	0.51	0.50	0.91	9.8%	
	385.99	208.05	183.75	0.46		0.47		0.53		0.88		
	368.44	208.08	190.50	0.44		0.45		0.48		0.92		
HD-12M12M	389.26	201.03	183.66	0.48	0.48	0.47	0.47	0.53	0.52	0.91	8.2%	
	378.49	202.23	186.43	0.47		0.46		0.51		0.92		
	<i>invalid</i>											
<i>decreasing rate of slip coefficient (C/H)</i>					4.2%		2.1%		2.7%			
CD-16M12M	422.93	210.67	191.31	0.50	0.53	0.52	0.55	0.55	0.59	0.91	10.2%	
	460.29	214.18	192.07	0.54		0.56		0.60		0.90		
	474.37	211.39	187.74	0.56		0.58		0.63		0.89		
HD-16M12M	469.89	198.80	181.42	0.59	0.60	0.57	0.58	0.65	0.66	0.91	9.6%	
	484.38	201.61	182.43	0.60		0.59		0.66		0.90		
	473.05	198.95	178.15	0.59		0.58		0.66		0.90		
<i>decreasing rate of slip coefficient (C/H)</i>					11.7%		5.2%		9.7%			
CD-32M16M	579.87	218.96	200.45	0.66	0.66	0.71	0.72	0.72	0.72	0.92	8.4%	
	593.38	220.53	202.19	0.67		0.72		0.73		0.92		
	588.19	228.85	209.69	0.64		0.72		0.70		0.92		
HD-32M16M	594.56	202.13	187.59	0.74	0.74	0.73	0.73	0.79	0.79	0.93	7.1%	
	<i>invalid</i>											
	602.19	203.97	189.85	0.74		0.73		0.79		0.93		
<i>decreasing rate of slip coefficient (C/H)</i>					10.8%		1.4%		9.2%			
<i>Single shear series</i>												
CS-12S16M	<i>invalid</i>				0.46		0.48		0.58		20.6%	
	195.20	216.53	171.96	0.45		0.48		0.57		0.79		
	198.72	211.42	167.76	0.47		0.48		0.59		0.79		
HS-12S16M	<i>invalid</i>				0.52		0.51		0.62		17.2%	
	202.30	202.11	171.21	0.50		0.49		0.59		0.85		
	213.53	200.34	162.20	0.53		0.52		0.66		0.81		
<i>decreasing rate of slip coefficient (C/H)</i>					11.5%		5.9%		7.1%			
CS-12M16M	237.48	213.85	174.41	0.54	0.51	0.58	0.56	0.66	0.62	0.82	17.6%	
	224.49	228.46	188.73	0.49		0.55		0.59		0.83		
	223.31	218.53	181.55	0.51		0.54		0.61		0.83		
HS-12M16M	234.17	214.29	181.69	0.55	0.54	0.57	0.55	0.64	0.63	0.85	13.7%	
	219.89	203.11	178.30	0.54		0.54		0.62		0.88		
	<i>invalid</i>											
<i>decreasing rate of slip coefficient (C/H)</i>					5.6%		-1.8%		1.3%			
CS-16M22M	264.10	215.49	182.37	0.61	0.57	0.64	0.62	0.72	0.65	0.85	12.9%	
	252.40	236.12	209.00	0.53		0.62		0.60		0.89		
	247.25	222.14	196.00	0.56		0.60		0.63		0.88		
HS-16M22M	257.65	212.71	189.32	0.61	0.61	0.63	0.63	0.68	0.68	0.89	11.0%	
	<i>invalid</i>											
	<i>invalid</i>											
<i>decreasing rate of slip coefficient (C/H)</i>					6.6%		1.6%		4.1%			

of local yielding around the countersunk bolt holes by increasing applied tensile load.

Slip coefficients of the double shear series are higher than those of the single shear series regardless of type of the bolt head. This is caused by that the contact pressure of the single shear joints is lower than that of the double shear joints because of eccentric bending between the base plate and the splice plate.

Fig.12 shows the relationship between slip coefficient  $\mu_2$  and slip to yield resistance ratio  $\beta_e$ . It can be confirmed that the slip coefficients  $\mu_2$  of all specimens are higher than the slip coefficients  $\mu_1$ .

It is also found that the variation of the slip coefficients  $\mu_2$  under the same slip to yield resistance ratio  $\beta$  is

smaller compared with the variation of the slip coefficients  $\mu_1$ . Because the slip coefficients  $\mu_2$  are evaluated by the slipping resistance force and total of bolt axial forces at slip occurrence, these values become higher and the variation becomes smaller by elimination of the bolt axial force decreasing during load transfer. It is concluded from the experimental results that the slip strength of the joints with countersunk head bolts exceeds the design required slip strength which has specified in JSHB by the slip coefficient 0.45.

#### 4. Conclusions

This paper deals with the applicability of high strength bolted friction grip joints with countersunk head bolts for steel bridge structures which can finish the surface of the connection plate flat smoothly and prevent from functional depression due to corrosion. The main conclusions obtained are as follows,

- (1) In order to clarify distribution of the contact pressure on the contact surface of the joints with countersunk heads, the FEA was carried out varying the angle of countersunk head. It has concluded that the most desirable angle of the countersunk head is 90 degrees from the viewpoint of distribution of the contact pressure and stress concentration of the bolt.
- (2) In the cases of CD series, the FEA results indicate that high contact pressure over yield strength occurs around the countersunk edge of the bolt hole and the distributing area is small comparing with HD series.
- (3) In order to clarify the behavior of friction joints with countersunk head bolts, the standard slippage test were executed considering variation of plate thickness and the yielding strength of the base and splice plates.
- (4) It has concluded from the experimental results that the slip strength of the joints with countersunk head bolts exceeds the design slip strength specified in JSHB calculated by the slip coefficient 0.45 and that its slip strength is about only 10% lower than that with normal head bolts. It is caused by that the contact pressure of the joints with countersunk head reduce due to progress of local yielding around the bolt holes as increasing applied tensile load.
- (5) In order to apply such joints to practical joints of bridge members, further researches on applicability of the over-sized holes and multiple arrangements of countersunk bolts and so on are should be required.

#### 5. References

- 1) SIMULIA:Abaqus Analysis User's Manual, Vol.1-5
- 2) Japan road association: Specifications for highway bridges, Part2 steel bridges, 2012 (in Japanese)
- 3) A Monta, Tanihira T.; Experimental Study on the Shape Improvement and application of High Tension Countersunk Head Bolts in Friction Grip Joints, JSSC Journal of Constructional Steel, Vol.6, pp.65-76, 1992 (in Japanese)
- 4) Architectural Institute of Japan: Recommendation for Design of Connections in Steel Structures, 2006 (in Japanese)

# **A Path to Creating an Opportunity for Communication using the “Machizukuri Pattern”**

Yasutomi SAKUMA\*

(Received October 9, 2014)

## **Synopsis**

In this report, I will discuss how we created a “Machizukuri pattern” in a graduate school class that could be used to create an opportunity for better communication about the skills and abilities of the local community.

From the results, the following was clear:

- 1) There were certain tendencies in those Machizukuri patterns that were selected before the dialogue. “I can explain” was chosen by many for those patterns involving spatial aspects. “I want to listen” was chosen by many for intangible, cultural, and historical patterns.
- 2) There was comparatively little bias in the Machizukuri patterns selected after the dialogue activity.
- 3) The opportunity for dialogue using the Machizukuri patterns was understood by most, but there were two people who answered, “It was hard to understand.” In addition, the degree of satisfaction was high.
- 4) It was indicated that the points in need of improvement were “expression of the Machizukuri pattern” and “method of communication.”
- 5) It was also indicated that the application possibilities of the Machizukuri pattern are as a “communication tool” between various people and for “application to a Machizukuri Workshop.”

**KEYWORDS:** Pattern-Language, Machizukuri Pattern, Workshop

## **1. Introduction**

It is inevitable in a shrinking population that our lives are increasingly supported by limited human resources. Though new people who desire to accept responsibility appear, the skills and abilities of the local community are not easily ascertained. Additionally, it is expected that the town hall staff and residents of the local community accept responsibility for implementing Machizukuri (community design, community-based planning) in a rural area. It is required that those town hall staff members who manage the local community projects possess some proficiency. Because every person is a member of a local community, they each can manage its projects. The result of the project depends on personal factors, and the description of their expertise is insufficient. As a result, a method is required for describing the capabilities of the local community’s members.

Therefore, I focus on “pattern-language” in this report. Pattern-language was developed by C. A. Alexander as a method of creating tools that enable communication between the professional and the layman<sup>1)</sup>. In Japan, pattern-language has been used to describe town-planning rules, such as the “Design Code” in Manazuru City, Kanagawa Prefecture (1992); “The standard of Machizukuri,” which was a voluntary agreement in Kawagoe City, Saitama Prefecture (1988); the “Icoma City Landscape Formation Master Plan” in Icoma City, Nara Prefecture (2014); and so on. Recently, use of pattern-language has decreased in the fields of architecture and city planning, but it has begun to garner attention in the field of software development<sup>3)</sup>. In addition, it is beginning to be applied as a method of describing aptitude in the fields of institutional design and educational design. It is expected that, through use of pattern-language to describe human action, the non-professionals can communicate on even ground. Therefore, we can create a “Creative Society” in which people take action to create a better future<sup>4)</sup>.

In this report, I discuss how a graduate school class created a Machizukuri pattern to describe the aptitude of local community members, thus creating an opportunity for communication.

---

\* Lecturer, Department of Urban Engineering, Osaka City University

## 2. Outline of survey

### (1) How to create a Machizukuri pattern

I submitted an assignment that requiring the making of three Machizukuri patterns to the class members of Urban Design Exercises, Department of Urban Engineering, Graduate school of Engineering, Osaka City University (Figure 1). I provided a format for writing a Machizukuri pattern. It was on May 30, 2014 that I assigned this task, and the due date was July 4, 2014.

Assignment: describe three important topics used for discussion about Urban Planning, Urban Design, and Community Design, using the method of “Pattern-Language.”  
1) You may choose a subject you have experience with, or not. <sup>(1)</sup>  
2) You should imagine the subject as if you were involved in a plan or a design.  
3) You should think beyond the definitions of “Urban Planning,” “Urban Design,” and “Community Design.” You should think of a series of activities used for approaching a space.

**Figure 1.** Instructions given for the task of making three Machizukuri patterns.

The format of a Machizukuri pattern.  
1) Title  
2) Context  
3) Problem  
4) Solution (and an example)  
5) Some comments (something you think, your impressions, your name)  
(These items were laid out in one A4 paper.)

**Figure 2.** Major items of the format for making a Machizukuri pattern.

### (2) How to arrange a Machizukuri pattern

I arrange a Machizukuri pattern using the KJ-method<sup>(2)</sup>, which was included in the assignment.

### (3) How to create dialogue with a Machizukuri pattern

I had the students talk with their friends using the Machizukuri pattern on the day of the exercise (July 18, 2014).

- 1) First of all, I showed the arranged Machizukuri patterns to the students. The students then read the Machizukuri pattern that they wrote so they would understand them.
- 2) I then had the students talk with their friend, following the method of Iba<sup>5)</sup>. The students then choose three patterns for which they thought “I can explain” or “I want to listen.” They then spoke with their friend about meaning of the Machizukuri pattern. This took about 5 minutes for each discussion of a pattern, and they spoke about three patterns.
- 3) After the dialogue, I executed a questionnaire survey. The items of the questionnaire survey were as follows in Figure 3.

1) For what pattern did you think, “I can explain?” (3 items)  
2) For what pattern did you think, “I want to listen?” (3 items)  
3) For what pattern did you think, “I have explained?” (3 items)  
4) For what pattern did you think, “I have listened?” (3 items)  
5) Was the Machizukuri pattern easy to understand? (5 grade points)  
6) Did you have fun with the Machizukuri pattern dialogue? (5 grade points)  
7) What point of the Machizukuri pattern needs improvement? (free answer)  
8) What do you think of the Machizukuri pattern’s application possibilities? (free answer)  
9) What do you think anything else? (free answer)

**Figure 3.** Items of the questionnaire survey.

## 3. Results

### 3.1. Machizukuri pattern

There were 70 patterns collected from 24 students (one student submitted only one pattern). The names

of these 70 patterns were provided by the students who originated them, so the degree of abstraction for each pattern varies. I changed the name of some patterns for clarity and arranged them using the KJ-method, ending up with 44 Machizukuri patterns.

**Table 1.** Machizukuri patterns arranged by KJ-Method.

No.	Name of Pattern	No.	Name of Pattern
1	Management to increase a community's value	23	A satellite office
2	Stimulation to create a community	24	Success of local business
3	Autonomy of a community	25	Space that residents can change
4	Imagining a future vision of a community	26	A back alley space
5	Making a community rule	27	Creating a waterfront space
6	Self-determination	28	Deregulation
7	Cooperation with a neutral person	29	Discussion of the outdoors
8	Corroboration with various people	30	A place of memories
9	Creation with everyone	31	Concentration of functions
10	To expand the persons concerned	32	Establishment of a symbol
11	Adoption of everyone's opinion	33	Formation of a compact city
12	Having a different point of view	34	Residence in downtown
13	Discussion with people who hold a different position	35	Public-built and privately operated
14	A series of small successes	36	Making an activity base
15	Learning a lesson from precedents	37	Opening a station to the local community
16	Thinking with a new set of values	38	Making use of the existing facilities
17	Welcome the new immigrant	39	Regeneration of an "old" new town
18	Making a technical term easier	40	To make something oneself
19	To inform non-residents of something	41	Planning comprehensively
20	Corroboration with residents and immigrants	42	Coexistence between the old and the new
21	Description of local culture	43	Review in a combined unit
22	Forming a new business	44	Optimization of a T junction

### 3.2. Dialogue using a Machizukuri pattern

I had the students talk with their friends, employing the method used by Iba. They spoke with their friends about the meanings of the Machizukuri patterns. This took about five minutes for each discussion, and they talked three times.



**Figure 4.** A scene depicting dialogue using a Machizukuri pattern.

### 3.3. The Results of the Questionnaire Survey Administered after the Dialogue

After the Machizukuri pattern dialogue activity, I executed a questionnaire survey. I collected 18

effective responses, because although there were 19 students present, there was one late comer.

**1) “I can explain,” “I want to listen,” “I have explained,” and “I have listened”**

Overall, there was great interest in “Space that residents can change”, “Creating a waterfront space”, “Thinking with a new set of values”, “Establishment of a symbol”, and “Coexistence between the old and the new”.

As for the results of “I can explain,” many students selected “Creating a waterfront space”, “Making use of the existing facilities”, “Thinking with a new set of values”, “Space that residents can change”, and “Regeneration of an ‘old’ new town”. It was determined that many students chose the items that were easiest to understand, like spatial designs. As for the results of, “I had explained,” many students chose “Creating a waterfront space” and “Space that residents can change”. I was able to confirm that there was almost no difference in the tendency to answer, “I can explain.”

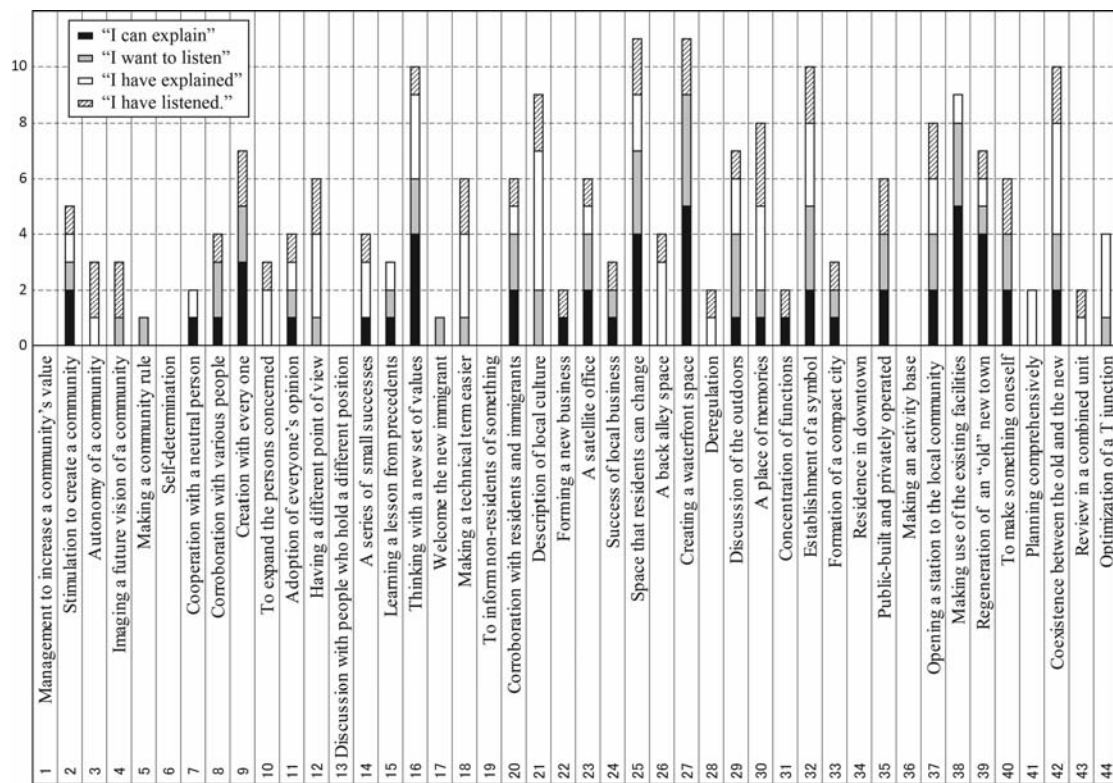


**Figure 5.** Machizukuri patterns to which the students answered, “I can explain,” “I want to listen,” “I have explained,” and “I have listened.”

As for the results of, “I want to listen,” Many students selected “Description of local culture”, “Coexistence between the old and the new”, “Thinking with a new set of values”, “A back alley space”, “A place of memories”, “Establishment of a symbol”, and “Optimization of a T junction”. It seems that many students were interested in the patterns of intangible, local, and historical things, like culture, a small alley, a personal memory, and so on. As for the results of “I have listened,” students selected “A place of memories” as the most common answer. However, there was a tendency for the number of answers to show low distribution.

There was a tendency toward certain items of the questionnaire (“I can explain” and “I want to listen”) before the dialogue. However, there was no tendency shown in the distribution of the items of the questionnaire (“I have explained” and “I have heard”) after the dialogue.

**2) Was the Machizukuri pattern easy to understand?**

There were 16 students who replied that the Machizukuri pattern was “Easy to understand”; 1 student who replied, “Hard to understand”; and 1 student who replied, “Very hard to understand.” Overall, most of students reported that they were able to understand the Machizukuri patterns.

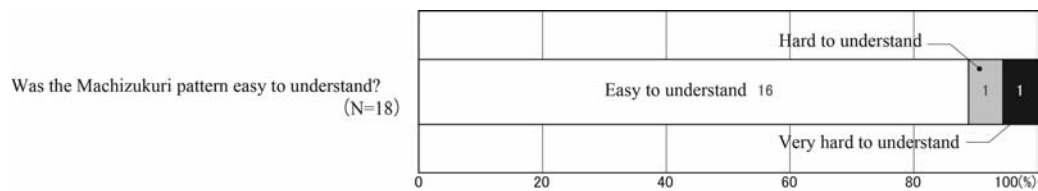


Figure 6. Was the Machizukuri pattern easy to understand?

### 3) Did you have fun with the Machizukuri pattern dialogue? (5 grade points)

Only 1 student replied, “Very Fun,” and 17 students replied “Fun.” Overall, most of students were satisfied.

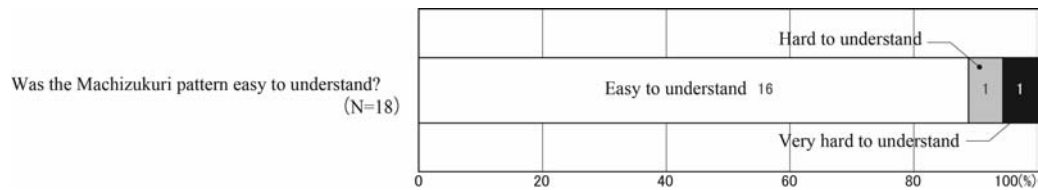


Figure 7. Did you have fun with the Machizukuri pattern dialogue?

### 4) What point of the Machizukuri pattern needs improvement?

Regarding the points that need improvement, many students selected “Expression of the Machizukuri pattern,” and “Method of Communication.” Regarding “Expression of the Machizukuri pattern,” it seemed that the abstraction degree leading to several interpretations of the same pattern is a factor in their confusion. Regarding “Method of Communication,” it seemed that they were confused about finding their partner in the dialogue activity.

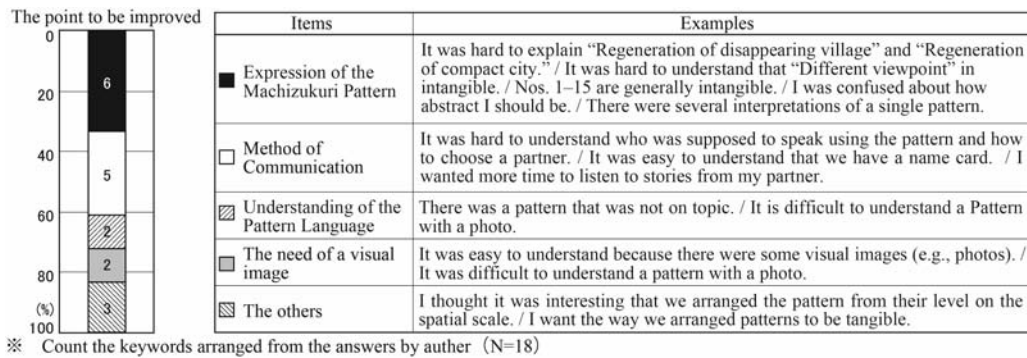


Figure 8. What point of the Machizukuri pattern needs improvement?

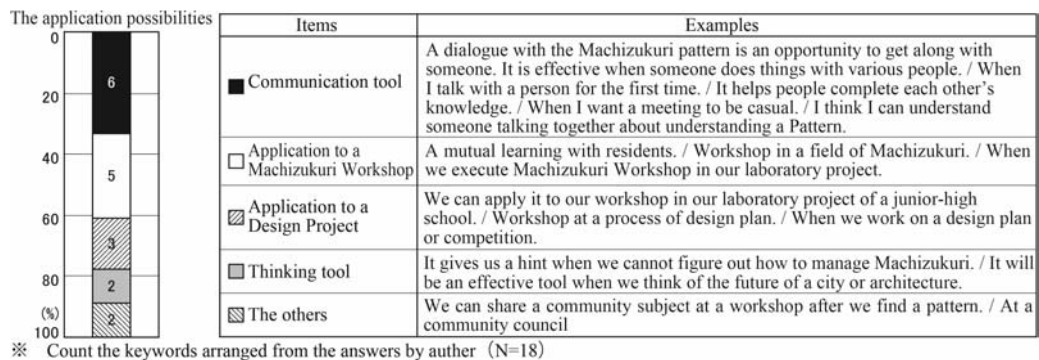


Figure 9. What do you think of the Machizukuri pattern’s application possibilities?

### 5) What do you think of the Machizukuri pattern's application possibilities?

Regarding the application possibilities, many students replied that it could be used as a “communication tool” or for “application to a Machizukuri Workshop.” As a “communication tool,” they proposed that the Machizukuri pattern is effective when people meet for the first time and when someone meets various people. As an “application to a Machizukuri Workshop,” they proposed that the Machizukuri pattern would be effective in a meeting of the inhabitants and in the dialogue of a student-managed project.

## 4. Conclusions

This study yielded some important results, as follows:

- 1) Machizukuri patterns selected before the dialogue had certain tendencies. Many students chose “I can explain” for items concerning spatial topics. Many chose “I want to listen” for intangible, cultural, and historical patterns, such as those about a small alley or personal memory.
- 2) Machizukuri patterns selected after the dialogue had comparatively little bias.
- 3) The opportunity for dialogue using the Machizukuri pattern was understood by most, but there were two people who answered, “It was hard to understand.” The degree of satisfaction was high.
- 4) It was indicated that the points in need of improvement were “Expression of the Machizukuri pattern” and “Method of Communication” regarding how to find a dialogue partner.
- 5) It was indicated that the application possibilities of the Machizukuri pattern were as a “communication tool” between various people and for “application to a Machizukuri Workshop.”

Further research should be conducted to accumulate knowledge about the Machizukuri pattern by applying it at a Machizukuri site.

## 5. Notes

- (1) This exercise was held for two hours every two weeks. Some students were in charge of one subject in four exercises.
- (2) The KJ-method is a method of analyzing data that was developed by Jiro Kawakita, who is a cultural anthropologist. This method uses cards to help someone apply broad thinking, and it then helps them use collective thinking by collecting the cards together and identifying relationships between them.

## 6. References

- 1) Christopher Alexander, Sara Ishikawa, Murray Silverstein, *A Pattern Language: Towns, Buildings, Construction*, Oxford University Press (1977).
- 2) Christopher Alexander, *The Nature of Order; Book One – Four*, The Centre for Environmental Structure (2002–2005).
- 3) Eto Koichiro, *Pattern, Wiki, XP: The Timeless Way to Creation*, Gijutsu-Hyohron (2009).
- 4) Takashi Iba, Iba Laboratory, *Presentation Pattern: As a Creative Media*, Keio University Press (2013).
- 5) Takashi Iba, Hiroshi Nakano, Koichiro Eto, Yasuto Nakanishi, Heizo Takenaka, Eiichi Hanyuda, *Pattern Language: As a Language for Creative Society*, Keio University Press (2013).

# Approach to Improve Driving Condition on Desert highway from Viewpoint of Road Safety

Zulpikar KERAM\* and Yasuo HINO\*\*

(Received October 9, 2014)

## Synopsis

Recently, the environmental problems caused by road construction and the road safety problems caused by desert climate have been getting more and more obvious. Especially, the road safety must be the most important issue against the desert whether. In this paper, the approach to improve the driving conditions on desert roads should be proposed from viewpoint of road safety, based on reviewing major results of a series of studies. As a result, an appropriate idea to prevent traffic accidents caused by desert weather from viewpoint of developing road facilities, in consideration of results of a series of studies.

**KEYWORDS:** Desert highway, Road safety, Desert whether, Road facility, Xinjiang Uygur

## 1. Introduction

In Xinjiang Uygur Autonomous Region, recently road development has progressed according to increase of vehicles. The developing areas have been spreading to desert area from the coastal or inland area. Therefore, the environmental problems caused by road construction and the road safety problems caused by desert climate have been getting more and more obvious.

Uygur has the vast area with complicated geographical features. Then, not only the weather also must be changeable, the abnormal weather as high temperature, storm, heavy snow, dense fog and so on must become the major cause of traffic accidents on the desert roads. On the other hand, the provision of road safety facilities was not yet enough on the desert road. Road safety facilities must be required to make the smoothness of traffic flow and to prevent the traffic accidents, by consideration of weather condition as well as road and traffic condition.

Then authors have tried to reveal the influences of desert weather to occurrence of traffic accidents and the problems to solve in concerns with road safety on desert road. Therefore, in this paper, the approach to improve the driving conditions on desert roads should be proposed from viewpoint of road safety, based on reviewing major results of a series of studies.

## 2. Influence of desert environment on traffic safety

In desert area, high temperature, dust cloud and storm in summer season and lower temperature and blizzard must become the bad influence to road safety. Here, these whether condition were reviewed by analyzing some actual data on some desert roads in Uygur, in order to reveal the influence of these weather condition to the occurrence of traffic accidents.

### 2.1 Whether in summer season<sup>1)</sup>

#### (1) Influence of hot-arid climate

The annual mean temperature of Taklamakan Desert is 10-11°C, and the normal temperature of summer in the desert road section is 35°C. On the other hand, the average temperature of pavement surface reaches 50-60°C, in addition the temperature of tire surface sometimes exceed 70°C<sup>2), 3)</sup>. As the high temperature weather may be a cause of accidents because of increasing the damage of tires, drivers must not only maintain the tire condition but also manage the distance of continuously driving.

#### (2) Influence by dust storm and black blizzard<sup>4)</sup>

It is understood that the dust cloud, dust storm and the black blizzard happen frequently in the vicinity of the desert road from March through September based on the report of Xinjiang Uygur Autonomous Region Weather Bureau (Photo 1)<sup>5)</sup>. Somewhere, the sand dust of visible degree (view) 10km or less is generated in these desert roads according to the data during ten years of the Weather Bureau. As for the black blizzard of 1km or less,

---

\* Student, Doctor Course of Dept. of Urban Engineering

\*\* Professor, Department of Urban Engineering

there are seven days under the 500m or less view and 29 days under the 1km view in a year (Table 1). Although these conditions are assumed to give the bad influence to safe driving, the safe running standard concerning the visible degree corresponding to the desert road is not enacted in China.

Table 1 Dust-sandstorm occurrence dates(1999-2008)(day)<sup>4)</sup>

Sight(km)	<0.5	<1	<5	<10	<15	<20	<25	<30
aral	7	20	39	146	281	911	3457	3599
hotan	41	126	643	1829	2955	3499	3602	3637
Middle	21	73	483	1177	1633	1633	2633	2818
Total	69	219	1165	3152	4869	6523	9692	10049

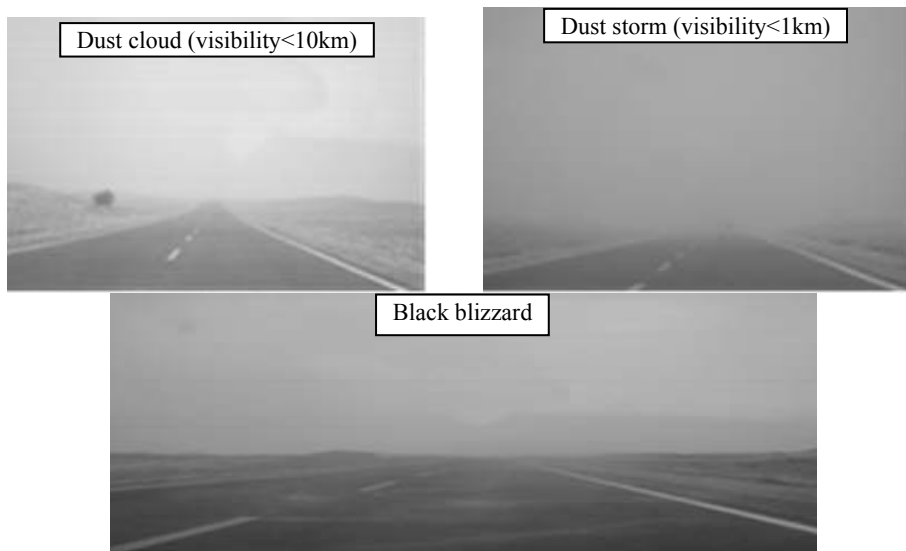


Photo 1 Condition of dust storm and fling sand<sup>4)</sup>

## 2.2 Whether in winter season<sup>5)</sup>

### (1) Influence by lower temperature

Although the accident of five months (November-March) in winter is about 30 percent, lower in comparison of the monthly average (40 percent), drivers must take care of the slipping accident by the road surface freezing at nighttime, because of temperature change of day and night (Photo 2).

### (2) Influence by snowstorm and snowfall

The drifting snow is a phenomenon that the fallen snow is blown up from the surface by grace of the wind, and the view decreases under 50m (Photo 3). In addition, the view of the strong wind and the heavy snow might become 10m or less. These conditions force drivers to be difficult to judge the road situation. In addition, because the snowfall made by snowstorm reduce the road width, drivers have to try safer driving.

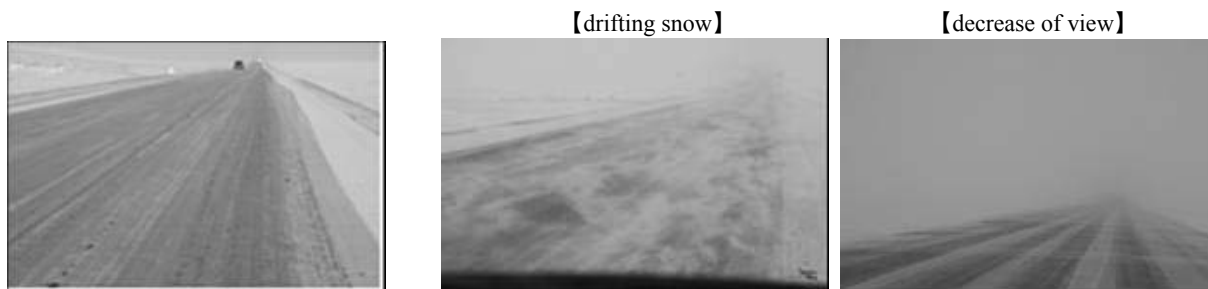


Photo 2 Condition of road surface freezing<sup>3)</sup>

Photo 3 Drafting snow and condition of decreasing view<sup>3)</sup>

### (3) Major problems caused by lower temperature and fallen snow

As mentioned above, the specific winter whether condition like lower temperature and fallen snow must be

causes of particular traffic accident in the north region of Xinjiang Uygur Autonomous Region. Therefore, nevertheless the road administrator should secure a safe and smooth traffic function in winter, road safety facilities to prevent the traffic accidents in winter have not been provided, because of the financial deficit for road extension and technological problems for road maintenance.

In concerns of these problems, the Xinjiang Traffic Science Academy and the Hokkaido Development Public Works Research Institute established the manual meeting on the road technology in winter from 2007. In near future, these results must help to improve the road safety on desert road in winter season.

### 3. Influence of driving behavior and road condition

#### 3.1 Excessive speed

The common cause of traffic accidents in both summer and winter must be the excessive speed, because of long straight section (Table 2). Especially, the excessive speed increases the risk of accidents in the curve section.

Table 2 Condition of excessive speed

Car Types	Flat sections(16:40~17:40)			Slope section(15:00~16:00)		
	G216 K495+500 80km/h			G216 K457+300 80km/h		
	Observed data	Speeding	Speeding rate (%)	Observed data	Speeding	Speeding rate (%)
Small car	92	51	55.4	69	33	47.8
Cargo car	67	7	10.4	48	6	12.5
Bus	3	1	33.3	5	3	60
Total	162	59	36.4	122	42	34.4

#### 3.2 Road condition<sup>6), 7)</sup>

The road condition as well as abnormal whether may influence to occurrence of traffic accidents. Especially, in the straight section which consists of the long part of the desert road, many accidents may occur caused by inattentive driving and speeding. And in the curve section, the fatal accidents must occur often by the combination whether condition and speeding. As shown in Table 3, the comparison of accident rate by vehicle-distance shows the characteristics of traffic accidents according to road conditions. From this table, it is clear that the accident rate on desert road section considerably higher than the rate of intersections in Urumqi city. Therefore, it must be necessary to establish the suitable warning signs against the excessive speed according to the road feature.

Table 3 Comparison of accident frequencies according to road section<sup>7)</sup>

Section	Road condition	Number of Accidents	Percentage (%)	hundred million accident rate (number/million vehicles km)
456~466	Straight	6	8.8	249.07
481~486	Straight	3	4.4	124.53
534~539	Straight	3	4.4	124.53
Sub total		12	17.6	498.13
486~513	Bump or Curve	15	22	622.66
539~545	Cross or change	8	11.7	332.09
Sub total		23	33.8	954.75
Intersection of inner city road (mal baziri ~ kizil bayrak)		28	48.3	85.34

### 4. Situation and problem of road safety facilities<sup>6)</sup>

In a series of studies, although the influence of whether condition to occurring traffic accidents on the desert roads must be revealed, the condition of establishing the road safety facilities was not considered. As some road safety facilities play the important role to prevent the traffic accident by giving the warning information to drivers, the planning of setting facilities must be important issues of the desert road construction. However, the problems of the lack of revenue because of long section of road.

Then, the survey was executed to investigate the condition of road safety facilities as the warning sign and road marks for curve section. In his chapter, some urgent issues in concern of road sign, road marks and service or parking areas to solve were shown based on the results of survey, in following sections.

#### 4.1 Road sign

It becomes clear that the rate of setting up necessary road signs and adequate road markings were respectively 58% and 50%, in 24 sections of K261-K405 of Aral~Hotan road (Table 4). And as for road markings, a half of them was provided as the dotted lines instead of solid lines as the central line and no overtaking line in curve and/or uneven sections. As these results were limited within onsite surveys, it must be necessary to build the database and to realize the deepen analyses based on the data base. However, above all, some problems revealed by these surveys must be improves immediately.

Table 4 Challenges Aral~Hotan desert road Continuous music section<sup>6)</sup>

Road signs	Number	Percentage (%)	Road Marking	Number	Percentage (%)
Being	14	58	Solid line	12	50
Nothing	10	42	Dotted line	12	50

#### 4.2 Service and parking Area

The road standard of China<sup>3)</sup> provided that the service and parking arear must be set up respectively at 50km and 10km interval on the average. Especially, in the service area, the provision of the lavatory, the gas station and the stalls. However, there are some sections without no service area during 100km and more between Aral and Hotan (Table 5).

Table 5 Interval of service and parking area on Araru-Hotan road<sup>6)</sup>

Section of no services		Distance(km)
hotan~tawakol	K0~K42	42
tawakol~kizil muna	K42~K147	105
kizil muna~aral	K147~K268	121
aral~hotan	K268~K399	131

#### 4.3 Communications equipment

In 70% of the 236km section of G314 and G216 which are a part of Aral~Hotan road, drivers cannot use the communication service because of no equipment, based on the survey in 2009(Table 6). The distance of this no service section may be equivalent to 30% of whole section of Aral~Hotan road.

Therefore, other survey reported that it took 13 hours and more to be rescued after occurring traffic accident. Thus, as the delay of setting up the communication equipment may occur the secondary victims, it can be said that the installation of the communication equipment as telephone plant of the wireless telecommunications base and cable facilities must be the pressing issue.

Table 6 Blank District of communication signals Alar~hotan desert road<sup>6)</sup>

No equipment Section	Distance of no equipment(km)	Communication Service	Distance of service (km)
K51~K56	5	K57~K73	16
K80~K96	16	K74~K79	5
K112~K146	20	K97~K103~K111	14
K161~K214	22	K147~K152~K161	14
K169~K214	34	K184~K188~K195	13
K228~K293	65	K215~K227	12
total distance(km)	162	total distance(km)	74

#### 4.4 Problems of road safety facilities from viewpoint of driving characteristics<sup>8)</sup>

The in-depth data is necessary in the research of the relations between bad weather and traffic accident. Though in this study, some investigations of the transportation facility according to the cause of a traffic accident in the region, the influence on drivers by bad weather in winter and summer and the problems of the lack of communication equipment were referred, the relativity of the direct influence on the driver by such factors was not able to be clarified only by the questionnaire survey result.

Then, a test of influence to drivers' psychological and physiological condition by such factors was executed on the desert road. As a result, the risk of traffic accident may rise by two hours or more driving on the desert road (Figure 1). That is, these results show that the traffic safety facilities on the desert road must be prepared and maintained in consideration of the road network, road conditions, traffic situation and weather condition overall.

## 5. Idea and problem of traffic safety facilities improvement<sup>9)</sup>

The road facilities of China must be planned to develop according to the Standard of Traffic Safety Facility Design in China<sup>10)</sup>. However, it is also reported that there are many risk of traffic accidents because a lot of sections were in completed the adequate safety facilities on the desert roads. Such condition may increase the possibility of the accidents in bad weather. Especially, the lack of communication equipment may become a serious problem which not to be able to be rescued after occurring accident.

Above all, as some important findings came out of this study, here, some concrete ideas obtained in this study are summarized.

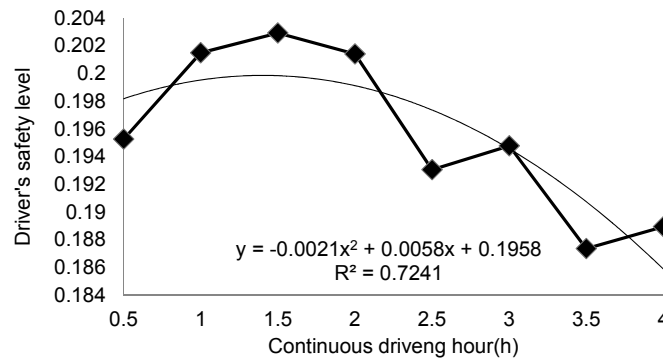


Figure 1 Safety driving level by driving hour<sup>8)</sup>

### (1) Telecommunication system

As there were many sections with no service of communication in G314 and G216 as a part of Takaramakan and Ara-Hotan road, the environment of communication facilities has been improved, such as, the available area of communication has been expanded to 45km after setting up of communication tower in 2009, 23 relay stations have been introduced and the GPS systems were introduced to the long distance buses. However, in order to prevent the secondary accident and to reduce the damage, some improvement measures are necessary, as follows.

- 1) Provision of emergency telephone booth by 25km was essential issue.
- 2) Introduction of a helicopter to rescue injured persons at the serious accident must be investigated.
- 3) Consideration of the communication system among drivers may be desirable.

### (2) Correspondence to abnormal whether condition in summer and winter

In summer, there are a lot of days that not only exceed 30°C but also the sand storm and the sand dust are generated around the desert road. Moreover, it is not few days with the snowstorm and snowfall in winter. Such bad weather gives the serious influence of road safety. Then, a part of ideas and methods to improve the road safety facilities are described according to the report and the survey in 2009, as follows.

- 1) The parking and/or service area must be prepared by 15km.
- 2) The prevent facilities for strong wind and snowstorm must be at least set up at some specified points which were considered to increase risk of traffic accident.

### (3) Province of communication and safety education

The safety education should be essential to understand the necessity of road safety, because the rationality of personal behavior must be acknowledged each other even though transport modes are different. Then, as for the influence by bad natural environment and whether of the desert area, the education with following contents may be necessary.

- 1) Relation between whether condition and occurrence of accident.
- 2) Necessity of first aid and rescue.
- 3) Influence of vehicle trouble to occurrence of accident and importance of maintenance.

### (4) Safety for driving on long straight section

As the driver becomes careless to road environments because of monotonous driving on the long straight section, it is necessary to introduce some warning facilities as the high brightness road marking with lower bumps, to warn to driver both by visual sensation and vibration.

### **(5) Safety against black blizzard caused by dust storm**

The black blizzard caused by dust storm are generated on 1/3 of one year in the desert area section. As such bad weather gives the bad influence to driving and may become the serious cause of accident, the drastic measures must be introduced as soon as possible, as follows.

- 1) Developing the measurement equipment of eyesight and the information system of visual condition to drivers.
- 2) Introducing the glance guidance facilities such as delineator and luminous facilities.
- 3) Enforcement of education for accidental risk caused by such bad weather.

### **(6) Introduction of ITS to secure the safer road environment on desert road**

In order to introduce some improvements for road safety, the intelligent transport (traffic) system (ITS) should be necessary and effective. ITS is an integrating effective road traffic system which is consisted of the computer processing technology, the information technology, the data communication transmission technology, the electronic automatic control technology, as the whole traffic management system. However, to introduce the ITS, it must be essential to develop the data base of various information concerned road and driving environment, as well as, to develop the latest technology both of computer and telecommunication. Therefore, first of all, some developed systems in some developed countries must be helpful.

## **6. Conclusions**

Some of roads in the desert area have the long distances with the bad weather such as higher temperature, storm, snowfall and Black blizzard, as well as the complicated geographical features. On the other hand, as the province of road safety facilities against such bad driving conditions were insufficient, the setting up their facilities must be essential to prevent the traffic accidents.

In this paper, some approaches to improve the driving environment on the desert road in the near future were proposed, based on reviewing the major results of a series of studies concerned with the relation between driving conditions between road and weather conditions, which were essential to consider the improvement of road safety facilities.

However, as there may be many issues to solve in order to realize the better driving conditions in the desert road, the more deepen analyses will be required based on the results of this study.

## **7. References**

- 1) Zulpikar KERAM and Yasuo HINO, *Influences on Road Safety by Desert Weather in Uighur*, Japan Society of Traffic Engineers, *Papers on Traffic Engineering*, No. 31, pp. 25-28(2011) (in Japanese)
- 2) Xinjiang Desert Institute and Lanzhou Desert Research Institute, *Comprehensive Evaluation Study of the Tarim Desert Road Environment Influence "R"*, Korla, Tarim Petroleum Exploration and Development Command Unit, 1994 (in Chinese)
- 3) Kerem ROZI, Liu LIHUA, Hu XINMIN, Jang Yan and Zulpikar KERAM et al, *Desert Road Security Process and Facility*, Technical Report of Xinjiang Communication Science Research Institute, 2011 (in Chinese)
- 4) Xinjiang Bureau of Meteorology, *Weather Statistics Data*, 1999-2008 (in Chinese)
- 5) Zulpikar KERAM and Yasuo HINO, *Analysis on the Influence of Winter Weather on Traffic Accidents in the North Desert Region of UYGUR*, Japan Society of Civil Engineers, *Proceedings of Infrastructure Planning*, No.44, 4pages (CD-ROM) (2011) (in Japanese)
- 6) Zulpikar KERAM and Yasuo HINO, *Review on Road Safety Facilities of Arterial Road in the Gobi Desert of Uighur*, Japan Society of Civil Engineers, *Proceedings of Infrastructure Planning*, No.45, 4pages (CD-ROM)(2012) (in Japanese)
- 7) Xinjiang Communication Science Research Institute, *Road Safety Evaluation Summary Report*, 2007
- 8) Zulpikar KERAM and Yasuo HINO, *An Investigation on Accident Prevention from Viewpoint of Physiological Change Caused By Long-time Driving and Accident Occurrence Interval on Roads at Desert Area*, Japan Society of Civil Engineers, *Proceedings of Infrastructure Planning*, No.50, 6pages (CD-ROM)(2014) (in Japanese)
- 9) Zulpikar KERAM and Yasuo HINO, *An Investigation on Improvement of Road Safety Facilities to cope with the Impact caused by Desert Climate*, Traffic Science Society, *Proceedings of Annual Meeting*, pp.29-30 (2012) (in Japanese)
- 10) Design Standard of Road Safety Facilities, *JTG81-2006*, Vol.16, 2006 (in Chinese)

# **Abstracts of Papers**

## **Published in Other Journals**



***Mechanical Engineering***

**Effects of Introducing Solar Heat to Absorption Cooling System, -Feasibility Study of Solar Thermal Energy Utilization to Plant Factory-**

Nobuya NISHIMURA, Tametoshi MATSUBARA (OSAKA GAS CO.,LTD.), Hiroyuki IYOTA, Yosuke SHIRAYANAGI and Yuuma YAMAGA

*Trans. of the Jpn Soc. Refrigerating and Air Conditioning Engineers*, Vol.31, No.2, pp.317-329 (2014) (in Japanese)

This paper presents the feasibility of solar thermal energy utilization to plant factory. Performance and operation characteristics of the solar driven absorption chiller heater of 352 kilowatt refrigeration capacity were investigated by using long term demonstration test data of June 2009 to October 2013. Effects of solar insolation to the absorption chiller heater performance were examined by changes of air conditioning load ratio and solar position. As a result, it was demonstrated that the COP in case of parallel operation by solar energy and town gas becomes 20 to 50 percent higher than that case of another operation modes. Also, Seasonal performance of the system is calculated based on the appearance frequency (weight) of the outdoor temperature. The air-conditioning load ratio was sorted out for every outdoor temperature based on the data measured during 5 seasons from 2009 to 2013 to obtain the averaged COP value. COP takes the maximum value at the air-conditioning load ratio of 30% and decreased at both higher and lower ratios than that.

**Thermal Evaluation of a Solar Assisted Absorption Air-Conditioning System**

Nobuya NISHIMURA, Tametoshi MATSUBARA (OSAKA GAS CO.,LTD.), Yosuke SHIRAYANAGI and Yuuma YAMAGA

*Proc. of Grand Renewable Energy 2014 (GRE2014) international conference*, Tokyo, Jul.28-Aug.1, (on CD-ROM)

This paper presents the thermal evaluation results on a solar-assisted absorption air conditioning system of 352 kilowatt refrigeration capacity from June 2009 to October 2013. About 70 to 90 degree Celsius hot water were made by three types of solar collectors, including two different (vacuum tube and flat plate) types. Daily average performances about the solar collector and the absorption chiller heater were investigated experimentally. As a result, it was found out that the seasonal performance (IPLV) throughout the four cooling period was 1.39, which is 12-26% larger compared to the case in which solar heat is not used.

**Evaluation of Shutter Speed of Digital Cameras for Color Measurement**

Hideki SAKAI and Hiroyuki IYOTA

*Proceedings of the 2nd Asia Color Association Conference (ACA2014)*, pp.196-199 (Sep., 2014, Taipei, Taiwan)

We measured the shutter speed of digital cameras and confirmed that the indicated values of the shutter speed of the cameras are not reliable. However, errors are systematic. It is probably caused by the fact that the decimal round numbers such as 3, 15 and 30 seconds are usually used as the indicated values, but inside the computer-controlled digital cameras, the binary round numbers such as 3.2, 16 and 32 are actually used instead. The measured values give close agreement with these binary round numbers. In any case, the mechanism of recent models' shutter, especially electrical ones, is a black box for users. Thus, the actual values must be measured and by using these actual (corrected) values of shutter speed, we can improve the color measurement accuracy of digital cameras.

**Development of Food Appearance Monitoring System for Oven Cooking**

Taiki MATSUMOTO, Shuhei NOMURA, Hiroyuki IYOTA and Hideki SAKAI

*Proceedings of the 2nd Asia Color Association Conference (ACA2014)*, pp.200-203 (Sep., 2014, Taipei, Taiwan)

We propose a color measurement method using a charge-coupled device (CCD) camera that can monitor a wide area. A commercially available oven (steam convection oven) is used as the cooking apparatus. Toast (sliced white bread) is used as the food material. Photographic images of the food material are recorded during oven cooking under two conditions (i.e., hot air and superheated steam). The lightness and chroma of the food surface are analyzed from the recorded images, and their history during oven baking is applied for evaluating the color of baked food. The results show that the use of a CCD camera to measure color change

can optimize the cooking procedure in an oven. Further, we propose a new evaluation index based on the recorded images showing the color of baked food.

### **Accuracy of Color Measurement by Using Digital Cameras and the Standard Color Chart**

Hideki SAKAI, Saya YOSHIKAWA and Hiroyuki IYOTA

*Proceedings of the 1st Asia Color Association Conference (ACA2013)*, pp. 248-251 (11-14 Dec. 2013, Thanyaburi, Thailand)

We examined five different digital cameras and evaluated their accuracies of color measurement. Commercially available digital cameras are not intended for use in color measurement. Thus, users have to calibrate the camera system by themselves for the purpose. We adopted the image correction method, in which, samples are photographed with some standard color charts side by side in one photo and the photographed images are color-corrected using the colorimetric data of the color charts. This method has an advantage that the measurement accuracy does not depend on the camera used; Users can freely replace the cameras. Using the X-rite ColorChecker 24-color chart as standard colors, we examined how the accuracy of color measurement depends on the camera used. As a result, we showed that the expected accuracy is less than 5 in the CIE L\*a\*b\* color difference unit within the color gamut of the standard colors, irrespective of the camera.

### **Characterization of Baked Color of Cookie, Toast and Chicken: A Model of Light-Colored Food**

Shuhe NOMURA, Hiroyuki IYOTA and Hideki SAKAI

*Proceedings of the 1st Asia Color Association Conference (ACA2013)*, pp. 252-255 (11-14 Dec. 2013, Thanyaburi, Thailand)

Producing delicious-looking food is one of the features required of cooking equipment. For optimizing the technical advantages of oven cooking, color changes of light-colored food during oven cooking were characterized based on time-series colorimetric data. Three types of food materials were used as samples: toast (sliced white bread), plain cookie, and raw chicken meat pate. The colorimetric data were measured in situ using an optical fiber and a spectrometer under various conditions, with two types of steam ovens. Prediction expressions for the chroma and lightness (quantitative attributes) history of the food surface during oven baking were developed. The profiles of changes in the chroma and lightness for each material and under each set of heating conditions were investigated using the measured data and calculated values. The profiles, prediction method, and "browning index" defined in this study can be applied for optimizing automatic oven operation using the preferences index.

### **A Study on Water Retention Control for a Humidity Sensor at High Temperature**

T. TSUJIOKA, H. IYOTA, M. OHMORI, M. TANAKA and H. KITAMURA

*Abstracts Book of Symposium on Temperature and Thermal Measurements in Industry and Science (TEMPMEKO 2013)*, p.408 (Oct. 2013, Funchal, Madeira, Portugal)

The authors develop a new prototype of the humidity sensor, using newly developed porous ceramic material for wet-bulb temperature measurement, having a heat resistance, with suitable porosity, formed into a cylindrical shape with a water supply hole. The water flow rate inside the hole is controlled by a pinch valve between a water tank and the sensor. The valve is opened and closed by a proposed water retention control algorithm. Suitable control algorithm is quite important, because excess water supply causes lowering the wet-bulb temperature, resulting in a decrease in measurement accuracy. The water retention control is based on two capacitance sensors; one is placed on the surface of the ceramic and the other is placed inside the ceramic, as moisture sensors. Excess supply of water can be detected by the first capacitance sensor on the surface, and short supply of water can be detected by the second surface capacitance sensor inside the ceramic. The authors implement the proposed water retention control algorithm to a microcontroller with valve motor drivers, thermocouple amplifiers and capacitance detection circuits. The microcontroller monitors moisture levels by the capacitance sensors and controls the pinch valve, for increasing reliability, for sustained long time measurement of humidity sensing at high temperature. Some experimental evaluations of the developed humidity sensor are also made in the conditions up to 200 degrees Celsius, from 0 to 100% humidity. The experimental results show the proposed water retention control is effective and suitable for long time measurement with high accuracy and high reliability.

### **Wide-Range Psychrometric Chart for Improved Utilization of Superheated Steam and Humid Air**

H. IYOTA, T. INOUE, J. YAMAGATA and T. TSUJIOKA

*Abstracts Book of Symposium on Temperature and Thermal Measurements in Industry and*

*Science(TEMPMEKO 2013)* , p.255 (Oct. 2013, Funchal, Madeira, Portugal)

We propose a wide-range psychrometric chart using the steam mole fraction as the vertical ordinate. Adiabatic saturated lines and the relationship among the wet-bulb, dry-bulb, and dew point temperatures of the humid air including superheated steam were figured on the proposed chart. In addition, we compared the theoretical adiabatic saturated temperatures with the experimentally measured wetted material temperatures. Wetted spherical gauze was used as a wet-bulb probe for measurements in the calibrating apparatus consisting of a boiler, an air blower, flow meters, and heaters, at temperatures ranging from 150 to 250°C, and the steam mole fraction ranging from 0.01 (approximately room air) to 1.0 (pure superheated steam). The results show that the steam mole fraction of the heating media including pure superheated steam can be predicted based on wetted-material temperature measurement using the proposed chart, the maximum error of the predicted value of the steam mole fraction was less than 0.09.

#### **Development of a Device That Uses Steam Condensation Heat to Disinfect Rice Seeds**

Takahiro NODA, Yasuyuki HIDAKA, Hiroyuki IYOTA, Toru NAKAMURA, Akihiko OCHI, Kazuhiko SAKAI, Toshiyuki MORIKAWA, Tetsuo YABU, Jun ISOTA, Shigeru HOSHINO and Tsutomu ARIE  
*Book of abstracts of the 11th Conference of the European Foundation for Plant Pathology*, p.88, (8-13 September 2014, Krakow, POLAND)

To increase efficiency and reduce costs associated with chemical-free, environment-friendly disinfection of rice seeds, we developed a device that uses steam condensation heat to disinfect rice seeds. Compared to the conventional aerated steam treatment, the high-temperature and short treatment administered using the device can be adjusted for rice seeds. To sterilize seed-borne pathogens that mainly exist around the husk layer and to not injure the rice kernel, which has organs necessary for seed germination, the device focused on surface heating by steam condensation. An optimum heating condition was designed by controlling the humidity of the heating media and regulating the heating time. Disinfection against rice seed-borne diseases caused by bacteria, fungi, and nematodes was evaluated under the optimal condition (maximum heating Without affecting germination). Under the optimal condition, this treatment was almost as effective as the conventional hot water treatment (60°C, 10 min). We observed that the artificial inoculation method to prepare infected seeds was greatly influenced by the extent of disinfection achieved using the physical seed treatments. In addition, heat tolerance of naturally infected and stunted seeds was lower than that of healthy seeds. We are currently developing a disinfection device for practical use on the basis of these findings.

#### **Influence of Spanwise Vorticity on Dissimilarity between Turbulent Momentum and Heat Transfer**

Kenji KATOH, Akira SAKAI, Ryouyusuke FUJII, Tatsuro WAKIMOTO and Genta KAWAHARA(Osaka Univ.).

*Trans. of Jpn Soc. Mech. Engrs., Ser. B*, Vol. 79, No. 806, pp. 2019-2029 (2013) (in Japanese)

The influence of transverse vorticity on the dissimilarity between turbulent heat flux and Reynolds stress was investigated by use of direct numerical simulation data for a channel flow. The theoretical relations regarding to Reynolds stress obtained from Lagrangian momentum equation shows that the correlation  $v(\partial p/\partial x)$  between wall-normal velocity  $v$  and streamwise pressure gradient fluctuation ( $\partial p/\partial x$ ) has an important effect on the dissimilarity. The correlation  $v(\partial p/\partial x)$  would be negative near the transverse clockwise vortex in the flow field because  $v$  and  $(\partial p/\partial x)$  have a different sign to each other around the vortex. The numerical results of turbulent flow and temperature field demonstrate a strong correlation between the strength of dissimilarity (difference between turbulent heat flux and Reynolds stress),  $-v(\partial p/\partial x)$  and the transverse clockwise vorticity. The dissimilarity would be mainly caused by the reduction of Reynolds stress near the vortex region, where the streamwise velocity fluctuation of fluid particle is accelerated (or decelerated) on the ejection (or sweep) side due to the pressure field around the vortex. The strength of dissimilarity increases remarkably where the ring-shaped vortex stands up from the wall and bends to the spanwise direction in the lag-law region.

#### **Experimental Investigation on the Effect of Accelerating Motion of Contact Line on the Dynamic Contact Angle**

Takahiro ITO(Nagoya Univ.), Shoji HIRUTA, Ryota SHIMURA(Toyohashi Univ. of Technology), Kenji KATOH, Tatsuro WAKIMOTO, Yasufumi YAMAMOTO(Kansai Univ.) and Susumu NODA(Toyohashi Univ. of Technology)

*Transaction of the JSME*, Vol. 80, No. 809, pp. 1-12 (2014) (in Japanese)

The dynamic contact angle, the angle between the surfaces of the liquid and the solid at a moving contact line, is one of the primary conditions for the dynamics of the liquid surface confined by solid wall. It has been commonly modeled as a function of the velocity of the contact line relative to the solid surface under

steady state condition. Some situations, such as the impact of a drop on a solid surface or sudden release of a contact line stuck on an edge of solid, however, involve a transient motion of the contact line, which would lead to a deviation of the dynamic contact angle from the steady one. In this study, dynamic contact angle for an accelerating or decelerating contact line advancing on glass surface is measured in two experimental systems different with other, i.e. one with a rapid meniscus formation after contact of a descending rod with the liquid surface, and the other with accelerating advance of liquid column in a circular tube. The experimental results revealed that the contact angle is increased with the (positive) acceleration of the contact line relative to the solid and vice versa. The critical condition for the appearance of the deviation of the contact angle brought with the acceleration is also discussed.

### **Modeling of the Dynamic Wetting Behavior in a Capillary Tube Considering the Macroscopic–Microscopic Contact Angle Relation and Generalized Navier Boundary Condition**

Yasufumi YAMAMOTO(Kansai Univ.), Katsunori TOKIEDA(Kansai Univ.), Tatsuro WAKIMOTO, Takahiro ITO (Nagoya Univ.) and Kenji KATOH

*International Journal of Multiphase Flow*, Vol. 59, pp. 106-112 (2014)

In this study, dynamic wetting phenomena in a capillary tube were studied by using numerical simulations based on the front-tracking method employing the generalized Navier boundary condition (GNBC) and by experimental measurements. For the GNBC, based on molecular dynamics simulations, the microscopic dynamic contact angle is estimated from the grid-scale contact angle using Cox's macroscopic–microscopic relation. The experimentally measured correlation between the apparent dynamic contact angle and the moving velocity of the contact line is well reproduced by the present simulation technique considering Cox's macroscopic–microscopic relation. Thus, we found that the dynamics of wetting are well described by combining molecular-scale behavior and macroscopic–microscopic relations.

### **Adhesive Force due to a Thin Liquid Film between Two Smooth Surfaces (Wringing Mechanism of Gage Blocks)**

Kenji KATOH and Tatsuro WAKIMOTO

*J. of JSEM*, Vol. 14, Special Issue, pp. 36-41 (2014)

It is well known as the wringing phenomenon of gage blocks that a strong adhesive force appears between two smooth surfaces when a thin liquid film is applied on the interface. A theoretical and experimental study is conducted to discuss the wringing mechanism. The liquid film may be separated into a large number of small puddles when two surfaces are rubbed together. One can expect a large adhesive force due to the resultant of surface tension acting on the circumference of each puddle. Numerical results for oil distribution between two surfaces show that the total perimeter length of liquid film reaches 10500 m on the surface of 3cm<sup>2</sup>, which leads to 1.0×10<sup>6</sup> (N/m<sup>2</sup>) for the adhesive force. The adhesive forces measured experimentally roughly agree with the theoretical value. A simple model is proposed to explain the adhesive force dependence on the velocity of pulling apart two surfaces.

### **A Study on Removal of Infinitesimal Particles on a Wall by High Speed Air Jet (Numerical Simulation of Hydrodynamic Removal Force)**

Sanghyeon SONG, Kazuhiko SOEMOTO(Shinko Co. Ltd.), Tatsuro WAKIMOTO, Kenji KATOH

*J. of JSEM*, Vol. 14, Special Issue, pp. 94-100 (2014)

A cleaning device equipped with a special nozzle containing triangular cavities is developed to add high-frequency turbulence to the impinging jet flow. In order to clarify the removal mechanism of fine particles adhered to a wall by van der Waals force, a numerical simulation is performed to estimate various removal forces acting on the particle. Here we examine the effect of the force due to a pressure gradient fluctuation of the impinging jet on removal performance. The numerical results show that viscous drag has the greatest influence, while the pressure gradient force is enhanced by the cavities and has a remarkable effect on the removal of particles larger than 1.5 μm. The numerical results qualitatively correspond to the tendency of measured removal rates for 1.6 μm particles.

### **A study on the Removal of Infinitesimal Particles on a Wall by High-Speed Air Jet—Measurements of Adhesive Force and Particle Removal Rate—**

Kenji KATOH, Sanghyeon SONG, Tatsuro WAKIMOTO and Kazuhiko SOEMOTO

*Journal of Fluid Science and Technology*, Vol. 9, No. 3, 13pages (2014)

We investigated the mechanism for the removal of fine particles from a solid wall using a high-speed impinging air jet. In general, it is difficult to remove fine particles of the order of micrometers by the

impingement of simple air flow because they strongly adhere to the surface by van der Waals forces and remain immersed in the viscous sublayer. To overcome this, we developed high-speed air jet nozzles with triangular cavities that add strong velocity and pressure fluctuations to the high-speed air flow. The experimental results showed that the cavity nozzle enhances the removal performance for particles larger than 1  $\mu\text{m}$ . The effect of the pressure fluctuation induced in the jet flow on the removal performance is discussed from the experimental results. First, the adhesive force was measured experimentally from the centrifugal force acting on particles with 5–25  $\mu\text{m}$  diameters set on a rotating disk. Based on a simple theoretical consideration regarding the balance of moments acting on a particle, we estimated the effects of hydrodynamic removal forces such as drag, lift, and pressure gradient fluctuation against measured adhesive forces. The theoretical estimation showed that drag plays a major role, and the force of the pressure gradient could be effective for the removal of large particles. The proposed model is able to explain the experimental results indicating that the removal rates for 3- $\mu\text{m}$ -sized particles are improved by the air flow velocity fluctuations generated by the cavity nozzle.

### **Effects of Surface Contamination and Cleaning with Hypochlorite Wipes on the Antibacterial Activity of Copper-Alloyed Antibacterial Stainless Steel**

H. KAWAKAMI, T. HAYASHI, H. NISHIKUBO, A. MORIKAWA, S. SUZUKI (Nisshin Steel Co., Ltd.), Y. SATO and Y. KIKUCHI

*Biocontrol Sci.*, Vol. 19, pp. 73-78 (2014)

Effects of surface contamination and cleaning with hypochlorite wipes on the antibacterial activity of copper-alloyed stainless steel were studied. The antibacterial activity of copper alloyed stainless steel decreased with the increase in the amount of surface contaminant, and the bacterial counts from specimens contaminated with a contaminant, e.g.  $1.6 \times 10^{-2} \mu\text{g}/\text{mm}^2$  of bovine serum albumin, were not significantly different from those from ordinary stainless steel specimens. The once contaminated surface could regain its antibacterial activity when it was sufficiently wiped clean with sterile wipes loaded with sodium hypochlorite solution.

### **Antimicrobiability of Cu Contained Stainless Steels**

S. SUZUKI (Nisshin Steel Co., Ltd.) , K. MIYAKUSU (Nisshin Steel Co., Ltd.) , Y. SATO, Y. KIKUCHI and H. KAWAKAMI

*Tetsu-to-Hagané*, Vol. 100, pp. 1021-1028 (2014) (in Japanese)

Antimicrobial ability of Cu contained stainless steels was investigated. Antimicrobial ability increased with elute fraction of Cu ion from stainless steel surface into antimicrobial test medium. It is necessary to promote eluting fraction of Cu ion, that is, to achieve giving antimicrobial ability to Cu contained stainless steel that sub-micron order or larger size  $\epsilon$ -Cu phases are dispersed in stainless steel, surface of stainless steel has high electrode potential and dissolved oxygen exist in the test medium.

### **Position Estimation of Small Robotic Fish Based on Camera Information and Gyro Sensors**

Yogo TAKADA, Keisuke KOYAMA and Takahiro USAMI

*Robotics*, Vol. 3, Issue 2, pp.149-162 (2014)

Robotic fish are ideal for surveying fish resources and performing underwater structural inspections. If a robot is sufficiently fishlike in appearance and does not use a screw propeller, real fish will not be easily surprised by it. However, it is comparatively difficult for such a robot to determine its own position in water. Radio signals, such as those used by GPS, cannot be easily received. Moreover, sound ranging is impractical because of the presence of rocks and waterweed in places where fish spend a lot of time. For practical applications such as photographing fish, a robotic fish needs to follow the target fish without losing awareness of its own position, in order to be able to swim autonomously. We have developed a robotic fish named FOCUS (FPGA Offline Control Underwater Searcher) which is equipped with two CMOS cameras and a field-programmable gate array (FPGA) circuit board for data processing. The forward-facing camera is used to track red objects, since this is the color of the fish of interest. In addition, using visual information obtained with the bottom-facing camera, the robot can estimate its present position. This is achieved by performing real-time digital image correlation using the FPGA. However, until now, the position estimation accuracy has been poor due to the influence of yaw and roll. In the present study, the position estimation method has been greatly improved by taking into account the yaw and roll values measured using gyro sensors.

### **Robotic Fish**

Yogo TAKADA, Keisuke KOYAMA and Takahiro USAMI

*Journal of Robotics and Mechatronics*, Vol. 26, No.3, Development Report, pp.391-393 (2014)

Based on our robotic fish studies since 2003, this paper introduces a FPGA offline control underwater searcher (FOCUS) and a bream robot equipped with advanced mechanism (BREAM). The performance of the first FOCUS prototype, built in 2011, is now being improved. FOCUS has 2 cameras and field-programmable gate arrays (FPGAs) with high arithmetic processing capabilities. The appearance of the FOCUS is so cute. The two FOCUS types now available are an autonomous underwater vehicle (AUV) and a remotely operated vehicle (ROV). BREAM, in contrast, is an entertainment robot prototype designed for Asutamuland Tokushima exhibition. BREAM has four joints based on analytical computational fluid dynamics (CFD) results showing that robotic fish with multiple joints achieve better propulsion performance than that with single joint. Two of the four joints are used for propulsion and two are used for turning the prototype. RC-FOCUS is also exhibited at Asutamuland Tokushima, together with BREAM.

### **Improving Accuracy of Acoustic Source Localization in Anisotropic Plates**

Hayato NAKATANI, Tribikram KUNDU and Nobuo TAKEDA

*Ultrasonics*, Vol. 54, No. 7, pp. 1776-1788 (2014)

The acoustic source localization technique for anisotropic plates proposed by the authors in an earlier publication (Kundu et al., *Ultrasonics*, 52, pp.740-746, 2012) is improved in this paper by adopting some modifications. The improvements are experimentally verified on anisotropic flat and curved composite plates. Difficulties associated with the original technique were first investigated before making any modification. It was noted that the accuracy of this technique depends strongly on the accuracy of the measured time difference of arrivals (TDOA) at different receiving sensors placed in close proximity in a sensor cluster. The sensor cluster is needed to obtain the direction of the acoustic source without knowing the material properties of the plate. Two modifications are proposed to obtain the accurate TDOA. The first one is to replace the recorded full time histories by only their initial parts – the first dip and peak – for the subsequent signal processing. The second modification is to place the sensors in the sensor cluster as close as possible. It is shown that the predictions are improved significantly with these modifications. These modifications are then applied to another sensor cluster based technique called the beamforming technique, to see if similar improvements are achieved for that technique also with these modifications.

### **Mechanical Properties in Quasi-Isotropic CFRP Laminates with Small Ply Orientation Angle Mismatch**

Hayato NAKATANI, Nurul Nabihah A. HAMID and Shinji OGIHARA

*Proc. of the Japan International SAMPE Symposium and Exhibition (JISSE-13)*, Nagoya, Japan, Nov. 11-13, paper No. 1401 (USB Memory) (2013)

Mechanical properties and damage behaviour are evaluated for the quasi-isotropic (QI) laminates with fibre orientation angle mismatch of 15° (15QI) and the conventional QI laminates with 45° mismatch (45QI) made by using thin prepregs under in-plane tensile, out-of-plane indentation and impact loading. Compared to the direction dependent tensile strength of the 45QI, the 15QI laminates show nearly isotropic tensile strength because fibre strength effectively contributes to the tensile strength under suppressed delamination which is due to the low interlaminar shear stress derived by small fibre mismatch and suppressed matrix cracking achieved by the thin ply. Localized damage has been exhibited in the 15QI laminates under out-of-plane indentation and drop-weight impact, however absorbed energy during the impact event is comparable between the 15QI and the conventional 45QI laminates. The isotropy in tensile strength and the localized damage under out-of-plane loading achieved by the QI laminates with small fibre orientation mismatch can offer us a large variety of structural designs of composites.

### **Effect of Distribution Media on Resin Flow during VaRTM Process for FRPs**

Hayato NAKATANI, Kentarou ADACHI and Katsuhiko OSAKA

*Proc. of the 16<sup>th</sup> U.S.-Japan Conference on Composites Materials*, San Diego, CA, USA, Sep. 8-10, Paper No. 726 (CD-ROM 12-pp.) (2014)

Multipoint measurements for resin flow during vacuum assisted resin transfer molding (VaRTM) process for fibre reinforced polymer composites are carried out by using embedded fibre optic sensors. These sensors monitor changes in intensity of Fresnel reflected light at the end of optical fibres due to the arrivals of resin. The resin flow in fibre preform is divided into two main flows; one is in-plane flow where resin proceeds in fibre preform directly from resin inlet, and the other is out-of-plane flow where resin is infused into fibre

preform in through-thickness direction via a distribution medium that is incorporated into the preform as a surface layer. By simultaneously infusing epoxy resin into two glass fibre preforms with or without a distribution medium that are separated by a plastic film and stacked together, time of arrivals of the resin flow in each fibre preform are obtained from output changes of fibre optic sensors. Flow rate of resin in each preform is calculated from the time difference of arrivals. The flow rate in the preform with the distribution medium is related to resin amount impregnated both in in-plane and out-of-plane flow in contrast to only in in-plane flow for that without the medium. By subtracting the resin amount infused only through in-plane flow from that contains two flows, the amount from the out-of-plane flow can be evaluated. Ratio of impregnated resin amount through out-of-plane / in-plane flow is also calculated at different measured regions. As a result, the out-of-plane flow via the distribution medium is found to be dominant especially at outlet side of the resin flow. Further investigations using multiple distribution media are also carried out.

### **Impact Induced Damage in CFRP / Thin Titanium Films Hybrid Laminates**

Hayato NAKATANI, Yuhei NEKOSHIMA and Shinji OGIHARA

*Proc. of the 11<sup>th</sup> International Conference on Durability Analysis of Composite Systems (DURACOSYS-2014)*, Tokyo, Japan, Sep. 15-17, Paper No. Or07 (USB memory), (2014)

Fibre-metal laminates (FMLs) that consist of carbon / epoxy composites and thin titanium films are subjected to drop-weight impact to assess their improved damage tolerance ability compared to that of conventional carbon / epoxy composite laminates. The thin titanium films 50  $\mu\text{m}$  in thickness used here are expected to not show their strength but suppress damage propagation in the composites by their existence during the impact loading. Hence volume fraction of metal layer in the hybrid laminates is suggested to be less than 10 %. The low velocity impact tests are conducted for the CFRP / thin titanium films hybrid laminates [45/0/Ti/-45/90]<sub>2S</sub> using a drop-weight tower under impact energy of 4, 6, 8, 10, 14 and 16 J/mm. The maximum load during the impact event increases linearly with applied impact energy before they reach a plateau with more than 10 J/mm of impact energy. Higher level of the plateau for the hybrid laminates compared to the CFRP laminates indicates their excellent load capacity without suffering severe damage. By cross-sectional observation, crack propagation in the hybrid laminates is found to be suppressed by the titanium films as opposed to the through-thickness cracking in the CFRP laminates. It is also shown that lower densities of matrix cracking and fibre breakage are achieved for the hybrid laminates. Interfacial delamination between CFRP plies and titanium films is considered to absorb the impact energy, this results in damage suppression in CFRP plies.

### **Effects of Initial Stresses on Piezoelectric Properties of PZT Disks Analyzed by Nonlinear Electroelastic Theory**

Naoki TAKAI, Shinya MOTOGI and Tomohiro YAMASAKI

*Trans. Jpn. Soc. Mech. Eng., Ser. A*, Vol.79, No.807, pp.1632-1647 (2013)(in Japanese)

The effects of applied stresses on dynamic characteristics of piezoelectric ceramics are analyzed based on the nonlinear electroelastic theory. Piezoelectric ceramics are used in many electric devices as functional elements, where mechanical constraint is usually applied. Estimation of piezoelectric properties under applied stresses is important in designing the devices. However, applied stresses cannot be considered in the basic equations in the linear piezoelectric theory, and the effects of the applied stresses cannot be predicted. In this study, we introduce additional terms related to the dissipation effects, specifically, electric conduction and internal viscosity resistance, and nonlinearity of elastic properties into electroelastic theory. As well, considered nonlinear effects are elastic, piezoelectric and dielectric constants up to 3rd order. Frequency dependence of admittance of PZT disks is measured under applied compressions, showing that applied stresses have certain influences on either of thickness and radial vibrations of PZT. Assuming proper material constants, experimental results can be well explained by the nonlinear electroelastic theory.

### **Relationship between Composition Gradient and Microhardness in Ni-Cu Alloy Films Fabricated by Electrodeposition**

Y. KANEKO and K. UEMORI

*Functionally Graded Mater.*, Vol. 27 pp.50-56 (2013)

Vickers microhardness of composition-gradient Ni-Cu alloy films having different gradients was measured. The composition-gradient films were fabricated by electrodeposition technique. Since content of electrodeposited Ni-Cu alloy depends on applied electrochemical potential, production of the composition-gradient microstructure is achieved by changing the potential continuously. By stacking the composition-gradient layers with positive and negative gradients alternately, we obtained relatively thick

Ni-Cu films having high composition gradient. In the present study, two kinds of the Ni-Cu films with the gradients  $dc/dx$  of  $3 \times 10^{-3} \text{nm}^{-1}$  and  $1.2 \times 10^{-2} \text{nm}^{-1}$  were prepared. Vickers microhardnesses of the films with  $dc/dx=3 \times 10^{-3} \text{nm}^{-1}$  and  $1.2 \times 10^{-2} \text{nm}^{-1}$  were Hv167 and Hv277, respectively. To understand the increase in the hardness, we estimated misfit dislocation density from the values of the composition gradients. In the three-dimensional dislocation model, the dislocation densities of these films were estimated to be  $6.1 \times 10^{14} \text{m}^{-2}$  and  $2.4 \times 10^{15} \text{m}^{-2}$ . These dislocation densities are consistent with the hardness values, assuming that strength of the composition-gradient Ni-Cu films owes to dislocation hardening.

### **EBSD Analysis of Microstructure Evolution of Pure Iron Subjected to Sliding Wear and Related Change in Vickers Microhardness**

Y. KANEKO and T. SUGIMOTO

*Mater.Trans.*, Vol.55, pp. 85-92 (2014)

Sliding wear tests were carried on pure iron to investigate evolution of microstructure below worn surface. After the wear tests, grain boundary formation and lattice rotation were analyzed with electron backscatter diffraction (EBSD) method. In the vicinity of the worn surface, submicron grains separated by high-angle grain boundaries were generated. Below the submicron grain region, dominant microstructures were two kinds of low-angle grain boundaries which were horizontal and inclined to the worn surface, respectively. At deeper area from the worn surface, continuous lattice rotation was detected. To correlate the microstructure and strength, Vickers microhardness was measured over a cross section of the wear-affected zone. In the submicron grain and the low-angle grain boundary regions, the microhardness was proportional to the reciprocal square root of boundary spacing. In the lattice rotation region, we calculated geometrically-necessary (GN) dislocation density from gradient of lattice rotation. The microhardness value in the lattice rotation region showed good correlation with the square root of the GN dislocation density.

### **Low-Cycle Fatigue of Fe-20%Cr Alloy Processed by Equal-Channel Angular Pressing**

Y. KANEKO, R. TOMITA and A. VINOGRADOV

*IOP Conf. Series: Mater.Sci.Eng.*, Vol. 63, pp.012160 (2014)

Low-cycle fatigue properties were investigated on Fe-20%Cr ferritic stainless steel processed by equal channel angular pressing (ECAP). The Fe-20%Cr alloy bullets were processed for one to four passes via Route-Bc. The ECAPed samples were cyclically deformed at the constant plastic strain amplitude  $\epsilon_{p1}$  of  $5 \times 10^{-4}$  at room temperature in air. After the 1-pass ECAP, low-angle grain boundaries were dominantly formed. During the low-cycle fatigue test, the 1-pass sample revealed the rapid softening which continued until fatigue fracture. Fatigue life of the 1-pass sample was shorter than that of a coarse-grained sample. After the 4-pass ECAP, the average grain size reduced down to about 1.5  $\mu\text{m}$ . At initial stage of the low-cycle fatigue tests, the stress amplitude increased with increasing ECAP passes. At the samples processed for more than 2 passes, the cyclic softening was relatively moderate. It was found that fatigue life of the ECAPed Fe-20%Cr alloy excepting the 1-pass sample was improved as compared to the coarse-grained sample, even under the strain controlled fatigue condition.

### **Micro-, Meso- to Macroscopic Modeling of Deformation Behavior of Semi-Crystalline Polymer**

M. UCHIDA and N. TADA

*Int. J. Plasticity*, Vol. 49, pp. 164-184 (2013)

To represent the elasto-viscoplastic deformation behavior of semi-crystalline polymer (SCP), which has a complicated hierarchical structure, a micro-, meso- to macroscopic computational model was developed. A laminar composite model and FE-based homogenization method were used to relate the mechanical behaviors in micro- to mesoscopic and meso- to macroscopic scales of the material. Using the proposed model, elasto-viscoplastic deformation behaviors of high density polyethylene under several macroscopic boundary conditions were computationally investigated. Material's parameters used in the constitutive equations for microstructure of SCP were defined by fitting the calculated stress-strain relation into the experimental data. Then, the effects of deformation mode and crystallinity on deformation behavior of SCP were investigated. Obtained stress-strain relations represented the experimentally observed characteristics such as an anisotropic strain hardening rate depending on the deformation mode and an increase in the Young's modulus and the flow stress with the crystallinity. Then, the neck propagation process in the uniaxial tension with different strain rate was investigated. The present model represented a development of macroscopic non-uniform deformation characterized by the mechanical response of micro- to mesoscopic deformation.

## **Establishment of Deformation Simulation Procedure by Finite Element Method Based on Second-Order Homogenization Using Characteristic Displacement Function for Macroscopic Strain Gradient**

M. UCHIDA and N. TADA

*Trans. Jpn. Soc. Mech. Eng., Ser. A*, Vol.79, No.806, pp. 1486-1503 (2013)

To evaluate effect of a relative scale of microstructure to macrostructure, a simulation procedure using second-order homogenization based finite element method was proposed. In this method, a microscopic characteristic displacement function for macroscopic strain gradient was added to the conventional first order homogenization method. Then, a procedure to solve a macroscopic boundary problem was established based on the principle of virtual work in macroscopic scale represented by the microscopic characteristic displacement function. To validate the proposed second-order homogenization method, computational simulations of deformation behavior of cavitated rubber (void) blended amorphous polymer were performed using the proposed second-order homogenization. From the result of bending deformation where tension or compression was given to upper side or lower side of the macroscopic model, the material containing larger void required a larger energy for the bending of the model. With decrease in the void size, the energy converged to that predicted by first-order homogenization method. Basically, the deformation behavior predicted by proposed homogenization model was qualitatively and quantitatively similar to that predicted by full scale model. The proposed model is expected to be applied for computational prediction of the scale-dependent deformation in various cases because the model does not limit the form of constitutive equation, shape of the unit cell and deformation mechanisms and structure of the material.

## **Non-Destructive Detection of Crack in HDPE Plate by Nanometric Change in Surface Profile**

N. TADA, M. UCHIDA and Y. MATSUKAWA

*Proc. ASME PVP2013*, pp. PVP2013-97732 (2013)

When a mechanical load is given to a cracked material, an undulation appears in surface profile around the crack. The undulation is caused by stress-strain concentration at the crack tip and its release near the crack center. If the load is very small and within the elastic deformation range, the material recovers the original shape after unloading and no damage remains. Therefore, this surface undulation by a small mechanical load can be used for detection of crack on the material surface. In this study, non-destructive crack detection method by nanometric change in surface profile is proposed, and the experiment and related finite element analyses were carried out for notched high-density polyethylene (HDPE) plates. Nonuniform height change by a small mechanical load around the notch on the surface of HDPE plate was measured by a laser scanning microscope. The height change distribution agreed with the analytical result.

## **Thermodynamic Analysis using First-Principles Calculations of Phases and Structures of $\text{Li}_x\text{Ni}_{0.5}\text{Mn}_{1.5}\text{O}_4$ ( $0 \leq x \leq 1$ )**

Ippei KISHIDA, Kengo ORITA, Atsutomu NAKAMURA and Yoshiyuki YOKOGAWA

*Journal of Power Sources*, Vol. 241, pp. 1-5 (2013)

$\text{LiNi}_{0.5}\text{Mn}_{1.5}\text{O}_4$ , which has a spinel framework structure, is a promising candidate for the cathode material of next-generation lithium-ion batteries with high energy density. We investigate the structural transition in  $\text{Li}_x\text{Ni}_{0.5}\text{Mn}_{1.5}\text{O}_4$  ( $0 \leq x \leq 1$ ) through first-principles calculations using the projector augmented wave method with the generalized gradient approximation. We calculate all the unique Li-site occupation configurations in a unit cell to obtain the total energies and the most stable structures for various compositions. Thermodynamic analysis shows that  $\text{Li}_{0.5}\text{Ni}_{0.5}\text{Mn}_{1.5}\text{O}_4$  with  $x=0.5$  is the only stable phase for  $0 < x < 1$ . The decomposition energy is lower than 0.1 eV for  $0 < x < 0.5$ , but is distinctly higher for  $0.5 < x < 1$ . The decomposition energy reaches 0.39 eV at  $x=0.75$ . The ratios of the structures at room temperature are calculated from Boltzmann factors by using the energy differences between structures. The crystal structure of the unit cell changes gradually from  $x = 0$  to 0.5, but changes markedly from  $x = 0.5$  to 1. This first-principles study provides a general evaluation of the variation in the crystal structure with the composition of the bulk material, which affects the cyclability of the electrode.

**Backward Uniqueness for Heat Equations with Coefficients of Bounded Variation in Time**

Shigeo TARAMA

*Electron. J. Diff. Equ.*, Vol. 2013, No. 189, pp. 1-14 (2013)

We consider heat equations with bounded coefficients satisfying Lipschitz condition with respect to space variables. We show, by using Carleman estimates, the backward uniqueness under the condition that coefficients are of bounded variation in the time variable, where we consider coefficients as functions of the time variable with values in the space of uniformly bounded continuous functions of space variables.

*Applied Physics and Electronics*

**Effects of thermal annealing process on the electrical properties of p<sup>+</sup>-Si/n-SiC heterojunctions**

J. LIANG, S. NISHIDA, M. ARAI (New Japan Radio Co. Ltd.), and N. SHIGEKAWA

*Appl. Phys. Lett.*, 104, 161604 [4 pages] (2014).

The effects of thermal annealing process on the interface in p<sup>+</sup>-Si/n-SiC heterojunctions fabricated by using surface-activated bonding are investigated. It is found by measuring their current-voltage (I-V) characteristics that the reverse-bias current and the ideality factor decreased to  $2.98 \times 10^6$  mA/cm<sup>2</sup> and 1.03, respectively, by annealing the junctions at 1000 °C. Observation by using transmission electron microscopy indicates that an amorphous layer with a thickness of ~6 nm is formed at the unannealed interface, which vanishes after annealing at 1000 °C. No structural defects at the interface are observed even after annealing at such a high temperature.

**Fabrication of nitride/Si tandem cell structures with low environmental burden by surface activated bonding**

N. SHIGEKAWA, J. LIANG, N. WATANABE (NTT Photonics Laboratories), and A. YAMAMOTO (Univ. of Fukui)

*Phys. Status Solidi C*, 11, No. 3–4, pp. 644–647 (2014).

Group-III nitride on Si tandem solar cell structures, which are free from materials with high impacts on the environment such as group-III arsenides or phosphides, were successfully fabricated using the surface activated bonding of nitride-based sub cells, which had been grown on (0001) GaN substrates, and (111) Si based sub cells. The backsides of the GaN substrates had been polished and their averaged roughness was smaller than 1 nm prior to bonding. The open-circuit voltage ( $V_{OC}$ ) of the tandem cells was almost equal to the sum of  $V_{OC}$  of the respective sub cells, while the conversion efficiency was limited by the properties of the nitride-based top cells. Nitride-on-(100) Si tandem cells were also fabricated and the enhancement in  $V_{OC}$  was observed.

**I-V characteristics in Surface-Activated Bonding (SAB) based Si/SiC junctions at raised ambient temperatures**

S. NISHIDA, J. LIANG, M. MORIMOTO, N. SHIGEKAWA, and M. ARAI (New Japan Radio Co., Ltd.)

*Materials Science Forum*, 778-780, pp. 718-721 (2014).

The physical and electrical properties of p<sup>+</sup>-Si/n-4H-SiC and n<sup>+</sup>-Si/n-4H-SiC heterojunctions fabricated by using surface-activated bonding (SAB) were investigated by scanning electron microscopy (SEM), current-voltage (I-V) and breakdown characteristics measurements at raised ambient temperatures. The I-V characteristics for the reverse bias voltages of the two junctions were compared with the expectations based on Frenkel-Poole, and trap-assisted tunneling models. The results of calculations using the trap-assisted tunneling model were close to the measurements.

**Surface-activated-bonding-based InGaP-on-Si double-junction cells**

N. SHIGEKAWA, M. MORIMOTO, S. NISHIDA, and J. LIANG

*Jpn. J. Appl. Phys.*, 53, 04ER05 [4 pages] (2014).

InGaP-on-Si double-junction cells were fabricated by the surface activated bonding of InGaP-based top cell layers grown on GaAs substrates to Si-based bottom cells and the selective etching of GaAs substrates. The open-circuit voltage of the double-junction cells in the tandem operation was close to the sum of the open-circuit voltages of the top and bottom cells. The efficiency in the tandem operation of the n-on-p InGaP/(100)-Si double-junction cells was higher than the efficiencies of the respective subcells.

**Demonstration of Nitride-on-Phosphide Hybrid Tandem Solar Cells by Using Surface-Activated Bonding**

N. SHIGEKAWA, J. LIANG, and N. WATANABE (NTT Photonics Laboratories)

*Proc. 39th IEEE Photovoltaic Specialists Conference*, pp. 2470-2473 (2013).

Group-III nitride-on-phosphide hybrid tandem solar cells were fabricated using surface-activated bonding. The bottom surface of nitride top cells grown on GaN substrates was bonded on the top surface of InGaP-based bottom cells grown on n-GaAs substrates. Their tandem-cell operation was successfully demonstrated by confirming that the open-circuit voltage ( $V_{OC}$ ) of tandem cells was enhanced. It was also found that the electrical properties of the bonding interface do not induce fatal effects on the performance of the tandem cells.

**Phase separation of thick (>1 μm) In<sub>x</sub>Ga<sub>1-x</sub>N (x > 0.3) grown on AlN/Si(111): Simultaneous emergence of**

### **metallic In–Ga and GaN-rich InGaN**

A. YAMAMOTO (Univ. of Fukui), Md. T. HASAN (Univ. of Fukui), A. MIHARA (Univ. of Fukui), N. NARITA (Univ. of Fukui), N. SHIGEKAWA, and M. KUZUHARA (Univ. of Fukui)

*Appl. Phys. Express*, 7, 035502 [4 pages] (2014).

0.3–2- $\mu\text{m}$ -thick  $\text{In}_x\text{Ga}_{1-x}\text{N}$  ( $x > 0.3$ ) films are grown at 650 °C on AlN/Si(111) substrates by metal organic vapor phase epitaxy. When the thickness of an epitaxial InGaN film exceeds  $>1 \mu\text{m}$ , peaks of GaN-rich InGaN(0002) and metallic In(101) appear in the X-ray diffraction profiles. The InN composition  $>0.03$  in the GaN-rich InGaN film is in agreement with the solubility of InN in GaN at 650 °C. The metallic In contains a small amount ( $>0.03$  at. %) of Ga. These results clearly show that the epitaxial InGaN film is phase-separated into GaN-rich and InN-rich InGaN. The latter is changed into metallic In–Ga owing to its thermal instability at 650 °C.

### **Output characteristics of piezoelectric lead zirconate titanate detector using high-energy heavy-ion beam**

S. TAKECHI, M. SEKIGUCHI, T. MIYACHI (Chiba Institute of Technology), M. KOBAYASHI (Chiba Institute of Technology), M. HATTORI (Tokyo Institute of Technology), O. OKUDAIRA (JAXA), H. SHIBATA (Osaka University), M. FUJII (Famscience), N. OKADA (Honda Electronics), T. MURAKAMI (NIRS), and Y. UCHIHORI (NIRS)

*Nucl. Instrum. Methods Phys. Res., Sect. A* Vol. 737, pp. 52-55 (2014).

A radiation detector fabricated using piezoelectric lead zirconate titanate (PZT) has been studied by irradiating it with a 400 MeV/n xenon (Xe) beam. The beam diameter was controlled to change the irradiation conditions. It was found that the magnitude of the output observed from the PZT detector may be related to the number of Xe ions per unit area per unit time within the limits of the experimental conditions.

### **Variation in resonant frequency of piezoelectric lead–zirconate–titanate element undergoing high-level radiation**

M. KOBAYASHI (Chiba Institute of Technology), T. MIYACHI (Chiba Institute of Technology), S. TAKECHI, T. MITSUHASHI, Y. MIURA, H. SHIBATA (Osaka University), N. OKADA (Honda Electronics), M. HATTORI (Tokyo Institute of Technology), O. OKUDAIRA (JAXA), M. FUJII (Famscience), T. MURAKAMI (NIRS), and Y. UCHIHORI (NIRS)

*Jpn. J. Appl. Phys.* Vol. 53, 066602 (6 pages) (2014).

A piezoelectric lead–zirconate–titanate (PZT) element was exposed to a 400MeV/n xenon beam and the radiation effect on the element was studied as a variation of resonant and antiresonant frequencies by the resonance method. A possible effect of heating the element on the resonant frequency was avoided by using data obtained while the temperature of the element was kept constant. Consequently, the variation of the resonant frequency was empirically represented by a simple function of the amount of accumulated energy in the element. We therefore discuss the piezoelectric PZT element as a potential detector for high-level radiation. We point out that a piezoelectric equation including the heat term is required to explain the experimental results.

### **Effects of annealing on GaAs/Si bonding interfaces for hybrid tandem solar cells**

L. CHAI, J. LIANG, S. NISHIDA, M. MORIMOTO, and N. SHIGEKAWA

*Abstract of 2014 IEEE International Workshop on Low Temperature Bonding for 3D Integration*, p. 51 (2014).

DOI: 10.1109/LTB-3D.2014.6886190

Effects of annealing on bonding interfaces of III–V-on-Si hybrid tandem solar cells were investigated. We observed amorphous layer at the interfaces prior to the annealing. We also investigated the effects of the annealing on the current-voltage characteristics of  $n^+$ -GaAs/ $n^{++}$ -Si and  $p^+$ -GaAs/ $n^{++}$ -Si junctions.

### **Annealing temperature dependence of SAB based Si/Si junctions**

M. MORIMOTO, J. LIANG, S. NISHIDA, L. CHAI, K. TAKEMURA, AND N. SHIGEKAWA

*Abstract of 2014 IEEE International Workshop on Low Temperature Bonding for 3D Integration*, p. 52 (2014).

DOI: 10.1109/LTB-3D.2014.6886191

Effects of annealing on SAB based Si/Si junctions were investigated by TEM observation and current-voltage (I–V) measurement. We observed amorphous like layer at the Si/Si interface prior to the annealing, which seemed to vanish after the annealing at 1000 °C. The I–V characteristics of Si/Si junctions showed that the current decreased when the junctions were annealed at comparatively lower temperatures. The current increased when the junctions were annealed at higher temperatures.

### **Investigation on the effects of annealing process on the electrical properties of $n^+$ -Si/n-SiC junctions**

J. LIANG, S. NISHIDA, T. HAYASHI, M. MORIMOTO, N. SHIGEKAWA, AND M. ARAI (New Japan Radio

Co., Ltd.)

*Abstract of 2014 IEEE International Workshop on Low Temperature Bonding for 3D Integration*, p. 53 (2014). DOI: 10.1109/LTB-3D.2014.6886192

The effects of annealing process on the electrical properties of  $n^+$ -Si/n-SiC junctions fabricated by using surface-activated bonding are investigated. It is found by measuring their current-voltage (I-V) characteristics that the reverse-bias current decreases and activation energy increases with increasing annealing temperature to 700 °C.

#### **Annealing characteristics of $p^+$ -Si/n-4H-SiC junctions by using surface-activated bonding**

S. NISHIDA, J. LIANG, T. HAYASHI, M. MORIMOTO, N. SHIGEKAWA, and M. ARAI (New Japan Radio Co., Ltd.)

*Abstract of 2014 IEEE International Workshop on Low Temperature Bonding for 3D Integration*, p. 54 (2014). DOI: 10.1109/LTB-3D.2014.6886193

The effects of annealing on  $p^+$ -Si/n-4H-SiC heterojunctions fabricated by using surface-activated bonding (SAB) were investigated by current-voltage (I-V) and capacitance-voltage (C-V) measurements. I-V characteristics were improved and the flat-band voltages extracted from C-V characteristics were smaller by annealing at higher temperatures.

#### **Fabrication and characterization of Si/~10- $\mu$ m mesa-etched Si junctions by surface activated bonding**

K. TAKEMURA, M. MORIMOTO, S. NISHIDA, J. LIANG, and N. SHIGEKAWA

*Extended Abstract of 2014 IEEE International Meeting for Future of Electron Devices, Kansai (IMFEDK)* [2 pages] (2014), DOI: 10.1109/IMFEDK.2014.6867078

Si/mesa-etched Si p-n junction was fabricated by the reactive ion etching and the surface activated bonding. The SEM observation of their cross section indicated that the height of the mesa was approximately 13  $\mu$ m. Their capacitance-voltage and current-voltage characteristics were also measured.

#### **Improvement in electrical properties in SAB-based $n^+$ -Si/n-4H-SiC junctions by annealing**

T. HAYASHI, J. LIANG, S. NISHIDA, M. MORIMOTO, N. SHIGEKAWA, and M. ARAI (New Japan Radio Co., Ltd.)

*Extended Abstract of 2014 IEEE International Meeting for Future of Electron Devices, Kansai (IMFEDK)* [2 pages] (2014), DOI: 10.1109/IMFEDK.2014.6867070

The effects of annealing on  $n^+$ -Si/n-4H-SiC junctions made by the surface activated bonding were investigated. Both the forward and reverse characteristics were improved by annealing at higher temperatures.

#### **Electrical properties of Si/Si interfaces by using surface-activated bonding**

J. LIANG, T. MIYAZAKI, M. MORIMOTO, S. NISHIDA, and N. SHIGEKAWA

*J. Appl. Phys.* Vol.114, 183703 [6 pages] (2013).

Electrical properties of  $n$ -Si/n-Si,  $p$ -Si/n-Si, and  $p^-$ -Si/ $n^+$ -Si junctions fabricated by using surface-activated-bonding are investigated. The transmission electron microscopy/energy dispersive X-ray spectroscopy of the  $n$ -Si/n-Si interfaces reveals no evidence of oxide layers at the interfaces. From the current-voltage (I-V) and the capacitance-voltage (C-V) characteristics of the  $p$ -Si/n-Si and  $p^-$ -Si/ $n^+$ -Si junctions, it is found that the interface states, likely to have formed due to the surface activation process using Ar plasma, have a more marked impact on the electrical properties of the  $p$ -Si/n-Si junctions. An analysis of the temperature dependence of the I-V characteristics indicates that the properties of carrier transport across the bonding interfaces for reverse-bias voltages in the  $p$ -Si/n-Si and  $p^-$ -Si/ $n^+$ -Si junctions can be explained using the trap-assisted-tunneling and Frenkel-Poole models, respectively.

#### **Band structures of Si/InGaP heterojunctions by using surface activated bonding**

J. LIANG, M. MORIMOTO, S. NISHIDA, and N. SHIGEKAWA

*Phys. Status Solidi C* Vol. 10, No. 11, pp. 1644–1647 (2013).

The band structure of  $p$ -Si/n-InGaP heterojunctions fabricated by using surface-activated bonding (SAB) was investigated by measuring their current-voltage (I-V) and capacitance-voltage (C-V) characteristics. The I-V characteristics of  $p$ -Si/n-InGaP junctions showed rectifying properties similarly to  $p$ -Si/n-GaAs junctions. The conduction band discontinuity of the  $p$ -Si/n-InGaP junctions was determined to be 0.41 eV from C-V measurements, which indicated that the Si/InGaP junctions revealed the type-I band line-up in contrast to the Si/GaAs junctions.

### **Marked suppression of In incorporation in heavily Si-doped $\text{In}_x\text{Ga}_{1-x}\text{N}$ ( $x\sim 0.3$ ) grown on GaN/ $\alpha\text{-Al}_2\text{O}_3(0001)$ template**

A. YAMAMOTO (Univ. of Fukui), A. MIHARA (Univ. of Fukui), N. SHIGEKAWA, and N. NARITA (The Kansai Electric Power Co.)

*Appl. Phys. Lett.*, 103, 082113 [4 pages] (2013).

$\text{In}_x\text{Ga}_{1-x}\text{N}$  ( $x\sim 0.3$ ) films doped with Si up to  $10^{22}\text{cm}^{-3}$  are grown on GaN/ $\alpha\text{-Al}_2\text{O}_3(0001)$  templates by the metal-organic vapor phase epitaxy using monomethylsilane (MMSi) as a Si source. The In composition in InGaN is markedly decreased with increasing MMSi flow rate; In compositions are 0.32 and 0.12 for 0 and 4.3  $\mu\text{mol}/\text{min}$  flow rates, respectively. The sum of concentrations of Si and In in InGaN is independent on MMSi flow rate and the Ga incorporation is not affected by the Si doping, suggesting that Si atoms are preferably incorporated into sites where In atoms should be incorporated.

### **Surface-activating-bonding-based low resistance Si/III-V junctions**

J. LIANG, S. NISHIDA, M. MORIMOTO, and N. SHIGEKAWA

*IEE Elec. Lett.*, Vol. 49 (13) pp. 830-832 (2013).

The electrical properties of pn junctions, with various semiconductor materials with different doping concentrations fabricated by using surface-activated-bonding (SAB), were investigated by measuring their current-voltage (I-V) characteristics. The I-V characteristics of  $\text{p}^+-\text{GaAs}/\text{n}^{++}\text{-Si}$ ,  $\text{p}^+-\text{GaAs}/\text{n}^+\text{-Si}$ ,  $\text{p}^+-\text{Si}/\text{n}^+\text{-Si}$ ,  $\text{p}^{++}\text{-Si}/\text{n}^+\text{-InGaP}$ , and  $\text{p}^+-\text{Si}/\text{n}^+\text{-InGaP}$  junctions showed ohmic-like properties. The interface resistance and the resultant electrical loss decreased with increasing impurity concentration at the interface. These results demonstrate the significance of SAB for fabricating tandem solar cells.

### **A Comparative Study on Metalorganic Vapor Phase Epitaxial InGaN with Intermediate In Compositions Grown on GaN/Sapphire Template and AlN/Si(111) Substrate**

A. YAMAMOTO (Univ. of Fukui), A. MIHARA (Univ. of Fukui), Y. ZHENG (Univ. of Fukui), and N. SHIGEKAWA

*Jpn. J. Appl. Phys.*, Vol. 52 08JB19 [4 pages] (2013).

The growth of InGaN with intermediate In compositions on GaN/sapphire template and AlN/Si(111) substrate has been comparatively studied. By using a metalorganic vapor phase epitaxy (MOVPE) system with a horizontal reactor, InGaN films are grown at a temperature of 600–800 °C in the pressure of 150 Torr. By optimizing growth temperature and trimethylindium/(trimethylindium + triethylgallium) molar ratio, single crystalline  $\text{In}_x\text{Ga}_{1-x}\text{N}$  with  $x = 0-1$  are successfully grown on both substrates. The films grown at a relatively high temperature ( $\geq 700$  °C) with In compositions of 0.3 or less show phase separation when their thickness exceeds a critical value (0.25–0.4  $\mu\text{m}$ ), while the samples grown at 600 °C with In compositions of 0.35–0.5 show no phase separation even if the thickness is increased to 0.7  $\mu\text{m}$ . To evaluate the crystalline quality of grown films, FWHM of X-ray rocking curve (XRC) for InGaN(0002), tilt, is measured. There is no marked difference in tilt data between films grown on GaN/ $\alpha\text{-Al}_2\text{O}_3(0001)$  and AlN/Si(111). For the samples grown at 600 °C with In contents of 0.35–0.5, tilt data are drastically increased and widely scattered suggesting the existence of important unknown parameters that govern crystalline quality of InGaN grown at a relatively low temperature.

### **Observation of Negative Differential Resistance in a GaN/AlGaN/GaN: Possible Tunneling Junction Using Polarization**

N. WATANABE (NTT Photonics Laboratories), H. YOKOYAMA (NTT Photonics Laboratories), and N. SHIGEKAWA

*Jpn. J. Appl. Phys.*, Vol. 52 08JN03 [3 pages] (2013).

We report an anomalous current–voltage behavior in an n-type GaN/undoped InGaN/undoped GaN/undoped AlGaN/n-type GaN diode grown by metalorganic chemical vapor deposition. The tunneling-junction-like band profile of the undoped GaN/undoped AlGaN/n-type GaN (GAG) structure is formed by a spontaneous and piezo polarization effect. We observe negative-differential resistance (NDR) behavior in the diode with the GAG structure. The NDR behavior suggests a possible tunneling junction consisting in the GAG structure.

### **MOVPE growth of $\text{In}_x\text{Ga}_{1-x}\text{N}$ ( $x\sim 0.5$ ) on Si(111) substrates with a pn junction on the surface**

A. YAMAMOTO (Univ. of Fukui) A. MIHARA (Univ. of Fukui), D. HIRONAGA (Univ. of Fukui), K. SUGITA (Univ. of Fukui), A. G. BHUIYAN (Univ. of Fukui), A. HASHIMOTO (Univ. of Fukui), N. SHIGEKAWA, and N. WATANABE (NTT Photonics Laboratories)

*Phys. Status Solidi C* Vol. 10, No. 3, pp. 437–440 (2013).

This paper reports the MOVPE growth of  $\text{In}_x\text{Ga}_{1-x}\text{N}$  ( $x\sim 0.5$ ) on Si(111) with a pn junction on the surface. By

optimizing growth temperature and TMI/(TMI+TEG) molar ratio, InGaN films with In content up to 0.5 are successfully grown without phase separation and metallic In incorporation. No significant differences in tilt fluctuation in grown InGaN are found among three different substrates; GaN/ $\alpha$ -Al<sub>2</sub>O<sub>3</sub>(0001) template, p-Si(111) and n-Si(111) with a p-type layer on the surface. The tilt fluctuation increases with increasing In content in InGaN and shows the maximum at around In composition 0.5. The n-InGaN/p-Si structures show good ohmic characteristics and the resistance obtained from the slope of I-V curves is markedly reduced with increasing In content in InGaN. The Si pn junction beneath the In<sub>0.42</sub>Ga<sub>0.58</sub>N layer behaves well as a solar cell with an InGaN filter. For both n-InGaN/p-Si and n-InGaN/pn-Si structures, the presence of an AlN interlayer between the epilayer and the substrate does not have a significant contribution to the series resistance.

### **Electrical Properties of p-Si/n-GaAs Heterojunctions by Using Surface-Activated Bonding**

J. LIANG, T. MIYAZAKI, M. MORIMOTO, S. NISHIDA, N. WATANABE (NTT Photonics Laboratories), and N. SHIGEKAWA

*Appl. Phys. Express* Vol. 6, 021801 [3 pages] (2013).

The electrical properties of p-Si/n-GaAs heterojunctions fabricated by using surface-activated bonding (SAB) were investigated by measuring their current–voltage (I–V) and capacitance–voltage (C–V) characteristics. The I–V characteristics showed rectifying properties. Their flat-band voltage obtained from C–V measurements was around 1.6 V. Observation by using field-emission-scanning electron microscopy and energy dispersive X-ray spectroscopy revealed neither structural deficits nor oxide layers at the interfaces. These results suggest that the SAB-based Si/GaAs heterojunctions are applicable for fabricating novel devices.

### **Study of Deterioration in a Piezoelectric Lead Zirconate Titanate Radiation Detector through Measurement of the Electromechanical Coupling Factor with 400 MeV/n Xenon Ions**

M. KOBAYASHI (Chiba Institute of Technology), T. MIYACHI (Chiba Institute of Technology), S. TAKECHI, M. SEKIGUCHI, H. SHIBATA (Osaka University), N. OKADA (Honda Electronics), M. HATTORI (Tokyo Institute of Technology), O. OKUDAIRA (JAXA), M. FUJII (Famscience), T. MURAKAMI (NIRS), and Y. UCHIHORI (NIRS)

*Jpn. J. Appl. Phys.* Vol. 52, 126604 (5 pages) (2013).

The variation of the electromechanical coupling factor (ECF) was measured by bombarding a piezoelectric lead zirconate titanate (PZT) element with 400 MeV/n xenon ions. The element was exposed to energies up to 104 J, during which time the ECF was observed by the resonance method. The ECF gradually decreased with the energy accumulated during irradiation, and its behavior was scaled with an empirical formula. This decrease suggests that the piezoelectric quality deteriorated; hence, the sensitivity of the PZT radiation detector was considered to be degraded as well. The variation ultimately originated in resonance-associated processes. A potential detector suitable for use in severe-radiation environments was discussed.

### **Type II band lineup in SAB-Based GaAs/Si heterojunctions**

M. MORIMOTO, J. LIANG, S. NISHIDA, T. MIYAZAKI, and N. SHIGEKAWA

*Extended Abstract of 2013 IEEE International Meeting for Future of Electron Devices, Kansai (IMFEDK)*, pp. 48-49 (2013). DOI: 10.1109/IMFEDK.2013.6602234

The electrical properties of GaAs/Si heterojunctions fabricated by using surface-activated bonding were experimentally investigated. The results of measurements suggested that the heterostructures revealed type-II band lineup.

### **Characteristics of TiO<sub>2</sub> surfaces etched by capacitively coupled radio frequency N<sub>2</sub> and He plasmas**

R. KAWAKAMI, M. NIIBE, Y. NAKANO, M. KONISHI, Y. MORI, H. TAKEUCHI, T. SHIRAHAMA, T. YAMADA, and K. TOMINAGA.

*Journal of Physics: Conference Series* Vol. 441, 012038 (6 pages) (2013).

We have investigated characteristics of anatase TiO<sub>2</sub> thin film surfaces etched by a capacitively coupled obtained with use of the N<sub>2</sub> plasma is compared with that obtained with use of the He plasma. The experimental O/Ti ratio at the surface etched by the N<sub>2</sub> plasma increases as a function of etching time. The increase in the experimental O/Ti ratio is independent of a change in gas pressure. The above-mentioned experimental results agree with the simulation result that the Ti atoms at the surface are preferentially removed by N<sub>2</sub><sup>+</sup> ions. The experimental O/Ti ratio at the surface etched by the He plasma also increases, which does not agree with the simulation result that the O atoms are preferentially removed by He<sup>+</sup> ions. The O-1s XPS spectra of the surface etched by the He plasma show the peak associated with oxygen and water adsorbed by the surface. In the case where the component of the

adsorbed oxygen and water in each spectrum is subtracted, the experimental O/Ti ratio at the surface etched by the He plasma shows a decrease. This is consistent with the simulation result. The adsorption of oxygen and water seems to be caused by ambient air. Morphology of the surface etched by the N<sub>2</sub> plasma is almost similar to that of the as-grown surface regardless of the changes both in etching time and in gas pressure. In contrast, morphology of the surface etched by the He plasma changes as the etching time increases. This result is independent of the gas pressure.

DOI: 10.1088/1742-6596/441/1/012038

### **Surface damage of 6H-SiC originating from Argon plasma irradiation**

R. KAWAKAMI, M. NIIBE, H. TAKEUCHI, M. KONISHI, Y. MORI, T. SHIRAHAMA, T. YAMADA, and K. TOMINAGA

*Nuclear Instruments and Methods in Physics Research Section B: Beam Interactions with Materials and Atoms* Vol. 315, pp. 213-217 (2013).

Damage characteristics of SiC surfaces etched by capacitively coupled radio frequency Ar plasmas at various gas pressures have been studied from the viewpoint of synergy effect of Ar plasma ion and plasma-induced ultraviolet (UV) light irradiations. In the absence of UV light emission at the low gas pressure of 10 mTorr, morphology of the etched SiC surface is similar to that of the as-grown surface regardless of an increase in etching time. In contrast, the experimental Si/C ratio at the surface decreases with an increase in etching time, which agrees with the simulation that Si atoms at the surface are preferentially removed by Ar<sup>+</sup> ions impinging on the surface. The agreement indicates that the physical etching effect, which originates from the Ar<sup>+</sup> impact, contributes to the decrease in the Si/C ratio. In the presence of the UV light emission, the surface morphology at the high gas pressure of 50-100 mTorr depends on the etching time. The surface morphology changes as the etching time increases to 200 min. The experimental etch depth at the etching time of 200 min does not agree with that of the simulation. The experimental etch depth is much higher than the simulated one. The difference connecting with the gas pressures can be related to the factor whether the UV light is emitted from the plasma: the result at the high gas pressure suggests the contribution of the synergy effect caused by the following possible phenomenon: Si-C bonding at the surface is weakened.

DOI: 10.1016/j.nimb.2013.05.084

### **Comparison in Internal Strain Sensitivity between Polariscopy and Raman Scattering Spectroscopy in a (110)-oriented ZnTe Single Crystal**

H. TAKEUCHI

*Physica Status Solidi C* Vol. 11, pp. 1194 -1197 (2014).

We present the experimental fact that, in a (110)-oriented ZnTe single crystal, polariscopy is highly sensitive to the internal strain, comparing with Raman scattering spectroscopy. We utilized X-ray topography and X-ray diffraction analysis to thoroughly investigate the crystal structure that is intimately associated with the internal strain. The two X-ray structure analyses clarified that the misalignment from the [110] direction is formed in some regions. We obtained the following main result: The polariscopic analysis detects the internal strain formed by the misalignment, whereas the Raman scattering measurement is insensitive to the internal strain. We, therefore, conclude that polariscopy has the strain-detection sensitivity higher than the Raman scattering spectroscopy. We have confirmed that the polariscopic analysis can detect the internal strain less than 0.5% in the ZnTe crystal.

DOI: 10.1002/pssc.201300608

### **Correlation between the intra-atomic Mn<sup>3+</sup> photoluminescence and antiferromagnetic transition in an YMnO<sub>3</sub> epitaxial film**

M. NAKAYAMA, Y. FURUKAWA, K. MAEDA, T. YOSHIMURA, H. UGA, and N. FUJIMURA

*Appl. Phys. Express* Vol.7, 023002 (4 pages) (2014)

We have investigated the temperature dependence of the intra-atomic Mn<sup>3+</sup> photoluminescence (PL) in a multiferroic YMnO<sub>3</sub> epitaxial film grown by pulsed laser deposition. The most significant result is that the temperature dependence of the Mn<sup>3+</sup> PL intensities is highly correlated with that of the magnetic spin order originating from the antiferromagnetic transition. In contrast, the decay times of the Mn<sup>3+</sup> PL bands are independent of temperature; namely, the transition probabilities are not affected by the antiferromagnetic transition. The above results suggest that the electron transfer process to the Mn<sup>3+</sup> excited state from the conduction band is dominated by the magnetic spin order.

DOI: 10.7567/APEX.7.023002

### **High-sensitivity polarization modulation reflectance spectroscopy of cavity polaritons in a ZnO microcavity**

T. HASEGAWA, R. KISHIMOTO, Y. TAKAGI, T. KAWASE, D. KIM, and M. NAKAYAMA

*Appl. Phys. Express* Vol.7, 032003 (4 pages) (2014)

We report that polarization modulation reflectance (PMR) spectroscopy is highly sensitive to the cavity polaritons in a ZnO microcavity with  $\text{HfO}_2/\text{SiO}_2$  distributed Bragg reflectors. We demonstrate that the cavity-polariton dispersion, even in the energy region of strong absorption by exciton continuum states, is clearly observed by PMR spectroscopy. The PMR spectra were quantitatively analyzed by a transfer-matrix method taking into account three types of excitons labeled A, B, and C. Line-shape analysis of the PMR spectra indicates that the anisotropy of the excitonic transitions is considerable in treating the cavity polariton in the ZnO microcavity.

DOI: 10.7567/APEX.7.032003

### **Observation of bound and antibound states of cavity polariton pairs in a CuCl microcavity**

S. MATSUURA, Y. MITSUMORI, H. KOSAKA, K. EDAMATSU, K. MIYAZAKI, D. KIM, M. NAKAYAMA, G. OOHATA, H. OKA, H. AJIKI, and H. ISHIHARA

*Phys. Rev. B* Vol. 89, 035317 (2014)

We observed the antibound state, as well as the bound state, for cavity polariton pairs in a planar CuCl microcavity by spectrally resolved four-wave mixing. We obtained dispersion curves of the bound and antibound states by changing the incident angle of the pump pulses corresponding to the cavity detuning. The dispersion curve for the bound state suggests that the bound state is mainly composed of a bare biexciton and is weakly coupled to the cavity photons. The dephasing time of the bound state was faster than that of a bare biexciton in a thin sample, supporting the hypothesis that the bound state is coupled to the cavity photons. On the other hand, the antibound state consists of two lower polaritons having the same spin. The clear observation of the antibound state can be qualitatively explained by the phase-space filling, which reduces the Rabi splitting.

DOI: 10.1103/PhysRevB.89.035317

### **Photon-field-shape effects on Rabi splitting energies in ZnO microcavities**

M. KAWAKAMI, T. KAWASE, D. KIM, and M. NAKAYAMA

*Opt. Materials* Vol. 36, 1622–1626 (2014)

We have investigated the photon-field-shape effect on the Rabi splitting energies in ZnO microcavities with  $\text{HfO}_2/\text{SiO}_2$  distributed Bragg reflectors (DBRs). The thickness of the ZnO active layer was fixed to  $\lambda/2$  corresponding to a half of an effective resonant wavelength of the lowest-lying exciton. The photon-field shape was tuned to a node type or an antinode type by changing the order of the refractive indices in the DBRs. We obtained the cavity-polariton dispersions from angle-resolved reflectance spectra measured at 10 K. The Rabi splitting energies were evaluated from the analysis of the cavity-polariton dispersions with a phenomenological Hamiltonian for the strong coupling between the three kinds of excitons peculiar to ZnO labeled A, B, and C and the cavity photon. It was found that the Rabi splitting energies in the antinode-type microcavity are almost a half of those in the node-type microcavity. We semi-quantitatively analyzed the photon-field-shape effect, taking account of the overlap between the exciton and photon-field envelope functions.

DOI: 10.1016/j.optmat.2013.11.029

### **Photoluminescence characteristics of polariton condensation in a CuBr microcavity**

M. NAKAYAMA, K. MURAKAMI, Y. FURUKAWA, and D. KIM

*Appl. Phys. Lett.* Vol.105, 021903 (4 pages) (2014)

We have investigated the photoluminescence (PL) properties of a CuBr microcavity at 10 K, including the temporal profiles, from the viewpoint of cavity-polariton condensation. The excitation energy density dependence of the PL intensity (band width) of the lower polariton branch at an in-plane wave vector of  $k_{\parallel}=0$  exhibits a threshold-like increase (decrease). A large blueshift in the PL energy of 10 meV caused by the cavity-polariton renormalization is correlated with the excitation energy density dependence of the PL intensity. The estimated density of photogenerated electron-hole pairs at the threshold is two orders lower than the Mott transition density. These results consistently demonstrate the occurrence of cavity-polariton condensation. In addition, we found that the PL rise and decay times are shortened dramatically by the cavity-polariton condensation, which reflects the bosonic final state stimulation in the relaxation process and the intrinsic cavity-polariton lifetime in the decay process.

DOI: 10.1063/1.4890216

### **Polariton Characteristics of Photoluminescence Dynamics of Exciton–Exciton Scattering in GaAs/AlAs Multiple Quantum Wells**

Y. FURUKAWA, H. TAKEUCHI, and M. NAKAYAMA

*J. Phys. Soc. Jpn.* Vol. 83, 054709 (6 pages) (2014)

We have investigated the photoluminescence (PL) dynamics of exciton–exciton scattering, the so-called P emission, at 10K in GaAs ( $d$  nm)/AlAs ( $d$  nm) multiple quantum wells (MQWs) with  $d = 10$  and 20. It was found that the decay rate of the P emission systematically increases with a decrease in detection energy. In contrast, the decay rate hardly depends on an excitation power, which suggests that exciton–exciton collisions do not affect the decay rate. We demonstrate that the energy dependence of the decay rate  $\tau_p^{-1}(E)$  in each MQW is consistently scaled by that of the group velocity,  $v_g(E)$ , of a photon-like polariton in the lower polariton branch that is the final state for the P emission:  $\tau_p^{-1}(E) = A v_g(E)$ . This fact provides us clear evidence for the polariton characteristics of the PL dynamics of exciton–exciton scattering.

DOI: 10.7566/JPSJ.83.054709

### **Radiation of Terahertz Electromagnetic Waves from Coherent Longitudinal Optical Phonons in Multiple Quantum Wells**

M. NAKAYAMA

*J. Nanoelectronics and Optoelectronics* Vol. 8, pp.415–424 (2013)

The radiation of terahertz electromagnetic waves from coherent longitudinal optical (LO) phonons in multiple quantum wells (MQWs) under illumination of a femtosecond pulse laser is reviewed from the viewpoint of the enhancement mechanism at room temperature, which is essential in applications to optoelectronics in a terahertz region. Two enhancement mechanisms in MQWs are focused on. One is that the impulsive quantum interference between the heavy-hole (HH) and light-hole (LH) excitons acts as a driving force to the coherent GaAs-like LO phonon in GaAs/AlAs MQWs under a condition that the splitting energy between the HH and LH excitons resonates with the LO-phonon energy. The other is that a piezoelectric field due to the lattice-mismatch strain along a  $[11\bar{n}]$  direction produces an initial polarization of the GaAs-like LO phonon via an electric susceptibility, which results in considerable enhancement of the intensity of the terahertz radiation from the coherent LO phonon, in  $(11\bar{n})$ -oriented GaAs/In<sub>0.1</sub>Al<sub>0.9</sub>As strained MQWs.

DOI: 10.1166/jno.2013.1501

### **Thickness dependence of photoluminescence-decay profiles of exciton-exciton scattering in ZnO thin films**

S. WAKAIKI, H. ICHIDA, T. KAWASE, K. MIZOGUCHI, D. KIM, M. NAKAYAMA, and Y. KANEMATSU

*Eur. Phys. J. B* Vol. 86 387 (4 pages) (2013)

We have investigated the photoluminescence (PL) dynamics of ZnO thin films under intense excitation conditions using an optical-Kerr-gating method. The PL bands originating from exciton-exciton scattering (P emission) and biexciton (M emission) have been observed at 10 K. The ultrashort gating time of 0.6 ps has enabled us to obtain precise information of the temporal profiles of the peak energies and the intensities of the P- and M-PL bands. We have found that the decay time of the P emission becomes longer with increasing film thickness, while that of the M emission is independent of the film thickness. Although the decay time of the P emission is an increasing function of the film thickness, the relation is not in proportion, which is contrary to the predicted proportionality based on a simple model of photon-like polariton propagation.

DOI: 10.1140/epjb/e2013-30631-5

### **Voltage-controllable terahertz radiation from coherent longitudinal optical phonons in a $p$ - $i$ - $n$ diode structure of GaAs**

M. NAKAYAMA, S. ASAI, H. TAKEUCHI, O. ICHIKAWA, and M. HATA

*Appl. Phys. Lett.* Vol. 103, 141109 (4 pages) (2013)

We propose and demonstrate the voltage-controllable terahertz radiation from coherent longitudinal optical (LO) phonons in a  $p$ - $i$ - $n$  diode of GaAs at room temperature under illumination of a femtosecond pulse laser. It was found that the intensity of the terahertz radiation is continuously and drastically enhanced by an increase in reverse bias voltage (electric field strength) from 0 (22) to 8.0V (140 kV/cm). The analysis of the electric-field-strength dependence of the intensity indicates that the initial polarization of the LO phonon induced by the electric field dominates the enhancement and that the second-order electric susceptibility is considerable.

DOI: 10.1063/1.4823595

### **Geometrical Excess Entropy Production in Nonequilibrium Quantum Systems**

T. YUGE, T. SAGAWA, A. SUGITA and H. HAYAKAWA

*J. Stat. Phys.* Vol. 153, pp 412-441 (2003)

For open systems described by the quantum Markovian master equation, we study a possible extension of the Clausius equality to quasistatic operations between nonequilibrium steady states (NESSs). We investigate the excess heat divided by temperature (i.e., excess entropy production) which is transferred into the system during the operations. We derive a geometrical expression for the excess entropy production, which is analogous to the Berry phase in unitary evolution. Our result implies that in general one cannot define a scalar potential whose difference coincides with the excess entropy production in a thermodynamic process, and that a vector potential plays a crucial role in the thermodynamics for NESSs. In the weakly nonequilibrium regime, we show that the geometrical expression reduces to the extended Clausius equality derived by Saito and Tasaki (*J. Stat. Phys.* 145:1275, 2011). As an example, we investigate a spinless electron system in quantum dots. We find that one can define a scalar potential when the parameters of only one of the reservoirs are modified in a non-interacting system, but this is no longer the case for an interacting system.

### **Typical Pure States and Nonequilibrium Processes in Quantum Many-Body Systems**

T. MONNAI and A. SUGITA

*J. Phys. Soc. Jpn.* Vol. 83, 094001 (5 pages) (2014)

We show that it is possible to calculate equilibrium expectation values of many-body correlated quantities such as the characteristic functions and probability distributions with the use of only a single typical pure state. It also means that we can apply the pure state approach to Heisenberg operators and their spectral fluctuation, and hence to nonequilibrium processes starting from equilibrium. In particular, we can accurately analyze the full statistics of entropy production in nonequilibrium mesoscopic systems. In this way, we can access the full information on higher-order fluctuations in the large deviation regime far from equilibrium.

### **The gas distributions of He and Ne at metal surface in the field ion microscope**

K. SAITO, and A. KOBAYASHI

*Proc. 7th Int. Symp. Surf. Sci. (ISSS-7)*, Shimane Nov.3-6, 3PN-74 (2013)

For investigating the mechanism of image formation in the field ion microscope (FIM), it is important to understand the image gas dynamics microscopically in the vicinity of specimen surface. Particularly concerned with FIM imaging in inert gas mixtures, it is well known that the addition of a trace of Ne to He image gas gives rise to strong flickering effects in FIM images with rapid variations in the intensity of individual image spots, and the effect is due to the results of alternative change between He field adsorption and Ne field adsorption at the corresponding surface atom site. In order to examine the details of Ne atom condensation near the surface, we demonstrate 2-dimensional gas dynamics in a mixed system of He and Ne in the presence of the electric field based on a classical gas kinetics model with parameters such as polarizabilities, masses and dimensions corresponding to each of He and Ne atoms. Coefficients which correspond to the rebound of He and Ne atoms at specimen surface are also taken into account to involve the thermal accommodation effect. With these four factors, we calculate the trajectories of He and Ne atoms that randomly travel and repeatedly collide each other in space while receiving dipole attractive force from the specimen surface, and we examine how these four factors affect the gas dynamics and eventually result in the superiority of Ne gas concentration near the surface.

### **Three-Dimensionally Integrated Micro-solution Plasma: Numerical Feasibility Study And Practical Applications**

T. SHIRAFUJI, A. NOMURA, and Y. HIMENO

*Plasma Chem. Plasma Process.*, Vol. 34, pp. 523-534 (2014).

This paper describes effects of design parameters for a three-dimensionally integrated micro-solution plasma (3D IMSP) reactor, which generates a large amount of microplasma in gas bubbles flowing with a liquid medium through a porous dielectric material. Electric fields in gas bubbles are calculated by solving Maxwell's equations under the electro-quasi-static approximation. The calculated electric fields in the bubbles can be high enough for igniting electrical discharge in the bubbles even if the bubbles are surrounded by electrically conductive liquid. We show importance of higher permittivity of a dielectric-reactor tube and a higher voltage-rise rate for obtaining higher electric fields in the bubbles. Using a proto type 3D IMSP reactor, we demonstrate synthesis of gold nanoparticles and decomposition of methylene blue molecules in aqueous solution.

DOI: 10.1007/s11090-014-9544-2

### **Numerical Simulation of Electric Double Layer in Contact with Dielectric Barrier Discharge**

T. SHIRAFUJI, A. NAKAMURA, and F. TOCHIKUBO (Tokyo Metropolitan Univ.)

*JPS Conf. Proc.*, Vol. 1, 015058 (4 pages) (2014).

A Numerical study has been carried out for understanding behavior of electric double layer (EDL) in liquid in contact with atmospheric dielectric barrier discharge (DBD) plasma of Ar gas. In the case of liquid with low ion concentration like de-ionized water, amount of liquid-phase ions generated by electron or ion irradiation from the DBD plasma is higher by approximately one order of magnitude than that in the pure EDL formed only with potential difference between the top and bottom of the liquid. Effects of molecular weight of the ions in liquid are investigated. If the molecular weight of the ions larger, residence time of the ions at the liquid surface becomes longer. If the molecular weight of positive and negative ions is different, heavier ions becomes dominant at the liquid surface. These characteristics are pronounced by employing higher frequency voltage, which implies possibility of preferential reactions at the plasma-liquid interface.  
DOI: 10.7566/JPSCP.1.015058

#### **Numerical Simulation of Electric Double Layer in Contact with Dielectric Barrier Discharge -Effects of Ion Transport Parameters in Liquid -**

T. SHIRAFUJI, A. NAKAMURA, and F. TOCHIKUBO (Tokyo Metropolitan Univ.)

*Jpn. J. Appl. Phys.*, Vol. 53, 03DG04 (6 pages) (2014).

The spatiotemporal distribution of charged particles has been investigated through numerical simulation of charged particle behavior in gas and liquid phases in the dielectric barrier discharge of Ar gas in contact with a liquid. In the case of a liquid with a low ion concentration such as deionized water, the amount of liquid-phase ions generated by electron or ion irradiation from gas-phase plasma is higher by approximately one order of magnitude than that in the pure electric double layer formed only with the potential difference between the top and bottom of the liquid. When the molecular weight of the ions is larger, the residence time of the ions at the liquid surface becomes longer. If the molecular weight of positive and negative ions is different, heavier ions become dominant at the liquid surface. These characteristics are pronounced by employing a higher frequency voltage, which implies the possibility of preferential reactions at the plasma-liquid interface.

DOI: 10.7567/JJAP.53.03DG04

#### **Time-resolved Optical Emission Spectroscopy on Three-dimensionally Integrated Micro-solution Plasmas**

T. SHIRAFUJI, Y. OGURA, and Y. HIMENO

*Jpn. J. Appl. Phys.*, Vol. 53, 010211 (6 pages) (2014).

Time-averaged and time-resolved optical emission spectroscopy (OES) has been performed on three-dimensionally integrated micro-solution plasma (3D IMSP). In comparison with that of conventional solution plasma generated in pure water vapor bubbles, the OES spectrum of our 3D IMSP, which is generated in Ar gas bubbles surrounded with water, shows more pronounced optical emission of OH radicals than of H and O radicals. In addition, time-resolved OES shows that the optical emission of OH radicals is sustained even after the emission of H and Ar almost disappears. The mechanisms of these phenomena are discussed by considering the dissociative recombination of  $\text{H}_2\text{O}^+$  and/or  $\text{H}_3\text{O}^+$  with low-temperature electrons.

DOI: 10.7567/JJAP.53.010211

#### **Gold Nanoparticles Synthesis by Using Three-dimensionally Integrated Micro-solution Plasmas**

T. SHIRAFUJI, J. UEDA, A. NAKAMURA, S.-P. CHO (Nagoya Univ.), N. SAITO (Nagoya Univ.), and O. TAKAI (Kanto Gakuin Univ.)

*Jpn. J. Appl. Phys.*, Vol. 52, 126202 (5 pages) (2013).

Three-dimensionally integrated micro-solution plasmas (3D IMSPs), in which microplasmas are generated in gas bubbles in an aqueous solution held in a porous dielectric material, have been applied to gold nanoparticle synthesis. Conventional solution plasma processes require additional chemicals to increase the electrical conductivity of the aqueous solution for generating plasmas. In contrast to this, 3D IMSPs have been found to generate plasmas without such a procedure when the aqueous solution has a low electrical conductivity as in the case of  $\text{HAuCl}_4$  for gold nanoparticle synthesis. The gold nanoparticle synthesis has been confirmed through the observation of optical absorption due to the plasmon resonance at 550 nm, and also through the characterization of their size, crystallinity, and composition by transmission electron microscopy and energy dispersive X-ray spectroscopy.

DOI: 10.7567/JJAP.52.126202

#### **Generation of Three-dimensionally Integrated Micro-solution Plasmas And Its Application to Decomposition of Methylene Blue Molecules in Water**

T. SHIRAFUJI and Y. HIMENO

*Jpn. J. Appl. Phys.*, Vol. 52, 11NE03 (5 pages) (2013).

Integrated micro-solution plasma was generated in gas bubbles in porous dielectric materials filled with a gas/liquid mixed medium. Methylene blue aqueous solution (3.8 mg/L, 150 mL) was treated with the integrated micro-solution plasma. The decomposition of methylene blue molecules was confirmed through the reduction in the optical absorption coefficient at 665 nm for methylene blue molecules, and through the fact that the absorption coefficient at 665 nm did not recover even after stirring in air. The decomposition efficiency of the integrated micro-solution plasma was 15.7-fold higher than that of conventional solution plasma.

DOI: 10.7567/JJAP.52.11NE03

#### **Functionalization of Multiwalled Carbon Nanotubes by Solution Plasma Processing in Ammonia Aqueous Solution and Preparation of Composite Material with Polyamide 6**

T. SHIRAFUJI, Y. NOGUCHI (Nagoya Univ.), T. YAMAMOTO (Nagoya Univ.), J. HIEDA (Tohoku Univ.), N. SAITO (Nagoya Univ.), O. TAKAI (Kanto Gakuin Univ.), A. TSUCHIMOTO (Toyo Jushi Corp.), K. NOJIMA (Toyo Jushi Corp.), and Y. OKABE (Toyo Jushi Corp.)

*Jpn. J. Appl. Phys.*, Vol. 52, 125101 (6 pages) (2013).

Solution plasma processing (SPP) has been performed on multiwalled carbon nanotubes (MWCNTs) in ammonia aqueous solution. The MWCNTs, which do not disperse in aqueous solution, uniformly dispersed after the SPP. Only 2 h was required to obtain 10 g of the dispersed MWCNTs, while 7 days and additional chemicals were required for 185 mg in a previous study. The X-ray photoelectron spectroscopy and Fourier-transform infrared spectroscopy of the SPP-treated MWCNTs revealed that nitrogen- and oxygen-containing groups are formed on the MWCNTs. Serious damage to the MWCNT structure was not observed in the Raman spectrum or transmission electron microscopy images of the SPP-treated MWCNTs. The composite materials prepared using polyamide 6 with the SPP-treated MWCNTs showed better tensile, bending, and impact strength than those prepared with non-treated MWCNTs.

DOI: 10.7567/JJAP.52.125101

#### **Decomposition of Methylene Blue Molecules in Aqueous Solution by Using Three-dimensionally Integrated Micro Solution Plasmas and Improvement of Its Energy Efficiency**

T. SHIRAFUJI, Y. HIMENO, N. SAITO (Nagoya Univ.), and O. TAKAI (Kanto Gakuin Univ.)

*J. Photopolym. Sci. Technol.*, Vol. 26, pp. 507-511 (2013).

Three-dimensionally integrated micro solution plasmas were generated in gas bubbles in porous dielectric materials filled with gas/liquid mixed medium. The methylene blue molecules in aqueous solution were decomposed by the treatment with the three-dimensionally integrated micro solution plasmas. Decomposition efficiency was 16 times higher than conventional solution plasma in the case of applied voltage of 5 kV. With decreasing applied voltage from 5 to 2 kV, the decomposition efficiency was improved up to 360% in comparison to that of 5 kV, while reduction in the decomposition rate was 40%.

DOI: 10.2494/photopolymer.26.507

#### **Numerical Investigation of Electric Field in Gas Bubbles Surrounded with Conductive Liquid And Dielectric Material**

T. SHIRAFUJI and A. NAKAMURA

*Trans. Mater. Res. Soc. Jpn.*, Vol. 38, pp. 321-323 (2013).

We propose a structure of integrated micro solution plasmas, in which a number of microplasmas can be generated in a liquid medium, and we can expect efficient plasma-liquid interaction. It consists of a non-isolated porous dielectric material filled with a gas-liquid mixed medium. Since the bubbles in this structure are surrounded with conductive liquid, electrical discharges in the bubbles are not expected if we use liquid with infinite electrical conductivity. However, numerical simulation has revealed that the electric field in the bubbles can be high enough to ignite atmospheric pressure discharge in it if the liquid has finite electrical conductivity, for example 200  $\mu\text{S}/\text{cm}$  for typical tap water, and that the concept of the integrated micro solution plasmas is feasible one.

DOI: 10.14723/tmrj.38.321

#### **Plasmas in Contact with Liquid: “Plasma Electrochemistry”**

T. SHIRAFUJI, N. SAITO (Nagoya Univ.), O. TAKAI (Kanto Gakuin Univ.), F. TOCHIKUBO (Tokyo Metropolitan Univ.), K. YASUOKA (Tokyo Inst. Technol.), T. KANEKO (Tohoku Univ.), T. ISHIJIMA (Kanazawa Univ.), K. TAKAHASHI (Kanazawa Univ.), N. TAKEUCHI (Tokyo Inst. Technol.), and N. SHIRAI (Tokyo Metropolitan Univ.)

*J. Surf. Sci. Soc. Jpn.*, Vol. 34, pp. 547-552 (2013) (in Japanese).

This paper describes historical overview and recent activity on “plasma electrochemistry”, which involves materials processing with plasmas in contact with liquids. Nano-materials synthesis and organic-pollutant decomposition are the most active application areas. The most important part of the plasma electrochemistry is the plasma/liquid interface. The physicochemical processes near the plasma/liquid interface have been gradually clarified through experiments and numerical simulations. These are briefly described in this paper together with future issues for understanding effects of electric double layer and nano-scale steep density gradient.

DOI: 10.1380/jsssj.34.547

### **Numerical Simulation of Spatiotemporal Behavior of Electric Double Layer in Aqueous Solution in Contact with Gas-phase Plasma Sheath**

T. SHIRAFUJI and A. NAKAMURA

*Proc. 21st International Symposium on Plasma Chemistry (ISPC 21)*, ID545 (4 pages), Aug. 4-9, 2013, Cairns, Australia.

Numerical simulation of electric double layer in contact with a dielectric barrier discharge has been performed. Preferential appearance of positive or negative ions has been observed on the top surface of the liquid. This means that the preferential interaction can be realized between gas-phase plasma species and liquid phase ions.

### **Three-Dimensional Integration of Micro Solution Plasmas and Its Application to Material Processing in Large Volume Liquid**

T. SHIRAFUJI

*Proc. 21st International Symposium on Plasma Chemistry (ISPC 21)*, ID315 (4 pages), Aug. 4-9, 2013, Cairns, Australia.

Three-dimensionally integrated micro solution plasma (3D IMSP), in which micro-plasmas are generated in Ar gas bubbles in aqueous solution being held in a porous dielectric material, has been proposed. Electric field in the bubbles is calculated with numerical simulation and is confirmed to be high enough for igniting electrical discharge in the bubbles even if the bubbles are surrounded with electrically conductive liquid. A proto type reactor for generating the 3D IMSPs has capability of generating large volume plasma in liquid. The 3D IMSP reactor is applied to material processing, in which the 3D IMSP is found to be able to synthesize gold nanoparticles and to decompose organic substance in water.

### **Decomposition of Acetic Acid Molecules on Three-dimensionally Integrated Micro Solution Plasma in Ar/H<sub>2</sub>O Mixture**

Y. HIMENO and T. SHIRAFUJI

*Proc. 8th International Conference on Reactive Plasmas and 31st Symposium on Plasma Processing*, 5A-AM-O2 (2 pages), Feb. 3-7, 2014, Fukuoka, Japan.

Three-dimensionally integrated micro-solution plasma (3D IMSP) was generated in gas bubbles in porous dielectric materials filled with gas/liquid medium. We have used this method to decompose acetic acid which is known as a persistent organic substance. The liquid after the 3D IMSP treatment has been characterized with Fourier transform infrared spectroscopy, in which we have observed changes in the IR absorption bands corresponding to OH (3700-3500 cm<sup>-1</sup>) and CO (1200-1300 cm<sup>-1</sup>) bonds of acetic acid molecules.

### **Optical Emission Spectroscopy on 3D Integrated Micro-solution Plasma**

Y. OGURA, Y. HIMENO, and T. SHIRAFUJI

*Proc. 8th International Conference on Reactive Plasmas and 31st Symposium on Plasma Processing*, 5P-PM-S09-P22 (2 pages), Feb. 3-7, 2014, Fukuoka, Japan.

We have performed time-averaged and time-resolved optical emission spectroscopy in order to investigate the mechanism of radical generation in 3D Integrated Micro-Solution Plasma, which is ignited in a large number of Ar bubbles surrounded by aqueous solution. We have found that the duration of optical emission of OH(A) is longer than H $\alpha$ . The causes of this difference are discussed with considering contribution of metastable excited Ar.

### **Chemical Vapor Deposition of SiO Thin Films Using an Atmospheric Pressure Helium Plasma Jet And Hexamethyldisiloxane**

R. TAGA, D. USA, and T. SHIRAFUJI

*Proc. 8th International Conference on Reactive Plasmas and 31st Symposium on Plasma Processing*, 5P-PM-S09-P23 (2 pages), Feb. 3-7, 2014, Fukuoka, Japan.

SiO thin films, which are usually deposited by plasma CVD in low pressure, have been deposited using an atmospheric pressure plasma jet (APPJ) and hexamethyldisiloxane (HMDSO). Although particles are generated on the surface of thin films deposited, generation of particles is suppressed by properly configuring the APPJ and the nozzle that supplies HMDSO. Film composition is also affected by the configuration of the jet and nozzle.

### **Time-resolved Optical Emission Spectroscopy on Micro-solution Plasma in a Single Bubble in a Capillary Tube**

R. TASHIRO, K. OBANA, and T. SHIRAFUJI

*Proc. 8th International Conference on Reactive Plasmas and 31st Symposium on Plasma Processing*, 5P-PM-S09-P24 (2 pages), Feb. 3-7, 2014, Fukuoka, Japan.

Three-dimensionally integrated micro-solution plasma (3D IMSP) was generated in gas bubbles in porous dielectric materials filled with gas/liquid medium. We have performed time-resolved OES. It has revealed that emission intensity of OH showed a unique time-dependence, in which the 2nd maximum appeared after the 1st main peak. In order to understand details of the 3D IMSP, we performed investigation of microplasma in a single bubble by time-resolved OES. We could not see the 2nd peak in the case of the single bubble, but long tail was observed after the 1st peak.

### **On The Contribution of Electrons, Ar(3P), H<sub>2</sub>O<sup>+</sup>, and H<sub>3</sub>O<sup>+</sup> to Production of OH(A) in a Micro DBD of Ar/H<sub>2</sub>O**

T. SHIRAFUJI and T. MURAKAMI (Tokyo Institute of Technology)

*Proc. 8th International Conference on Reactive Plasmas and 31st Symposium on Plasma Processing*, 6A-PM-O4 (2 pages), Feb. 3-7, 2014, Fukuoka, Japan.

Numerical simulation of a micro DBD of Ar/H<sub>2</sub>O gas mixture has been performed for understanding behavior of OH(A) in 3D IMSP. During the discharge ignition sequence in 0-200 ns, major OH(A) production reactions are dissociation of H<sub>2</sub>O by high- $T_e$  electrons and metastable excited Ar. After the main discharge, OH(A) production becomes dominated by the dissociative recombination of H<sub>3</sub>O<sup>+</sup> and low- $T_e$  electrons.

### **Coherent time-domain detection of terahertz pulses generated from noncollinear phasematched, picosecond terahertz parametric oscillator**

Y. TADOKORO, Y. TAKIDA, H. KUMAGAI, S. NASHIMA, and M. HANGYO

*Applied Physics Express*, Vol. 7, pp. 022701(3pages) (2014).

With a photoconductive antenna, we demonstrate time-domain detection of terahertz (THz) pulses generated from a noncollinear phase-matched, picosecond THz parametric oscillator. Since time-domain detection enables us to detect THz waves sensitively, the dynamic range of the power spectrum is ~1000 times improved in comparison with that of a pyroelectric detector. Furthermore, multiple THz pulses are observed because of the time delay between arrayed Si prism couplers. When a single, larger Si prism coupler or a trapezoidal MgO:LN crystal is employed instead, single monocycle THz pulses are observed.

### **Metal mesh device sensor immobilized with a trimethoxysilane-containing glycopolymer for label-free detection of proteins and bacteria**

H. SETO, S. KAMBA, T. KONDO, M. HASEGAWA, S. NASHIMA, Y. EHARA, Y. OGAWA, Y. HOSHINO, and Y. MIURA

*ACS Applied Material and Interfaces*, Vol. 6, No. 15, pp. 13234-13241 (2014).

Biosensors for the detection of proteins and bacteria have been developed using glycopolymer-immobilized metal mesh devices. The trimethoxysilane-containing glycopolymer was immobilized onto a metal mesh device using the silane coupling reaction. The surface shape and transmittance properties of the original metal mesh device were maintained following the immobilization of the glycopolymer. The mannose-binding protein (concanavalin A) could be detected at concentrations in the range of 10<sup>-9</sup> to 10<sup>-6</sup> mol L<sup>-1</sup> using the glycopolymer-immobilized metal mesh device sensor, whereas another protein (bovine serum albumin) was not detected. A detection limit of 1 ng mm<sup>-2</sup> was achieved for the amount of adsorbed concanavalin A. The glycopolymer-immobilized metal mesh device sensor could also detect bacteria as well as protein. The mannose-binding strain of *Escherichia coli* was specifically detected by the glycopolymer-immobilized metal mesh device sensor. The glycopolymer-immobilized metal mesh device could therefore be used as a label-free biosensor showing high levels of selectivity and sensitivity toward proteins and bacteria.

**Volumetric display using rotating prism sheets arranged in a symmetrical configuration**

Yuki MAEDA, Daisuke MIYAZAKI, Takaaki MUKAI and Satoshi MAEKAWA (Univ. of Hyogo)

*Opt. Express* Vol.21, 27074-27086 (2013).

A volumetric display that creates a distortion-free three-dimensional (3D) image in midair is described. The proposed system consists of rotating prism sheets used as an optical scanner and a dihedral corner reflector array (DCRA), which is a distortion-free imaging element. Two prism sheets are arranged in a symmetrical configuration to reduce an unnatural motion parallax caused by optical aberrations. A cross-section of the 3D image is formed by the DCRA in midair and moved by the rotating prism sheets to create a 3D displayable space. A 3D volume image was displayed without image distortion or unnatural motion parallax.

**Floating multi-view image formation with micro-mirror array imaging element**

Daisuke MIYAZAKI

*The 3rd Japan-Korea Workshop on Digital Holography and Information Photonics*, Session 2- 3 (2013).

A volumetric display that creates a distortion-free three-dimensional (3D) image in midair is described. The proposed system consists of rotating prism sheets used as an optical scanner and a dihedral corner reflector array (DCRA), which is a distortion-free imaging element. Two prism sheets are arranged in a symmetrical configuration to reduce an unnatural motion parallax caused by optical aberrations. A cross-section of the 3D image is formed by the DCRA in midair and moved by the rotating prism sheets to create a 3D displayable space. A 3D volume image was displayed without image distortion or unnatural motion parallax.

**Floating volumetric display using an imaging element that consists of a 90° prism sheet and a linear Fresnel lens**

Yuki MAEDA, Daisuke MIYAZAKI, Takaaki MUKAI and Satoshi MAEKAWA (Univ. of Hyogo)

*Proc. Soc. Photo-Opt. Instrum. Eng.*, Vol. 9011, 90111N (2014).

We propose a floating volumetric display system using a novel imaging element whose aperture is large and can be made easily at low cost. Diffuse rays in a horizontal direction for an observer are formed by a 90° prism sheet, which has a shape of an array of 90° V-grooves, as a result of twice total internal reflection. On the other hand, the diffuse rays in a longitudinal direction for the observer are formed by a linear Fresnel lens. A formed image by the proposed imaging element does not distort in the horizontal direction because the rays in the horizontal direction converge by retroreflection. The proposed imaging element can be produced easier than a conventional distortion-free imaging element and display a larger floating image. A floating three-dimensional image was displayed by a volumetric display system based on optical scanning of an inclined image plane. A position of a two-dimensional real image formed by the proposed imaging element was moved by an optical scanner at a faster rate than the duration time of persistence of vision. A stack of moved images created the floating three-dimensional volume image.

**Multi-user autostereoscopic display based on direction-controlled illumination using a slanted cylindrical lens array**

Daisuke MIYAZAKI, Yui HASHIMOTO, Takahiro TOYOTA, Kenta OKODA, Tetsuro OKUYAMA (Panasonic), Toshikazu OHTSUKI (Panasonic), Akio NISHIMURA (Panasonic), and Hiroyuki YOSHIDA (Panasonic)

*Proc. Soc. Photo-Opt. Instrum. Eng.*, Vol. 9011, 90111G (2014).

This research aims to develop an auto-stereoscopic display, which satisfies the conditions required for practical use, such as, high resolution and large image size comparable to ordinary display devices for television, arbitrary viewing position, multiple viewer availability, suppression of nonuniform luminance distribution, and compact system configuration. In the proposed system, an image display unit is illuminated with a direction-controlled illumination unit, which consists of a spatially modulated parallel light source and a steering optical system. The steering optical system is constructed with a slanted cylindrical array and vertical diffusers. The direction-controlled illumination unit can control output position and horizontal angle of vertically diffused light. The light from the image display unit is controlled to form narrow exit pupil. A

viewer can watch the image only when an eye is located at the exit pupil. Auto-stereoscopic view can be achieved by alternately switching the position of an exit pupil at viewer's both eyes, and alternately displaying parallax images. An experimental system was constructed to verify the proposed method. The experimental system consists of a LCD projector and Fresnel lenses for the direction-controlled illumination unit, and a 32 inch full-HD LCD for image display.

#### **Optical design for heterogeneous imaging based on retro reflection using parallel roof mirror arrays**

Yuki MAEDA, Daisuke MIYAZAKI, and Satoshi. MAEKAWA (Univ. of Hyogo)

*JSAP-OSA Joint Symposia 2014, Information Photonics*, 20a-C4-3 (2014).

#### **Floated integral imaging display viewable from surrounding area**

Daisuke MIYAZAKI, Go MIYAZAKI, Yuki MAEDA, and Takaaki MUKAI

*Imaging and Applied Optics 2014, OSA Technical Digest*, DW2B.5 (2014).

A full-parallax auto-stereoscopic display method that enables formation of a floating three-dimensional image viewable from a surrounding area is proposed. This method utilizes integral imaging, a rotating mirror scanner, and a hemisphere concave mirror.

#### **Wide-Viewing Angle Three-dimensional Display Using Multiple LCDs**

Hirofumi YABU, Joji KANDA, and Hideya TAKAHASHI

*ICIC Express Letters Part B*, Vol.5, 1, pp.195-200 (2014).

We propose an omnidirectional three-dimensional (3D) display system. This is a tool for communication around a 3D image among a small number of people. This 3D display system consists of multiple basic 3D display units. The basic unit consists of an LCD, a lenticular lens array sheet, and a relay lens. In this basic unit, the light rays from an LCD pass through a lenticular lens sheet and observed directly. Thus, the spatial density distribution of projected light rays is partial. To average the spatial density of projected light rays, we use a relay lens. To increase the viewing angle, we aligned multiple basic units in a circle, and displayed 3D images at the center of the circle. To verify the effectiveness of the proposed 3D display, we constructed the prototype system. This prototype consists of 3 basic units. They are aligned 18.5-degree apart in a circle and the radius is 613.2 mm. The shape of the maximum size of displayed 3D images is a cylinder and the radius is 25 mm, the height is 50 mm. The viewing angle of a 3D image is 55.5-degree. This paper describes the principle of proposed 3D display system, and also describes the experimental results.

#### **Silicone Rubber Membrane Tactile Sensor for Endoscope Based on Image Processing**

Yuma KITANOUMA, Hideya TAKAHASHI, Kayo YOSHIMOTO (Osaka University), and Kenji YAMADA (Osaka University)

*ICIC Express Letters Part B*, Vol.5, 1, pp.279-284 (2014).

We propose the silicone rubber membrane tactile sensor for an endoscope. The proposed system consists of the transparency silicon rubber membrane and the image sensor. Our proposed system can estimate the stiffness of the target object by measuring the deformation of the silicone rubber which includes markers inside. When the silicone rubber is deformed by contacting with the target object, the position of each marker shifts. By using the displacement information of markers measured by the imaging device, the system can measure the deformation of the silicone rubber. The purpose of this study is to evaluate the proposed system. At first, we introduce the approximated models of the silicone and the object. We formulate the stiffness of the object, the deformation of silicone, and the whole object. To verify the effectiveness of the proposed system, we constructed the prototype system.

#### **Retinal projection type super multi-view head-mounted display**

Hideya TAKAHASHI, Yutaka ITO, Seigo NAKATA, and Kenji YAMADA (Osaka University)

*Proc.SPIE-IS&T Electronic Imaging*, Vol.9012, pp. 90120L-1-90120L-6 (2014).

We propose a retinal projection type super multi-view head-mounted display (HMD). The smooth motion parallax provided by the super multi-view technique enables a precise superposition of virtual 3D images on the real scene. Moreover, if a viewer focuses one's eyes on the displayed 3D image, the stimulus for the accommodation of the human eye is produced naturally. Therefore, although proposed HMD is a monocular HMD, it provides observers with natural 3D images. The proposed HMD consists of an image projection

optical system and a holographic optical element (HOE). The HOE is used as a combiner, and also works as a condenser lens to implement the Maxwellian view. Some parallax images are projected onto the HOE, and converged on the pupil, and then projected onto the retina. In order to verify the effectiveness of the proposed HMD, we constructed the prototype HMD. In the prototype HMD, the number of parallax images and the number of convergent points on the pupil is three. The distance between adjacent convergent points is 2 mm. We displayed virtual images at the distance from 20 cm to 200 cm in front of the pupil, and confirmed the accommodation. This paper describes the principle of proposed HMD, and also describes the experimental result.

#### **Evaluation of the three-dimensional endoscope system for assessing the gastrointestinal motility**

Kayo YOSHIMOTO (Osaka University), Kenji YAMADA (Osaka University), Kenji WATABE (Osaka University), Maki TAKEDA (Osaka University), Takahiro NISHIMURA (Osaka University), Michiko KIDO (Osaka University), Toshiaki Nagakura (Osaka Electro-Communication University), Hideya TAKAHASHI, Tsutomu NISHIDA (Osaka University), Hideki IJIMA (Osaka University), Masahiko TSUJII (Osaka University), Tetsuo TAKEHARA (Osaka University), and Yuko OHNO (Osaka University) *Proc.SPIE-BiOS2014 Advanced Biomedical and Clinical Diagnostic System XII*, Vol.8935, pp. 89351G-1-89351G -6 (2014).

This paper described evaluation of the three-dimensional endoscope system for assessing the gastrointestinal motility. Gastrointestinal diseases are mainly based on the morphological or anatomical abnormality. However, sometimes the gastrointestinal symptoms are apparent without visible abnormalities. Such diseases are called functional gastrointestinal disorder, for example, functional dyspepsia, and irritable bowel syndrome. One of the major factors of these diseases is the gastrointestinal dysmotility. Assessment procedures for motor function are either invasive, or indirect. We thus propose a three-dimensional endoscope system for assessing the gastrointestinal motility. To assess the dynamic motility of the stomach, three-dimensional endoscopic imaging of stomach lining is performed. Propagating contraction waves are detected by subtracting estimated stomach geometry without contraction waves from one with contraction waves. After detecting constriction waves, their frequency, amplitude, and speed of propagation can be calculated. In this study, we evaluate the proposed system. First, we evaluate the developed three-dimensional endoscope system by a flat plane. This system can measure the geometry of the flat plane with an error of less than 10 percent of the distance between endoscope tip and the object. Then we confirm the validity of a prototype system by a wave simulated model. The detected wave is approximated by a Gaussian function. In the experiment, the amplitude and position of the wave can be measure with 1 mm accuracy. These results suggest that the proposed system can measure the speed and amplitude of contraction. In the future, we evaluate the proposed system in vivo experiments.

#### **Gastric contraction imaging system using a three-dimensional endoscope**

Kayo YOSHIMOTO (Osaka University), Kenji YAMADA (Osaka University), Kenji WATABE (Osaka University), Maki TAKEDA (Osaka University), Takahiro NISHIMURA (Osaka University), Michiko KIDO (Osaka University), Toshiaki Nagakura (Osaka Electro-Communication University), Hideya TAKAHASHI, Tsutomu NISHIDA (Osaka University), Hideki IJIMA (Osaka University), Masahiko TSUJII (Osaka University), Tetsuo TAKEHARA (Osaka University), and Yuko OHNO (Osaka University) *IEEE Journal of Translational Engineering in Health and Medicine*, Vol.2, 1, pp.1-8 (2014).

Objective: This paper presents a gastric contraction imaging system for assessment of gastric motility using a three-dimensional endoscope. Gastrointestinal diseases are mainly based on morphological abnormalities. However, gastrointestinal symptoms are sometimes apparent without visible abnormalities. One of the major factors for these diseases is abnormal gastrointestinal motility. For assessment of gastric motility, a gastric motility imaging system is needed. Method: To assess the dynamic motility of the stomach, the proposed system measures three-dimensional gastric contractions derived from a three-dimensional profile of the stomach wall obtained with a developed three-dimensional endoscope. After obtaining contraction waves, their frequency, amplitude, and speed of propagation can be calculated using a Gaussian function. Results: The proposed system was evaluated for three-dimensional measurements of several objects with known geometries. The results showed that the surface profiles could be obtained with an error of less than 10 percent of the distance between two different points on images. Subsequently, we evaluated the validity of a prototype system using a wave simulated model. In the experiment, the amplitude and position of waves

could be measured with 1-mm accuracy. Conclusions: The present results suggest that the proposed system can measure the speed and amplitude of contractions. Clinical Impact: This system has low invasiveness and can assess the motility of the stomach wall directly in a three-dimensional manner. Our method can be used for examination of gastric morphological and functional abnormalities.

*Applied Chemistry and Bioengineering*

**Characterization of Lithium Insertion Electrodes by Precision Dilatometer: Area-Specific Deformation of Single Electrode**

Masatoshi NAGAYAMA, Kingo ARIYOSHI, Yuki YAMAMOTO and Tsutomu OHZUKU

*J. Electrochem. Soc.*, Vol. 161, pp. A1388-A1393 (2014)

A dilatometric method to characterize the electrodes in lithium and lithium-ion batteries is described in terms of the deformation of electrodes. A precision dilatometer consists of a main body and a flexible bag cell, in which a counter electrode is selected to be the zero-strain insertion electrode of lithium titanium oxide (LTO:  $\text{Li}[\text{Li}_{1/3}\text{Ti}_{5/3}]\text{O}_4$ ). Change in thickness of the cell consisting of a target electrode and an LTO electrode is measured in a sub-micron scale as a function of area-specific capacity stored or delivered electricity in  $\text{mAh cm}^{-2}$ , and the area-specific deformation in  $\mu\text{m} / (\text{mAh cm}^{-2})$  is defined as a common measure to evaluate the deformation or swelling of the electrodes. The method is applied to the electrodes of lithium metal, LTO, and  $\text{LiNi}_{1/3}\text{Mn}_{1/3}\text{Co}_{1/3}\text{O}_2$ . A dilatometer shows  $\pm 4.8 \mu\text{m} / (\text{mAh cm}^{-2})$  for a lithium metal electrode and nearly  $0 \mu\text{m} / (\text{mAh cm}^{-2})$  for an LTO electrode, indicating that the dilatometer works well to measure the electrode thickness. A  $\text{LiNi}_{1/3}\text{Mn}_{1/3}\text{Co}_{1/3}\text{O}_2$  electrode is shown to be dimensionally highly stable, i.e., nearly  $0 \mu\text{m} / (\text{mAh cm}^{-2})$ , when it operates under an upper restriction of 4.15 V vs. Li.

**Characterization of Lithium Insertion Electrodes: A Method to Measure Area-Specific Impedance of Single Electrode**

Kensuke NAKURA, Kingo ARIYOSHI, Fujika OGAKI, Kenji TAKAOKA, and Tsutomu OHZUKU

*J. Electrochem. Soc.*, Vol. 161, pp. A841-A846 (2014)

A basic concept on the area-specific impedance (ASI) of a single lithium insertion electrode is described in order to characterize lithium insertion electrodes. A common electrode selected to measure the ASI is the zero-strain lithium insertion material of lithium titanium oxide (LTO). The ASI of a single LTO electrode in  $\Omega\text{cm}^2$  is measured in the state of charge (SOC) ranging from 0 to 100% by using the zero-volt lithium-ion cell of LTO with a symmetric parallel-plate electrode configuration. Because the ASI of an LTO electrode is empirically known to be independent of SOC ranging from 10 to 90% with a margin of 5%, the impedance of a cell having any combination with the LTO electrode can be measured at any SOC of a target electrode. Consequently, the ASI of every lithium insertion electrode can be obtained by the impedance measurements. Significance of determining the ASI of a single lithium insertion electrode is described in terms of polarization and power dissipation generating heat in a full cell, and the methods to characterize lithium insertion electrodes in a basic research are discussed.

**Scanning removal of ion-implanted novolak resist by using a laser irradiation**

T. KAMIMURA, Y. KUROKI, T. KIRIYAMA, H. MURAOKA, K. KAWASAKI, T. MURAKAMI, Y. HARADA, H. KURAMAE, and H. HORIBE

*J. Photopolym. Sci. Technol.*, Vol. 27(2), pp. 237-241 (2014)

Laser resist stripping for the ion-implanted novolak resist was successfully performed without occurring laser damage to the Si wafer. In order for the advanced laser resist stripping method to be successful, it is important for the pulsed laser beam to pass through the ion-implanted resist and absorb into the Si wafer surface. The novolak resists which are implanted with B, P, and As ions, respectively, were irradiated with a pulsed 532 nm laser. Regardless of the implanted ion species and density, more than 74 % of the laser power was found to absorb into the Si wafer surface. For the laser irradiation of 1 pulse, the ion-implanted resist with a density of  $5.0 \times 10^{13}$  atoms/cm<sup>2</sup> was completely stripped in the same way as that of a non-implanted resist. The optical absorption of the resist surface increased as the density of the ion-implantation increased. In case of the ion-implanted resist with a density of  $5.0 \times 10^{15}$  atoms/cm<sup>2</sup>, the resist was stripped by 20 pulses

irradiation without occurring laser-induced surface damage. A scanning removal of the highly ion-implanted resist was also successfully stripped by using an optimized irradiation condition. A highly ion-implanted resist was continuously stripped by the scanning laser irradiation with 20 pulses.;

#### **High removal rate of cross-linked SU-8 resist using hydrogen radicals generated by tungsten hot-wire catalyze**

A. KONO, Y. ARAI, T. MARUOKA, M. YAMAMOTO, Y. GOTO, S. TAKAHASHI, T. NISHIYAMA, and H. HORIBE

*Thin Solid Films*, Vol. 562, pp. 632-637 (2014)

This paper discusses the removal of chemically amplified negative-tone *i*-line resist SU-8 using hydrogen radicals generated by the catalytic decomposition of H<sub>2</sub> molecules in H<sub>2</sub>/N<sub>2</sub> mixed gas (H<sub>2</sub>:N<sub>2</sub> = 10:90 vol.%) using a tungsten hot-wire catalyzer. SU-8 resists with exposure doses from 7 to 280 mJ/cm<sup>2</sup> were removed by hydrogen radicals, although the SU-8 removal rate was independent of the exposure dose. The SU-8 removal rate increased with both substrate and catalyzer temperature, in addition to a decrease in the distance between the catalyzer and substrate. A high removal rate for cross-linked SU-8 with an exposure dose of 14 mJ/cm<sup>2</sup> of approximately 4 μm/min was achieved with a catalyzer to substrate distance of 20 mm, and catalyzer and initial substrate temperatures of 2400 and 165 °C, respectively.

#### **Reaction mechanism of polymer removal using wet ozone**

Y. GOTO, Y. ANGATA, E. TSUKAZAKI, S. TAKAHASHI, K. KOIKE, T. YAMAGISHI, and H. HORIBE

*Jpn. J. Appl. Phys.*, Vol. 53, p. 02BB04 (2014)

We evaluated the removal of polymers with various chemical structures using wet ozone, and investigated the reaction mechanism between wet ozone and polymers using fourier-transform infrared (FT-IR) and in situ FT-IR. The removal rate of poly(vinyl phenol) (PVP), which has a carbon-carbon double bond (C=C) in the side chain was lower than that of the novolak resin, which has C=C in the main chain. Poly(methyl methacrylate) (PMMA), which has no C=C, was not removed. It was considered that the ozone reaction is an electrophilic reaction, and the wet ozone should react with C=C with ease. The removal rate of PVP with rinsing was higher than that without rinsing. This result indicates that the reaction products remain on the Si wafer. However, in the novolak resin, there was no difference between with and without rinsing. It was considered that the main chain of the novolak resin was decomposed to gas by the reaction with wet ozone. In the FT-IR measurement of PVP, the peak intensity of C=O stretching of carboxylic acid increased with increasing wet ozone processing time. However, in the novolak resin, there was no difference between with and without rinsing. Moreover, the peak intensity of the C=O stretching of carboxylic acid did not increase with increasing wet ozone processing time after 10 s of wet ozone processing time. From the result of in situ FT-IR, in the removal of the novolak resin using wet ozone, the main chain of the novolak resin was decomposed, and the reaction products of the wet ozone and novolak resin (low-molecular-weight carboxylic acid) should change to CO<sub>2</sub>.

#### **Sensitivity of a chemically amplified three-component resist containing a dissolution inhibitor for extreme ultraviolet lithography**

H. HORIBE, K. ISHIGURO, T. NISHIYAMA, A. KONO, K. ENOMOTO, H. YAMAMOTO, M. ENDO, and S. TAGAWA

*Polym. J.*, Vol. 46, pp. 234-238 (2014)

A chemically amplified three-component resist was prepared by adding a dissolution inhibitor as the third component in an X-ray resist, and its sensitivity and resolution were evaluated for the application in extreme ultraviolet (EUV) lithography. The chemically amplified three-component resist, which consists of a base resin, a photo-acid generator (PAG) and a dissolution inhibitor, achieved high sensitivity with an exposure dose below 10 mJ cm<sup>-2</sup>. Furthermore, the chemically amplified three-component resist exhibited higher resolution and sensitivity than a resist without a dissolution inhibitor. The dissolution inhibitor was converted

to a dissolution promoter containing carboxylic groups by exposure to EUV light, and it acted as a plasticizer in the resist, resulting in facile diffusion of the protons generated from the PAG. Thus, novel EUV resists with high sensitivity and resolution could be designed utilizing chemically amplified three-component resist containing a dissolution inhibitor.

#### **UV-Light Irradiation Effect on Photocatalytic Polymer Sheet Prepared by Solvent Casting Process**

S. SONE, M. MAEDA, and H. HORIBE

*KOBUNSHI RONBUNSHU*, Vol. 70(9), pp. 496–501 (2013) (in Japanese)

TiO<sub>2</sub> doped poly(vinylidene fluoride) (PVDF) sheet was prepared by solvent casting process. Both PVDF and TiO<sub>2</sub> powders were dissolved in *N,N*-dimethylformamide (DMF) solution and then spin-coated on the Si or glass substrate. The flexible TiO<sub>2</sub> doped PVDF sheets are transparent and have PVDF II-type crystallinity. The TiO<sub>2</sub> particles distribute in the PVDF sheet with cohesion. Photocatalytic pigment degradation was observed when the sheet was irradiated by UV-light. After 840 hours UV-light irradiation, remarkable change in XRD patterns and FT-IR spectra of the TiO<sub>2</sub> doped PVDF sheets was not observed, however, the sheets became cloudy because the sub-micrometer surface roughness were formed due to local photocatalytic decomposition of PVDF structure. As a result, the photocatalytic rate of pigment decreased because of UV-light scattering.

#### **A High Speed Photoresist Removal Process Using Multibubble Microwave Plasma under a Mixture of Multiphase Plasma Environment**

T. ISHIJIMA, K. NOSAKA, Y. TANAKA, Y. UESUGI, Y. GOTO, and H. HORIBE

*Appl. Phys. Lett.*, Vol. 103(14), pp. 142101/1-142101/5 (2013)

This paper proposes a photoresist removal process that uses multibubble microwave plasma produced in ultrapure water. A non-implanted photoresist and various kinds of ion-implanted photoresists such as B, P, and As were treated with a high ion dose of  $5 \times 10^{15}$  atoms/cm<sup>2</sup> at an acceleration energy of 70 keV; this resulted in fast removal rates of more than 1 μm/min. When the distance between multibubble microwave plasma and the photoresist film was increased by a few millimeters, the photoresist removal rates drastically decreased; this suggests that short-lived radicals such as OH affect high-speed photoresist removal.

#### **Organotellurium-Mediated Living Radical Polymerization (TERP) of Acrylates Using Ditelluride Compounds and Binary Azo Initiators for the Synthesis of High-Performance Adhesive Block Copolymers for On-Demand Dismantlable Adhesion**

Tadashi INUI, Keisuke YAMANISHI, Eriko SATO, and Akikazu MATSUMOTO

*Macromolecules*, Vol. 46(20), pp. 8111-8120 (2013)

We report the organotellurium-mediated living radical polymerization (TERP) using diphenylditelluride (DT-Ph) and di-*n*-butylditelluride (DT-Bu) in the presence of a binary azo initiator system consisting of 2,2'-azobis(isobutyronitrile) (AIBN) and 2,2'-azobis(4-methoxy-2,4-dimethylvaleronitrile) (AMVN) with different decomposition rates for the facile synthesis of high-molecular-weight block copolymers containing a polar side group. The block copolymers containing the poly(*tert*-butyl acrylate) (PtBA) sequence as the reactive segment and the random copolymer sequences of *n*-butyl acrylate (nBA) or 2-ethylhexyl acrylate (2EHA) with 2-hydroxyethyl acrylate (HEA) as the adhesive segment were synthesized. The concurrent use of the binary initiators was revealed to effectively increase both the polymerization reactivity and the molecular weight of the polymers along with a narrow molecular weight distribution. The produced block copolymers exhibited high performance for the dismantlable adhesion responsible for the dual external stimuli consisting of photoirradiation and postbaking in the presence of a photoacid generator.

#### **One-Step Synthesis of Thermally Curable Hyperbranched Polymers by Addition-Fragmentation Chain Transfer Using Divinyl Monomers**

Eriko SATO, Izumi UEHARA, Hideo HORIBE, and Akikazu MATSUMOTO

*Macromolecules*, Vol. 47(3), pp. 937-943 (2014)

Free radical bulk and solution polymerizations of a divinyl monomer, ethylene glycol dimethacrylate (EGDMA), in the presence of methyl 2-(bromomethyl)acrylate as an addition-fragmentation chain transfer agent were investigated to synthesize thermally curable hyperbranched polymers by a one-step reaction. Soluble polymers were obtained up to high conversion of EGDMA, and the molecular weight and molecular weight distribution of the polymers increased with increasing EGDMA conversion. <sup>1</sup>H NMR and MALDI-MS analyses revealed that the soluble polymers were obtained after the consumption of a considerable amount of the pendant methacryloyl groups, and one polymer chain contained a number of end groups indicating the formation of hyperbranched polymers. The isolated hyperbranched polymers underwent thermal curing above 110 °C without curing agents, and the polymers having a large number of pendant methacryloyl groups resulted in a significant increase in glass transition temperature, i.e., from around room temperature to above 210 °C.

### **High-Molecular-Weight and Polar Acrylate Block Copolymers as High-Performance Dismantlable Adhesive Materials in Response to Photoirradiation and Postbaking**

Tadashi INUI, Eriko SATO, and Akikazu MATSUMOTO

*RSC Adv.*, Vol. 4(47), pp. 24719-24728 (2014)

We synthesized high-molecular-weight acrylate block copolymers as high-performance dismantlable adhesives consisting of a poly(*tert*-butyl acrylate) (PtBA) sequence as the reactive segment and a random copolymer sequence of *n*-butyl acrylate (nBA) or 2-ethylhexyl acrylate (2EHA) with 2-hydroxyethyl acrylate (HEA) as the adhesive segment, using an organotellurium-mediated living radical polymerization (TERP). The adhesion strength of PtBA/P2EHA and PtBA/PnBA block copolymers containing polar HEA repeating units in their soft segments was sufficiently high for use as a pressure-sensitive adhesive. A quick change in the adhesion properties was observed in response to the dual external stimuli of photoirradiation and postbaking during the dismantling process. We discuss the adhesion strength and failure mode as a function of the HEA content, the sequence structure of the copolymers, and the external stimulus conditions.

### **Dismantling Behavior of Pressure Sensitive Adhesives Using Acrylic Block and Random Copolymers in Response to Photoirradiation and Postbaking**

Eriko SATO, Kentaro TANIGUCHI, Tadashi INUI, Keisuk. YAMANISHI, Hideo HORIBE, and Akikazu MATSUMOTO

*J. Photopolym. Sci. Technol.*, Vol. 27(4), pp. 531-534 (2014)

### **Synthesis, Thermal, Optical, and Mechanical Properties of Sequence-Controlled Poly(1-adamantyl acrylate)-*block*-Poly(*n*-butyl acrylate) Containing Polar Side Group**

Yoshinori NAKANO, Eriko SATO, and Akikazu MATSUMOTO

*J. Polym. Sci., Part A: Polym. Chem.*, Vol. 52(20), pp. 2899-2910 (2014)

We prepared the sequence-controlled block copolymers including poly(1-adamantyl acrylate) (PAdA) and poly(*n*-butyl acrylate) sequences as the hard and soft segments, respectively, by the organotellurium-mediated living radical polymerization. The thermal, optical, and mechanical properties of the adamantane-containing block copolymers with polar 2-hydroxyethyl acrylate (HEA) and acrylic acid (AA) repeating units were investigated. The microphase-separated structures of the block copolymers were confirmed by the differential scanning calorimetry and atomic force microscopy observations as well as dynamic mechanical measurements. The  $\alpha$ - and  $\beta$ -dispersions due to the main-chain and side group molecular motions, respectively, of the hard and soft segments were observed. Their transition temperatures and activation energies increased due to the formation of intermolecular hydrogen bonding by the introduction of the HEA and AA repeating units. The effects of the hydrogen bonding on their tensile elasticity, strength, and strain were also evaluated.

### **Molecular Interaction of Polymer Side-Chains and Thermoresponsive Properties in Organic Solvent**

Eriko SATO

*Annual Review of Research Group on Supramolecules*, Vol. 34, pp. 6-7 (2013) (in Japanese)

### **Design of Dismantlable Adhesives Using Reactive Polymers**

Eriko SATO and Akikazu MATSUMOTO

*Fine chemical*, Vol. 43, pp. 5-11 (2014) (in Japanese)

### **Enhancement of Performance and Functionality of Dismantlable Adhesives by Design of Reactive Polymer Materials**

Eriko SATO

*The 135th Regular Meeting of Workshop on Pressure-Sensitive Adhesion, The Adhesion Society of Japan*, Invited Lecture, Tokyo, November 29, 2013 (in Japanese)

### **Design of Property Changeable Polymer Materials: Functionalization at Interface**

Eriko SATO

*The 146<sup>th</sup> Regular Meeting of Tokai Branch of The Society of Polymer Science*, Invited Lecture, Nagoya, December 12, 2013 (in Japanese)

### **Design of Functional Adhesives Using Reactive Polymers**

Eriko SATO

*Seibutsu Kougaku Settyaku Nentyaku Renkei Kenkyuukai (Cooperative Workshop on Biology, Engineering, and adhesives)*, Invited Lecture, Hiroshima, February 6, 2014 (in Japanese)

### **Property Transformation of Reactive Polymers and Application to Functional Materials**

Eriko SATO

*The Regular Meeting of the Consortium of Dismantlable Adhesion*, Invited Lecture, Osaka, May 9, 2014 (in Japanese)

### **Controlled Synthesis of Reactive Polymers and Their Application to Functional Adhesives**

Eriko SATO

*5th World Congress on Adhesion and Related Phenomena (WCARP-V)*, Invited Lecture, Nara, November 11, 2014, Proceedings, pp. 39-40

### **Fundamental Characteristics of Hybrid X-ray Focusing Optics for Micro X-ray Fluorescence Analysis**

Shintaro KOMATANI, Kazuo NAKAMACHI, Kazuhiko NAKANO, Sumito OHZAWA, Hiroshi UCHIHARA, Atsushi BANDO and Kouichi TSUJI

*Nucl. Instrum. Methods Phys. Res., Sect. B*, Vol. 309, pp. 260-263 (2013)

We developed a hybrid X-ray focusing optics, which consisted of a polycapillary X-ray lens (PCXL) and a tungsten conical pinhole (WCP) for micro X-ray fluorescence ( $\mu$ -XRF) analysis. A single PCXL produced an X-ray micro beam with a spot size of 12  $\mu$ m. We developed a WCP by using a laser-ablation technique with an input diameter of 39  $\mu$ m, an output diameter of 2.5  $\mu$ m, and a thickness of 0.5 mm in a conical shape. This hybrid X-ray optics gave a small spot size of 2.8  $\mu$ m with a small divergent angle of 12 mrad.

### **Elemental Depth Profiling of Forensic Samples by Confocal 3D-XRF Method**

Seiji EMOTO, Kazunori OTSUKI, Kazuhiko NAKANO and Kouichi TSUJI

*Advances in X-ray Analysis*, Vol. 56, pp. 217-224 (2013)

We report the feasibility of discrimination of leather samples related to forensic science by applying confocal 3D-XRF method. The laboratory made confocal 3D-XRF has a spatial

resolution of about 14 $\mu$ m at an energy of 11.4 keV. The characteristic elemental depth profiles and of multilayered leather samples were nondestructively obtained by using confocal 3D-XRF. Elemental depth profiles showed a layered structure obtained at a certain position on the sample. We tried to classify leather samples (natural, synthetic, and artificial) by cluster analysis concerning maximum intensity and maximum depth. The cluster analysis regarding maximum depth and maximum intensity suggested the possibility of discrimination of leather samples.

#### **Micro X-ray Beam Produced with a Single Glass Capillary for XRF Analysis**

Shintaro KOMATANI, Shintaro HIRANO, Tomoki AOYAMA, Yoshihiro YOKOTA, Hideo UEDA and Kouichi TSUJI

*Advances in X-ray Analysis*, Vol. 56, pp. 225-233 (2013)

XRF analysis is available for the quantification of elements and provides a great advantage in material science. Although XRF analysis has the advantage of nondestructive analysis, SEM-EDS gives elemental maps with a spatial resolution of a few micrometers. Thus, the developments and applications of micro-XRF analysis are important research trends of XRF analysis. A single glass capillary lens is the effective X-ray optics for micro-XRF in the laboratory. Actually, a beam diameter of 10 micrometers is available with commercial instruments such as X-ray analytical microscope. In the author's research group, a combination of a single glass capillary and a conical pinhole was studied for improving a spatial resolution in a micro XRF analysis.

In this study, another approach is discussed. We used a micro-focused X-ray tube (focal spot size: 50 x 50 micrometers, Mo anode, 50 kV, 0.5 mA) and a single glass straight capillary evaporated with Au and a small metal ball (400  $\mu$ m). The center part of X-rays emitted from the X-ray tube was stopped by the metal ball, while the outer part of X-rays was totally reflected on the inner wall of the single capillary. A focused X-ray beam had 107.5  $\mu$ m in diameter, and was observed at a distance of 43 mm from the output of the glass capillary.

Moreover, the divergence angle of the beam was 6 mrad. This long working distance with low divergence angle will be a practically useful advantage of this X-ray optic.

#### **Wavelength Dispersive X-ray Fluorescence Imaging using a High-sensitivity Imaging Sensor**

Takashi OHMORI, Shuichi KATO, Makoto DOI, Takashi SHOJI and Kouichi TSUJI

*Spectrochim. Acta, Part B*, Vol. 83-84, pp. 56-60 (2013)

A new wavelength-dispersive X-ray fluorescence (WD-XRF) imaging spectrometer equipped with a high-sensitivity imaging sensor was developed in our laboratory. In this instrument, a straight polycapillary optic was applied instead of a Soller slit as well as a 2D imaging X-ray detector instead of X-ray counters, which are used in conventional WD-XRF spectrometers. Therefore, images of elemental distribution were available after a short exposure time. Ni K $\alpha$  images and Cu K $\alpha$  images were clearly obtained at corresponding diffraction angles for a short exposure time of 10 s. By optimizing the spectrometer, the time required for imaging is reduced, leading to XRF image movies. It is difficult to distinguish two peaks (Ti K $\alpha$  (4.508 keV) and Ba L $\alpha$  (4.465 keV)) due to the poor energy resolution of EDXRS. However, Ti and Ba images could be successfully observed by the WD-XRF imaging spectrometer. The energy resolution of the developed spectrometer was 25 eV at the Ti K $\alpha$  peak.

#### **Depth-selective Elemental Imaging of MicroSD Card by Confocal Micro-XRF Analysis**

Takashi NAKAZAWA and Kouichi TSUJI

*X-Ray Spectrom.*, Vol. 42, pp. 123-127 (2013)

A semiconductor device, a microSD card, was measured by using two XRF instruments. 2D elemental images were obtained using a micro-XRF system with a spatial resolution of 10 $\mu$ m. Elemental distributions of the near-surface region of the sample were clearly shown. Titanium was observed in the resin constituting

the sample. Nickel and gold were observed on a terminal and localization of the sample. Elemental distribution of copper reflected the circuit structure of the measurement area that was in the neighborhood of the sample surface. Moreover, the elemental depth distributions of the sample were measured by using a confocal micro-XRF instrument. The confocal micro-XRF instrument was constructed in the laboratory with fine-focus polycapillary x-ray optics. The depth resolution of the developed spectrometer was 13.7 nm at an energy of Au L $\beta$  (11.4 keV). The elemental images obtained at near-surface by confocal micro-XRF were the same as the results obtained from 2D micro-XRF. However, different Cu images were obtained at a depth of several tens of micrometers. This indicates that microSD cards consist of a few different Cu-circuit structure designs. The elemental depth distributions of each circuit structure of the semiconductor device were clearly shown by confocal micro-XRF.

### **Development of a High Resolution Confocal Micro-XRF Instrument Equipped with a Vacuum Chamber**

Takashi NAKAZAWA and Kouichi TSUJI

*X-Ray Spectrom.*, Vol. 42, pp. 374-379 (2013)

A confocal micro-X-ray fluorescence (micro-XRF) instrument equipped with a vacuum chamber was newly developed. The instrument is operated under a vacuum condition to reduce the absorption of XRF in the atmosphere. Thin metal layers were developed to evaluate the confocal volume, corresponding to depth resolution. A set of thin metal layers (Al, Ti, Cr, Fe, Ni, Cu, Zr, Mo, and Au) was prepared by a magnetron sputtering technique. The depth resolutions of the new instrument were varied from 56.0 to 10.9  $\mu\text{m}$  for an energy range from 1.4 to 17.4 keV, respectively. The lower limit of detection (LLD) was estimated by comparison with a glass standard reference material NIST SRM 621). The LLDs obtained by a conventional micro-XRF were compared with the LLDs obtained by a confocal micro-XRF instrument. The LLDs were improved in the measurement under confocal configuration because of the reduction of background intensity. Finally, layered materials related to forensic investigation were measured. The confocal micro-XRF instrument was able to nondestructively obtain the distribution of light elements that cannot be detected by measurement in air.

### **SEM Observation of Inclusions in Steel Samples after Fast Surface Cleaning by Glow Discharge**

Kouichi TSUJI and Kenichi SHIMIZU

*ISIJ International*, Vol. 53, pp. 1936-1938 (2013)

SEM (scanning electron microscopy) is a useful technique for the observation of the surface morphology of various materials. Compared to TEM (transmission electron microscope), one of the advantages of SEM is easy sample preparation, although the spatial resolution of SEM is normally less than that of TEM. To improve the spatial resolution of SEM observation, it is well known that a low accelerating voltage SEM is an effective technique. We have proposed the application of glow discharge surface treatment before high-resolution SEM observation. An rf-glow discharge was applied with Ar gas for a steel sample just for 6 sec., leading to surface cleaning, that is, removing the surface oxidation or contamination layer. Besides the surface cleaning, a glow discharge sputtering modified the surface of the steel sample depending on crystal orientation. This surface modification was useful for high-resolution SEM observation. The surface of the steel sample was observed by FE (field emission)-SEM with a low accelerating voltage. A fine structure of grains and inclusions in the sample was clearly observed. The density of the inclusions was roughly determined as being  $4 \times 10^4/\text{cm}^2$ .

### **X-Ray Elemental Imaging in Depth by Combination of FE-SEM-EDS and Glow Discharge Sputtering**

Fumiya ONOUE and Kouichi TSUJI

*ISIJ International*, Vol. 53, pp. 1939-1942 (2013)

SEM-EDS is a powerful tool for fast, nondestructive x-ray elemental analysis of a localized region. Elemental mapping is also possible by scanning the electron beam. Since the penetration depth of the

electron beam is about a few  $\mu\text{m}$ , SEM-EDS is useful for determining elemental composition near the surface of the sample. To obtain information regarding the depth of the sample, the surface layer must be removed. For this purpose, we attempted to use glow discharge sputtering. A commercially available rf glow discharge sputtering device (Horiba, Tensec) enables fast sputtering in an area 4 mm in diameter. The combination of SEM-EDS and glow discharge sputtering would be useful for observation of the distribution of inclusions buried in metal samples.  $\text{Al}_2\text{O}_3$  particles were mixed with Cu powders, and then pressed into a disk, which was measured. The same area of the sample was analyzed by FE-SEM-EDS and sputtered. The result indicated the possibility of 3D distribution analysis of inclusions in the sample.

### **Elemental Depth Analysis of Corroded Paint-Coated Steel by Confocal Micro-XRF Method**

Kazuhiko NAKANO, Koji AKIOKA, Takashi DOI, Masahiro ARAI, Hideki TAKABE and Kouichi TSUJI  
*ISIJ International*, Vol. 53, pp. 1953-1957 (2013)

A confocal micro-XRF method combined with two individual polycapillary lenses was applied to steel sheets coated with anti-corrosive paint in order to nondestructively observe 3D elemental distribution of paint steels and corroded paint-coated steels. Nondestructive depth analysis and 3D elemental mapping of the painted steel sheets were demonstrated under the confocal XRF configuration. Three different painted steel sheets were prepared by cation electrodeposition coating for automotive onto flat steel sheets modified with a zinc phosphate conversion coating. These painted sheets were then caused to corrode by means of accelerated exposure to a salt bath (5 mass% NaCl) at 55°C for 240 hours. Depth elemental profiles of Ti, Zn, and Fe obtained by confocal micro-XRF measurements were in excellent agreement with that of the prepared sample. Elemental depth profiles and maps of the corroded painted sheets showed some blisters caused by crevice corrosion, which started from the site of a scratch. The distributions of Ti and Fe were approximately homogeneous in both the paint layer and the steel substrate, while the distributions of Zn, Mn, Ca, and Cl were heterogeneous.

### **X-ray Fluorescence Imaging**

Kouichi TSUJI

*Journal of the Spectroscopical Society of Japan*, Vol. 62, pp. 119-127 (2013) (in Japanese)

X-ray Fluorescence (XRF) analysis is a powerful tool for elemental analysis of solid and liquid samples. Compared to other instrumental analytical methods, such as SEM-EDS, XRF analysis has an advantage of nondestructive analysis at ambient air pressure. XRF analysis at small region is possible with advanced x-ray focusing optics in the laboratory. This micro-XRF technique with scanning the sample gives us elemental images. The spatial resolution of micro-XRF depends on the size of the x-ray beam. The drawback of micro-XRF for elemental imaging would be its long acquisition time for a large sample with high-resolution. On the other hand, projection type XRF imaging has been studied using a two-dimensional x-ray detector. The advantage of this projection type technique is a fast elemental imaging. In this paper, scanning type and projection type XRF imaging techniques will be discussed showing recently developed instruments based on wavelength dispersive and energy dispersive x-ray spectrometers.

### **Development and Evaluation of Micro XRF Instrument with Hybrid X-Ray Optics**

Junki MATSUYA and Kouichi TSUJI

*Advances in X-Ray Chemical Analysis, Japan*, Vol. 44, pp. 111-119 (2013) (in Japanese)

We developed a micro-XRF instrument with a hybrid X-ray optic in order to obtain an intense micro X-ray beam in laboratory. The hybrid X-ray optic consists of the polycapillary X-ray lens and the Zr pinhole. The Zr pinhole, which was inserted between the X-ray tube and the polycapillary X-ray lens, was useful for reducing the spot size of micro X-ray beam. In addition, the divergence of micro X-ray beam was reduced by applying the Zr pinhole with a diameter of 400  $\mu\text{m}$ . Moreover, SB ratio of X-ray fluorescence was also improved by using the Zr pinhole.

### **Catalytic Hydrothermal Oxidation of *p*-Chlorophenol with Cu or Fe-Grafted TiO<sub>2</sub>. Enhanced Decomposition by Fenton-Type Reaction**

Ai SHIMOKAWA, Hiroki HONDA, Kyohei NAKAO, and Noritsugu KOMETANI

*Journal of Chemical Engineering of Japan*, Vol. 46, No. 12, pp. 821–826 (2013)

Catalytic hydrothermal oxidation of *p*-chlorophenol has been examined using two types of reactor systems, i.e., a flow-type reactor system in which the catalyst powder was suspended in the reaction mixtures and a fixed-bed reactor system in which the sintered catalyst was packed in the reactor. Cu- or Fe-grafted TiO<sub>2</sub> was employed as a catalyst and hydrogen peroxide was used as an oxidizing reagent. The decomposition efficiency of *p*-chlorophenol treated by the flow-type reactor system is considerably enhanced with the help of Cu-grafted TiO<sub>2</sub> at reaction temperatures around 200°C; whereas, little effect is observed at any temperature for Fe-grafted TiO<sub>2</sub>. It is suggested that the Fenton-type reaction catalyzed by Cu ions contained in the Cu-grafted TiO<sub>2</sub> and/or dissolved out in the solution undergoes substantial acceleration at high temperatures, leading to the increased generation of OH· radicals that can effectively oxidize *p*-chlorophenol. On the other hand, it appears that the Fe-ion-catalyzed Fenton reaction is suppressed in the hydrothermal environment. The prolonged treatment of *p*-chlorophenol using the fixed-bed reactor system, that is more suitable for practical use than the flow-type one, has also been performed with Cu-grafted TiO<sub>2</sub> catalyst at a reaction temperature of 200°C. The result demonstrates that it is possible to treat *p*-chlorophenol continuously for up to 36 h without significant loss of the catalytic activity.

### **Spectroscopic Study of Solvation Properties of Room-Temperature Ionic Liquids and Solvent Effect on Bimolecular Fluorescence Quenching Reaction at High Pressures**

Noritsugu KOMETANI and Yoshinori MINAMIKAWA

*Review of High Pressure Science & Technology*, Vol. 23, No. 4, pp. 332-338 (2013)

The solvation properties of some room-temperature ionic liquids (RTILs) and the solvent effect on bimolecular fluorescence quenching reaction have been examined at high pressures ranging from 0.1 to 300 MPa. It is found that Kamlet-Taft parameters ( $\pi^*$ ,  $\beta$ ) are sensitive to the type of anions, but not so dependent on the type of imidazolium cations consisting of RTILs. The pressure dependence of microviscosity is found to obey the empirical power-law equation. It is revealed that the rate constant for bimolecular fluorescence quenching reaction is significantly higher than theoretical rate constant of diffusion estimated from microviscosity, suggesting the occurrence of microscopic free space within RTILs which may facilitate the solute diffusion.

### **In Situ Observation of Heat- and Pressure-Induced Gelation of Methylcellulose by Fluorescence Measurement**

L. SU, Z. WANG, K. YANG (Zhengzhou Univ. of Light Industry), Y. MINAMIKAWA, N. KOMETANI, and K. NISHINARI (Hubei Univ. of Technology)

*International Journal of Biological Macromolecules*, Vol. 64, pp. 409-414 (2014)

In situ observation of heat- and pressure-induced gelation of methylcellulose (MC) aqueous solution has been studied by using dynamic viscoelastic and fluorescence measurements. The storage modulus  $G'$  decreased gradually first on heating, and then leveled off in the temperature range from 25°C to 75°C. Methylcellulose solutions were subjected to pressures up to 450 MPa by using a high pressure cell. It was indicated that the microviscosity showed a dramatic change in the vicinity of the phase transition point. The T vs. P phase diagram of methylcellulose aqueous solution was constructed, and it indicated that the melting point was an increasing function of pressure. In situ microscopic observation of pressure-induced gelation of methylcellulose aqueous solution was also performed with a microscope, and it could be seen that gel phase of the sample disappeared and sol formed gradually. Pressure-released study by fluorescence measurement also showed that the phase transition of MC solution was reversible.

### **Crystal Thickness Dependence of Photoinduced Crystal Bending of 1,2-Bis(2-methyl-**

### **5-(4-(1-naphthoylethoxymethyl)phenyl)-3-thienyl)perfluorocyclopentene**

Daichi KITAGAWA and Seiya KOBATAKE

*J. Phys. Chem. C*, Vol. 117(40), pp. 20887–20892 (2013)

The photoinduced crystal bending of a photochromic diarylethene derivative, 1,2-bis(2-methyl-5-(4-(1-naphthoylethoxymethyl)phenyl)-3-thienyl)perfluorocyclopentene (**1a**), has been particularly investigated. The rod-like crystal of **1a** shows reversible photoinduced bending upon alternating irradiation with ultraviolet (UV) and visible light. The photoinduced crystal bending can be repeated over 80 cycles. The rod-like crystal of **1a** shows different bending behavior depending on the faces irradiated with UV light. This is ascribed to the molecular orientation viewed from the faces. Furthermore, we found that the bending speed depends on the crystal thickness and the curvature change against the crystal thickness is well fitted to Timoshenko's bimetal model. These findings provide a new useful strategy to design for the photomechanical actuators.

### **Alkyl Substituent Effects in Photochemical and Thermal Reactions of Photochromic Thiophene-*S,S*-Dioxidized Diarylethenes**

Hiroaki SHOJI, Daichi KITAGAWA, and Seiya KOBATAKE

*New J. Chem.*, Vol. 38(3), pp. 933–941 (2014)

Thiophene-*S,S*-dioxidized diarylethenes introducing various alkyl groups at the reactive positions were newly synthesized. The diarylethenes showed reversible photochromism, whereas the photocycloreversion reaction was suppressed by thiophene-oxidation. The diarylethene closed-ring isomers with secondary alkyl groups at the reactive positions were found to undergo thermal bleaching reactions to produce byproducts. The thermal bleaching reactions were accelerated by introducing a more bulky substituent at the reactive positions. The relationship between the rate constant of the thermal bleaching reactions and the bulkiness of the substituent at the reactive positions can be correlated using a steric substituent constant. Moreover, it was noted that introduction of a methyl group at the 4-position of the thiophene in the oxidized diarylethenes accelerates the thermal byproduct formation. The rate of the thermal bleaching reactions was found to depend on the difference in the ground state energy between the closed-ring isomer and one of the byproducts, as can be estimated by theoretical calculation of the energy level. Such materials can be used in application such as light-starting irreversible thermosensors.

### **Thermodynamic Phase Transition Through Crystal-to-Crystal Process of Photochromic 1,2-Bis(5-phenyl-2-propyl-3-thienyl)perfluorocyclopentene**

Daichi KITAGAWA and Seiya KOBATAKE

*Chem. –Asian J.*, Vol. 9(1), pp. 289–293 (2014)

A photochromic diarylethene, 1,2-bis(5-phenyl-2-propyl-3-thienyl)perfluorocyclopentene (**1a**), was found to have two polymorphic crystal forms,  $\alpha$ - and  $\beta$ -crystals. From X-ray crystallographic analysis, the space groups of  $\alpha$ - and  $\beta$ -crystals are  $P2_1/c$  and  $C2/c$ , respectively. The difference between two crystal forms is ascribed to orientation of two of four molecules in the unit cell. The thermodynamic phase transition from  $\alpha$ - to  $\beta$ -forms occurred via a crystal-to-crystal process, as confirmed by differential scanning calorimetry measurement, optical microscopic observation in reflection mode and under crossed nicols, and powder X-ray diffraction profile. The movement of the molecules in the crystal was evaluated by the change of face indices before and after the phase transition.

### **Crystal Thickness Dependence of Photoinduced Crystal Bending of 1-(5-Methyl-2-(4-(*p*-vinylbenzoyloxy)methyl)phenyl)-4-thiazolyl)-2-(5-methyl-2-phenyl-4-thiazolyl)perfluorocyclopentene**

Daichi KITAGAWA and Seiya KOBATAKE

*Photochem. Photobiol. Sci.*, Vol. 13(5), pp. 764–769 (2014)

Rod-like crystals of 1-(5-methyl-2-(4-(*p*-vinylbenzoyloxy)methyl)phenyl)-4-thiazolyl)-2-(5-methyl-2-phenyl-4-thiazolyl)perfluorocyclopentene with lengths of over 1 mm showed photoreversible bending over 100

cycles upon irradiation with alternating ultraviolet (UV) and visible light. The crystals bent toward the incident light due to a contraction of the crystal length and a gradient of the crystal thickness, which depend on the extent of photoisomerization. It was observed that the bending speed depends on the crystal thickness, and the curvature change on changing the crystal thickness agrees well with Timoshenko's bimetal model, as well as with the observation that crystals of 1,2-bis(2-methyl-5-(4-(1-naphthoyloxymethyl)phenyl)-3-thienyl)perfluorocyclopentene bend away from the incident light due to an expansion of the crystal length and a gradient of the crystal thickness, which depend on the extent of photoisomerization. It was revealed that Timoshenko's bimetal model can be applied to photoinduced crystal bending behaviors caused by both contraction and expansion. These findings are very useful for evaluating and designing photomechanical actuators.

### **Photoresponsive Molecular Machinery of Photochromic Diarylethene Crystals**

Seiya KOBATAKE and Daichi KITAGAWA

*Joint Congress of Asian Crystallization Technology Symposium-2014 (ACTS-2014) and 11th International Workshop on Crystal Growth of Organic Materials (CGOM11)*, Invited Oral Communication, OC-CGOM-31, Nara, Japan, June 17–20, 2014; Abstract, CD-ROM, OC-CGOM-31 (2014)

Some diarylethene derivatives are designed and synthesized for study on the photoinduced crystal shape changes. Upon irradiation with UV light to the diarylethene crystals, the molecules in the crystals underwent a photocyclization reaction that transforms the initial open-ring isomers into the photogenerated closed-ring isomers. The rod-like crystal of diarylethene **1a** showed the crystal bending away from the incident UV light. The bent crystal returned to the initial straight crystal by irradiation with visible light. The bending speed depended on the crystal thickness and the curvature change against the crystal thickness was well fitted to Timoshenko's bimetal model. The rod-like crystal of diarylethene **2a** bent toward the incident UV light. The bending speed also depended on the crystal thickness and the curvature change against the crystal thickness was well fitted to Timoshenko's bimetal model. Furthermore, we have found specific crystal ribbon deformation of diarylethene **3a**. This crystal reversibly changed from the straight thin crystal to the spiral crystal. Such deformation depends on the crystal packing. These materials can be potentially applied for novel organic solid devices, and it is possible not only to become a new organic device but also to open a new possibility as the crystal materials.

### **Polymorphism and Phase Transition between Polymorphic Forms of Photochromic Diarylethene Crystals**

Daichi KITAGAWA and Seiya KOBATAKE

*Joint Congress of Asian Crystallization Technology Symposium-2014 (ACTS-2014) and 11th International Workshop on Crystal Growth of Organic Materials (CGOM11)*, Poster Presentation, PC-22, Nara, Japan, June 17–20, 2014; Abstract, CD-ROM, PC-22 (2014)

Diarylethene **1a** was found to have two polymorphic crystal forms,  $\alpha$ - and  $\beta$ -crystals. From X-ray crystallographic analysis, the space groups of  $\alpha$ - and  $\beta$ -crystals were determined to be  $P2_1/c$  and  $C2/c$ , respectively. The difference between two crystal forms is ascribed to the orientation of two of four molecules in the unit cell. The thermodynamic phase transition from  $\alpha$ - to  $\beta$ -forms occurred via a crystal-to-crystal process, as confirmed by differential scanning calorimetry measurements, optical microscopic observations in the reflection mode and under crossed Nicols, and powder X-ray diffraction measurements. The movement of the molecules in the crystal was evaluated by analyzing the change of face indices before and after the phase transition. A photochromic diarylethene crystal of **2a** was found to undergo a thermodynamic phase transition from plate-like  $\alpha$ -crystal to needle-like  $\gamma$ -crystal at 180 °C. The phase transition involves melting of the initial  $\alpha$ -crystal and growth of the  $\gamma$ -crystal. The phase transition temperature decreased with the presence of the closed-ring isomer (**2b**) in the crystal because of the decrease in the melting temperature. Upon irradiation with ultraviolet (UV) light, compound **2a** in the  $\alpha$ -crystal was converted into **2b** to an extent of 20%. Consequently, the  $\alpha$ -crystal containing 20% of **2b** underwent the phase transition

accompanied by melting of the crystal and growth of the  $\gamma$ -crystal even at 170 °C. Photomicro patterning by the phase transition upon irradiation with UV light using a photomask, followed by heating at 170 °C, was successfully accomplished with a resolution in the microcrystalline pattern of about 20  $\mu\text{m}$ .

### **Photoresponsive Molecular Machinery of Photochromic Diarylethene Crystals**

Seiya KOBATAKE and Daichi KITAGAWA

*Joint Congress of Asian Crystallization Technology Symposium-2014 (ACTS-2014) and 11th International Workshop on Crystal Growth of Organic Materials (CGOM11)*, Poster Presentation, PC-49, Nara, Japan, June 17–20, 2014; Abstract, CD-ROM, PC-49 (2014)

Some diarylethene derivatives are designed and synthesized for study on the photoinduced crystal shape changes. Upon irradiation with UV light to the diarylethene crystals, the molecules in the crystals underwent a photocyclization reaction that transforms the initial open-ring isomers into the photogenerated closed-ring isomers. The rod-like crystal of diarylethene **1a** showed the crystal bending away from the incident UV light. The bent crystal returned to the initial straight crystal by irradiation with visible light. The bending speed depended on the crystal thickness and the curvature change against the crystal thickness was well fitted to Timoshenko's bimetal model. The rod-like crystal of diarylethene **2a** bent toward the incident UV light. The bending speed also depended on the crystal thickness and the curvature change against the crystal thickness was well fitted to Timoshenko's bimetal model. Furthermore, we have found specific crystal ribbon deformation of diarylethene **3a**. This crystal reversibly changed from the straight thin crystal to the spiral crystal. Such deformation depends on the crystal packing. These materials can be potentially applied for novel organic solid devices, and it is possible not only to become a new organic device but also to open a new possibility as the crystal materials.

### **Photoinduced Bending Behavior of Diarylethene Crystals**

Daichi KITAGAWA and Seiya KOBATAKE

*XXVth IUPAC Symposium on Photochemistry*, Poster Presentation, P151, Bordeaux, France, July 13–18, 2014; Abstract, CD-ROM, P151 (2014)

We have focused on the quantitative evaluation of photoinduced crystal bending among various diarylethene derivatives. All of diarylethenes **1–5** showed the photoinduced crystal bending behavior caused by expansion and contraction of the photoreacted crystal surface and the dependence on the crystal thickness in their bending speed. The correlation between the initial speed of the curvature change and the crystal thickness in all of the diarylethene crystals can be explained by Timoshenko's bimetal model. When the thickness of photoreacted layer ( $h_2$ ) in bimetal model is the same among different crystals, the bending speed can be compared quantitatively using the value of actuation strain  $\alpha$ . In most cases, it cannot be discussed because the  $h_2$  values are different. Then, we focused on the relationship between  $h_2$  and  $\alpha$  in the same crystal. As a result, it was theoretically and experimentally clarified that the value of  $\alpha$  is proportional to  $1/h_2$ . By using this relationship, the effect of  $h_2$  on the value of  $\alpha$  can be normalized. In other words, the slope of a line through the origin in the relationship between  $\alpha$  and  $1/h_2$  is the unique value in each crystal. The relative bending speed was determined to be 1.00 (**1**), 0.65 (**2**), 1.22 (**3**), 1.98 (**4**), and 2.96 (**5**). The values mean the relative potential capability of the photoinduced crystal bending speed in the diarylethene crystals.

### **Photoresponsive Bending and Twisting of Photochromic Diarylethene Crystals**

Seiya KOBATAKE and Daichi KITAGAWA

*XXVth IUPAC Symposium on Photochemistry*, Poster Presentation, P171, Bordeaux, France, July 13–18, 2014; Abstract, CD-ROM, P171 (2014)

Diarylethene derivatives are designed and synthesized for study on the photoinduced crystal shape changes. Upon irradiation with UV light to the diarylethene crystals, the molecules in the crystals underwent a photocyclization reaction that transforms the initial open-ring isomers into the photogenerated closed-ring isomers in the crystalline phase. The rod-like crystal of diarylethene **1a** showed the crystal bending away

from the incident UV light. The bent crystal returned to the initial straight crystal by irradiation with visible light. The bending speed depended on the crystal thickness and the curvature change against the crystal thickness was well fitted to Timoshenko's bimetal model. The rod-like crystal of diarylethene **2a** bent toward the incident UV light. The bending speed also depended on the crystal thickness and the curvature change against the crystal thickness was well fitted to Timoshenko's bimetal model. Furthermore, we have found specific crystal ribbon deformation of diarylethene **3a**. This crystal reversibly changed from the straight thin crystal to the spiral twisting crystal. Such deformation depends on the crystal packing. These materials can be potentially applied for novel organic solid devices, and it is possible not only to become a new organic device but also to open a new possibility as the crystal materials.

### **Preparation and Photoinduced Bending Behavior of Diarylethene Microfibers**

Hajime TSUJIOKA and Seiya KOBATAKE

*XXVth IUPAC Symposium on Photochemistry*, Poster Presentation, P238, Bordeaux, France, July 13–18, 2014; Abstract, CD-ROM, P238 (2014)

When the microfiber was irradiated with ultraviolet light from the left side, the microfiber was found to be bent in the direction toward the incident light. The bent fibers did not return to the initial-shaped fibers by irradiation with visible light. To examine the preparation condition of the microfibers, the microfibers were prepared by stretching each of the melting viscous at 95 °C and 125 °C. The bending speed was increased by the preparation at 95 °C compared to 125 °C. When the microfiber was observed by polarizing microscopy under crossed Nicols, the birefringence was confirmed. From observations of the birefringence, this microfiber was found to be optically positive uniaxial material. The birefringence means that the diarylethene molecules were oriented in the microfiber. This orientation was improved by the preparation at 95 °C compared to 125 °C. These results suggest that the orientation of molecules relates to photoinduced bending behavior of microfibers. This molecular orientation in the microfiber was not disturbed by UV irradiation, but was disturbed by visible light irradiation after UV light irradiation.

### **Amazing Catalytic Activity of *Epi*-Quinine-Derived 3,5-Bis(trifluoromethyl)benzamide in Asymmetric Nitro-Michael Reaction of Furanones**

Tohru SEKIKAWA, Takayuki KITAGUCHI, Hayato KITAURA, Tatsuya MINAMI, and Yasuo HATANAKA  
*J. Am. Chem. Soc.*, accepted

Unusually high catalytic activity of novel *epi*-quinine-derived 3,5-bis(CF<sub>3</sub>)benzamide in the asymmetric nitro-Michael reaction is described. With 0.1-5 mol % loadings of this catalyst, the addition of 5-substituted 2(3-*H*)furanones to a wide range of nitroalkenes involving traditionally challenging substrates,  $\beta$ -alkyl nitroalkenes smoothly proceeded, giving the Michael adducts in high yields (> 90%) with excellent diastereo- and enantioselectivity (> 98 : 2 dr, *syn* major; 90-98% ee). DFT calculation was carried out to account the high catalytic activity.

### **Bell-Shaped Dependence of the Rate of Ultrafast Photoinduced Electron Transfer from Aromatic Amino Acids to the Excited Flavin on the Donor–Acceptor Distance in FMN Binding Proteins**

Nadtanet NUNTHABOOT, Kiattisak LUGSANANGARM, Somsak PIANWANIT, Sirirat KOKPOL, Fumio TANAKA, Seiji TANIGUCHI, Haik CHOSROWJAN, Takeshi NAKANISHI, and Masaya KITAMURA  
*Comput. Theor. Chem.*, Vol. 1030, pp. 9–16 (2014)

Flavin mononucleotide (FMN)-binding proteins (FBP) from *Desulfovibrio vulgaris*, Miyazaki F, contain FMN as a cofactor. Upon photo-excitation of the FBP, photoinduced electron transfer (ET) takes place from tryptophan (Trp)<sup>32</sup>, tyrosine (Tyr)<sup>35</sup> and Trp<sup>105</sup> residues to the excited isoalloxazine ring (Iso\*) of FMN. The ultrafast fluorescence dynamics of the wild type, and the E13K, E13R, E13T and E13Q substitution isoforms of FBP were simultaneously analyzed with molecular dynamics simulation structures and Kakitani-Mataga ET theory, to obtain the time-dependent ET rates. A bell-shaped behavior of the logarithmic ET rates ( $\ln k_{ET}$ ) from Trp<sup>32</sup> and Trp<sup>106</sup> to Iso\* versus the centre-to-centre donor–acceptor distances ( $R_c$ ) was

obtained in the time domain of sub-ps to ps in all five FBP isoforms. The  $\ln k_{ET}$  from Tyr35 to Iso\* linearly decreased with the  $R_c$  distance, which were much slower than those of Trp32 and Trp105. These findings suggest that the nuclear term in the ET theory is important in the ultrafast time domain, whereas the electronic coupling term may be dominant in slower ET rates.

### **Crystallization Behavior of Ibuprofen under Microwave Irradiation**

K. IGARASHI, S. KIHARA and H. OOSHIMA

*Journal of Chemical Engineering of Japan*, Vol. 46, pp. 797–801 (2013)

The batch cooling crystallization of the organic compound, ibuprofen, was carried out under 2.45 GHz microwave irradiation. *n*-Hexane containing a small amount of acetone (5 mol%) and Fluorinert™, which did not absorb microwave, were selected as the solvent and coolant circulating through the jacket of crystallizer, respectively. The ibuprofen-hexane solution was cooled from 40 to  $-1^{\circ}\text{C}$  under microwave irradiation and no irradiation. When the solution was not irradiated to the solution, ibuprofen crystals appeared at  $35^{\circ}\text{C}$ . On the other hand, when irradiation with 300 W microwave was carried out, nucleation did not occur even when the solution temperature reached to  $-1^{\circ}\text{C}$ . At that time, the supersaturation ratio was 9.5. Thus, crystal nucleation of ibuprofen was inhibited by the microwave irradiation. The effect of microwave irradiation continued for at least 100 min after the irradiation was stopped at  $-1^{\circ}\text{C}$ . By adding a small amount of crystals to the highly supersaturated solution, small crystals with a narrow size distribution were produced.

### **Structure of supersaturated solution and crystal nucleation induced by diffusion**

H. OOSHIMA, K. IGARASHI, H. IWASA, R. YAMAMOTO

*Journal of Crystal Growth*, Vol. 373, pp. 2-6 (2013)

The effect of a seed crystal on nucleation of L-alanine from a quiescent supersaturated solution was investigated. When a seed crystal was not used, nucleation did not occur at least for 5 h. When a seed crystal was introduced into the supersaturated solution with careful attention to avoid convection of the solution, fine crystals appeared at the place far from the seed crystal. At that time, there was no convection at the place that fine crystals appeared. Namely, there was no possibility that those fine crystals came from the surface of seed crystal. We supposed that nucleation was induced by directional diffusion of solute molecules caused by growth of the seed crystal. In order to prove this hypothesis, we designed an experiment using an apparatus composed of two compartments divided by a dialysis membrane that L-alanine molecules could freely permeate. Two supersaturated solutions having a supersaturation ratio of 1.2 and a smaller ratio were placed in the two compartments in the absence of seed crystals. This apparatus allowed the directional diffusion of solute molecules between two solutions. Nucleation occurred within 30 min. The frequency of nucleation among 7-times repeated experiments was in proportion to the difference of supersaturation ratio between the two solutions. This result poses a new mechanism of the secondary nucleation that the directional diffusion caused by growth of existing crystals induces nucleation.

### **Effect of a Small Amount of Water on Crystallization of Ergosterol**

K. NAKAHASHI, K. IGARASHI, and H. OOSHIMA

*Joint Congress of ACTS-2014 and CGOM11*, Nara, Japan (2014)

Many of organic or inorganic compounds crystallize as a hydrate or a solvate form. In industrial crystallization, the control of hydrate is important as well as control of polymorphs. For example, in the cooling crystallization of Ergosterol (ERG) from the hexane solution, two types of precipitates may appear, namely mono hydrate crystal and globular amorphous form. In the case that enough amount of water exists in the solution ( $> 1173$  ppm), the needle-like monohydrate crystals can be obtained. However, the water content is insufficient, only amorphous form precipitates. Fig.1 shows SEM images of the ERG mono hydrate crystals and amorphous. In this study, the effect of the water content in the solution on the cooling crystallization of ERG mono hydrate was investigated. Though water hardly dissolves in hexane ( $\sim 20$  ppm),

more water can dissolve in the ERG-hexane solutions. It means that the water molecules interact with the ERG molecules in hydrophobic environment. To control the activity of water in the solution, a small amount of 2-propanol (IPA) was added to the solution. Fig. 2 shows XRD profiles of crystals obtained from the solution with different content of IPA. The XRD of crystals decreased increase of the IPA content. It suggested that the water molecules interact with the IPA molecules instead of the ERG molecules. The interaction between water and IPA molecules was investigated by Isothermal titration calorimetry.

### **Development of a novel fines dissolver to produce uniform large crystals**

K. IGARASHI, M. ARIMOTO, H. OOSHIMA

*Joint Congress of ACTS-2014 and CGOM11*, Nara, Japan (2014)

In the industrial crystallization, there are many characteristics of product crystals that must be well controlled. Crystal size distribution (CSD) is one of the most important characteristics of crystals. In many cases, large crystals with a narrow CSD are preferred to make filtration easy. Various methods have been attempted to obtain uniform large crystals. As an effective solution, we have proposed the WWDJ-batch crystallizer, which can dissolve undesirable fine crystals on the heated inner wall of the head space of crystallizer. In the present paper, we propose a novel batch crystallizer suitable for production of large and uniform crystals. The crystallizer is composed of a jacketed-glass vessel, a newly developed fines-dissolver equipped with an induction-heating (IH) system, and an agitation propeller (Fig.1). The fines-dissolver is a connected body of a stainless-steel cylinder and a circular truncated cone at lower side. It was set on a coaxial rotation rod with an agitation propeller. The rotation speed of the dissolver and the agitation propeller can be individually controlled. The lower end of the dissolver is placed in crystallization solution at a given depth from solution level. To heat the fines-dissolver, the IH coil sealed from crystallization slurry is put around the fines-dissolver. The rotating fines-dissolver was directly heated by a high-frequency alternating current flows through the IH coil. The slurry is lifted up along the inner wall of the heated fines-dissolver by the centrifugal force, and is returned to the crystallization phase from the top of the dissolver. Fine crystals in the lifted slurry can be expected to partially dissolve. The surviving large crystals are also expected to grow further, at the expense of fine crystals, after returning to the crystallization phase. Using the novel crystallizer, cooling crystallization of glycine was performed by controlling the temperature from 50 to 25°C at the initial concentration of glycine of 268 mg/ml. The performance of the crystallizer was compared with that of a conventional batch cooling crystallization without the fines-dissolver. The average particle size obtained in a conventional crystallization was 622 µm. On the other hand, when the novel crystallizer was used, the average size of crystals was 1544 µm.

### **Kojic Acid-Appended Carborane/Hydroxypropyl-β-Cyclodextrin Complex: A Novel Boron Carrier for Melanoma Targeting**

Riku KAWASAKI, Takeshi NAGASAKI, Jiawei LI, Hideki AZUMA, Shin-ichiro MASUNAGA, Mitsunori KIRIHATA, Yoshihide HATTORI and Naoyuki KADONO

*KURRI Progress Report 2011*, pp. 107 (2012)

Metastatic melanoma remains a highly lethal cancer. BNCT has been attracted great deal of attention as a potentially useful modality for this disease. The delivery of <sup>10</sup>B compounds deeply inside the tumor cells and, possibly, close the nucleus is also an important requirement in order to improve the efficacy of BNCT. Kojic acid is well known to work as an excellent whitening agent for melanocytes by a strong tyrosinase inhibition. This fact suggests that kojic acid possess a specific affinity for melanocytes. In this paper, we evaluate kojic acid-appended o-carborane (CKA) as BNCT boron agent for melanoma. It was found that CKA has melanoma affinity based on possessing of kojic acid moiety although detail mechanism is unclear yet. In B16BL6 cells, CKA was interestingly localized in the nucleus.

### **Intracellular Distribution of BSH-Appended Polyamine at Tumor Tissue of Colon 26 Carcinoma-Bearing Mice**

Masayuki UMANO, Jiawei LI, Hideki AZUMA, Takeshi NAGASAKI, Hironobu YANAGIE, Mitsunori KIRIHATA, Koji ONO, Shin-ichiro MASUNAGA and Yoshinori SAKURAI

*KURRI Progress Report 2011*, pp. 274 (2012)

The neutron irradiation experiment by using polyion complex nanoparticle composed of mercaptoundecahydrododecaborane-appended high molecular weight polyamine (BPP) showed suppressive effect for the tumor growth in colon 26 carcinoma-bearing mice. Although the boron concentration at tumor tissue was less than 10 ppm, the sufficient BNCT effect was observed. Here, we report the intracellular distribution of fluorescently labeled BPP and BSH residues introduced into the polymeric carrier using an immunostaining with anti-BSH antibody. BPP remain at perinuclear regions. The intracellular distribution in which BSH is close to genome DNA might contribute higher BNCT efficacy by BPP complex.

### **Kojic Acid-Appended Carborane/Hydroxypropyl- $\beta$ -Cyclodextrin Complex for BNCT of Murine Melanoma**

Riku KAWASAKI, Takeshi NAGASAKI, Jiawei LI, Hideki AZUMA, Shin-ichiro MASUNAGA, Mitsunori KIRIHATA and Yoshihide HATTORI

*KURRI Progress Report 2012*, pp. 153 (2013)

Kojic acid is well known to work as an excellent whitening agent for melanocytes by a strong tyrosinase inhibition. This fact suggests that kojic acid possess a specific affinity for melanocytes. Previously, we found that kojic moiety functionalized not only to accumulate selectively into melanoma cells, but also to localize nuclei. As these results indicated that CKA was promising to be a boron agent for melanoma BNCT, herein, we evaluated CKA as BNCT agent *in vivo*. When 1500 ppm of  $^{10}\text{B}$  solutions was used, average survival rate were 19 and 22 days with L-BPA/fructose and CKA/HP- $\beta$ -CD complex, respectively. Moreover, long survival rates (25 days) were observed with 4500 ppm of  $^{10}\text{B}$  solutions of CKA/HP- $\beta$ -CD complex. CKA is promising to be an efficient boron agent toward melanoma BNCT.

### **Mechanism Involved in Tumor Tissue of Colon 26 Carcinoma-Bearing Mice Irradiated with Neutron in the Presence of BSH-Appended Polyamine**

Takeshi NAGASAKI, Riku KAWASAKI, Masashi Sakuramoto, Hideki AZUMA, Hironobu YANAGIE, Yoshihide HATTORI, Mitsunori KIRIHATA, Koji ONO, Shin-ichiro MASUNAGA and Yoshinori SAKURAI

*KURRI Progress Report 2012*, pp. 259 (2013)

Since BSH-appended polymeric  $^{10}\text{B}$  carrier has anionic zeta-potential, polyion complexes with cationic polymer afford nanoparticles suitable for safe and effective delivery into tumor tissues due to EPR effect. The neutron-irradiation experiment was carried out with the complex in colon 26 carcinoma-bearing mice. Significant depression effect for the tumor proliferation was observed. Herein, mechanism of tumor growth suppression was assessed using well-characterized TUNEL assay. Obtained results indicated that BNCT with BSH-appended polyamine induced apoptosis of tumor cells *in vivo*.

### **Carborane-Kojic Acid Conjugate for Melanoma-Targeting Boron Neutron Capture Therapy**

Takeshi NAGASAKI, Riku KAWASAKI, Koji ONO, Shin-ichiro MASUNAGA, Yoshinori SAKURAI and Mitsunori KIRIHATA

*2013 Material Research Society Fall Meeting & Exhibit*, Poster Presentation, Boston, MA, USA, December 1-6, 2013; Preprints.

### **Melanoma-targeted Boron Delivery by Kojic Acid-appended Carborane/Cyclodextrin Complexes for BNCT of Malignant Melanoma**

Takeshi NAGASAKI, Riku KAWASAKI, Yoshihide HATTORI, Yoshinori SAKURAI, Hiroki TANAKA, Shin-ichiro MASUNAGA, Koji ONO and Mitsunori KIRIHATA

*The 6<sup>th</sup> Trilatereal BNCT Meeting between Taiwan and Japan*, Invited Lecture, Taipei, Taiwan, December

13, 2013; Preprints.

**Stimuli-responsive Drug Delivery System: Photoresponsive Gene Delivery System for Gene Therapy and Boron Delivery System for Neutron Capture Therapy**

Takeshi NAGASAKI

*7th KIFEE International Symposium on Environment, Energy and Materials*, Invited Lecture, Kyoto, Japan, March 16-19, 2014; Preprints.

**Boron-containing Rare Earth Oxides Nanoparticles for Boron Neutron Capture Therapy**

Takeshi NAGASAKI, Riku KAWASAKI, Shin-ichiro MASUNAGA, Yoshinori SAKURAI and Koji TOMITA

*2014 Material Research Society Spring Meeting & Exhibit*, Poster Presentation, San Francisco, CA, USA, April 21-24, 2014; Preprints.

**Kojic Acid Modified o-Carborane/Hydroxypropyl- $\beta$ -Cyclodextrin Complex as Novel BNCT Drug for Melanoma**

Takeshi NAGASAKI, Riku KAWASAKI, Yoshinori SAKURAI, Shin-ichiro MASUNAGA, Koji ONO and Mitsunori KIRIHATA

*16<sup>th</sup> International Congress on Neutron Capture Therapy*, Oral Presentation, Helsinki, Finland, July 14-19, 2014; Preprints.

**Application of Novel Boron-containing Nanoparticles to BNCT**

Koji TOMITA and Takeshi NAGASAKI

*Isotope News*, Vol. 718, pp. 9-15 (2014) (in Japanese)

**The Synergistic Effect of 1'-Acetoxychavicol Acetate and Sodium Butyrate on the Death of Human Hepatocellular Carcinoma Cells**

Rie KATO, Isao MATSUI-YUASA, Hideki AZUMA and Akiko KOJIMA-YUASA.

*Chem. Biol. Interact.*, Vol. 212, pp. 1-10 (2014)

It has been suggested that the combined effect of natural products may improve the effect of treatment against the proliferation of cancer cells. In this study, we evaluated the combination of 1'-acetoxychavicol acetate (ACA), obtained from *Alpinia galangal*, and sodium butyrate, a major short chain fatty acid, on the growth of HepG2 human hepatocellular carcinoma cells and found that treatment had a synergistic inhibitory effect. The number of HepG2 cells was synergistically decreased via apoptosis induction when cells were treated with both ACA and sodium butyrate. In ACA- and sodium butyrate-treated cells, intracellular reactive oxygen species (ROS) levels and NADPH oxidase activities were increased significantly. The decrease in cell number after combined treatment of ACA and sodium butyrate was diminished when cells were pretreated with catalase. These results suggest that an increase in intracellular ROS levels is involved in cancer cell death. AMP-activated protein kinase (AMPK), a cellular energy sensor, plays an essential role in controlling processes related to tumor development. In ACA- and sodium butyrate-treated cells, AMPK phosphorylation was induced significantly, and this induction improved when cells were pretreated with catalase. These results suggest that the increase in intracellular ROS is involved in the increase of AMPK phosphorylation. In normal hepatocyte cells, treatment with ACA and sodium butyrate did not decrease cell numbers or increase ROS levels. In conclusion, combined treatment with ACA and sodium butyrate synergistically induced apoptotic cell death via an increase in intracellular ROS and phosphorylation of AMPK. Our findings may provide new insight into the development of novel combination therapies against hepatocellular carcinoma.

**Preparation of keratin hydrogel/hydroxyapatite composite and its evaluation as a controlled drug**

### **release carrier**

R. NAKATA, A. TACHIBANA, T. TANABE

*Mater. Sci. Eng. C*, Vol. 41, pp. 59-64 (2014)

Infection after artificial joint replacement is a serious problem, which requires the re-implantation of prosthesis. To aim at developing bone filling materials having both osteoconductivity and ability as a sustained drug release carrier, composites of wool keratin or carboxymethylated (CM) keratin hydrogels with hydroxyapatite were prepared and evaluated as a sustained drug release carrier. CM-keratin was prepared by the reaction of keratin extracted from wool with iodoacetic acid. Hydrogels were obtained by dropping keratin or CM-keratin solution into CaCl<sub>2</sub> solution. The composites were obtained by immersing hydrogels in simulated body fluid (SBF). The introduction of carboxymethyl groups to keratin facilitated the deposition of hydroxyapatite on hydrogel. After 7 days immersion in SBF, 4 – 5 times higher amount of hydroxyapatite was accumulated on CM-keratin hydrogel than that on keratin hydrogel. When salicylic acid was loaded on keratin and CM-keratin hydrogels, a good sustained release was observed; that is, 90% of drug was released up to 14 days after 60 and 45% of initial burst in 1 day. On the other hand, initial release within 1 day was suppressed by forming composite with hydroxyapatite and the release was almost ceased at 3 days when 60% of drug was released. Although further improvement to prolong drug release might be necessary, CaKHA and CaCMKHA are expected to be a promising novel type of bone filling materials which has both osteoconductivity and sustained drug release ability.

### **Long DNA passenger strand highly improves the activity of RNA/DNA hybrid siRNAs**

H. IDA, K. FUKUDA, A. TACHIBANA, T. TANABE.

*J. Biosci. Bioeng.*, Vol. 117, pp. 401-406. (2014)

Small interfering RNAs (siRNAs) are potent tools in biomedical research, which can reduce the expression level of target proteins through RNAi pathway. They are composed of 19-25 bp double strand RNA (dsRNAs), therefore, stimulate dsRNAs dependent interferon responses in a non-specific manner. This problem has prevented siRNAs from being applied as new therapeutic agents. In the present paper, we tried to circumvent interferon responses using RNA/DNA hetero siRNAs (HsiRNAs) composed of RNA guide and DNA passenger strands. It was previously reported that siRNAs which were partially substituted with DNA had RNAi activity and that DNA substitution often caused the activity loss. In our results, HsiRNAs, in which the passenger strand of siRNAs were exchanged with DNA also showed much lower activity than that of parental siRNAs. Here, we found that attachment of 5' flanking sequence to DNA passenger strand improved the activity of HsiRNAs. Furthermore, the effective HsiRNAs induced much lower interferon responses than parental siRNAs. Thus, HsiRNAs with 5' flanking sequence are expected to be novel siRNA drug candidates.

### **Binding affinity of ssDNA is improved by attachment of dsDNA regions**

H. IDA, A. TACHIBANA, T. TANABE.

*J Biosci Bioeng.*, Vol. 118, pp. 239-241. (2014)

LidNA, a microRNA inhibitor consisting of a microRNA binding ssDNA region sandwiched between dsDNA regions had higher affinity to target oligonucleotides than that without dsDNA region. This enhancement in affinity was found to be owing to the suppressed mobility of ssDNA region by the presence of dsDNA regions.

### **Isolation and characterization of baker's yeast capable of strongly activating a macrophage**

Y. TAKADA, Y. NISHINO, C. ITO, H. WATANABE, K. KANZAKI, T. TACHIBANA, M. AZUMA

*FEMS Yeast Res.*, Vol. 14(2), pp. 261-269. (2014)

A physiological function of the  $\beta$ -glucans which constitute the cell wall of *Saccharomyces cerevisiae* is to activate immune cells. Here, we focused on the immunostimulation ability of *S. cerevisiae* itself to give this ability to fermented foods including yeast. Previously, we found that in *S. cerevisiae* the deletion of MCD4

gene causes exposure of  $\beta$ -glucans on the cell surface and that the *mcd4* deletion mutant strongly enhances immunity in vitro and in vivo. However, this is not a practical strain but a genetically modified strain with an antibiotic resistance gene, and growth was very slow. The aim of this study was to acquire a practical strain capable of strongly activating a macrophage. The parental strain y-21 was mutated with ethyl methanesulfonate, and the resulting strain was screened. Two mutants (AP-57 and AQ-37) were obtained. AQ-37 had the same fermentation capacity as y-21. In addition, a mutation point of AQ-37 was identified, suggesting that the mutation of NDD1 gene affects the cell wall structure and confers a high ability for macrophage stimulation. The obtained yeast may activate immune cells in materials to which the yeast is added.

#### **Isolation of diploid baker's yeast capable of strongly activating immune cells and analyses of the cell wall structure**

Y. TAKADA, A. MIZOBUCHI, T. KATO, E. KASAHARA, C. ITO, H. WATANABE, K. KANZAKI, S. KITAGAWA, T. TACHIBANA, M. AZUMA

*Biosci Biotechnol Biochem.*, Vol. 78(5), pp. 911-915. (2014)

Diploid baker's yeast capable of strongly activating a mouse macrophage was constructed based on haploid mutant AQ-37 obtained previously. The obtained strain BQ-55 activated also human immune cells. To clarify a factor for the activation, the cell wall structure, especially the  $\beta$ -glucan structure, was analyzed, suggesting that the length of branching,  $\beta$ -1,6-glucan, may be one of the factors.

#### **Cell wall structure suitable for surface display of proteins in *Saccharomyces cerevisiae***

H. MATSUOKA, K. HASHIMOTO, A. SAIJO, Y. TAKADA, A. KONDO, M. UEDA, H. OOSHIMA, T. TACHIBANA, M. AZUMA

*Yeast.*, Vol. 31(2), pp. 67-76. (2014)

A display system for adding new protein functions to the cell surfaces of microorganisms has been developed, and applications of the system to various fields have been proposed. With the aim of constructing a cell surface environment suitable for protein display in *Saccharomyces cerevisiae*, the cell surface structures of cell wall mutants were investigated. Four cell wall mutant strains were selected by analyses using a GFP display system via a GPI anchor.  $\beta$ -Glucosidase and endoglucanase II were displayed on the cell surface in the four mutants, and their activities were evaluated. *mnn2* deletion strain exhibited the highest activity for both the enzymes. In particular, endoglucanase II activity using carboxymethylcellulose as a substrate in the mutant strain was 1.9-fold higher than that of the wild-type strain. In addition, the activity of endoglucanase II released from the *mnn2* deletion strain by Zymolyase 20T treatment was higher than that from the wild-type strain. The results of green fluorescent protein (GFP) and endoglucanase displays suggest that the amounts of enzyme displayed on the cell surface were increased by the *mnn2* deletion. The enzyme activity of the *mnn2* deletion strain was compared with that of the wild-type strain. The relative value (*mnn2* deletion mutant/wild-type strain) of endoglucanase II activity using carboxymethylcellulose as a substrate was higher than that of  $\beta$ -glucosidase activity using p-nitrophenyl- $\beta$ -glucopyranoside as a substrate, suggesting that the cell surface environment of the *mnn2* deletion strain facilitates the binding of high-molecular-weight substrates to the active sites of the displayed enzymes.

#### **A milliliter-scale yeast-based fuel cell with high performance**

K. KANESHIRO, K. TAKANO, Y. TAKADA, T. WAKISAKA, T. TACHIBANA, M. AZUMA

*Biochemical Engineering Journal*, Vol. 83, pp. 90-96. (2014)

Microbial fuel cells are attracting attention as one of the systems for producing electrical energy from organic compounds. We used commercial baker's yeast (*Saccharomyces cerevisiae*) for a glucose fuel cell because the yeast is a safe organism and relatively high power can be generated in the system. In the present study, a milliliter (mL)-scale dual-chamber fuel cell was constructed for evaluating the power generated by a variety of yeasts and their mutants, and the optimum conditions for high performance were investigated.

When carbon fiber bundles were used as an electrode in the fuel cell, high volumetric power density was obtained. The maximum power produced per volume of anode solution was 850 W/m<sup>3</sup> under optimum conditions. Furthermore, the power was examined using seven kinds of yeast. In *Kluyveromyces marxianus*, not only the power but also the power per consumed glucose was high. Moreover, as fuel for the fuel cell. The fuel cell powered by *K. marxianus* may prove to be helpful for the effective utilization of woody biomass.

### **Expression of the Clustered NeuAca $\alpha$ 2-3Gal $\beta$ O-Glycan Determines the Cell Differentiation State of the Cells**

K. HIGASHI, K. ASANO, M. YAGI, K. YAMADA, T. ARAKAWA, T. EHASHI, T. MORI, K. SUMIDA, M. KUSHIDA, S. ANDO, M. KINOSHITA, K. KAKEHI, T. TACHIBANA, K. SAITO

*J. Biol. Chem.*, Vol. 289(37), pp. 25833-25843. doi: 10.1074/jbc.M114.550848. (2014)

Human embryonic stem cells (hESCs) are pluripotent stem cells from early embryos, and their self-renewal capacity depends on the sustained expression of hESC-specific molecules and the suppressed expression of differentiation-associated genes. To discover novel molecules expressed on hESCs, we generated a panel of monoclonal antibodies against undifferentiated hESCs and evaluated their ability to mark cancer cells, as well as hESCs. MAb7 recognized undifferentiated hESCs and showed a diffuse band with molecular mass of >239 kDa in the lysates of hESCs. Although some amniotic epithelial cells expressed MAb7 antigen, its expression was barely detected in normal human keratinocytes, fibroblasts, or endothelial cells. The expression of MAb7 antigen was observed only in pancreatic and gastric cancer cells, and its levels were elevated in metastatic and poorly differentiated cancer cell lines. Analyses of MAb7 antigen suggested that the clustered NeuAca $\alpha$ 2-3Gal $\beta$  O-linked oligosaccharides on DMBT1 (deleted in malignant brain tumors 1) were critical for MAb7 binding in cancer cells. Although features of MAb7 epitope were similar with those of TRA-1-60, distribution of MAb7 antigen in cancer cells was different from that of TRA-1-60 antigen. Exposure of a histone deacetylase inhibitor to differentiated gastric cancer MKN74 cells evoked the expression of MAb7 antigen, whereas DMBT1 expression remained unchanged. Cell sorting followed by DNA microarray analyses identified the down-regulated genes responsible for the biosynthesis of MAb7 antigen in MKN74 cells. In addition, treatment of metastatic pancreatic cancer cells with MAb7 significantly abrogated the adhesion to endothelial cells. These results raised the possibility that MAb7 epitope is a novel marker for undifferentiated cells such as hESCs and cancer stem-like cells and plays a possible role in the undifferentiated cells.

### **DBZ, a CNS-specific DISC1 binding protein, positively regulates oligodendrocyte differentiation**

S. SHIMIZU, Y. KOYAMA, T. HATTORI, T. TACHIBANA, T. YOSHIMI, H. EMOTO, Y. MATSUMOTO, S. MIYATA, T. KATAYAMA, A. ITO, M. YOHYAMA

*Glia.*, Vol. 62, pp. 709-724. (2014)

Recent studies have shown changes in myelin genes and alterations in white matter structure in a wide range of psychiatric disorders. Here we report that DBZ, a central nervous system (CNS)-specific member of the DISC1 interactome, positively regulates the oligodendrocyte (OL) differentiation *in vivo* and *in vitro*. In mouse corpus callosum (CC), DBZ mRNA is expressed in OL lineage cells and expression of DBZ protein peaked before MBP expression. In the CC of DBZ-KO mice, we observed delayed myelination during the early postnatal period. Although the myelination delay was mostly recovered by adulthood, OLs with immature structural features were more abundant in adult DBZ-KO mice than in control mice. DBZ was also transiently upregulated during rat OL differentiation *in vitro* before myelin marker expression. DBZ knockdown by RNA interference resulted in a decreased expression of myelin-related markers and a low number of cells with mature characteristics, but with no effect on the proliferation of oligodendrocyte precursor cells. We also show that the expression levels of transcription factors having a negative-regulatory role in OL differentiation were upregulated when endogenous DBZ was knocked down. These results strongly indicate that OL differentiation in rodents is regulated by DBZ.

**N-ethylmaleimide-sensitive factor interacts with the serotonin transporter and modulates its trafficking: implications for pathophysiology in autism**

K. IWATA, H. MATSUZAKI, T. TACHIBANA, K. OHNO, S. YOSHIMURA, H. TAKAMURA, K. YAMADA, S. TATSUZAKI, K. NAKAMURA, K. J. TSUCHIYA, K. TASTUMOTO, M. TSUJII, T. SUGIYAMA, T. KATAYAMA, N. MORI

*Mol. Autism* 5:33. doi: 10.1186/2040-2392-5-33. (2014)

Changes in serotonin transporter (SERT) function have been implicated in autism. SERT function is influenced by the number of transporter molecules present at the cell surface, which is regulated by various cellular mechanisms including interactions with other proteins. Thus, we searched for novel SERT-binding proteins and investigated whether the expression of one such protein was affected in subjects with autism.

**Generation of a monoclonal antibody for INI1/hSNF5/BAF47**

A. HARADA, M. HAYASHI, Y. KUNIYOSHI, Y. SEMBA, S. SUGAHARA, T. TACHIBANA, Y. OHKAWA, M. FUJITA

*Monoclon Antib Immunodiagn Immunother*, Vol. 33(1), pp. 49-51. doi: 10.1089/mab.2013.0065. (2014)

INI1/hSNF5/BAF47, which has an SNF5 domain, belongs to the SWI/SNF family. This family is known as ATP-dependent regulators of gene expression by remodeling chromatin structure during cell differentiation. However, the detailed function of INI1/hSNF5/BAF47 is unclear. Here we report the generation of a specific monoclonal antibody for INI1/hSNF5/BAF47 by the mouse iliac lymph node method. The obtained antibody recognized two isoforms of INI1/hSNF5/BAF47 in immunoblotting and precisely recognized the nuclear localization of INI1/hSNF5/BAF47 in immunostaining. This antibody can contribute to further elucidation of the mechanisms of gene expression regulation by INI1/hSNF5/BAF47 during cell differentiation.

**Production of a monoclonal antibody for C/EBP $\beta$ : the subnuclear localization of C/EBP $\beta$  in mouse L929 cells**

A. HARADA, E. OKAZAKI, S. OKADA, T. TACHIBANA, Y. OHKAWA

*Monoclon Antib Immunodiagn Immunother*, Vol. 33(1), pp. 34-37. doi: 10.1089/mab.2013.0069. (2014)

The CCAAT/enhancer-binding protein (C/EBP) $\beta$  belongs to the C/EBP family of proteins that possesses a basic leucine zipper DNA-binding domain. These proteins bind DNA by dimerization and play a role in the transcriptional regulation of various cells. There are six different types of C/EBPs, and some form isoforms through the use of alternative translation initiation sites. The functional analysis of the C/EBP family is therefore difficult to achieve. Here we report on the production of specific monoclonal antibodies against mouse C/EBP $\beta$  using a rat medial iliac lymph node method. Immunoblotting using C/EBP $\beta$  monoclonal antibodies identified two types of isoforms, while immunostaining revealed a subnuclear localization for C/EBP $\beta$ . Use of this antibody should contribute to the further elucidation of the transcriptional regulatory function of C/EBP $\beta$ .

**Generation of a monoclonal antibody against the extracellular domain of IGF-1R**

Y. NAKADATE, S. YOSHIMURA, N. NAKATANI, M. AZUMA, T. TACHIBANA

*Monoclon Antib Immunodiagn Immunother*, Vol. 33(2), pp. 126-128. doi: 10.1089/mab.2013.0083. (2014)

Type I insulin-like growth factor receptor (IGF-1R) is a receptor tyrosine kinase that is involved in the transformation of cells, cancer proliferation, and metastatic events in various types of cancer. The present study reports on the generation of a mouse monoclonal antibody (MAb) to IGF-1R using the mouse lymph node method. MAb 1B1, which reacts specifically with the extracellular domain of IGF-1R, was obtained using flow cytometry (FCM) screening using MCF-7 cells. Using immunostaining, MAb 1B1 detected IGF-1R mainly on the plasma membrane of MCF-7 cells. MAb 1B1 would be useful in FCM and immunofluorescence assays to detect IGF-1R-expressing cells for basic and clinical research.

*Architecture and Building Engineering*

**A Study on Conditions to Release Initial Displacement for Tuned Mass Dampers with Initial Displacement**

Susumu YOSHINAKA and Yoshiya TANIGUCHI

*Journal of Structural and Construction Engineering (Transactions of AIJ)*, AIJ, No. 703, pp. 1247-1257 (2014) (in Japanese)

We propose tuned mass dampers with initial displacement that are possible to control impulsive seismic responses effectively. In our previous study, we focused on the considerably high modal damping ratio of the second mode compared to the first mode and proposed the design formulas for high control performance under impulse loading. The proposed design formulas are based on the principle that by giving the specific TMD initial displacement under the specific structural initial condition the structural response of the first mode can be eliminated. In this paper, we introduce a formula for initial conditions to release initial displacement by the theoretical solution and study about TMD initial displacement and structural conditions by using the complex plane. Next, we propose a design method that can change initial structural conditions.

**Estimation of the Global Optimality for Multiple Tuned Mass Damper Systems Using Order Statistics**

Makoto YAMAKAWA (Tokyo Denki University), Susumu YOSHINAKA, Yoshikazu ARAKI (Kyoto University), Koji UETANI (Setsunan University) and Ken'ichi KAWAGUCHI (Institute of Industrial Science, the University of Tokyo)

*Proceedings of the 11th World Congress on Computational Mechanics (WCCM XI)*, Barcelona, Spain, July 20-25, pp. 4362-4372 (2014)

In the design of passive tuned mass damper (TMD) on the vibration control performance of spatial structures, we have to decide the both of a spatial arrangement and characteristics. To find an optimum design of the system is formulated as Mixed-Integer Programming (MIP) problem. It is difficult to obtain the exact global optimum solution in general form. We present a method which can guarantee to find a near-optimal solution with pre-assigned accuracy. The key concept of the method is random search based on prediction by order statistics. Through a numerical example, we investigate the applicability and effectiveness of the method to the design of TMD systems.

**Mood States and Light Environment Evaluation**

Noriko UMEMIYA, Tetsuro ARAI, Tomoko IWATA and Tamami SUZUKI

*Proceedings of CIE Centenary Conference „Towards a New Century of Light“*, Paris, pp. 1180-1185 (2013).

The light environment in a climate chamber was evaluated at two levels of lighting. Differences in evaluations offered by 440 student subjects were analyzed. Results revealed the following. 1) The light environment evaluation related to brightness, brightness for writing, uniformity of lighting, glare, color, comfort, preference, and performance changed according to the level of lighting for all subjects. 2) Profiles of Mood States response patterns were classifiable into five groups. In low vigor Pattern 3, most evaluations did not change according to the illuminance level.

**Relation between School Building Configuration and Heat Mitigation Effects of Lawns in Urban Regions**

Noriko UMEMIYA, Takayuki HARADA, Masato TOKUDA, Tatsuya SAKANE and Satoshi HIRATA

*Proceedings of the 13th International Building Performance and Simulation Association Conference, Building Simulation 2013*, Chambery, pp. 742-746 (2013)

Results of this study show how heat mitigation effects of planting elementary school lawns in urban regions differ according to eight school building configurations and two surrounding building models. Results show the following. 1) Heat mitigation effects with high-rise buildings (MODEL\_H) are higher than those with normal height buildings (MODEL\_N) for eight school building configurations. 2) For MODEL\_H, with higher surrounding buildings, enclosure-type school building configurations show high heat mitigation effects of lawns in terms of temperature differences. 3) School building configurations with no west-facing school buildings show high heat mitigation effects of lawns for the new effective temperature for outdoors

(OUT\_SET\*) both for Model\_H and Model\_L.

**Faults and Claims about Thermal Environments in Relation to Energy Saving Measures in Smaller Office Buildings**

Noriko UMEMIYA, Taiji OBUCHI and Ryota MATSUI

*Journal of Civil Engineering and Architecture*, 8(4), pp.413-424 (2014)

Building equipment, energy-saving systems, and claims of inappropriate indoor thermal environments were analyzed in relation to the floor area using responses to a questionnaire survey of service managers of 157 buildings built in Osaka, Kyoto and Hyogo prefectures in Kinki area of Japan. Results show the following: (1) In smaller buildings (< 5,000 m<sup>2</sup>), setting temperatures are higher in summer and lower in winter, effects of “uncomfortable radiation from windows” are greater, energy-saving systems decrease indoor thermal comfort, but claims of “hot” and “cold” are fewer; (2) Claims of “hot” and “cold” are unrelated to the setting temperature and whether the air-conditioning control system is central or local; (3) the adoption rates of mitigation of dress codes (“COOL-BIZ” and “WARM-BIZ”) are higher than those of temperature mitigation of air conditioning.

## ***Urban Design and Engineering***

### **An Analysis on Influencing Factors on Difficulty of Shopping Accessibility by Considering Individual Attributes and Area Characteristics**

Noboru ISE and Yasuo HINO

*Osaka City University, Memoirs of the Faculty of Engineering, Vol. 54, pp. 37-45(2013)*

Ministry of Economy, Trade and Industry (METI) forecasted that the number of people in food desert (PFD), who have difficulty of shopping accessibility, may be about six million in Japan. However, this forecasting method would not be suitable for forecasting the number of PFD at local level, because of lack of taking consideration into the factors such as individual attributes and area characteristics. Therefore, this paper mainly aims to gain the fundamental knowledge to develop the model for forecasting the number of PFD at local level, from the analysis on influencing factors on difficulty for shopping accessibility by considering individual attributes and area characteristics. As a result in this study, some major findings related to shopping accessibility came out as follows; 1) some influencing factors on difficulty of shopping accessibility were revealed, 2) shopping accessibility aids such as mobile shopping and delivery service had the complementary role of improving the shopping access problem, 3) actual conditions of needs for shopping accessibility aids were clear, 4) both average WTP (Willingness to Pay) and average usage frequency of each aids for shopping by PFD were revealed. These findings may be useful to develop the forecasting model for not only the number of PFD but also the shopping behavior among some specialized shopping styles.

### **Introduction and Evaluation of Some Trial Bus Services to Support Elderly Persons**

Yasuo HINO, Kazuo MUKAI, Kazuya MIZUKAMI and Junichi MORITA

*Japan Society of Traffic Engineers, Papers on Traffic Engineering, No. 34, pp. 478-484(2014) (in Japanese)*

Activity of residents in town must be one of the important factors to develop the future city planning, in population decrease with both aging declining birthrate. Therefore, some suitable support services for mobility of aged persons to provide the opportunity of going out with accompanying person. In this study, new trials of bus services to improve the mobility of aged persons were introduced and evaluated based on the questionnaire surveys for bus passengers and residents. Their new bus services were “free charge for accompanied person on Sunday”, “cut in fare of regular route bus to adjust the fare of small bus of same route” and “free place of getting on and off the bus”. These services were introduced to aim to mainly support the mobility of aged persons. As a result, some important findings to evaluate the utility of these services and investigate the future approaches to realize the purpose came out of some analyses of surveys. Furthermore, these results must be a precedent of valid bus services to realize the active town planning.

### **Evaluation of Road Space based on Analysis of Influence Factors from viewpoint of Pedestrians**

Tatsuya OGIHARA and Yasuo HINO

*Japan Society of Civil Engineers, Proceedings of Infrastructure Planning, No.46, 4pp (CD-ROM)(2013) (in Japanese)*

Recently, the improvement of urban environment has been essential factor in comprehensive plan at many cities. Therefore, various keywords like “creation of new environment” were proposed in such plan. However, as the understandings of urban environment may be different according to values, it must be not easy to not only define the meaning of urban environment, but also fix the composing factors to it. In this study, the activity, attachment, land scape as well as urban environment, which must be differently evaluated according to values of persons, conditions of road, traffic situation and so on, were defined as the fundamental four indicators to evaluate the road space in urban area. Then the evaluation to each indicator and the relations among them were analyzed based on the data of questionnaire to pedestrians, in order to find some key factors influenced to each evaluation. As a result, some important findings came out as follows; four indicators were related respectively, traffic conditions must as well as road conditions as road width, degree of tree planting and road side conditions influenced to evaluation. That is, the road space for urban environment must be improved by improving some factors mentioned above, in addition, its improvement may influence well to all indicators.

### **Important Issues and Better Prospect of Road Safety Education from viewpoint of Traffic Accidents Involved children – Mainly Behavior and Consciousness of Risk for Bicycle Use -**

Yasuo HINO

*Traffic Safety Education, Vol.49, No.9, pp.6-18 (2014) (in Japanese)*

The reports of traffic accident of children have kept in news, nevertheless the number of accidents involved children has not increased. This must be considered to show that the safety of children should be the one of greatest concern of society. How do we prevent children from traffic accident? A few number of road safety event by cooperation of police office in each primary school. Usually, parents may teach children how to ride bicycle. However, it must not be understandable for both teachers and parents to understand how to teach children for road safety. In this study, the features and problems of traffic accidents involved children, the consciousness for road safety of children, parents and teachers, and the conditions and problems of road safety educations were evaluated by using the data of questionnaire for all concerns. In addition, the road safety education reflected the useful findings came out of surveys must be necessary to prevent children from accidents as a better prospect.

### **Verbal Map Guidelines of Audio-AR Application for Visually-impaired People**

Mei TAKAHASHI, Kazuyuki NEKI and Takashi UCHIDA

*Japan Society of Traffic Engineers, Papers on Traffic Engineering, No. 33, pp. 509-514(2013) (in Japanese)*

A typical smartphone has a global positioning system (GPS) function and a web access function. Furthermore, augmented reality (AR) applications of smartphones have become commonplace. Such phones may enable visually-impaired people to use navigation system by using “verbal maps” instead of graphical maps. This paper describes outline of guidelines of “verbal map” that explains feature information to visually-impaired people using audio guidance. An example of verbal map sequence adopted in real town is also shown.

### **A Formulation of Long-term Trip Mode Choice Game considering Altruistic Attitudes and Bus-captive People.**

Masaki OCHI and Takashi UCHIDA

*Japan Society of Traffic Engineers, Papers on Traffic Engineering, No. 33, pp. 433-438(2013) (in Japanese)*

This paper formulates collective decision concerning transportation system by using game-theory. The players choose their long-term (for some decades) mode among transportation alternatives including public-supported transport system. The players are classified and characterized into 4 types considering altruistic attitudes and captivity to bus. This formulation reflects real situation of “transportation poor” problems. Numerical examples are explained to show that the formulation is useful to examine public policies of transportation system.

### **Citizen Awareness of Community Buses from the Public Support Perspective**

Yusuke KURASHIMA and Takashi UCHIDA

*Japan Society of Traffic Engineers, Papers on Traffic Engineering, No. 33, pp. 569-574(2013) (in Japanese)*

### **Study on the Process of Review and Improvement of the Community Bus for Continuation and Improvement of the Civic Will**

Yusuke KURASHIMA and Takashi UCHIDA

*Japan Society of Civil Engineers, Proceedings of Infrastructure Planning, No.48, 4pp. (CD-ROM) (2013) (in Japanese)*

### **LIFECYCLE ANALYSIS OF REPLACEABLE BRIDGES**

Masahiro UTSUMI and Takashi UCHIDA

*Japan Society of Civil Engineers, Proceedings of Infrastructure Planning, No.48, 4pp. (CD-ROM) (2013) (in Japanese)*

This paper describes an optimization technique of repair and replacement for deteriorated bridges. In addition, a new concept of bridges called “ECO-Bridges” is introduced. The genetic algorithm (GA) that is search algorithm based on the mechanics of natural selection and natural genetics is adopted in order to search optimal maintenance planning with both of the minimum maintenance costs and minimum external cost. By applying this algorithm both to existing bridges and Eco-Bridges, it has been verified that employed optimization system is effective for examining superior type of bridges under various conditions.

### **An Empirical Study of Verbal Map Guidelines for Visually-impaired people to Enhance Daily Mobility**

Mei TAKAHASHI, Takashi UCHIDA

*Osaka City University, Memoirs of the Faculty of Engineering, Vol. 54, pp. 37-45(2013)*

This study is to revise verbal map guidelines for a pedestrian navigation system. The guidelines show rules for describing features in a town to enhance everyday mobility. The paper presents a review of earlier studies and explains the concept of an audio augmented reality (AR) application for visually-impaired people. Then, field experiments are conducted to assess methods to encourage visually-impaired people to use audio guidance through courses and to advance hearing research. Outlines, results, and consideration of the experiments are presented. Finally, verbal map guidelines are revised. This study was conducted as a part of a Grant in Aid for Scientific Research during Heisei 24-26 year (Scientific Research B, 24360209) “Practical Use Study of the Town Walk Support Navigation System Fused in Audio AR and RFID for Visually-impaired people”

### **An Experimental Study on Characteristics of Cyclist’s Eye Movement and Behavior on Bicycle Facilities**

Takanori OKAWA, Nagahiro YOSHIDA, Yasuo HINO and Takashi UCHIDA

*Japan Society of Civil Engineers, Journal of JSCE, Division D3, Vol. 69, No.5, pp. I\_571-I\_578 (2013) (in Japanese)*

Bicycle lanes with legal control have been introduced on carriageway as a governmental pilot project since 2008 in Japan. However the facility design standard for cyclists on roadways is not determined yet while many standards remain the same as for cars/drivers. There are few researches on cyclists’ specific eye movement and behavior with road conditions. The amount of information on road should be minimized to avoid confusion, but required to be an informative road space for bicyclists even without driving license. Therefore, some empirical experiments have been conducted to understand differences of cyclist’s eye movement and behavior on various types of facilities.

### **Study on Ultimate Strength and Deformation of Compression Chord Member considering Gusset Plate in a Truss Bridge**

Masahide MATSUMURA, Junpei YOSHIYAMA and Takashi YAMAGUCHI

*Journal of Structural Engineering, Vol. 59A, JSCE, pp.169-179 (2013) (in Japanese)*

Investigated in this study is the ultimate strength of a compression chord member in a truss bridge, which is designed according to the Specification for Highway Bridges in Japan. An adequate modeling method of the member, and the support condition of the member considering gusset plates at the end of the member are checked through FEM analysis. It is revealed that the ultimate strength and deformation of the member in the truss bridge is very much similar to those of a fixed supported column in compression. Also proposed is an economic and rational design of the truss bridge.

### **Strengthening Effects of Eccentric Compression Steel Columns bonded CFRP Plate of High Elastic Modulus**

Masahide MATSUMURA, Shinya KODA, Nobuhiro HISABE (Mitsubishi Plastics Inc.) and Takashi YAMAGUCHI

*Journal of Structural Engineering, Vol. 59A, JSCE, pp.190-198 (2013) (in Japanese)*

In conventional strengthening techniques for existing steel structures, steel plates are additionally welded or bolted to the existing steel members to reduce working stress. Here, FRP materials can be alternatives of conventional techniques in terms of easier applicability. Among the FRPs, CFRP strips of high elastic modulus provide higher strengthening effects. Then, carried out in this paper are loading tests of eccentric and more effective compression steel columns adhered the CFRP strips separately onto the flange plates. It is concluded that strengthening effect of the CFRP strips for bending not for axial loading decreases when the CFRP strips are separately adhered onto the flange plates of the steel columns subjected to predominant compression axial force.

### **Structural Rationalization of the Undersurface Retrofitting Method with Splice Plates and Mortar-filling into the Trough Ribs for Existing Orthotropic Steel Decks**

Yoshio TAMBA (Hanshin Expressway Technology Center), Satoshi KIMURA (Yokogawa Bridge Corp.), Takashi YAMAGUCHI, Hiroki SUGIYAMA (Hanshin Expressway Co., Ltd.), Akiko TABATA (Hanshin Expressway Co., Ltd.), and Yoshihiko TAKADA (Hanshin Expressway Co., Ltd.)

*Journal of Structural Engineering, Vol. 59A, JSCE, pp.767-780 (2013) (in Japanese)*

The undersurface retrofitting method (installation of splice plates between the trough ribs and filling of mortar into the trough ribs) for existing orthotropic steel decks is proposed. This retrofitting method does not require the traffic restriction. In this study, FEM analysis and static load test are carried out in order to rationalize this retrofitting method by evaluating the bolt pitch and the stress reduction effect. As a result, we understand that it is possible to apply the bolt pitch of 300(mm) to this retrofitting method and that the adhesives between the orthotropic steel deck and the splice plate are important.

### **Study on Mechanical Property of High Durability Friction Grip Joints with High Strength Countersunk Head Bolts for Steel Bridge Structures**

Akiko TABATA (Hanshin Expressway Co., Ltd.), Hidesada KANAJI (Hanshin Expressway Co., Ltd.), Yoshihide KURONO and Takashi YAMAGUCHI

*Journal of Structural Engineering, Vol. 59A, JSCE, pp.808-819 (2013) (in Japanese)*

The authors focused on the high strength bolted friction grip joints with countersunk head bolts which can finish the surface of the connection plate flat smoothly and prevent from functional depression due to corrosion. In this study, we have compared the slip strength of the joints which has the optimum countersunk head angle with that of the joint with the normal high strength bolt through the standard slippage test considering variation of plate thickness and the yield strength of the base and splice plates. It was concluded from the experimental result that the slip strength of the joints with countersunk head bolts exceeds the design slip strength specified in JSHB calculated by the slip coefficient 0.45 and that its slip coefficient is about 10% lower than that with normal head bolts. It is caused by that the contact pressure of the joints with countersunk head reduces due to local yielding around the bolt holes.

### **Small-sized Steel Bellows as Energy Absorbing and Displacement Restraining Device for Bridge**

Masahide MATSUMURA

*Proceedings of the 6th Taiwan-Japan workshop on structural and bridge engineering, pp.119-123, (2013)*

### **Characterization of Mechanical Properties of Welding Materials using Fabrication of Steel Bridges**

Kuniaki MINAMI (Japan Railway Construction, Transport and Technology Agency) and Takashi YAMAGUCHI

*Journal of JSCE, Ser.A1 (SE/EE), Vol.69, No.3, JSCE, pp.452-466, (2013) (in Japanese)*

Recently, many kinds of welding materials were widely used in fabrication of steel bridges. It was considered that the quality of these welding materials has been remarkably improved. However, the statistical characteristics of the material are not clarified. In this paper, we have investigated the 638 of welding materials on the basis of the mill sheet in order to clarify their quality. Investigated items were tensile strength, yield strength, Charpy-absorbed-energy, elongation and yield ratio, and these mechanical properties were shown. We also showed improvement in the quality, comparing with the conventional steel data and welding procedure tests date, which were SM490Y, SMA490W, SM570Q and SMA570W.

### **Study on Slip Behaviour of High Strength Bolted Friction Type Joint with Extremely Thick Plates by Using Finite Element Analysis**

Toshikazu TAKAI, Xue PENG, Honghe SUN and Takashi YAMAGUCHI

*IABSE Conference Rotterdam 2013, Vol. 99, 8pages (on CDROM), Rotterdam (2013)*

High strength bolted friction type joints are commonly used to join members of steel bridge structures. Recently, such joints have become larger, because members of bridges tend to be large to seek structural simplicity. Since large members consist of extremely thick plates, large size joints are needed with many bolts in a line, containing thick plates including splice plates. It is of concern that many bolts and thick plates affect the slip behaviour of such large size joints. So, FEA focused on joints with many bolts and thick plates is carried out. Based on the results, it is clear that a non-uniform distribution of friction force exists. And, it is also shown that a certain combination of thicknesses of connected plates and splice plates has the large capacity of slip resistance. It is concluded that such results can be explained by the influence of the additional bending moment due to thick plates.

### **Study on Applicability of High Durability Friction Grip Joints with High Strength Countersunk Head Bolts for Steel Bridge Structures**

Akiko TABATA (Hanshin Expressway Co., Ltd.), Hidesada KANAJI (Hanshin Expressway Co., Ltd.), Yoshihide KURONO and Takashi YAMAGUCHI

*IABSE Conference Rotterdam 2013, Vol. 99, 8pages (on CDROM), Rotterdam (2013)*

The authors focused on the high strength bolted friction grip joints with countersunk head bolts which can finish the surface of the connection plate flat smoothly and prevent from functional depression due to corrosion. Firstly we carried out Finite Element Analysis in order to evaluate the contact pressure of double shear connected friction joints with countersunk heads varying the angle of countersunk head. Secondly, we have compared the slip strength of the joints which has the optimum countersunk head angle with that of the joint with the normal high strength bolt through the standard slippage test considering variation of plate thickness and the yield strength of the base and splice plates. As a result, it was concluded that the slip strength of the joints with countersunk heads exceeds the required design slip strength which has specified in JSHB and that its slip coefficients is about 10% lower than that with normal head bolts.

### **Experimental Study on Ultimate Strength and Ductility of Steel Short Column with Longitudinal Stiffeners made of SBHS700**

Keita HAMAMURA (Osaka University), Kiyoshi ONO (Osaka University), Masahide MATSUMURA, Takahiro TARUI (Osaka University) and Shinya KODA

*Proceedings of the 16th Symposium on Performance-based Seismic Design Method for Bridges*, pp.391-394, JSCE (2013) (in Japanese)

SBHS700 indicates higher yield strength and higher yield ratio like high strength steel. Focused on in this study is a hybrid stiffened plate, in which longitudinal stiffeners made of SBHS700 and flange and web plates made of SS400. Then compression test of short and rectangular steel hollow column with the hybrid stiffened plates are conducted. It is concluded that the use of the hybrid stiffened plate can be expects almost the same ultimate strength and higher ductility compared with non-hybrid stiffened plate.

### **Experimental Study on Rapture Characteristics of Knock-off Steel Side Block as Displacement Restrainers**

Takahiro KANATA and Masahide MATSUMURA

*Proceedings of the 16th Symposium on Performance-based Seismic Design Method for Bridges*, pp.309-316, JSCE (2013) (in Japanese)

Steel side block with slit, which is designed to break when seismic force corresponding to the ultimate shear force the cross section with the slit is subjected, is developed and proposed as a trigger to control restricting condition of superstructure. In this study, breaking tests are carried out to understand how shape of the slit influences on breaking characteristics of the steel side block with slit. Then it is revealed that the proposed shape of the slit can provide stable break load with less fluctuation and the braking displacement is calculated based on braking mechanism of the side block.

### **FEA Study on the Slip Behavior of High Strength Multi Bolted Friction Type Joints with Thick Plates by Structural Dimensions**

Xue PENG, Takashi YAMAGUCHI, Toshikazu TAKAI, Jun MURAKOSHI (Public Works Research Institute) and Mamoru SAWADA (Public Works Research Institute)

*Journal of JSCE, Ser.A1 (SE/EE), Vol.69, No.3, JSCE, pp.452-466, (2013) (in Japanese)*

Recent years, from the viewpoint of rational structural members of steel bridges, the high strength bolted friction type joints tend to be large. Since the slip behavior of high strength multi bolted friction type joints with thick plates is not clear, the slip strength tests for such joints had been carried out. And from the experimental results, it can be found that slip coefficient varies depending on the number of rows of bolts in a line. In this study, in order to clarify the slip behavior of such joints, FE analysis has been conducted with various structural dimensions, such as slip/yielding strength ratio, section shape of the connected plate etc. As a result, the slip coefficient of the joint with many bolts in a line becomes low because each frictional force per one bolt is unequal, and the plate width effects on the slip strength more significantly than other structural dimensions.

### **Analytical Study on Mechanical Behavior of Friction Grip Joints with High Strength Countersunk Head Bolts and Its Geometrical Configurations**

Akiko TABATA (Hanshin Expressway Co., Ltd.), Hidesada KANAJI (Hanshin Expressway Co., Ltd.), Yoshihide KURONO and Takashi YAMAGUCHI

*Steel Construction Engineering, Vol.20, No.79, JSSC, pp.19-28, (2013) (in Japanese)*

The authors focused on the high strength bolted friction grip joints with countersunk head bolts which can finish the surface of the connection plate flat smoothly and prevent from functional depression due to corrosion. In this study, we carried out FE analysis varying the angle of countersunk head in order to evaluate the contact pressure of double shear connected friction joints with countersunk heads. Also, we have investigated the influence on load transferring mechanism by using countersunk head bolt for frictional joints. It has concluded that the most desirable angle of the countersunk head is 90 degrees. CD series's slip strength is about only 4% lower than that with normal head bolts.

#### **Fundamental Study on Structural Soundness Evaluation of Existing Arch Bridge by using SOM**

Yoshinori IKEDA, Takashi YAMAGUCHI, Takeshi KITAHARA (Kanto Gakuin University), Kunitomo SUGIURA (Kyoto University) and Kouji MORIWAKA

*Steel Construction Engineering, Vol.20, No.79, JSSC, pp.53-66, (2013) (in Japanese)*

The authors focused on the high strength bolted friction grip joints with countersunk head bolts which can finish the surface of the connection plate flat smoothly and prevent from functional depression due to corrosion. In this study, we carried out FE analysis varying the angle of countersunk head in order to evaluate the contact pressure of double shear connected friction joints with countersunk heads. Also, we have investigated the influence on load transferring mechanism by using countersunk head bolt for frictional joints. It has concluded that the most desirable angle of the countersunk head is 90 degrees. CD series's slip strength is about only 4% lower than that with normal head bolts.

#### **Slippage Test of Frictional High Strength Bolted Joints with Adhesives for Corroded Damaged Steel Members**

Yoshio TAMBA (Hanshin Expressway Technology Center), Shinya YUKITO, Takashi YAMAGUCHI, Haruyuki SAKODA (Hanshin Expressway Technology Center), Akito HIGATANI (Hanshin Expressway Co., Ltd.) and Akiko TABATA (Hanshin Expressway Co., Ltd.)

*Proceedings of the 13th East Asia-Pacific Conference on Structure Engineering and Construction (EASEC-13), 8pages (on CDROM), Sapporo, JAPAN (2013)*

In this study, FE analysis for the girder ends with corrosion has been carried out in order to understand the collapse process and to evaluate its ultimate strength. At first, the strength of the girder end with various corroded damages is evaluated based on the current design standards, "Specifications for Highway Bridges in Japan". Secondly, these collapse mechanism are analyzed from the analytical results, such as shapes of the deformation mode, stress distribution, and load-deflection relationships and so on. Finally, we had summarized a flow diagram of a process of failure mode and the limit strength such as elastic, full-plastic and ultimate limit states taking into account for local buckling.

#### **Strength Evaluation for a Corroded Damaged Steel Girder End Considering Its Collapse Mechanism**

Makoto USUKURA (Tokyo Consultants Co., Ltd.), Takashi YAMAGUCHI, Yasuo SUZUKI (Utsunomiya University) and Yukiko MITSUGI (Ishikawa National College of Technology)

*Proceedings of the 13th East Asia-Pacific Conference on Structure Engineering and Construction (EASEC-13), 8pages (on CDROM), Sapporo, JAPAN (2013)*

In this study, FE analysis for the girder ends with corrosion has been carried out in order to understand the collapse process and to evaluate its ultimate strength. At first, the strength of the girder end with various corroded damages is evaluated based on the current design standards, "Specifications for Highway Bridges in Japan". Secondly, these collapse mechanism are analyzed from the analytical results, such as shapes of the deformation mode, stress distribution, and load-deflection relationships and so on. Finally, we had summarized a flow diagram of a process of failure mode and the limit strength such as elastic, full-plastic and ultimate limit states taking into account for local buckling.

#### **Fundamental Study on the Dynamic Behavior of Sliding Bearing with Trigger for Bridge Structures**

Takahiro KANATA, Masahide MATSUMURA, Yasuyuki NAKANISHI (NEWJEC Inc.) and Takashi YAMAGUCHI

*Proceedings of the 13th East Asia-Pacific Conference on Structural Engineering*, 8pages (on CDROM) (2013)

Isolation rubber bearings are widely used for damage mitigation of structures. However, isolation and damping effects tend to be optimized against the short-period earthquake ground motions defined by the Specifications for Highway Bridges in Japan. That is, as the isolation effects of the rubber bearings show strong frequency dependence, applicability against a long-period earthquake ground motion is not clear, for instance. Then the authors have focused on combination use of low friction and elastic sliding bearings, triggers and displacement restrainers for bridge bearings. Fundamental responses of the proposed bearings are checked through shaking table tests in this study and also discussed are analysis procedure of the proposed bearings with the trigger in the seismic response analysis. Application example of the proposed bearings to a viaduct is simulated through seismic response analysis. It is concluded that the analytical results show good agreement with the experimental results when considering the changes in the vibration modes and damping conditions before/after releasing the displacement of the superstructure by the triggers and the maximum displacement is approximately computed even when without considering them in the seismic response analysis.

#### **An Experimental Study on Mechanical Properties of SBHS700 and Application of SBHS700 to Stiffened Plates**

Keita HAMAMURA (Osaka University), Kiyoshi ONO (Osaka University), Masahide MATSUMURA, Takahiro TARUI (Osaka University) and Shinya KODA

*Proceedings of the 13th East Asia-Pacific Conference on Structural Engineering*, 6pages (on CDROM) (2013)

Higher yield strength steel plates for bridges, SBHS, has been standardized by Japanese Industrial Standard (JIS). However, there is not enough information on the mechanical properties of SBHS700 compared with SM490 and SM570. In this study, tensile tests of SBHS700 were conducted to earn the information on mechanical properties and stress-strain relationship. Moreover, axial compressive tests were conducted with the stiffened box section test specimens whose stiffeners are made of SBHS700. According to the axial compressive tests, the ultimate strength and the ductility of hybrid stiffened plates by applying SBHS700 were investigated.

#### **Cyclic Loading Test of Small-sized Steel Bellows made of Different Steel Materials subjected to Axial Displacement**

Masahide MATSUMURA, Kentaro TANAKA (Setsunan University), Hiroshi ZUI (Setsunan University) and Takashi YAMAGUCHI

*Proceedings of Constructional Steel, Vol.21, JSSC*, pp.125-130 (2013) (in Japanese)

Steel bellows as energy absorbing bridge connectors, having been investigated by the authors, show stable hysteresis loop and energy absorbing capacity when subjected to axial displacement. In this paper, cyclic behaviors of small sized steel bellows by bended in the same shape and made of different steel materials are investigated through cyclic loading test subjecting a larger axial displacement. Also discussed is a simplified stress-strain relationship of steel materials of the steel bellows considered in FEM analysis to approximate the load-displacement relationships and energy absorbing capacities of the steel bellows. It is concluded that a method considering the yield stress increase by bending process of steel plate is effective in the analysis of the steel bellows but against a larger displacement where tensile load greatly increases due to strain hardening.

#### **Effect of Ultimate Strength Behavior due to the Support Eccentricity of the Girder End with Corrosion of Highway Bridges**

Makoto USUKURA (Tokyo Consultants Co., Ltd.), Yasuo SUZUKI (Utsunomiya University), Takashi YAMAGUCHI and Yukiko MITSUGI (Ishikawa National College of Technology)

*Proceedings of Constructional Steel, Vol.21, JSSC*, pp.193-200 (2013) (in Japanese)

In recent years, it has been well known that some of steel bridges are deteriorated by corrosion at the girder ends. On the other hand, it is reported that the support is moved by the earthquake. If the phenomenon of both events is occurred, it is expected that the ultimate strength of the girder ends decline. In this study, FE analysis for the girder ends with corrosion has been carried out in order to understand effect of ultimate

strength behavior due to the eccentricity of the support of the girder end with corrosion of a plate girder for Highway Bridges.

#### **Discussion on A Design Method for a Emergency Crack Repair by Using High-strength Bolted Cover Plates**

Chao Pan, Takashi YAMAGUCHI, Akihisa KONDO (SOGO Engineering Inc.) and Yukiko MITSUGI (Ishikawa National College of Technology)

*Proceedings of Constructional Steel, Vol.21, JSSC, pp.216-223 (2003) (in Japanese)*

High-strength bolted cover plates often use for an emergency crack repair, designed as a friction-type joint. A friction-type joint should be designed must not slip in service for a structural connection. Actually, even if the friction-type joint slipped, it still has the shear and bearing resistance. So a design for the emergency crack repair may consider the shear and bearing resistance for repairing crack, and it is discussed based on a performance for a design method.

#### **Considerations on Seismic Behavior of Steel Bridge Piers installed Isolation Bearing with Triggers**

Masahide MATSUMURA, Takahiro KANATA, Yasuyuki NAKANISHI (NEWJEC Inc.) and Takashi YAMAGUCHI

*Proceedings of Constructional Steel, Vol.21, JSSC, pp.437-440 (2003) (in Japanese)*

Resent year, from the viewpoint of rational fabrication of the steel bridges, there are some applications using Side blocks are installed besides isolating bearings for restricting displacement of superstructure. The authors consider an adoption of trigger type of steel side blocks, which restrict the displacement of superstructure against a small and medium earthquake grand motion and release it against strong earthquake grand motions, in order to obtain isolation effect even in the transverse direction of the bridge axis. In this study, the fundamental behavior of the proposed bearing system is examined by shaking table test, analysis procedure to approximate the response is proposed, and installation effects of the trigger type of steel side blocks into an isolated viaduct on bridge pier response is computed through dynamic response analysis.

#### **Compression Tests of Steel Columns bonded CFRP Strips of High Elastic Modulus focusing on Adhesive Length**

Masahide MATSUMURA, Shinya KODA, Nobuhiro HISABE (Mitsubishi Plastics Inc.) and Takashi YAMAGUCHI

*Proceedings of the 7th International Symposium on Steel Structures, ISSS, Jeju, Korea, pp.92-93 (2013)*

Presented in this paper is strengthening technique of steel columns using CFRP strips as alternatives of steel plates bolted in conventional one. As both the axial and flexural rigidity can be improved more effectively when the elastic modulus of the strips is higher, so applications of the CFRP strips of high elastic modulus to steel columns are focused on in this study. Then carried out are compression tests of pin-connected steel column specimens adhered the CFRP strips with different adhesive patterns onto the flange plates. It is concluded that improvements of the initial stiffness and enhancement of the elastic range can be obtained by the adhered CFRP strips unless the debonding does not occur.

#### **Study on Dynamic Behavior of Isolated Viaduct with Triggers; Modeling and Analysis Procedure**

Masahide MATSUMURA, Takahiro KANATA, Yasuyuki NAKANISHI (NEWJEC Inc.) and Takashi YAMAGUCHI

*Proceedings of the 7th International Symposium on Steel Structures, ISSS, Jeju, Korea, pp.264-265 (2013)*

Bridge isolation using isolation rubber bearings effectively reduces damages of bridge pier and foundation and is widely used in Japan. Here as the isolation effects are required only against a strong earthquake, the authors propose combination use of the isolation bearings and triggers, which restrict the displacement of superstructure against a small and medium earthquake grand motion and release it against a strong earthquake grand motion. In the study, combination use of sliding bearings and the triggers are examined. Then, modeling and analysis procedure of a vibration system with the trigger is verified through shaking table test. And the break characteristics of the trigger are varied in seismic response analysis targeted a viaduct. It is concluded that the break load of the trigger greatly influences on the maximum displacement of the bridge pier and the trigger will be used for the maximum displacement control of the pier.

### **An Experimental Study on Seismic Performance of Hybrid Steel Piers with Vertical Ribs Made from SBHS700**

Kiyoshi ONO (Osaka University), Masahide MATSUMURA and Seiji OKADA (IHI Infrastructure System Co., Ltd.)

*US-Japan Bridge Workshop*, 10pages (2013)

Some methods for evaluating the seismic performance of steel bridge piers have been already proposed in the previous studies. Steel bridge piers are sometimes required to have seismic performance that ductility is improved with restraining increase in ultimate strength but it is difficult to fulfill such seismic performance by the proposed methods in previous studies. By the way, "Higher yield strength steel plates for bridges" has been standardized in Japanese industrial Standard (JIS). The major feature of higher yield strength steel plates for bridges, SBHS, is high yield strength and high weldability. Among SBHS, SBHS700 has the highest yield strength and the highest tensile strength. There is possibility of fulfilling the seismic performance of steel bridge piers which has been difficult to gain so far by applying SBHS700 to them. Therefore, the purpose of this study is to investigate material properties of SBHS700 and the seismic performance of hybrid steel bridge piers whose vertical ribs are made from SBHS700.

### **Prediction of Liquefaction and Countermeasure due to Groundwater Lowering Method in Osaka and Wakayama plains**

Akihiko OSHIMA, Yuji HAYASHI, Teruyuki HAMADA and Mari KASUGAI

*Journal of the Society of Materials Science Japan*, Vol.63, No. 8, pp.614-619, 2014 (in Japanese)

The influence of groundwater rising for the liquefaction potential in Osaka and Wakayama plains was examined using GIS in which a digital database of underground information provided by Kansai Geo-informatics Database was introduced. The detailed geotechnical properties were calculated and given to Holocene sandy and clayey deposits that are representative value in each digital mesh of 250m×250m areas. Then, liquefaction safety assessments were carried out by estimating pumping possible quantity of Holocene sandy deposits and considering negative effect of them against consolidation settlement problem that will occur in Holocene clayey deposits underneath. The efficacy of groundwater lowering method against liquefaction of Holocene sandy deposits was verified.

### **Comparison of Various Sounding Tests on General Site Investigations**

*Symposium of Ground Investigation Method for Small Buildings, Architectural Institute of Japan*, pp.7-16, 2013 (in Japanese)

Akihiko OSHIMA

### **Shaking Model Tests on Mitigation of Liquefaction-Induced Ground Flow by New Configuration of Embedded Columns**

Naoki TAKAHASHI, Derakhshani ALI, Rasouli ROUZBEH, Ikuo Towhata and Suguru YAMADA

*Proc. of the 18th International Conference on Soil Mechanics and Geotechnical Engineering, Paris*, pp. 1623-1626, 2013.

Traditionally, countermeasures against seismic liquefaction aimed to prevent significant development of excess pore water pressure. Although this aim was achieved by a variety of measures, the limitation has been understood as well in the recent times. The limitation is typically found in lifelines and transportation lines (road embankment) together with river levees for which financial requirement is more strict and also residual deformation is allowed to occur to a certain extent. In this regard, the present study addresses installation of stable cement-mixed soil columns in liquefaction-prone subsoil so that ground deformation may be constrained during earthquakes and lateral flow of liquefied sand may be reduced. For its validation, two types of shaking-table model tests have been conducted in 1-G environments.

### **A Study on Effect of Discharge of Thermal Water on Structure of Water Temperature in an Enclosed Bay**

Takaaki SHIGEMATSU and Masatoshi MAEKAWA

*Proceedings of the Twenty-third (2013) International Offshore and Polar Engineering*, pp. 1314-1320 (2013)

Numerical simulation is carried out to evaluate effect of urban heat release into an enclosed sea on the water temperature. To improve the condition of releasing the thermal effluent, the resolution near release point was made higher using two-way nesting method. As a result, it is found that the effect was not influenced by only

conditions of release but tidal range, tidal elevation, and wind condition. Moreover, it is found that sea surface temperature in Osaka Bay strongly depends on wind stress.

#### **An Experimental Study on Development of a Breakwater Using Circular Cylinder Array**

Kotaro TAKATA, Takaaki SHIGEMATSU, Kenji KATOH, Tatsuro WAKIMOTO and Shinya YOSHIOKA  
*Journal of Japan Society of Civil Engineers, Ser. B2 (Coastal Engineering)*, Vol. 69, No. 2, pp. I\_996-I\_1000 (2013)

In this study, a new type breakwater with a submerged circular cylinder array was developed. Laboratory experiments were carried out for investigation on effect of the height of submerged circular cylinder array on wave absorber function. Experimental results were compared with theoretical solutions. For the other type of a new breakwater with rotatable circular cylinder array, the characteristics of wave absorption were investigated.

#### **An Experimental Study on Microscopic Flow Over and Inside Porous Medium Placed on Oscillatory Flow**

Yuya OKADA, Takaaki SHIGEMATSU and Sota NAKAJO

*Journal of Japan Society of Civil Engineers, Ser. B2 (Coastal Engineering)*, Vol. 69, No. 2, pp. I\_036-I\_040 (2013)

In order to investigate interaction between upper and inside flow of a porous medium, the microscopic structure of upper and inside flow of the porous medium placed in oscillatory flow was measured by the Particle Tracking Velocimetry (PTV) with the refractive index matching method. The strong shear flow was observed in the vicinity of the porous medium and the depth of shear flow varied with the phase of the oscillatory flow. The depth of non-dimensional shear flow was almost constant and it independent with the Reynolds number. Besides, the phase difference of oscillatory flow between upper and inside flow of the porous medium was observed.

#### **An Experimental Study on Properties of Turbulence induced by Oscillatory Flow Over Porous Medium**

Yuya OKADA, Takaaki SHIGEMATSU and Sota NAKAJO

*Journal of Japan Society of Civil Engineers, Ser. B2 (Coastal Engineering)*, Vol. 69, No. 2, pp. I\_041-I\_045 (2013)

The internal and external fluid flows induced by oscillatory flow over a porous medium were measured by the Particle Tracking Velocimetry (PTV) with matching the refraction index method using two high-speed cameras. The characteristics of spatial variance of velocity components were shown in detail with the time phase variance. Further, the properties of the turbulent quantities such as turbulent kinematic energy and the Reynolds' stress were presented and the relationship among the turbulence properties, the Reynolds' number, and the KC number was discussed.

#### **The Evaluation of Sewage Temperature and Flow Rate for Estimating Sewage Temperature and Flow Rate in Sewer Line**

Masahito MIKE, Minako NABESHIMA, Masatoshi NISHIOKA, Koichi SAWABE, Masaki NAKAO, Yoshinori KANJO

*Journal of the Society of Heating, Air-Conditioning and Sanitary Engineers of Japan, No.202, pp.11-21, 2014 (in Japanese)*

In order to promote the opportunity of using heat energy of sewage, it is required to estimate sewage temperature and sewage flow rate near domestic and industrial the buildings. In this study, we measured the sewage temperature and flow rate at 17 locations in three different sewer lines in Osaka city. As the result, we observed that the trend of the hourly sewage flow rate and the hourly ratio of house water consumption are similar in the sewage lines corresponding to large housing ratios. Analyzed the correlation of the monthly average sewage temperature and air temperature, we obtained highly accurate regression equation.

#### **Proposal for Estimating Sewage Flow on Sunny Days in Sewer Line using Sewage Heat**

Masahito MIKE, Minako NABESHIMA, Masatoshi NISHIOKA, Koichi SAWABE, Masaki NAKAO and Yoshinori KANJO

*Journal of the Society of Heating, Air-Conditioning and Sanitary Engineers of Japan, No.204, pp.47-55, 2014 (in Japanese)*

In order to increase the opportunity of using sewage heat from sewer lines, the sewage flow in sewer lines near buildings needs to be estimated. We determined the sewage characteristics by measuring the sewage flow of a sewer line in Osaka City, and proposed a method to estimate the sewage flow in a sewer line. This method can be applied to combined sewage on sunny days, and it can be estimate the sewage flow in an optional area by referring to a known source at sewage plants. The Sewage flow is calculated by multiplying the known sewage flow by the ratio of the estimated total floor area of buildings in the catchment area to the measured total floor area of such buildings. The estimation method can be applied to a separate sewer system and combined sewer system on a sunny day. The estimated values were approximately 0.7 - 1.1 of the measured data. We proposed a method for estimating the hourly flow rate in a single regression model. The explanatory variable of this model is the residential floor area ratio.

### **Reducing Excess Sludge from Bread Plant Wastewater Treatment: Combined Process of Contact Oxidation and Aerobic Digestion**

Shojiro OSUMI, Katsutoshi NAKAYAMA, Akihito KUMAMI, Yoshinori KANJO

*Journal of Environmental Conservation Engineering, Vol.43, No.3, pp.162-171, 2014 (in Japanese)*

Seeking to reduce the amount of excess sludge at a bread plant, we designed the following process first, wastewater, including oil, is treated by contact oxidation; then it is separated into supernatant and floating scum by pressurized floatation. After aerobic digestion of the scum, the supernatant and the treated scum are mixed and discharged as sewage. If the mixed fluid suits for the standard for discharge into sewage, excess sludge disposal is not necessary. We tested whether the above system was workable or not. We conducted experiments on continuous contact oxidation for 230 days and continuous aerobic digestion of scum for 60 days, which resulted in a BOD removal ratio of 97% and a BOD to SS conversion ratio of 0.13 g-SS/g-removed BOD by contact oxidation and a SS degradation ratio of 58.9% by aerobic digestion of the scum. We also showed that it is possible to express the results of the batch-wise aerobic digestion experiment with a model based on the first-order reaction supposing the existence of easily degradable, persistent, and undegradable compounds in the sludge. Finally, we calculated the material balance of the entire system and showed that the wastewater from the bread plant where we tested, including 1,200 mg/L of BOD and 450 mg/L of SS, could be treated by the process we designed with no excess sludge disposal required. This treated water includes 80 mg/L of BOD and 99 mg/L of SS and could be discharged into sewers.

### **Recovery of the Rare Metals from Various Waste Ashes with the Aid of Temperature and Ultrasound Irradiation Using Chelants**

Hiroshi HASEGAWA, Ismail M. M. RAHMAN, Yuji EGAWA, Hikaru SAWAI, Zinnat A. BEGUM, Teruya MAKI, Satoshi MIZUTANI

*Water Air Soil Pollut.* 225, 2112, (2014)

The incineration fly ash (IFA), molten fly ash (MFA), thermal power plant fly ash (TPP-FA), and nonferrous metal processing plant ash (MMA) have been screened in terms of the following rare-termed metal contents: B, Ce, Co, Dy, Eu, Ga, Gd, Hf, In, Li, Lu, Mn, Nb, Nd, Ni, Pr, Rb, Sb, Se, Sm, Sr, Ta, Tb, Te, Ti, Tm, V, W, Y, and Yb. The pseudo-potential for recycling of the waste ashes, as compared to the cumulative concentration in the crust ( $\text{mg kg}^{-1}$ ), was determined as follows: MMA>IFA>MFA>TPP-FA. The comparison with the crude ore contents indicates that the MMA is the best resource for reprocessing. The recovery of the target metals using aminopolycarboxylate chelants (APCs) has been attempted at varying experimental conditions and ultrasound-induced environment. A better APC-induced extraction yield can be achieved at  $0.10 \text{ mol L}^{-1}$  concentration of chelant, or if the system temperature was maintained between 60 to 80 °C. Nevertheless, the mechanochemical reaction induced by the ultrasound irradiation has been, so far, the better option for rare metal dissolution with chelants as it can be conducted at a minimum chelant concentration ( $0.01 \text{ mol L}^{-1}$ ) and at room temperature ( $25 \pm 0.5 \text{ }^\circ\text{C}$ ).

### **Selective Separation of Tri- and Pentavalent Arsenic in Aqueous Matrix with a Macrocyclic-Immobilized Solid-Phase Extraction System**

Ismail M. M. RAHMAN, Zinnat A. BEGUM, Yoshiaki FURUSHO, Satoshi MIZUTANI, Teruya MAKI, Hiroshi HASEGAWA

*Water Air Soil Pollut.* 224, 1526, 2013

A simple flow-based method was developed for the selective separation of arsenic species (+3 and +5) using a macrocycle-immobilized solid phase extraction (SPE) system, commonly known as molecular recognition technology (MRT) gel. Arsenic species in solution or in the eluent were subsequently quantified with graphite furnace atomic absorption spectrometry. The separation behaviors of As(III) and As(V) on MRT–SPE were investigated. It was found that As(V) can be selectively collected on the SPE system within the range of pH 4 to 9, while As(III) was passed through the MRT–SPE. The retention capacity of the MRT–SPE material for As(V) was found to be  $0.25 \pm 0.04 \text{ mmol g}^{-1}$ . The detection limit of the method for As(V) was  $0.06 \mu\text{g L}^{-1}$ , and the relative standard deviation was 2.9 % ( $n=10$ ,  $C=1 \mu\text{mol L}^{-1}$ ). Interference from the matrix ions was studied. In order to validate the developed method, certified reference materials of effluent wastewater and groundwater samples were analyzed, and the determined values were in good agreement with the certified values. The proposed method was successfully applied to the speciation analysis of tri- and pentavalent arsenic in natural water samples showing satisfactory recoveries ( $\geq 98.7 \%$ ).

#### **Effect of Extraction Variables on the Biodegradable Chelant-Assisted Removal of Toxic Metals from Artificially Contaminated European Reference Soils**

Zinnat A. BEGUM, Ismail M. M. RAHMAN, Hikaru SAWAI, Satoshi MIZUTANI, Teruya MAKI, Hiroshi HASEGAWA

*Water Air Soil Pollut*, 224, 1381, (2013)

Development of aminopolycarboxylate chelants (APCs) having enhanced biodegradability is gaining increasing focus to replace the EDTA and its homologs with those used widely for the ex situ treatment of contaminated soils and are potential eco-threats. The paper reports the chelant-assisted extraction of the toxic metals (Cd, Cu, Pb, and Zn) from the metal-spiked European reference soils (Eurosoil 1 and Eurosoil 4) using biodegradable APCs, namely EDDS, GLDA, and HIDS. The effects of chelant-to-metal molar ratio, solution pH, and metal/chelant stability constants were evaluated, and compared with that of EDTA. The selectivity aptitude of the biodegradable chelants towards the toxic metals was assumed from the speciation calculations, and a proportionate correlation was observed at neutral pH. Pre- and post-extractive solid phase distributions of the target metals were defined using the sequential extraction procedure and dissolution of metals from the theoretically immobilized fraction was witnessed. The effect of competing species (Al, Ca, Fe, Mg, and Mn) concentrations was proven to be minimized with an excess of chelant in solution. The highlight of the outcomes is the superior decontamination ability of GLDA, a biodegradable APC, at minimum chelant concentration in solution and applicability at a wide range of pH environments.

#### **Validity Verification of Measurement Method of Carbon Dioxide Concentration in Water using Water-resistant Breathable Tube**

Toru ENDO, Toshiyuki TANAKA, Sosuke OTANI, Tetsuro FUJITA and Susumu YAMOCHI

*Journal of Japan Society of Civil Engineers, Ser. B2 (Coastal Engineering)*, Vol. 69, No. 2, pp. I\_1251-I\_1255 (2013) (in Japanese)

A carbon dioxide meter with water-resistant breathable tube was developed in order to measure  $\text{CO}_2$  concentration in water. Laboratory experiments were conducted for verification of the effectiveness of this method. After measuring the time variations of  $\text{CO}_2$  concentration in water aerating by air pump or adding carbonic water, it was confirmed that this method was useful to evaluate the carbon cycle in coastal zone. Furthermore, the  $\text{CO}_2$  production from sediment by decomposition of organic matter was confirmed by measuring the time variations of  $\text{CO}_2$  and DO concentrations in the water above sediment at the same time.

#### **A Study on Mitigation of Density Stratification with Jet by Using Visualization Experiments**

Tetsuya KOJO and Toru ENDO

*Journal of Japan Society of Civil Engineers, Ser. B2 (Coastal Engineering)*, Vol. 69, No. 2, pp. I\_1226-I\_1230 (2013) (in Japanese)

Mitigation of density stratification with jet was evaluated by using visualization experiments. First, we developed a simple and high accuracy image analysis method to estimate the spatial distribution of density of water. Then, we experimented on various types of stratified field changing Froude number of the jet. We verified that entrainment by jet and internal wave breakings are important to consider water mixing in density stratified fields. Furthermore, we defined the practical parameter including both the impact on the field and the potential energy of the field. The parameter has a linear relation to the volume of new layer formed after water mixing.

### **A Method for Preventing the Outbreak of Green Tides at the Osaka Nanko Bird Sanctuary**

Ryo SHIMANAMI, Toru ENDO and Susumu YAMOCHI

*Journal of Japan Society of Civil Engineers, Ser. B2 (Coastal Engineering)*, Vol. 69, No. 2, pp. I\_1161-I\_1165 (2013) (in Japanese)

Field surveys and laboratory experiments were carried out to prevent the outbreak of green tides at the north pond of Osaka Nanko bird sanctuary. Dense blooms of green algae, *Ulva pertusa*, *Ulva ohnoi* and *Rhizoclonium riparium* were frequently observed in 2005-2012 and the most dominant species gradually changed from *Ulva pertusa* to *Ulva ohnoi*, which is partly due to temperature increase and low salinity at a growing season. Laboratory experiments revealed that photosynthesis was inhibited when they were exposed to air for 6 hours at 35°C followed by a low salinity of 20psu. These results suggest the possibility of controlling green tides of *Ulva pertusa* and *Ulva ohnoi* by a combination of exposure to air with low salinity in summer.

### **The Problem and Improvement on the Quantification Method of CO<sub>2</sub> Absorption at an Artificial Tidal Flat**

Toshiyuki TANAKA, Tetsuro FUJITA and Susumu YAMOCHI

*Journal of Japan Society of Civil Engineers, Ser. B2 (Coastal Engineering)*, Vol. 69, No. 2, pp. I\_1176-I\_1180 (2013) (in Japanese)

CO<sub>2</sub> concentrations were measured with light and dark chambers at an artificial tidal flat of Osaka Nanko bird sanctuary in the spring and summer of 2012 to examine the effect of benthic microalgae, macrobenthos and bacteria. CO<sub>2</sub> emission rate from the sediment was almost constant during a measuring interval in the dark chamber, while its absorption rate markedly decreased with time in the light chamber. The rapid decrease of CO<sub>2</sub> absorption rate was thought to be caused by low CO<sub>2</sub> concentration in the light chamber in accompanied with increasing photosynthetic activity of the benthic microalgae. To measure the absorption of CO<sub>2</sub> with a difference less than 40ppm from the atmosphere level, a ventilation rate of 10L air/min is indispensable for the light chamber along with a bottom area below 450cm<sup>2</sup>.

### **A Research on the Fluctuation of CO<sub>2</sub> Flux from the Sediment of a Tidal Flat in accompanied with Tidal Change**

Tetsuro FUJITA, Toru ENDO, Toshiyuki TANAKA and Susumu YAMOCHI

*Journal of Japan Society of Civil Engineers, Ser. B2 (Coastal Engineering)*, Vol. 69, No. 2, pp. I\_1181-I\_1185 (2013) (in Japanese)

Field surveys and indoor experiments were conducted at the north tidal flat of Osaka Nanko bird sanctuary in 2012 in order to measure the amount of discharge of the carbon dioxide (CO<sub>2</sub>) which is an index of the amount of organic matter decomposition. The field survey revealed that CO<sub>2</sub> flux increased with decrease of the groundwater level when the bottom sediment emerged. The CO<sub>2</sub> flux in the submerged period showed 0.2-1.2 mgCO<sub>2</sub>/m<sup>2</sup>/min which was less than 1/5 to 1/40 of the emerged period. In addition, the result of field surveys together with indoor experiments suggested that CO<sub>2</sub> flux changed depending on the flood tide or falling tide as well as the groundwater level.

